

The Pennsylvania State University
The Graduate School
College of Engineering

**NOVEL FREQUENCY DOMAIN TECHNIQUES AND ADVANCES
IN FINITE DIFFERENCE TIME DOMAIN (FDTD) METHOD FOR
EFFICIENT SOLUTION OF MULTISCALE ELECTROMAGNETIC
PROBLEMS**

A Dissertation in
Electrical Engineering
by
Kadappan Panayappan

© 2013 Kadappan Panayappan

Submitted in Partial Fulfillment
of the Requirements
for the Degree of

Doctor of Philosophy

May 2013

The dissertation of Kadappan Panayappan was reviewed and approved* by the following:

Raj Mittra
Professor of Electrical Engineering
Dissertation Adviser
Co-Chair of Committee

James Breakall
Professor of Electrical Engineering
Co-Chair of Committee

Douglas Werner
John L. and Genevieve H. McCain Chair Professor

Michael T. Lanagan
Professor of Engineering Science and Mechanics

Kultegin Aydin
Professor of Electrical Engineering
Head of the Department of Electrical Engineering

*Signatures are on file in the Graduate School.

Abstract

With the advent of sub-micron technologies and increasing awareness of Electromagnetic Interference and Compatibility (EMI/EMC) issues, designers are often interested in full-wave solutions of complete systems, taking to account a variety of environments in which the system operates. However, attempts to do this substantially increase the complexities involved in computing full-wave solutions, especially when the problems involve multi-scale geometries with very fine features. For such problems, even the well-established numerical methods, such as the time domain technique FDTD and the frequency domain methods FEM and MoM, are often challenged to the limits of their capabilities. In an attempt to address such challenges, three novel techniques have been introduced in this work, namely Dipole Moment (DM) Approach, Recursive Update in Frequency Domain (RUFD) and New Finite Difference Time Domain (ν FDTD). Furthermore, the efficacy of the above techniques has been illustrated, via several examples, and the results obtained by proposed techniques have been compared with other existing numerical methods for the purpose of validation.

The DM method is a new physics-based approach for formulating MoM problems, which is based on the use of dipole moments (DMs), as opposed to the conventional Green's functions. The absence of the Green's functions, as well as those of the vector and scalar potentials, helps to eliminate two of the key sources of difficulties in the conventional MoM formulation, namely the singularity and low-frequency problems. Specifically, we show that there are no singularities that we need to be concerned with in the DM formulation; hence, this obviates the need for special techniques for integrating these singularities. Yet another salutary feature of the DM approach is its ability to handle thin and lossy structures, or whether they are metallic, dielectric-type, or even combinations thereof. We have found that the DM formulation can handle these types of objects

with ease, without running into ill-conditioning problems, even for very thin wire-like or surface-type structures, which lead to ill-conditioned MoM matrices when these problems are formulated in the conventional manner. The technique is valid over the entire frequency range, from low to high, and it does not require the use of loop-star type of basis functions in order to mitigate the low frequency problem.

Next, we have introduced the RUFD, which is a general-purpose frequency domain technique, and which still preserves the salutary features of the time domain methods. RUFD is a frequency domain Maxwell-solver, which neither relies upon iterative nor on inversion techniques. The algorithm also preserves the advantages of the parallelizability—which is a highly desirable attribute of CEM solvers—by using the difference form of Maxwell’s equations. Since RUFD solves the Maxwell’s equations in a recursive manner, without using either iteration or inversion, the problems of dealing with ill-conditioned matrices, or constructing robust pre-conditioners are totally avoided. Also, as a frequency domain solver, it can handle dispersive media, including plasmonics, relatively easily.

The conventional time domain technique FDTD demands extensive computational resources when solving low frequency problems, or when dealing with dispersive media. The ν FDTD (New FDTD) technique is a new general-purpose field solver, which is designed to tackle the above issues using some novel approaches, which deviate significantly from the legacy methods that only rely on minor modifications of the FDTD update algorithm. The ν FDTD solver is a hybridized version of the conformal FDTD (CFDTD), and a novel frequency domain technique called the Dipole Moment Approach (DM Approach). This blend of time domain and frequency domain techniques empowers the solver with potential to solve problems that involve: (i) calculating low frequency response accurately and numerically efficiently; (ii) handling non-Cartesian geometries such as curved surfaces accurately without staircasing; (iii) handling thin structures, with or without finite losses; and (iv) dealing with multi-scale geometries.

Table of Contents

List of Figures	x
List of Tables	xix
Acknowledgements	xxi
1 Introduction	1
1.1 Electromagnetics	1
1.2 Theoretical Methods of Analysis	2
1.3 Computational Methods	3
1.4 Motivation	4
1.5 Outline of Research Methodology	5
1.6 Organization of the Thesis	6
2 Dipole Moment Approach	7
2.1 Introduction	7
2.2 Dipole Moment Concept	8
2.3 Formulation for PEC Objects	9
2.3.1 Geometry Modeling	9
2.3.2 Numerical Results	11
2.4 Formulation for Dielectric Objects	17

2.4.1	Geometry Modeling	17
2.4.2	Numerical Results	18
2.5	Formulation for Inhomogeneous Objects	22
2.5.1	Geometry Modeling	22
2.5.2	Numerical Results	23
2.6	Quasi-Static Formulation	24
2.7	Order of Singularity	27
2.8	Observations and Conclusions	27
3	Performance Enhancement of DM Approach	29
3.1	Introduction	29
3.2	Higher Order Macro-Basis Function	30
3.2.1	Numerical Results	31
3.3	Characteristic Basis Functions	34
3.4	Fast Matrix Generation	36
3.5	Closed-form Field Expressions	38
3.5.1	Numerical Results using Triangular Basis Functions	42
3.5.2	Numerical Results Obtained by using Rooftop Basis Functions	48
3.6	Some Embellishments to the Basic DM Approach	50
3.6.1	Incorporating Lumped Loads	50
3.6.2	Input Impedance of Nano Antennas	53
3.6.3	Irregular Geometries	55
3.6.4	Curved Surfaces	57
3.6.5	Geometries with Apertures	60
3.6.6	Microstrip-based Structures	64

3.7	Observations and Conclusions	67
4	Recursive Update in Frequency Domain (RUFD)	69
4.1	Introduction	69
4.2	RUFD Algorithm	70
4.3	Stability Condition	71
4.4	Source Settings	71
4.5	Incorporating Lumped Resistance	72
4.6	Absorbing Boundary Conditions	72
4.7	Types of Formulation	73
4.7.1	Total Field Formulation	74
4.7.2	Total Field/Scattered Field Formulation	76
4.7.3	Scattered Field Formulation	78
4.8	Performance Enhancement of RUFD	81
4.8.1	Post-Processing	81
4.8.2	Effect of Time Step on Convergence	86
4.8.3	Effect of Losses on Convergence	87
4.8.4	Initializing Using DM Approach	88
4.8.5	S-Parameter Calculations	90
4.8.6	Sub-Gridding Approach	92
4.8.7	Improving the Computational Efficiency	93
4.8.8	Calculation of Frequency Response	96
4.9	Observations and Conclusions	97
5	On the Hybridization of RUFD Algorithm	99
5.1	Introduction	99

5.2	Iterative Approach	101
5.3	Self-Consistent Approach	105
5.4	Vicinity of PML	111
5.5	Multi-Grid Approach	112
5.6	Handling Inhomogeneous Objects with Fine Features	120
5.6.1	Large Objects with Coating	121
5.6.2	Coated Small Objects	122
5.7	Observations and Conclusions	124
6	New Finite Difference Time Domain (νFDTD) Algorithm	126
6.1	Introduction	126
6.2	ν FDTD Solver	127
6.3	Low Frequency Response	128
6.3.1	RF and Digital Circuits	131
6.3.2	Scattering Problems	133
6.4	Non-Cartesian Geometries	138
6.4.1	Asymptotic Method	141
6.4.2	Averaging Technique	149
6.4.3	Advantages	154
6.5	Multiscale Problems	155
6.6	Performance Enhancement	157
6.6.1	Signal Processing Techniques	157
6.6.2	Absorbing Boundary Condition	160
6.6.3	Well-Logging Applications	163
6.7	Observations and Conclusions	165

7 Conclusions and Future Work	167
Bibliography	174

List of Figures

2.1	A PEC rod.	12
2.2	Amplitude comparison of backscattered electric field E_y from the PEC rod in Fig. 2.1.	12
2.3	A PEC circular loop.	13
2.4	Frequency variation of the feed current for a PEC loop shown in Fig. 2.3. .	14
2.5	A PEC helix.	15
2.6	Amplitude comparison of radiated electric field E_x from the PEC helix in Fig. 2.5.	15
2.7	The magnitude of current calculated using a commercial MoM solver for the PEC helix shown in Fig. 2.5.	16
2.8	A PEC sphere.	16
2.9	Amplitude comparison of backscattered electric field E_z from the PEC sphere in Fig. 2.8.	17
2.10	A dielectric rod.	19
2.11	Amplitude comparison of backscattered electric field E_y from the dielectric rod in Fig. 2.10.	19
2.12	A dielectric plate.	20
2.13	Amplitude comparison of backscattered electric field E_y from the dielectric plate in Fig. 2.12.	20
2.14	Plasmonic nano-spheres.	21

2.15	Amplitude comparison of scattered electric field E_y from the plasmonic spheres in Fig. 2.14.	22
2.16	A PEC rod with a dielectric coating.	23
2.17	Amplitude comparison of backscattered electric field E_y from the coated rod in Fig. 2.16.	24
2.18	A PEC helix.	26
2.19	Amplitude comparison of backscattered electric field E_x from the PEC helix in Fig. 2.5.	26
3.1	A dielectric plate.	30
3.2	A PEC sphere.	31
3.3	Amplitude comparison of scattered electric field E_z from the PEC sphere in Fig. 3.2.	32
3.4	Amplitude comparison of backscattered electric field E_y from the dielectric plate in Fig. 3.1.	33
3.5	A PEC rod.	35
3.6	Calculated CBFs for the PEC rod in Fig. 3.5.	35
3.7	Amplitude comparison of backscattered electric field E_y from the PEC rod in Fig. 3.5.	36
3.8	Amplitude comparison of backscattered electric field E_y from the dielectric plate in Fig. 3.1.	37
3.9	Triangular current distribution placed along Z axis from $-\lambda/20$ to $\lambda/20$	39
3.10	Amplitude variation of E_z at a $z = \lambda/50$ radiated by the current distribution shown in Fig. 3.9.	40
3.11	Amplitude variation of E_z at a $z = 500\lambda$ radiated by the current distribution shown in Fig. 3.9.	41
3.12	A bent wire.	41
3.13	A wire geometry.	43
3.14	Amplitude variation of E_y along the observation line in λ for the wire geometry in Fig. 3.13.	43

3.15 A PEC rod.	44
3.16 Frequency variation of peak current for the PEC rod in Fig. 3.15.	45
3.17 Frequency variation of condition number for the PEC rod in Fig. 3.15.	46
3.18 A PEC circular loop.	47
3.19 Amplitude variation of the induced current for the PEC loop in Fig. 3.18.	47
3.20 A Rooftop basis function.	48
3.21 A PEC plate.	49
3.22 Amplitude comparison of backscattered electric field E_y from the PEC plate in Fig. 3.21.	50
3.23 A PEC circular loop with a capacitor.	51
3.24 Frequency variation of the input current in a PEC loop shown in Fig. 3.23.	52
3.25 A geometry of a power coil.	53
3.26 Frequency variation of the peak output current for a power coil shown in Fig. 3.25.	54
3.27 A vertical monopole antenna.	55
3.28 Amplitude variation of the current for a monopole shown in Fig. 3.27.	55
3.29 A PEC plate with a staircase corner.	56
3.30 Amplitude comparison of scattered electric field E_θ at $\phi = 45^\circ$ from the PEC geometry in Fig. 3.29.	57
3.31 A corner reflector.	58
3.32 Amplitude comparison of backscattered electric field E_z from the corner reflector in Fig. 3.31.	59
3.33 A faceted PEC surface.	59
3.34 Amplitude comparison of backscattered electric field E_z from the faceted PEC surface in Fig. 3.33.	60
3.35 A PEC plate with a split.	61
3.36 Amplitude comparison of backscattered electric field E_y from the PEC surface in Fig. 3.35.	61

3.37	A PEC plate with a square slot.	62
3.38	Equivalent magnetic current.	63
3.39	Amplitude variation of the radiated electric field E_y from the equivalent magnetic current in Fig. 3.38.	63
3.40	Amplitude comparison of backscattered electric field E_y from the PEC surface in Fig. 3.37.	64
3.41	A PEC plate with a rectangular slot.	65
3.42	Amplitude comparison of backscattered electric field E_y from the PEC geometry in Fig. 3.41.	65
3.43	A microstrip geometry.	66
3.44	Variation of I_x along the trace of a microstrip line in Fig. 3.43.	67
3.45	A microstrip geometry.	67
3.46	Amplitude comparison of backscattered field E_x from a microstrip line in Fig. 3.45.	68
4.1	A square PEC sheet.	73
4.2	Amplitude variation of the scattered E_z from a square PEC sheet shown in Fig. 4.1.	74
4.3	Geometry of a PEC dipole antenna (Not to Scale).	75
4.4	Amplitude variation of the feed current for a PEC dipole antenna shown in Fig. 4.3.	75
4.5	A 2D computational domain.	76
4.6	A dielectric cube.	77
4.7	Amplitude variation of the forward scattered field E_z from a dielectric cube shown in Fig. 4.6.	78
4.8	A PEC cube embedded in a dielectric cube.	79
4.9	A square PEC plate.	79
4.10	Amplitude variation of the total field E_z from a PEC plate shown in Fig. 4.9.	80

4.11 A typical signature generated in the RUFD algorithm.	82
4.12 A patch antenna.	83
4.13 A waveguide filter.	83
4.14 A RF filter.	84
4.15 Signature generated in RUFD algorithm for a PEC plate shown in Fig. 4.9.	85
4.16 A square PEC patch.	86
4.17 Amplitude variation of the scattered field E_y from a PEC patch shown in Fig. 4.16.	87
4.18 Signature generated in RUFD algorithm for a PEC patch shown in Fig. 4.16.	88
4.19 Amplitude variation of the scattered field E_y from a PEC patch shown in Fig. 4.16.	89
4.20 Signature generated in RUFD algorithm for a PEC patch shown in Fig. 4.16.	90
4.21 Amplitude variation of the scattered field E_y from a PEC patch shown in Fig. 4.16.	91
4.22 Signature generated in RUFD algorithm for a PEC patch shown in Fig. 4.16.	92
4.23 Variation of S_{11} for the RF filter shown in Fig. 4.14.	93
4.24 Variation of S_{21} for the RF filter shown in Fig. 4.14.	94
4.25 A computational domain with sub-gridding.	94
4.26 Amplitude variation of the backscattered field E_z from a PEC sheet shown in Fig. 4.1.	97
5.1 A multiscale problem.	100
5.2 A multiscale problem meshed for RUFD simulation.	101
5.3 A multiscale problem meshed for hybrid RUFD simulation.	102
5.4 A $\lambda/20$ dipole antenna over a finite ground plane (not to scale).	103
5.5 Amplitude comparison of E_y field for the multiscale problem shown in Fig. 5.4.	104
5.6 A $\lambda/2$ dipole antenna over a finite ground plane (not to scale).	106

5.7	Amplitude comparison of E_y field for the multiscale problem shown in Fig. 5.6.	107
5.8	Amplitude comparison of E_y field for the multiscale problem with a $\lambda/20$ thick finite ground plane.	108
5.9	A lossy sphere over a finite ground plane (not to scale).	109
5.10	Amplitude comparison of scattered E_y field for the problem shown in Fig. 5.9.	109
5.11	A circular loop over a finite ground plane (not to scale).	110
5.12	Amplitude comparison of E_y field for the loop shown in Fig. 5.11 with a feed gap source.	110
5.13	Amplitude comparison of total E_y field for the loop shown in Fig. 5.11 with a plane wave illumination.	111
5.14	A square PEC sheet.	112
5.15	Amplitude comparison of scattered E_z field for different distances between the PML boundary and the PEC sheet shown in Fig. 5.14.	113
5.16	A multiscale problem meshed for multi-grid RUFD simulation.	114
5.17	A square PEC plate.	115
5.18	Amplitude comparison of scattered E_y field for the PEC plate shown in Fig. 5.17.	115
5.19	A PEC loop over a finite ground plane (not to scale).	116
5.20	Amplitude comparison of scattered E_y field for the PEC loop shown in Fig. 5.19.	117
5.21	A PEC helix over a finite ground plane (not to scale).	118
5.22	Amplitude comparison of radiated E_z field for the PEC helix shown in Fig. 5.21.	118
5.23	A PEC dipole placed over a finite ground plane (not to scale).	119
5.24	Amplitude comparison of radiated E_y field for the PEC dipole shown in Fig. 5.23.	120
5.25	A PEC dipole placed over a coated finite ground plane (not to scale). . . .	121

5.26	Amplitude comparison of radiated E_y field for the PEC dipole shown in Fig. 5.25.	122
5.27	A coated PEC dipole placed over a finite ground plane (not to scale). . . .	123
5.28	Amplitude comparison of radiated E_y field for the PEC dipole shown in Fig. 5.27.	123
6.1	An elliptical geometry.	127
6.2	A very thin sheet.	128
6.3	PEC loop over a finite ground plane.	128
6.4	A 32 port connector with a overall dimension of 5.6 x 11.88 x 27.35 mm (Housing not shown here).	130
6.5	Variation of the transmission co-efficient S_{21} for the 32 port connector shown in Fig.6.4.	130
6.6	Variation of the isolation co-efficient S_{31} for the 32 port connector shown in Fig.6.4.	131
6.7	Variation of the transmission co-efficient S_{21} for the 32 port connector shown in Fig.6.4 calculated using ν FDTD.	133
6.8	Variation of the isolation co-efficient S_{31} for the 32 port connector shown in Fig.6.4 calculated using ν FDTD.	133
6.9	A 8 port connector (Housing not shown here).	134
6.10	Variation of the S_{31} for the 8 port connector shown in Fig.6.9.	134
6.11	A PEC sphere of diameter $\frac{\lambda}{20}$ at 10 GHz.	137
6.12	Amplitude variation of the scattered E_y at a point $z = 0.25cm$ with frequencies from 1Hz to 30 GHz.	137
6.13	Amplitude variation of the scattered E_y with distance along z from $\frac{\lambda}{67}$ to $\frac{\lambda}{10}$, at 1.8 GHz.	138
6.14	A PEC cube of side length $\frac{\lambda}{20}$ at 10 GHz.	138
6.15	Amplitude variation of the scattered E_y at a point with frequencies from 1Hz to 30 GHz.	139
6.16	Meshing of a non-Cartesian geometry by the conventional FDTD	140

6.17 A partially-filled cell.	140
6.18 A inclined PEC sheet(not to scale).	142
6.19 Amplitude variation of the scattered E_x with distance along y at 10 GHz. .	143
6.20 Amplitude variation of the scattered E_x with distance along y at 10 GHz. .	144
6.21 A faceted PEC surface (not to scale).	144
6.22 Amplitude variation of the backscattered E_z with distance along y at 10 GHz.	145
6.23 A PEC wedge.	146
6.24 Amplitude variation of the scattered E_z with distance along x at 10 GHz. .	146
6.25 A PEC cylinder.	147
6.26 Amplitude variation of the backscattered E_z with distance along x at 10 GHz.	147
6.27 A dielectric slab (not to scale).	148
6.28 Amplitude variation of the backscattered E_z with distance along y at 10 GHz.	149
6.29 Phase variation of the backscattered E_z at $y = \lambda/40$	150
6.30 A PEC rectangular cylinder with mitered corner.	151
6.31 Principle behind the averaging technique.	151
6.32 Amplitude variation of the backscattered E_y with distance along x at 10 GHz.	152
6.33 A faceted PEC geometry (not to scale).	152
6.34 Amplitude variation of the backscattered E_y with distance along x at 10 GHz.	153
6.35 A curved PEC surface (with a height of 4λ).	153
6.36 Amplitude variation of the scattered E_y at 10 GHz.	154
6.37 A computational domain with small dipole.	155
6.38 Approach handling for multiscale problems in FDTD.	156

6.39	Amplitude variation of the radiated E_x at 10 GHz.	157
6.40	A multilayer problem (not to scale).	158
6.41	Time signature at the origin from the conventional FDTD for the multilayer problem shown in Fig. 6.40.	159
6.42	Frequency variation of the transmitted field E_y amplitude at the origin for the multilayer problem shown in Fig. 6.40.	159
6.43	A 2D computational domain.	161
6.44	Frequency variation of the E_y -field amplitude at point A shown in Fig. 6.43.	161
6.45	A 2D computational domain.	162
6.46	Amplitude variation of the E_y -field at observation point A, for different domain sizes for the problem shown in Fig. 6.45.	163
6.47	Geometry of a PEC dipole (not to scale).	163
6.48	Variation of input resistance with frequency for the PEC dipole.	164
6.49	Variation of input reactance with frequency for the PEC dipole.	164
6.50	Geometry of a stratified medium with oil (not to scale).	165
6.51	Variation of E_x component of the incident pulse.	165
6.52	Variation of E_x component of the reflected pulse.	166

List of Tables

3.1	Comparison of unknowns required for DM approach using MBF and HBFs for the PEC sphere shown in Fig.3.2.	32
3.2	Comparison of unknowns required for DM approach using MBFs for the dielectric plate shown in Fig.3.1.	33
3.3	Comparison of unknowns required for DM approach using CBFs for the PEC rod shown in Fig.3.5.	36
3.4	Comparison of simulation time for DM approach using FMG for the dielectric plate shown in Fig.3.1.	38
3.5	Number of TBFs used in different frequency ranges for the PEC rod shown in Fig.3.15.	45
3.6	Comparison of simulation times using DM approach with and without closed-form expressions for the PEC loop shown in Fig.3.18.	46
3.7	Comparison of simulation times using the DM approach, with and without closed-form expressions, for the PEC plate shown in Fig.3.21.	49
3.8	Comparison of input impedance calculated by using DM approach, Harrington's approach (3.5) and a simplified transmission model for the monopole shown in Fig.3.27.	56
4.1	Comparison of simulation times required by RUFD and the commercial MoM for the PEC plate shown in Fig.4.9.	80
4.2	Comparison of iterations required by RUFD using different processing technique and the commercial FDTD for the patch antenna shown in Fig.4.12.	82
4.3	Comparison of iterations required by RUFD using different processing technique for the waveguide filter shown in Fig.4.13.	84

4.4	Comparison of iterations required by the RUFD, when using the smoothing technique for the RF filter shown in Fig.4.14.	84
4.5	Comparison of iterations required by ν FDTD, RUFD using Smoothing and the commercial FDTD for the patch antenna shown in Fig.4.12.	95
4.6	Comparison of iterations required by ν FDTD, RUFD using polynomial fit for the waveguide filter shown in Fig.4.13.	95
5.1	Comparison of computational resources required by the different RUFD hybrid approaches for the multiscale problem shown in Fig.5.6.	106
5.2	Comparison of computational resources required by the self-consistent approach with those required by the commercial MoM.	107
5.3	Comparison of computational resources required by the multi-grid approach and the commercial MoM solver for the helix problem shown in Fig.5.21.	117
5.4	Comparison of computational resources required by the multi-grid approach and the commercial MoM solver for the dipole problem shown in Fig.5.23.	120
5.5	Comparison of computational resources required by the multi-grid approach and the commercial MoM solver for the dipole problem shown in Fig.5.25.	122
5.6	Comparison of computational resources required by the multi-grid approach and the commercial MoM solver for the coated dipole problem shown in Fig.5.27.	124
6.1	Comparison of time steps required for convergence for the circuit shown in Fig.6.4.	130
6.2	Comparison of mesh size and memory required for convergence for PEC geometry shown in Fig.6.18.	143
6.3	Comparison of time steps required by conventional FDTD and ν FDTD for the multilayer problem shown in Fig.6.40.	158

ACKNOWLEDGEMENTS

I would like to express my sincere gratitude to my PhD supervisor Prof. Raj Mittra. It has been an honor to work with Prof. Mittra. His perpetual energy and enthusiasm has been my primary source of motivation for my research work. He has always been available for answering my questions patiently and every time he makes sure that I grasp the basic principles right. This dissertation would not have been possible without him. I would also like to thank him for all the corrections and revisions made to text that is about to be read.

I would like to acknowledge my colleagues in the Electromagnetics Communication Laboratory, Dr. Jonathan Bringuier, Dr. Kyungho Hoo, Dr. Chiara Pelletti, Xialong Yang, Dr. Kai Du, Dr. Giacomo Bianconi, Dr. Wenhau Yu, Dr. Yongjun Liu, Ravi Kumar Arya, Yuda Zhou, Muhammed Hassan, Dr sidharath jain, and Shailesh Pandey, without them this dissertation would not have been complete. I would like to sincerely thank all of my committee members, Dr. James K. Breakall, Dr. Doug Werner, and Dr. Michael T. Lanagan, who set aside their busy schedules to review this work. I would also like to thank Dr. Randy Haupt for his valuable inputs.

I am thankful to my friends Nikhil Mehta, Harisha Kinilakodi, Deepti Jain, Nithya Vasudevan, Nidhi Sikarwar, Umamahesh, Mahesh Shastri, Himanshu Madan, and Aditya Hariharan who made my stay enjoyable and lovable through thick and thin. I would like to especially mention Vishesh Karwa who has always been there for me from the very beginning of my PhD. I would like to thank Sathish Raj, Nehmat Gereige and Vanitha Mohan whom I always relied on during the difficult times.

I would like to thank my professors: Prof. Dattatreyan, Prof. M. K. Achuthan, Prof. G. T. Manohar, Prof. Subrata Sanyal, and Prof. Ramesh Garg back home at Indian Institute of Technology without whom my life would not have been the same. I

would also like to acknowledge the consistent support from my friends back home: Siva Sankar, Vivek Subramanian, K. Sathappan, Divyabramham, Dr. Ravi Shankar, Praveen Ilango, Swapna Arun, Dr. Ashesh, Dr. Bijilash Babu, and M. Kadappan.

I would like to express my sincere gratitude to my sisters Yegammai and Meenakshi. I would like to especially acknowledge the sacrifices made by my sister Unnamalai, without whose support I could not have pursued this PhD degree. My youngest and the latest sister Nidhi Agrawal, whom I met just less than a year ago, has always been there for me. In a very short period of time our friendship blossomed in to sister hood and she has left me touched in her own beautiful ways making it the most memorable times I have ever had in my whole life, not just during my PhD.

I bow down to my mother who has given herself in every possible way, without thinking about her own well being, to make sure that we succeed in our lives. It was she who instilled in me the strong urge to achieve the highest in my life. My sincere gratitudes to Sadhguru who has given me the meditative practices that improved my perception and enhanced my clarity. Without him, my whole life would have been a constant struggle.

Kadappan Panayappan

“Our lives become beautiful not because we are perfect.
Our lives become beautiful because we put our heart into what we are doing.”

- *Sadhguru Vasudev*

Founder, Isha Foundation

1. Introduction

1.1 Electromagnetics

Electromagnetics is the branch of physics which describes the behavior of the EM field and its interaction with matter. All the equations governing this behavior can be mathematically derived by using the well-known *Maxwell's Equations* [1, 2]. The Maxwell's equation can be written down either in the differential form (1.1), or in integral form (1.2), by using the Stoke's theorem and the Divergence theorem [3].

$$\nabla \times \mathbf{E} = -\frac{\partial \mathbf{B}}{\partial t} \tag{1.1a}$$

$$\nabla \times \mathbf{H} = \mathbf{J}_s + \frac{\partial \mathbf{D}}{\partial t} \tag{1.1b}$$

$$\nabla \cdot \mathbf{D} = \rho \tag{1.1c}$$

$$\nabla \cdot \mathbf{B} = 0 \tag{1.1d}$$

$$\oint \mathbf{E} \cdot d\mathbf{l} = -\frac{\partial}{\partial t} \iint \mathbf{B} \cdot d\mathbf{s} \quad (1.2a)$$

$$\oint \mathbf{H} \cdot d\mathbf{l} = \iint \mathbf{J}_s \cdot d\mathbf{s} + \frac{\partial}{\partial t} \iint \mathbf{D} \cdot d\mathbf{s} \quad (1.2b)$$

$$\oiint \mathbf{D} \cdot d\mathbf{s} = \iiint \rho dv \quad (1.2c)$$

$$\oiint \mathbf{B} \cdot d\mathbf{s} = 0 \quad (1.2d)$$

In the above equations (1.1) and (1.2),

- $\mathbf{E}(\mathbf{r}, t)$ is electric field intensity in V/m ;
- $\mathbf{H}(\mathbf{r}, t)$ is magnetic field intensity in A/m ;
- $\mathbf{D}(\mathbf{r}, t)$ is electric flux density in C/m^2 ;
- $\mathbf{B}(\mathbf{r}, t)$ is magnetic flux density in Wb/m^2 ;
- $\mathbf{J}_s(\mathbf{r}, t)$ is impressed electric surface current density in A/m^2 ;
- $\rho(\mathbf{r}, t)$ is impressed electric charge density in C/m^3 ;

1.2 Theoretical Methods of Analysis

Analysis of electromagnetic problems, often begins with the use of a suitable theoretical method, instead of an experimental one, at least during the initial phase, since experimental methods are more expensive and time-consuming. The methodologies used for the theoretical or computational analyses of an electromagnetic problem can be broadly classified into four types [1], namely:

1. **Analytical methods:** These methods are accurate and efficient, but can be used only for regular shaped geometries involving symmetry. Perturbation methods and Variational techniques are some of the typical examples of analytical methods.
2. **Model-based methods:** Transmission line models and Cavity models are grouped under Model based methods. These methods provide insight in to the problem, but often involves simplifying assumptions to reduce the complexities involved.
3. **Computational methods:** Finite Difference Time Domain (FDTD), Finite Element Method (FEM) and Method of Moments (MoM) are the most widely used techniques. The computational methods, typically referred to as *Computational Electromagnetic (CEM)*, are highly versatile and accurate in nature, though they are often computationally expensive.
4. **Computational intelligence methods:** These methods are used to predict values from the existing database and also for optimization purposes. The techniques that come under this category are Neural network and Neuro-fuzzy techniques, for example.

1.3 Computational Methods

Computational methods are often the preferred choice because of their versatile nature. Most of the commercial softwares in computational electromagnetics are based on the following three techniques, namely:

1. **FDTD:** As the name suggests, FDTD algorithm solves the difference form of the Maxwell's differential equations, [1.1a](#) and [1.1b](#). The most salient feature of this time domain technique is that it is highly parallelizable and can be used to efficiently solve

problems involving inhomogeneous media.

2. **MoM:** The MoM algorithm formulates the electromagnetic analysis problem in terms of integral equations, via the use of Green's function. Since MoM is a frequency domain technique, it can easily handle dispersive media.
3. **FEM:** FEM algorithm is a finite method, solves the differential equations by using the weighted residual method, which leads to a large sparse matrix. As in case of the MoM, FEM is also a frequency domain technique and, hence, it can handle dispersive media with ease.

1.4 Motivation

With the advent of sub-micron technologies and increasing awareness of Electromagnetic Interference and Compatibility (EMI/EMC) issues, designers are often interested in full-wave solutions of complete systems, taking to account a variety of environments in which the system operates. However, attempts to do this increase the complexities involved in computing full-wave solutions manifold, especially when the problems involve multi-scale geometries with very fine features. For such problems, even the well-established numerical methods, such as the time domain technique FDTD and the frequency domain methods FEM and MoM, are often challenged to the limits of their capabilities. On the basis of our experience with the conventional frequency domain methods, we can identify the following areas of concern:

- Handling thin wires and/or sheets, with or without finite losses
- Deriving a universal approach for PEC, dielectric and inhomogeneous bodies
- Accurately modeling multi-scale geometries

- Accurately integrating the Green’s function for curved geometries
- Dealing with singular and hypersingular behaviors of the Green’s function when generating the MoM matrix
- Dealing with the low-frequency breakdown problem, which is introduced by the dominance of the scalar potential term over the vector potential, as the frequency approaches zero.

In addition, the conventional FDTD technique demands extensive computational resources when solving low-frequency problems, or when dealing with dispersive media. To tackle some of these challenges, conventional techniques are often modified, and tailored, to solve a particular problem of interest. Even though this strategy helps to solve a particular problem, it is often computationally expensive, and numerically unstable as well. Consequently, techniques that can overcome the above limitations without compromising their advantages are very desirable additions to the CEM repertoire.

1.5 Outline of Research Methodology

The underlying theme of this study is to research into new approaches for meeting the challenges listed in the Section 1.4. The proposed techniques are formulated for canonical problems and are implemented using either Matlab or C++. The generated results are compared against the conventional approach, and are then validated and benchmarked by using commercial codes that are best suited for the problem at hand. Amplitude comparisons of the results have been shown for all the problems investigated, while the phase comparison is included only for those problems for which there is a mismatch between results derived by the proposed method, and those obtained by using the commercial codes.

1.6 Organization of the Thesis

In Chapter 2, we introduce a universal MoM-like formulation, called the Dipole Moment Approach (DM Approach), which bypasses the use of the Green's function, and overcomes some of the disadvantages of the conventional frequency domain techniques. Then, in Chapter 3, we propose techniques to improve the efficiency of the Dipole Moment Approach and also ways to handle lumped loads, apertures, slits and irregular geometries, Non-Cartesian geometries and microstrip structures. In chapter 4, we introduce RUFD (Recursive Update in Frequency Domain), which is a frequency domain technique uses the difference form of Maxwell's equations, and which preserves some of the desirable properties of FDTD, the time domain method, such as generating the solution by using a recursive approach, as opposed to matrix inversion or iteration, typically employed in the frequency domain. Next, Chapter 5 introduces ways to hybridize the RUFD with DM approach to solve a variety of multi-scale problems. Chapter 6 deals with techniques to improve the performance of FDTD algorithm when solving low frequency problems, handling non-Cartesian geometries, and dealing with multi-scale problems. It also introduces signal processing techniques and new mesh truncation schemes to further improve the efficiency of the FDTD algorithm. Chapter 7 discusses the results, summarizes the contributions of this thesis and concludes with the identification of some possible avenues of future research.

2. Dipole Moment Approach

2.1 Introduction

Formulating integral equations via the use of Green's functions is a well-established and universally accepted method [2, 4, 5] in the context of MoM, and it has been a staple for CEM problems in the past. But MoM requires special treatment at low frequencies where it runs in to difficulties, and it switches to loop-star basis functions to mitigate the problem. Furthermore, MoM needs to deal with the singular and/or hyper-singular behaviors of the Green's functions, and designs special techniques for integrating them when generating the matrix elements. Additionally, both the frequency domain techniques, namely FEM and MoM, experience difficulties when handling multiscale geometries, because the associated matrices for these problems can become ill-conditioned. To mitigate these problems, we introduce a universal MoM-type formulation, which bypasses the use of Green's function to overcome the disadvantages of the conventional frequency domain techniques alluded to above.

2.2 Dipole Moment Concept

The sphere, whose geometry is uniquely defined by its radius, has been extensively used as a canonical object for validating various CEM algorithms, used to compute Radar Cross Section(RCS) for instance. Here, we exploit the analytical tractability of the problem of scattering by a sphere, and use the sphere as a building block for modeling arbitrary geometries in a manner that generates the scattered electric field directly, rather than using the Green's function in conjunction with vector and scalar potentials.

For the case of a sphere illuminated by a plane wave, the scattered fields can be determined analytically. Consider a PEC sphere of radius a , which is immersed in free space, and is illuminated by a plane wave $E_x = E_o e^{-jkz}$. In the limit of $ka \rightarrow 0$, the scattered electric far fields can be written:

$$\lim_{ka \rightarrow 0} E_\theta^s = E_o \frac{e^{-jkr}}{kr} (ka)^3 \cos\phi (\cos\theta - 1/2) \quad (2.1a)$$

$$\lim_{ka \rightarrow 0} E_\phi^s = E_o \frac{e^{-jkr}}{kr} (ka)^3 \sin\phi \left(\frac{1}{2}\cos\theta - 1\right) \quad (2.1b)$$

The equations (2.1) have been derived by using the spherical wave functions [6]. A close examination of ((2.1)) reveals the fact that the expressions in ((2.1)) resemble the far fields radiated from a combination of an x-directed electric dipole and a y-directed magnetic dipole, whose moments are given by:

$$Il_x = E_o \frac{4\pi j}{\eta k^2} (ka)^3 \quad (2.2a)$$

$$Kl_y = E_o \frac{2\pi}{jk^2} (ka)^3 \quad (2.2b)$$

Along the same lines, we can show that the equivalent dipole moments for a lossless dielectric sphere of radius a , whose relative permittivity and permeability are ϵ_r and μ_r respectively, can be written as:

$$Il_x = E_o \frac{4\pi j}{\eta k^2} (ka)^3 \frac{\epsilon_r - 1}{\epsilon_r + 2} \quad (2.3a)$$

$$Kl_y = E_o \frac{2\pi}{jk^2} (ka)^3 \frac{\mu_r - 1}{\mu_r + 2} \quad (2.3b)$$

Equations (2.3) can be readily modified for a lossy medium by replacing the real valued ϵ_r and μ_r , with their complex permittivity $\bar{\epsilon}$ and permeability $\bar{\mu}$. It's important to note that the magnetic dipole moment goes to zero for non-magnetic media ($\mu_r = 1$).

Hence the dipole moment representation of a scatterer generates the same *far* fields as those scattered by the original object. However, what has not been realized in the past – and what can be proven analytically [7] – is that for a sphere whose radius is electrically small, the dipole moment fields exactly match the original ones scattered by the sphere, all the way up to its surface, and not just in the far field.

2.3 Formulation for PEC Objects

2.3.1 Geometry Modeling

When formulating a problem that involves only PEC objects, the first step is to represent the original scatterer by using a collection of PEC spheres. Next these spheres are replaced by their corresponding Dipole Moments(DMs) and a set of them are used to form a suitable set of macro-basis functions. We then evaluate the electric fields generated by these macro basis functions and compute the reactions between them and the testing functions, which are also the same as the basis functions (Galerkin method), to generate the elements of the MoM matrix. The right-hand side of this matrix is obtained by applying the boundary condition on the total tangential E-Field, by testing it with the same functions as those used to generate the matrix elements.

$$\mathbf{E}_{\text{inc}}^{\text{tan}} + \mathbf{E}_{\text{scat}}^{\text{tan}} = 0 \quad (2.4)$$

Hence, with the incident E-field polarized along \hat{z} , the matrix equation for a thin PEC rod oriented along \hat{z} and modeled by using N macro basis functions, will have the form:

$$\begin{bmatrix} E_z^{11} & E_z^{12} & E_z^{13} & \dots & E_z^{1N} \\ E_z^{21} & E_z^{22} & E_z^{23} & \dots & E_z^{2N} \\ \vdots & \vdots & \vdots & \vdots & \vdots \\ E_z^{N1} & E_z^{N2} & E_z^{N3} & \dots & E_z^{NN} \end{bmatrix} \times \begin{bmatrix} Il_z^1 \\ Il_z^2 \\ \vdots \\ Il_z^N \end{bmatrix} = \begin{bmatrix} E_{z-inc}^1 \\ E_{z-inc}^2 \\ \vdots \\ E_{z-inc}^N \end{bmatrix} \quad (2.5)$$

In the above equation (2.5),

- Il_z^n represents the effective dipole moment of the n^{th} macro basis function - directed along \hat{z} .
- E_{z-inc}^n represents the tangential incident field component at the location of the n^{th} macro basis function and
- E_z^{mn} represents the scattered field component along \hat{z} on the m^{th} macro basis function by the n^{th} macro basis function.

The above matrix equation (2.5) is solved for Il' s, i.e., the co-efficient of the macro basis functions, and used to compute the induced currents. In order to calculate the resulting scattered fields, the following expressions for the fields radiated by a DM oriented along \hat{z} is used [8]:

$$E_r = \eta \frac{Il \cos \theta}{2\pi r^2} \left[1 + \frac{1}{jkr} \right] e^{-jkr} = C_r \cos \theta \quad (2.6a)$$

$$E_\theta = j\eta \frac{kIl \sin \theta}{4\pi r} \left[1 + \frac{1}{jkr} - \frac{1}{(kr)^2} \right] e^{-jkr} = C_\theta \sin \theta \quad (2.6b)$$

$$H_\phi = j \frac{kIl \sin \theta}{4\pi r} \left[1 + \frac{1}{jkr} \right] e^{-jkr} = C_\phi \sin \theta \quad (2.6c)$$

$$E_\phi = 0; \quad H_r = 0; \quad H_\theta = 0 \quad (2.6d)$$

The field expression in (2.6) can be rewritten in Cartesian co-ordinates as shown below, with source and observation points represented by (x_s, y_s, z_s) and (x_o, y_o, z_o) , respectively:

$$E_x = \frac{(x_o - x_s)(z_o - z_s)}{r^2} (C_r + C_\theta) \quad (2.7a)$$

$$E_y = \frac{(y_o - y_s)(z_o - z_s)}{r^2} (C_r + C_\theta) \quad (2.7b)$$

$$E_z = \frac{(z_o - z_s)^2}{r^2} C_r - \frac{(x_o - x_s)^2 + y^2}{r^2} C_\theta \quad (2.7c)$$

$$H_x = -\frac{(y_o - y_s)}{r} C_\phi \quad (2.7d)$$

$$H_y = \frac{(x_o - x_s)}{r} C_\phi \quad (2.7e)$$

$$H_z = 0 \quad (2.7f)$$

2.3.2 Numerical Results

For the first example we consider a PEC rod, whose length and diameter are $\lambda/10$ and $\lambda/400$, respectively. It is illuminated by a plane wave, incident from broadside (note: the angle of incidence can be arbitrary), as shown in the Fig. 2.1. Fig. 2.2 compares the backscattered field calculated by using the DM approach as described in Section 2.3.1, with those obtained from a commercial MoM package.

As we can see from the Fig. 2.2, the comparison with the commercial MoM program

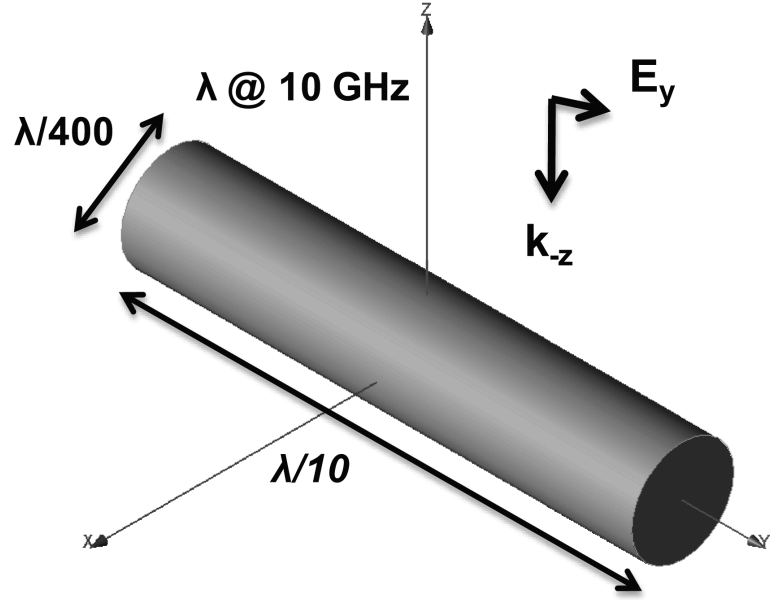


Figure 2.1: A PEC rod.

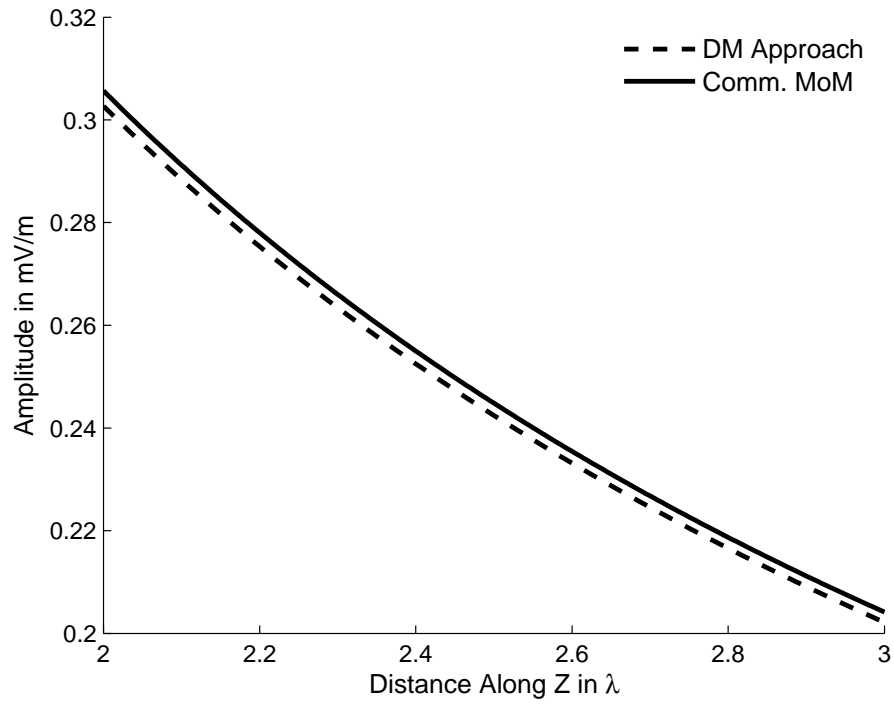


Figure 2.2: Amplitude comparison of backscattered electric field E_y from the PEC rod in Fig. 2.1.

is good. However when the radius of the PEC rod becomes smaller than 10^{-5} units, some of the commercial MoM codes (not including the NEC code) give a warning flag about their inability to mesh the geometry, while the DM approach is able to handle it without any special modification to the approach.

Next we consider a circular PEC loop with a diameter of 600 mm and a thickness of 18.6 mm as shown in Fig. 2.3. The loop is fed with a voltage gap source. Fig. 2.4 compares the frequency variation of the feed current calculated by using DM approach with those obtained using NEC.

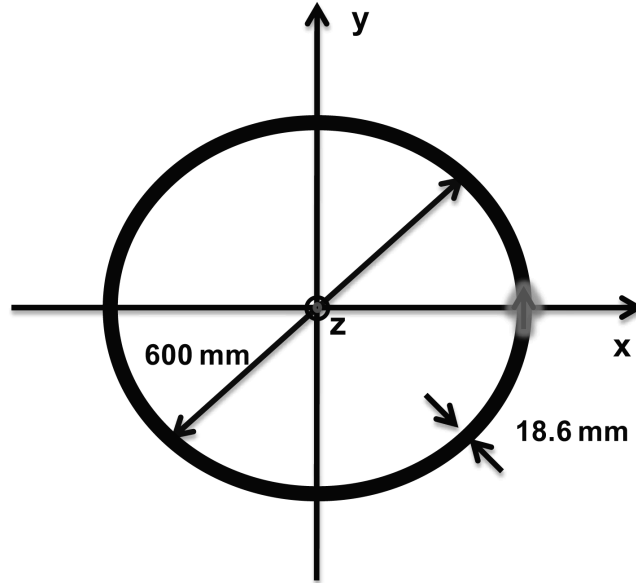


Figure 2.3: A PEC circular loop.

From Fig. 2.4 we can see that the comparison of the feed current is good all the way down to 50 MHz. It is important to point out that the strength of the DM approach lies in the fact that we can further go down in frequency all the way up to DC, without any special treatment.

For the next example we consider a PEC helix, whose length is $\lambda/10$ with a diameter of $\lambda/30$ and a thickness of $\lambda/200$ at 10 GHz, as shown in Fig. 2.5. The helix is fed by using

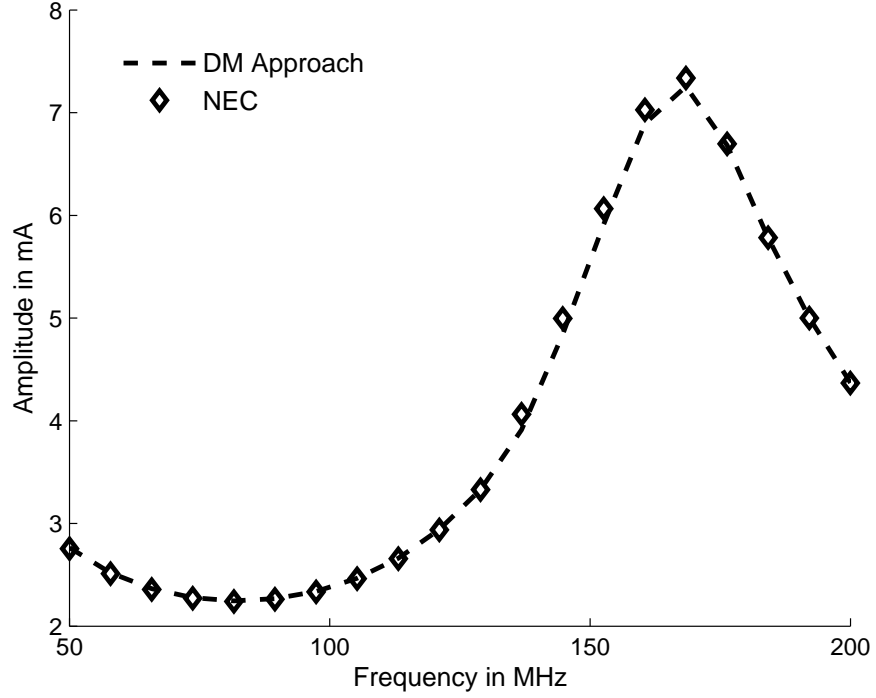


Figure 2.4: Frequency variation of the feed current for a PEC loop shown in Fig. 2.3.

a voltage gap source. Fig. 2.6 compares the amplitude of dominant component of the radiated field E_x calculated using DM approach with those obtained from a commercial MoM code.

As we can see from the Fig. 2.6, the comparison with the commercial MoM program is good. However, as may be seen from Fig. 2.7, some of the commercial MoM codes (not including the NEC code) were unable to calculate the current correctly along the helix, apparently because of the non-Cartesian nature of its geometry which makes the meshing difficult for these codes, while the DM approach was able to solve for the current along the helix with ease.

For the final example we consider a PEC sphere, whose diameter is $\lambda/60$ with λ at 10 GHz. It is illuminated by a plane wave, incident from \hat{x} , and polarized along \hat{z} , as shown in the Fig. 2.8. Fig. 2.9 compares the scattered E_z field at $x = \lambda/46$ calculated by

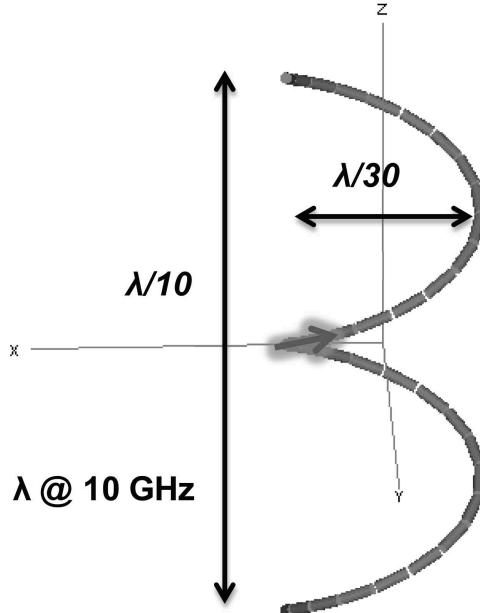


Figure 2.5: A PEC helix.

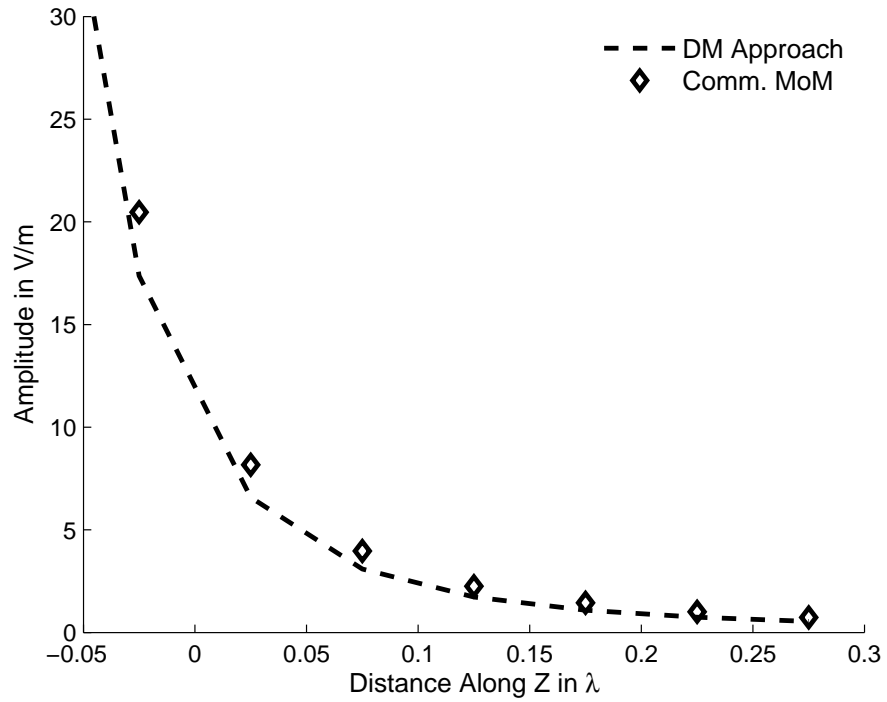


Figure 2.6: Amplitude comparison of radiated electric field E_x from the PEC helix in Fig. 2.5.

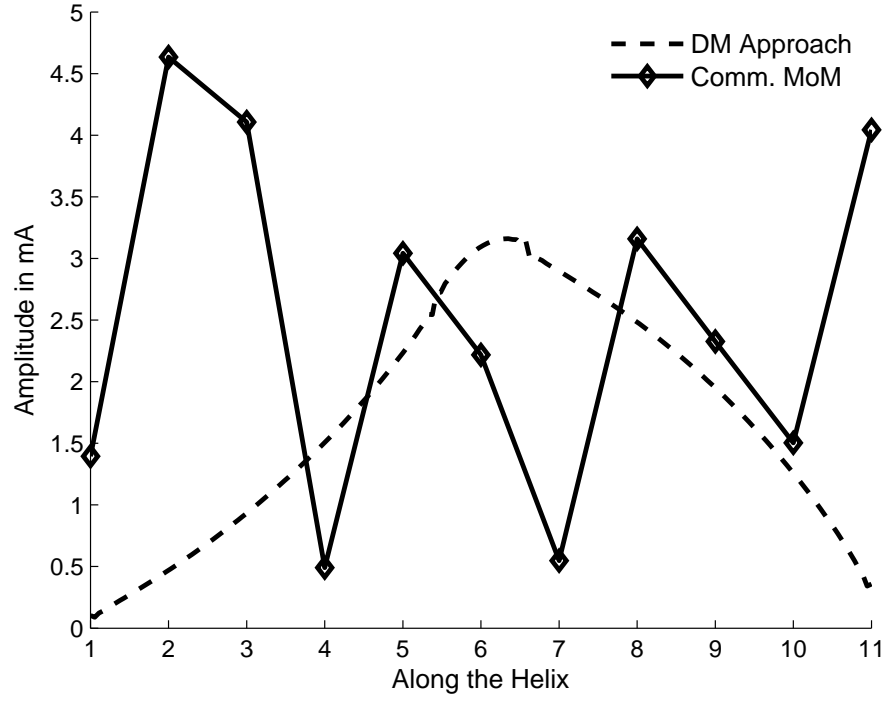


Figure 2.7: The magnitude of current calculated using a commercial MoM solver for the PEC helix shown in Fig. 2.5.

using the DM approach as described in Section 2.3.1 with those obtained from Mie Series [6] for different frequencies of incident plane wave.

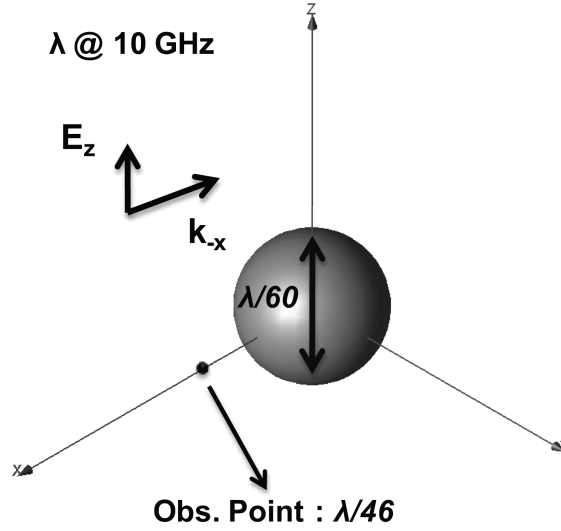


Figure 2.8: A PEC sphere.

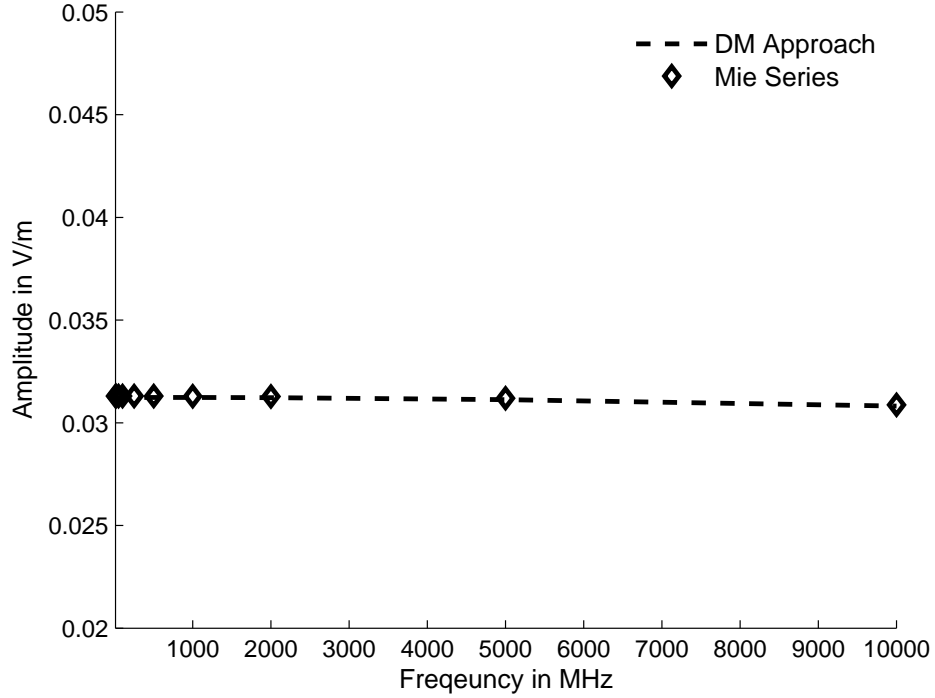


Figure 2.9: Amplitude comparison of backscattered electric field E_z from the PEC sphere in Fig. 2.8.

As we can see from Fig. 2.9, the comparison with the Mie series results is good, all the way down to very low frequencies, which is one of the major advantages of the DM formulation, as we have pointed out before.

2.4 Formulation for Dielectric Objects

2.4.1 Geometry Modeling

The first step in the formulation of the dielectric scattering problem essentially follows along the same line as in the case of PEC objects, in that we again represent the original scatterer as a collection of small-size dielectric spheres. As before, we then go on to replace these spheres by their corresponding DMs, and use them to form a set of macro-

basis functions. At this point we differ from the PEC case and generate the MoM matrix by imposing a boundary condition but by applying a consistency condition (2.8) on the tangential E-Field, which reads:

$$\epsilon_o(\epsilon_r - 1)(\mathbf{E}_{\text{inc}} + \mathbf{E}_{\text{scat}}) = F(\mathbf{\Pi}) \quad (2.8)$$

where F , called as the consistency factor, is derived by analytically solving the problem of a dielectric sphere with a small radius. This factor, obtained in the manner described above, is given by:

$$F \approx \frac{-3j}{4\pi\omega a^3} \quad (2.9)$$

2.4.2 Numerical Results

For the first example we consider a Dielectric rod with the relative permittivity ϵ_r of 6 , whose length and diameter are $\lambda/4$ and $\lambda/400$, respectively, at 10 GHz. It is illuminated by a plane wave, incident from broadside, as shown in Fig. 2.10. Fig. 2.11 compares the backscattered field calculated by using the DM approach as described in Section 2.4.1, with those obtained from a commercial FEM package.

As we can see from Fig. 2.11, the comparison with the commercial FEM program is good. However the commercial MoM code failed due to the fine thickness of the dielectric rod, while the DM approach was able to handle it with ease.

Next we consider a square-shaped dielectric plate with $\epsilon_r = 6$, which is $\lambda/40$ on the side and whose thickness is $\lambda/400$. The plate is illuminated by a plane wave traveling along the negative-z direction, as shown in the Fig. 2.12. The backscattered field, calculated by using the DM approach described in section 2.4.1, is presented in Fig. 2.13, which also compares these results with the corresponding ones from a commercial MoM package.

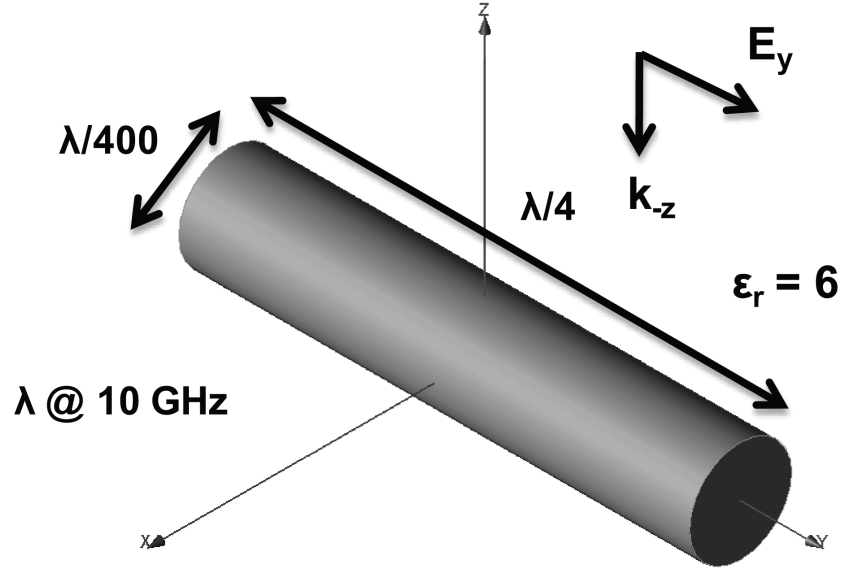


Figure 2.10: A dielectric rod.

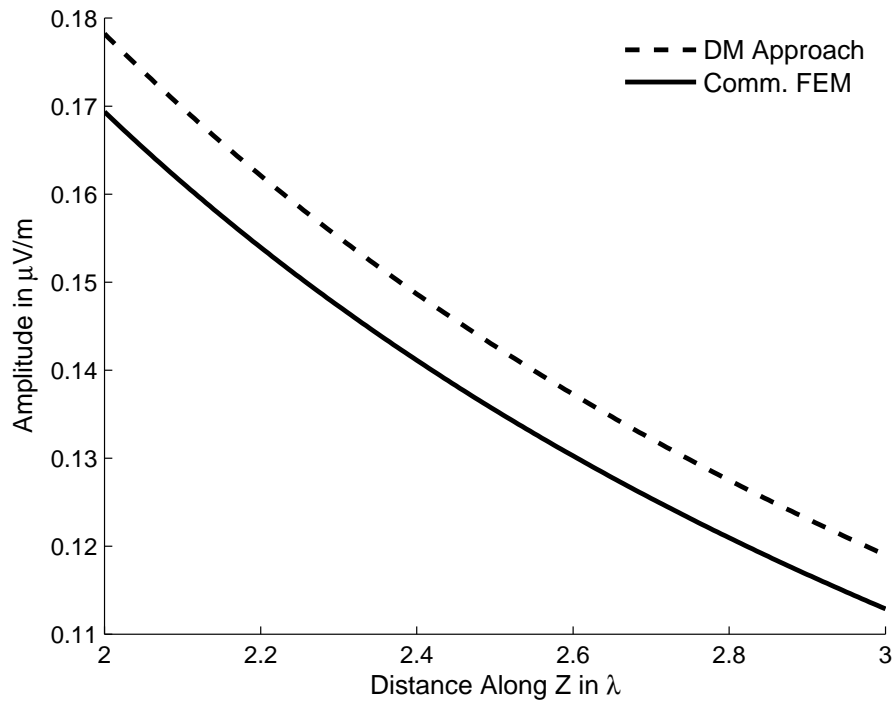


Figure 2.11: Amplitude comparison of backscattered electric field E_y from the dielectric rod in Fig. 2.10.

Once again, the comparison of the DM results with those from a commercial solver is good. It should be pointed out, that the commercial MoM solvers become unstable and

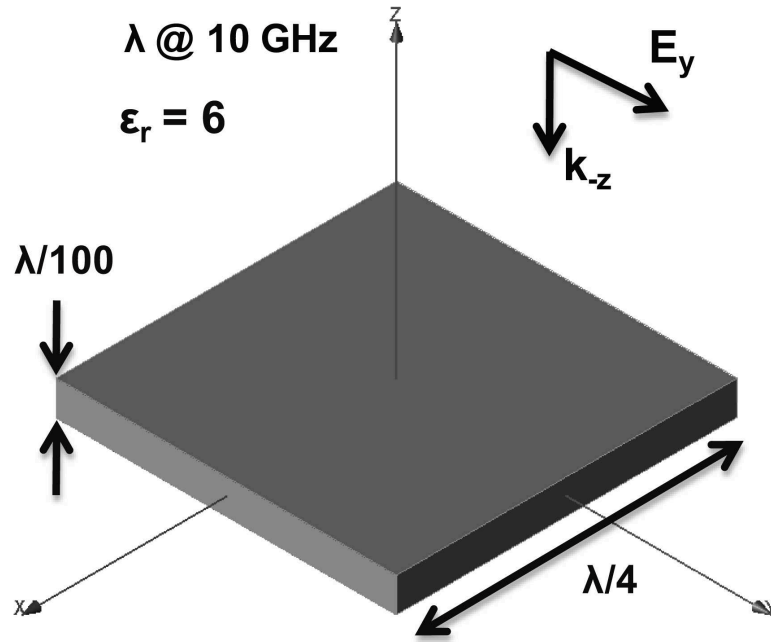


Figure 2.12: A dielectric plate.

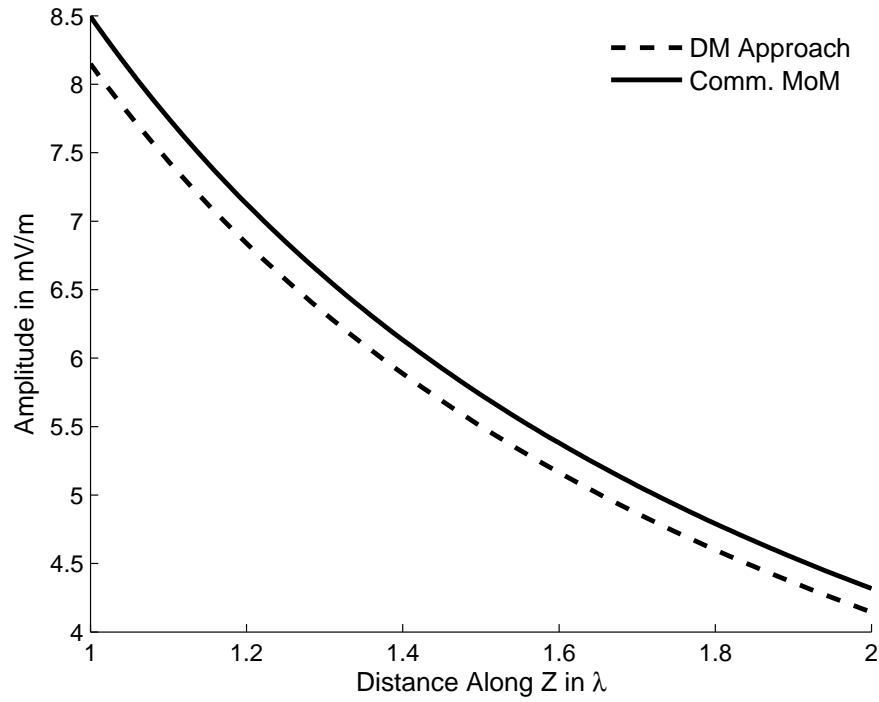


Figure 2.13: Amplitude comparison of backscattered electric field E_y from the dielectric plate in Fig. 2.12.

inaccurate for very thin scatterers, especially at low frequencies.

As a final example, we consider plasmonic nano-spheres randomly spread in 3D space, with a diameter of $\lambda/20$ at 300 THz and $\bar{\epsilon}_r = -47.5378 - 1.1383j$ (corresponding to Gold). It is illuminated by a plane wave, incident from \hat{z} , and polarized along \hat{y} , as shown in the Fig. 2.14. The scattered fields are calculated by using the DM approach described in section 2.4.1 but with the dipole moments Ils calculated using the complex permittivity in the consistency condition 2.8 and compared with those generated using a commercial FEM code.

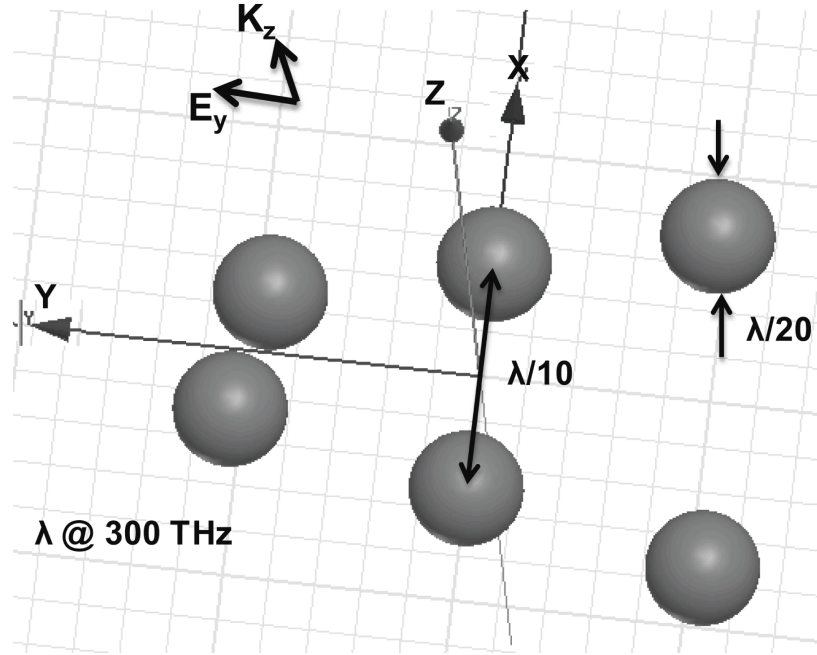


Figure 2.14: Plasmonic nano-spheres.

From Fig. 2.15 we can see that the scattered fields generated by using the commercial FEM code shows numerical artifacts near the origin, while the fields calculated using the DM approach is more physical.

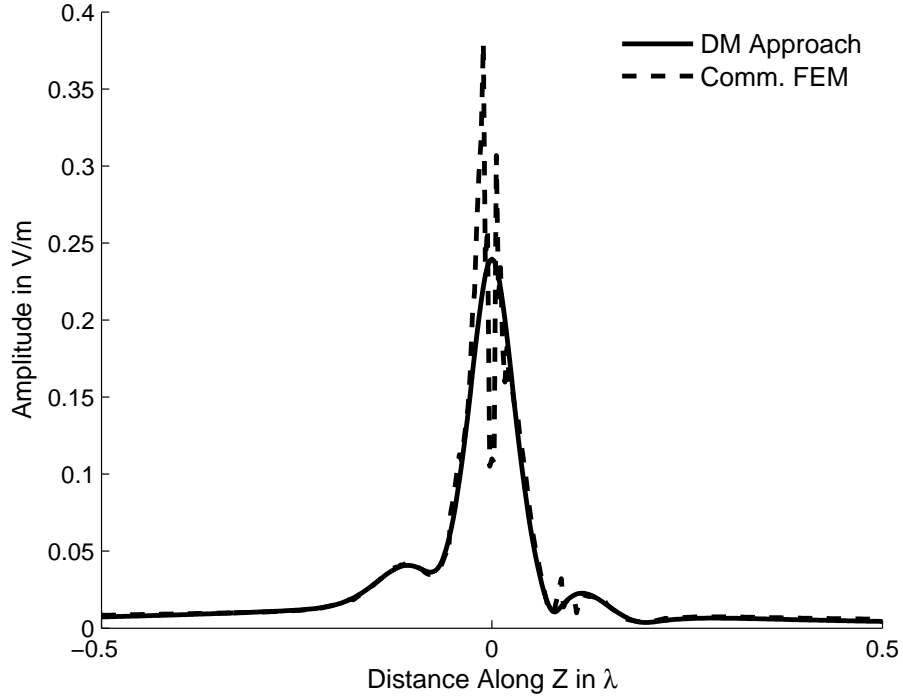


Figure 2.15: Amplitude comparison of scattered electric field E_y from the plasmonic spheres in Fig. 2.14.

2.5 Formulation for Inhomogeneous Objects

2.5.1 Geometry Modeling

For formulating inhomogeneous problems, the first step essentially follows along the same line as in the case of PEC and dielectric objects, in that we again represent the original scatterer as a collection of small-size PEC spheres in the PEC regions and small-size dielectric spheres in the dielectric regions. As before, we then go on to replace these spheres by their corresponding DMs, and use them to form a set of macro-basis functions. We generate the MoM matrix by imposing the boundary condition 2.4 for PEC spheres and the consistency condition 2.8 for the dielectric spheres, on the tangential E-Field. However while applying these conditions it is important to note the fact that the E_{scat}

should include the contributions from both the PEC and dielectric regions.

2.5.2 Numerical Results

As an example we consider a PEC rod with a square cross-section and uniformly coated with a dielectric constant ϵ_r of 6. The length and thickness of the PEC rod are $3\lambda/100$ and $\lambda/100$ respectively at 5 GHz. The thickness of the dielectric coating is $\lambda/100$. It is illuminated by a plane wave, incident from broadside, as shown in the Fig. 2.16. Fig. 2.17 compares the backscattered field calculated by using the DM approach, as described in Section 2.5.1, with those obtained from a commercial MoM package.

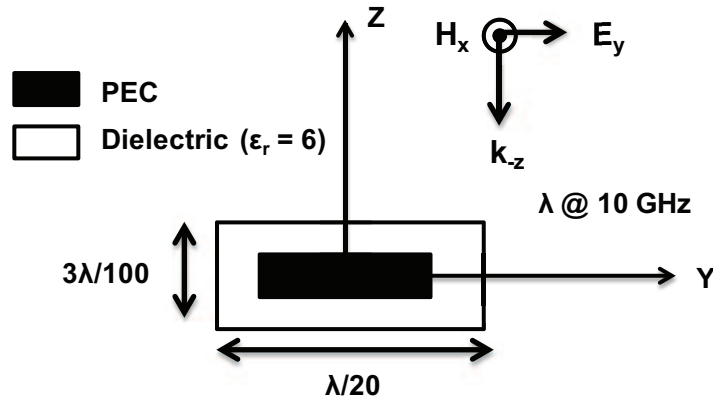


Figure 2.16: A PEC rod with a dielectric coating.

An alternate approach to solving the above problem is to define a PEC rod with an equivalent thickness, but whose length is same as that of the original geometry. An equivalent PEC rod for this problem has a thickness of $2.8\lambda/100$ and a length of $\lambda/20$, which is same as that of the original problem.

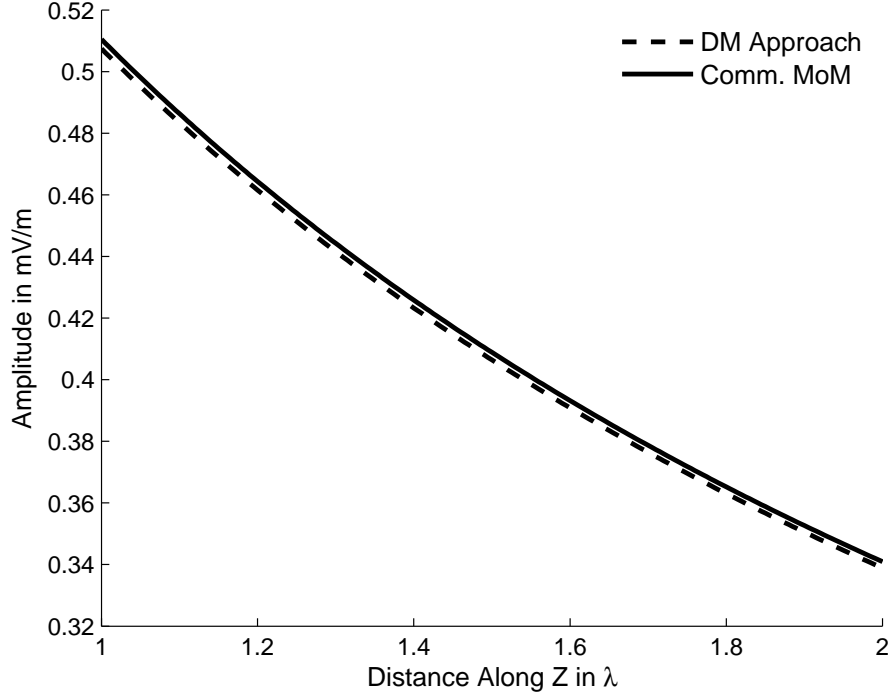


Figure 2.17: Amplitude comparison of backscattered electric field E_y from the coated rod in Fig. 2.16.

2.6 Quasi-Static Formulation

In this section, we introduce the quasi-static type of DM formulation in order to hybridize DM approach with FDTD algorithm, which will be described later in Chapter 6. Lets consider the electric fields radiated by a DM oriented along \hat{z} :

$$E_r = \eta \frac{Il \cos \theta}{2\pi r^2} \left[1 + \frac{1}{jkr} \right] e^{-jkr} \quad (2.10a)$$

$$E_\theta = j\eta \frac{kIl \sin \theta}{4\pi r} \left[1 + \frac{1}{jkr} - \frac{1}{(kr)^2} \right] e^{-jkr} \quad (2.10b)$$

$$E_\phi = 0 \quad (2.10c)$$

When the size of problem geometry is very small when compared to the wavelength

at the frequency of interest i.e., $r \rightarrow 0\lambda$, then the $\frac{1}{r^3}$ term in the above equations will dominate. Hence the expressions for E_r and E_θ in the limit of $r \rightarrow 0\lambda$ and using the expression for Il from equation 2.2a, can be rewritten as:

$$\lim_{r \rightarrow 0\lambda} E_r = \eta \frac{Il \cos \theta}{2\pi j k r^3} = 2E_o \cos \theta \frac{a^3}{r^3} \quad (2.11a)$$

$$\lim_{r \rightarrow 0\lambda} E_\theta = \eta \frac{k Il \sin \theta}{4\pi j k^2 r^3} = E_o \sin \theta \frac{a^3}{r^3} \quad (2.11b)$$

$$E_\phi = 0 \quad (2.11c)$$

The above equations shows that the electric fields are real and time-independent. These expressions resemble the fields of a static charge dipole. Since this quasi-static approach produces real and time-independent fields, we can use this to hybridize DM approach with FDTD to solve a variety of multi-scale problem. This quasi-static approximation can be used for problems for which near field calculations are of interest, since it is predominantly dictated by the $\frac{1}{r^3}$ term; also, this approach is computationally less expensive.

Consider a PEC helix, whose length is $\lambda/10$, a diameter of $\lambda/30$, and a thickness of $\lambda/200$ at 10 GHz. It is illuminated by a plane wave, incident from \hat{x} , and polarized along \hat{z} , as shown in the Fig. 2.18. Fig. 2.19 compares the amplitude of backscattered field E_z calculated by using the DM approach, with and without the quasi-static approximation.

As we can see from the Fig. 2.19, the comparison between the two, namely with and without the quasi-static approximation, is good. Even though the quasi-static approximation is computationally less expensive, it is important to note the fact that this approximation is valid only when the problem geometry is small when compared to the wavelength at the frequency of interest, while the DM approach is valid throughout the

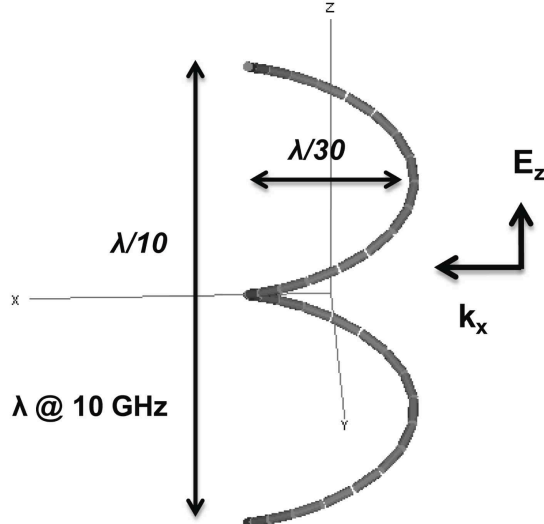


Figure 2.18: A PEC helix.

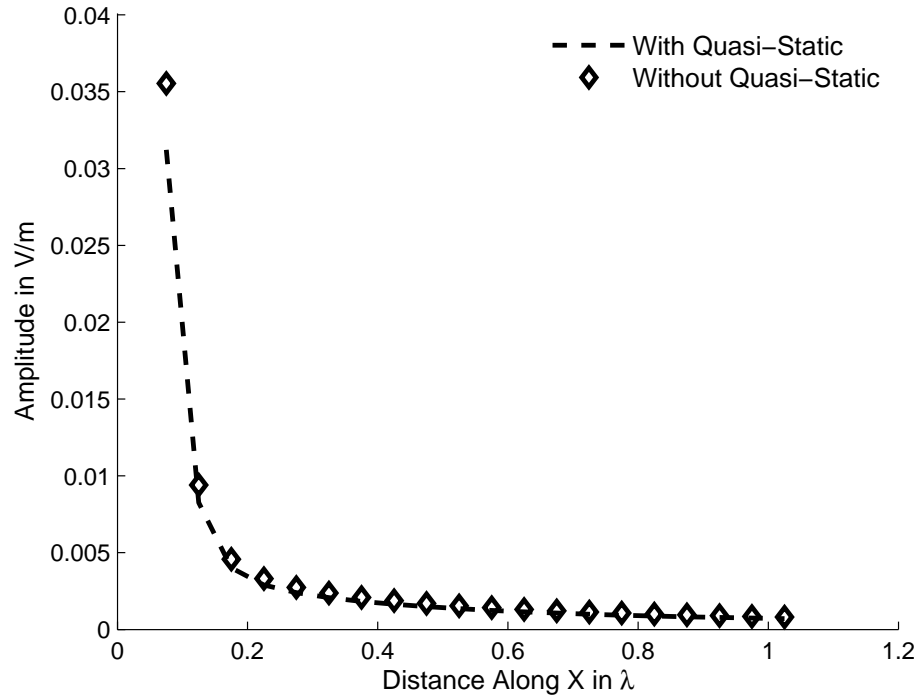


Figure 2.19: Amplitude comparison of backscattered electric field E_x from the PEC helix in Fig. 2.5.

entire frequency range.

2.7 Order of Singularity

The boundary condition or the consistency condition is always applied on the surface of the geometry. So for a problem geometry comprising of only PEC objects, the field values at the geometry's surface $r = a$ can be calculated from Equation (2.11) as follows:

$$E_r = 2E_o \cos\theta \quad (2.12a)$$

$$E_\theta = E_o \sin\theta \quad (2.12b)$$

$$E_\phi = 0 \quad (2.12c)$$

Hence in the DM approach the fields are always bounded and the order of the singularity is zero. The same can be proven to be true for dielectric and inhomogeneous objects.

2.8 Observations and Conclusions

In this chapter we have presented a new physics-based approach for formulating MoM problems that is based on the use of dipole moments (DMs) – as opposed to the conventional Green's functions. The absence of the Green's function, as well as those of the vector and scalar potentials, helps to eliminate two of the key sources of difficulties in the conventional MoM formulation, namely the singularity and low-frequency problems. Specifically, we have shown that there are no singularities that we need to be concerned with in the DM formulation; hence, this obviates the need for special techniques for integrating these singularities.

Yet another salutary feature of the DM approach is its ability to handle thin and lossy structures, whether they be metallic, dielectric-type, or even combinations thereof.

We have found that the DM formulation can handle these types of objects with ease, without running into ill-conditioning problems, even for very thin wire-like or surface-type structures, which lead to ill-conditioned MoM matrices when these problems are formulated in the conventional manner.

The technique is valid over the entire frequency range, from low to high, and it does not require the use of loop-star or other special types of basis functions in order to mitigate the low frequency problem. The DM formulation is universal, and can be used for both PEC and dielectric objects, and it requires only a relatively minor change in the formulation when we go from PEC to dielectric scatterers. The approach is also well suited for hybridization with Finite methods, such as the FEM and the FDTD, and such an embellishment renders it suitable for handling multi-scale problems conveniently and efficiently.

3. Performance Enhancement of DM Approach

3.1 Introduction

Though the DM approach described in Chapter 2, is accurate and captures all the physics, is not the most efficient from numerical point of view. This is because the number of spheres used to represent a three-dimensional object can grow very rapidly if the diameter of the sphere is small, as is often the case. For instance, for a thin-wire scatterer, the diameter of the spheres used to represent it is the same as that of the wire. Hence, for the example shown in Fig.3.1, the number of constituent spheres needed to form the plate can be quite large, even when the length of the plate is relatively small in comparison to the wavelength. In this chapter, we introduce techniques to enhance the performance of DM approach and to adapt this approach to solve a number of representative electromagnetic scattering problems.

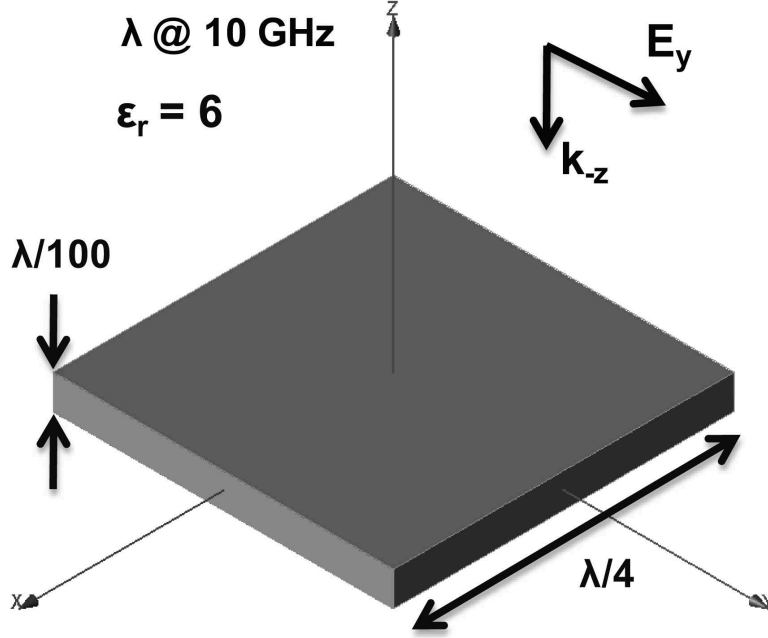


Figure 3.1: A dielectric plate.

3.2 Higher Order Macro-Basis Function

Our strategy for reducing the number of unknowns significantly and to make it comparable to that needed in the conventional MoM formulation, is to use macro-basis functions (MBF). These basis functions belong to a level higher than that of the dipole moments used to model the geometry in the initial step of the DM approach. The low-level dipole moments associated with such macro-basis functions are represented by a single unknown, with the variation of the dipole moments following the shape of the associated macro-basis function. In order to further improve the performance by reducing the number of unknowns, we introduce higher-order basis functions (HBFs). Towards this end, we use a set of macro-basis functions and form a set of suitable higher-order macro-basis functions and represent them by using a single unknown. The coefficients of the macro-basis function follow the shape of the higher-order macro-basis function. The MBFs can be categorized as sub-domain basis functions, as opposed to entire domain basis

functions. Some of the commonly used low-level basis functions used in the concept of MoM formulation are triangles, pulses and RWGs [9], but we will use them as MBFs for the DM approach.

3.2.1 Numerical Results

As a first example, let us consider a PEC sphere with a diameter of $\lambda/60$ at 10 GHz. It is illuminated by a plane wave, incident from \hat{x} , and polarized along \hat{z} , as shown in Fig. 3.2. Fig. 3.3 compares the scattered E_z field along the negative-x axis, computed by using DM approach; DM approach using MBFs; DM approach with HBFs; and, with those obtained from Mie Series [6]. For this problem, triangular basis functions were used, both as MBFs and HBFs, in the context of the DM approach.

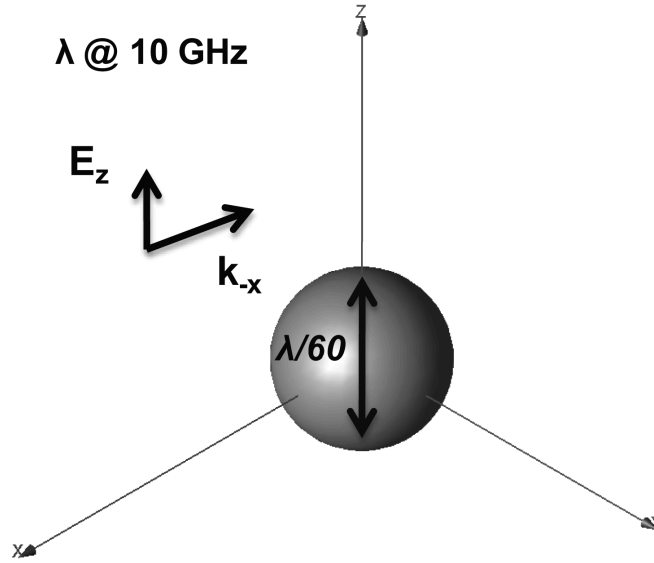


Figure 3.2: A PEC sphere.

Table 3.1 compares the number of unknowns required to solve the problem using (i) DM approach alone; (ii) with MBFs and (iii) with HBFs. Table 3.1 shows that the use of HBFs significantly reduces the number of unknowns, without sacrificing the accuracy, as may be seen by referring to Fig. 3.3.

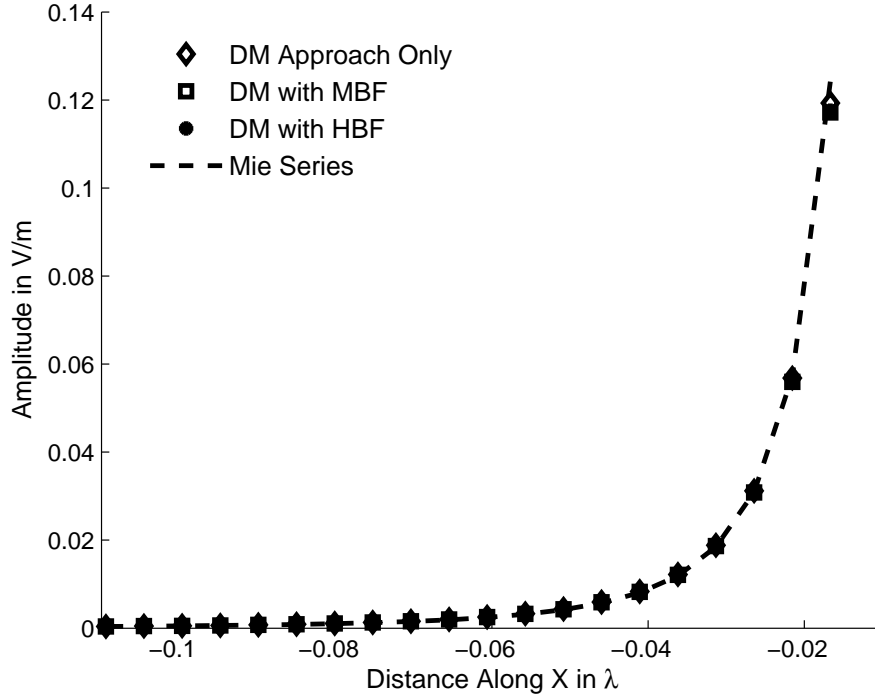


Figure 3.3: Amplitude comparison of scattered electric field E_z from the PEC sphere in Fig. 3.2.

Table 3.1: Comparison of unknowns required for DM approach usings MBF and HBFs for the PEC sphere shown in Fig.3.2.

Method	No. of Unknowns
DM Approach Only	2322
DM Approach with MBF	86
DM Approach with HBF	43

For the next example, we consider a square-shaped dielectric plate with $\epsilon_r = 6$, which is $\lambda/40$ on the side and whose thickness is $\lambda/400$ (see Fig. 3.1). The plate is illuminated by a plane wave traveling along the negative-z direction. Fig. 3.4 compares the backscattered field calculated by using: (i) the DM approach only; (ii) the DM approach with MBFs; and, (iii) a commercial MoM solver. Table 3.2 compares the required number of unknowns in each of these cases. For this problem the rooftop basis function was used as MBFs in the context of DM approach.

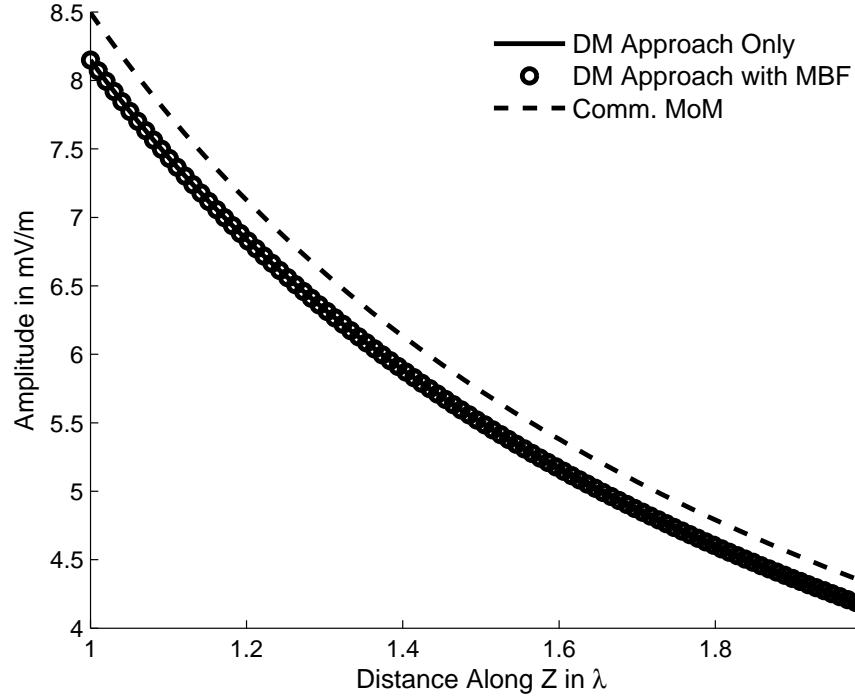


Figure 3.4: Amplitude comparison of backscattered electric field E_y from the dielectric plate in Fig. 3.1.

Table 3.2: Comparison of unknowns required for DM approach using MBFs for the dielectric plate shown in Fig. 3.1.

Method	No. of Unknowns
DM Approach Only	14112
DM Approach with MBFs	50

The results show, once again, that the comparison of the fields is good and the use of MBFs greatly reduces the number of unknowns without compromising the accuracy of the results. As we can see from the previous examples, it is relatively easy to choose these macro-basis functions. In order to better capture the current behavior near the corners and edges, we can increase the number of MBFs near the corners and edges to refine the level of discretization. Also, we can reduce the number of HBFs as we go down in frequency, since the current distribution will not vary very rapidly at lower frequencies.

3.3 Characteristic Basis Functions

Characteristic basis functions (CBFs) [10] are higher-level entire domain macro-basis functions and their use helps reduce the size of the matrix rather significantly. The CBFs are tailored for the geometry at hand and often just one or two CBFs are sufficient to solve the problem if the object is relatively small in size. The use of CBFs enables one to solve electrically large problems, because the size of the reduced matrix is often orders of magnitude smaller than one required in the original MoM formulation to achieve the same level of accuracy. The CBFs, are physics-based and they lead to well-conditioned matrices [11], because their redundancy is removed via the use of Singular Value Decomposition (SVD).

It is a common practice to generate the CBFs by solving for the current distributions using a number of independent excitations, which the angle of incidence and polarization of the illuminating wave is varied. Next, a matrix is generated by using the resulting current distributions, as its columns and a SVD of this matrix is performed. The threshold for the singular values, is typically chosen to be 1% of the highest singular value. Finally, we use the vectors corresponding to these singular values to construct the CBFs [12].

Consider a PEC rod, whose length and diameter are $\lambda/10$ and $\lambda/400$, respectively as shown in the Fig. 3.5. The CBFs for this problem were calculated as explained above and are plotted in Fig. 3.6. As we can see from this figure, only two out of the twelve originally generated solutions survived the SVD thresholding.

To test the method just described, we consider the case of the above PEC rod illuminated by a plane wave, incident from the broadside direction. Fig. 3.7 compares the backscattered field calculated by using: (i) the DM approach only; (ii) DM approach using CBFs; and, (iii) commercial MoM solver.

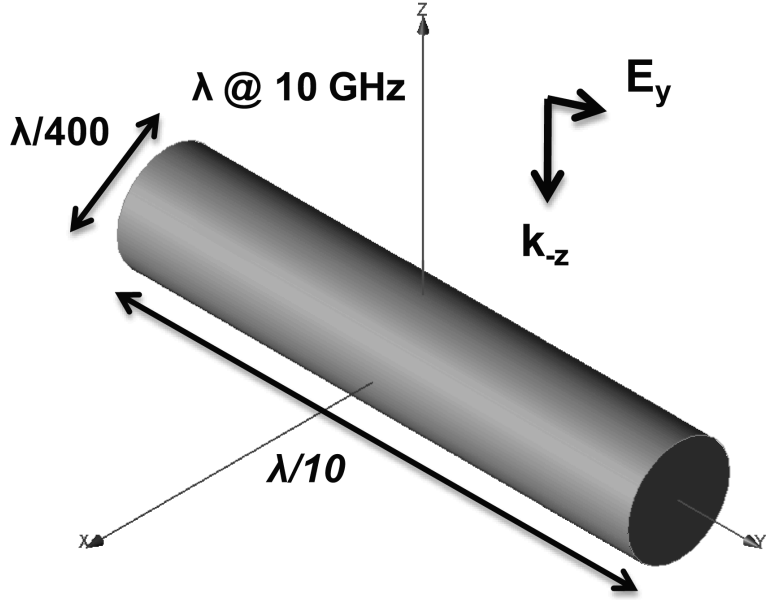


Figure 3.5: A PEC rod.

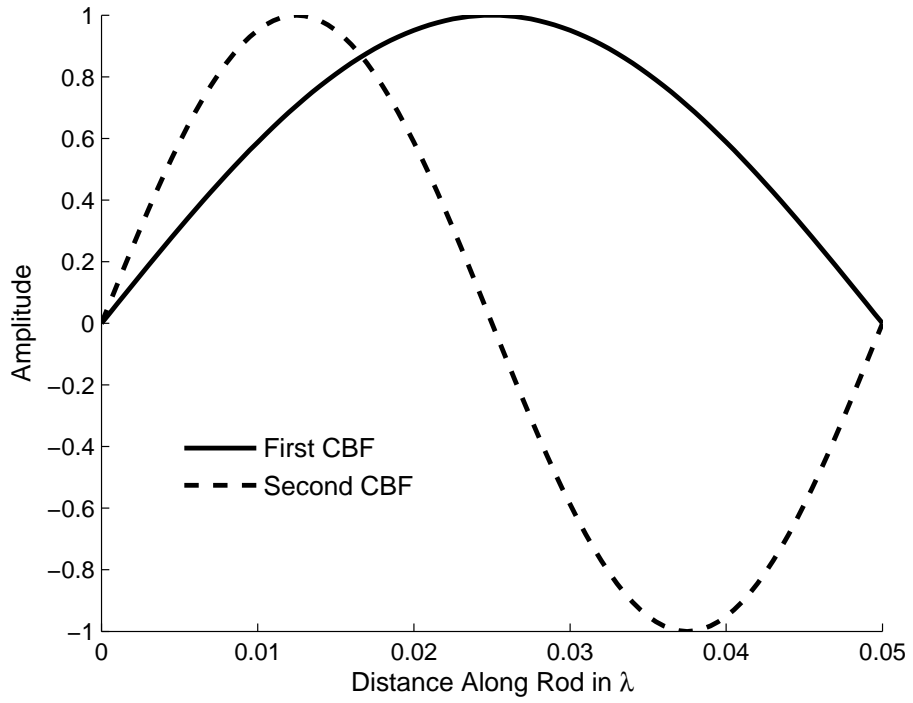


Figure 3.6: Calculated CBFs for the PEC rod in Fig. 3.5.

From the Fig. 3.7 and Table 3.3 we see a that both the DM results compare with those obtained by using commercial MoM solver. However, the DM/CBF approach re-

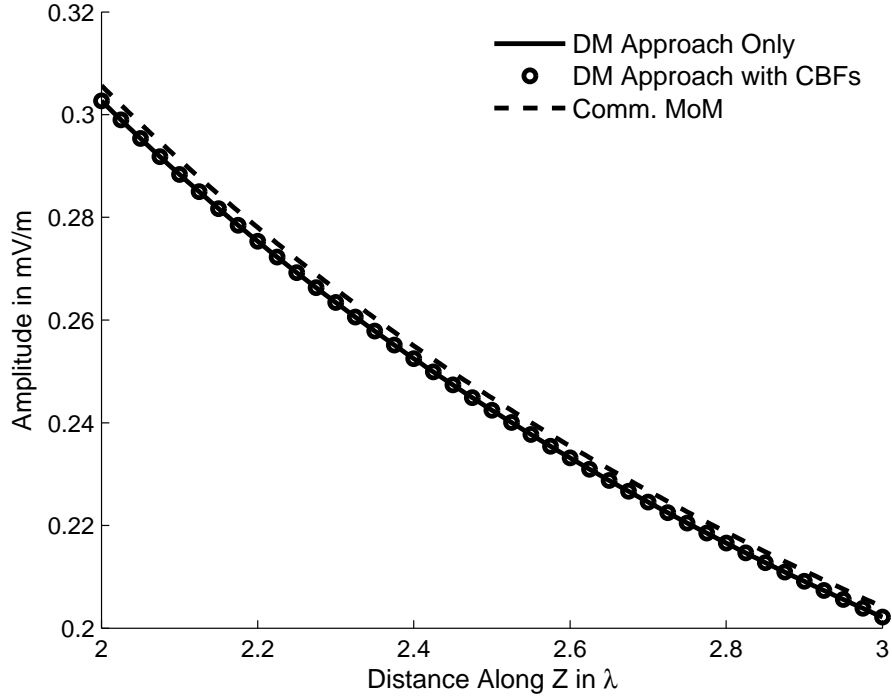


Figure 3.7: Amplitude comparison of backscattered electric field E_y from the PEC rod in Fig. 3.5.

Table 3.3: Comparison of unknowns required for DM approach using CBFs for the PEC rod shown in Fig. 3.5.

Method	No. of Unknowns
DM Approach Only	100
DM Approach with CBFs	2

duces the number of unknowns by a large factor, namely 50 in this example.

3.4 Fast Matrix Generation

Another way to improve the performance of DM approach is to adapt the Fast Matrix Generation (FMG) technique [13], proposed for the generation of matrix elements in the context of the conventional MoM formulation. To adapt this technique for the DM

approach, we consider only the $\frac{1}{r}$ term in the field expression while calculating the interaction between basis functions separated by a distance greater than or equal to $\lambda/10$ and while we consider the $\frac{1}{r^2}$ and $\frac{1}{r^3}$ terms when the distance is less than $\lambda/10$ separation.

Consider a square-shaped dielectric plate, shown in Fig. 3.1. The backscattered field, calculated by using the DM approach with and without the use of FMG algorithm, is presented in Fig. 3.8, which also compares these results with the corresponding ones from a commercial MoM package. Table 3.4 compares the CPU time required by these two different approaches.

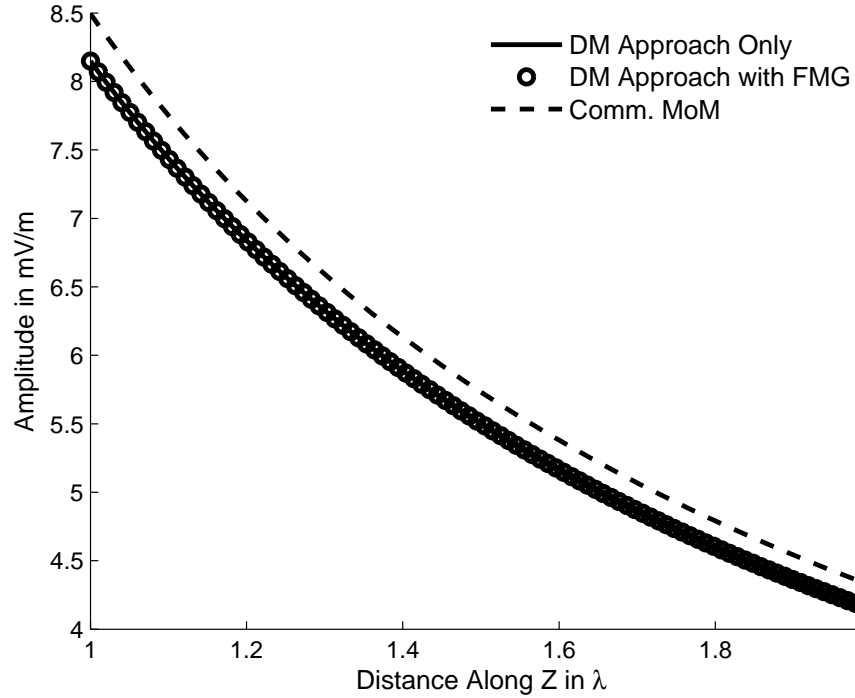


Figure 3.8: Amplitude comparison of backscattered electric field E_y from the dielectric plate in Fig. 3.1.

Fig. 3.8 shows a good comparison of the electric field calculated by using DM approach, with and without the FMG, and also with those from a commercial solver. Even though the Table 3.4 shows only a slight time advantage of FMG over the DM, it has been shown elsewhere this advantage grows rapidly as we increase the electrical length

Table 3.4: Comparison of simulation time for DM approach using FMG for the dielectric plate shown in Fig.3.1.

Method	Simulation Time
DM Approach Only	19.22 minutes
DM Approach with FMG	18.98 minutes

of the geometry. Here we were simply demonstrating that we do not scarifice the accuracy when we use the FMG along with the DM approach.

3.5 Closed-form Field Expressions

To calculate the elements of the interaction matrix we need to sample the macro basis-function for the purpose of approximating the integration with a numerical summation. Let us consider a triangular current distribution which extends over a length of $\lambda/10$, as shown in Fig. 3.9. The fields radiated by this triangular current element is calculated along a parallel line, at an offset of $\lambda/50$, using different number of samples of the current element. Fig. 3.10 compares the E_z -field variation, for different number of samples, with the closed form field expression [14] for the same current distribution.

We note from Fig. 3.10 that we need at least 200 samples to achieve a good match between the closed-form result for the integration and its approximation via numerical summation, when the offset distance is of $\lambda/50$. However, as shown in Fig. 3.11, when we move further, say to a distance of 500λ , we can achieve a good match between the direct integration and numerical approximation with just 2 samples. This implies that to compute the matrix entries for each macro basis function we may need up to 200 samples, depending on the distance where we apply the boundary condition. It would be even more computationally expensive if we use a fine mesh, or if the object is electrically large.



Figure 3.9: Triangular current distribution placed along Z axis from $-\lambda/20$ to $\lambda/20$.

Hence, it would be useful to find a closed-form expression for the field, generated by the current distribution, by representing it in a suitable form as shown below.

A typical current distribution on a wire is piecewise sinusoidal in nature, as represented in equation 3.1 for a wire length of $H_1 + H_2$.

$$I(z) = \begin{cases} I_m \sin(k(H_2 + z)), & \text{if } 0 > z \geq -H_2 \\ I_m \sin(k(H_1 - z)), & \text{if } H_1 \geq z \geq 0 \end{cases} \quad (3.1)$$

where I_m is the maximum amplitude of the current.

The closed-form expression for the field from this type of current distribution along a bent wire (see Fig. 3.12) can be derived, with separate expressions for the top-half and bottom-half of the current distribution, as follows:

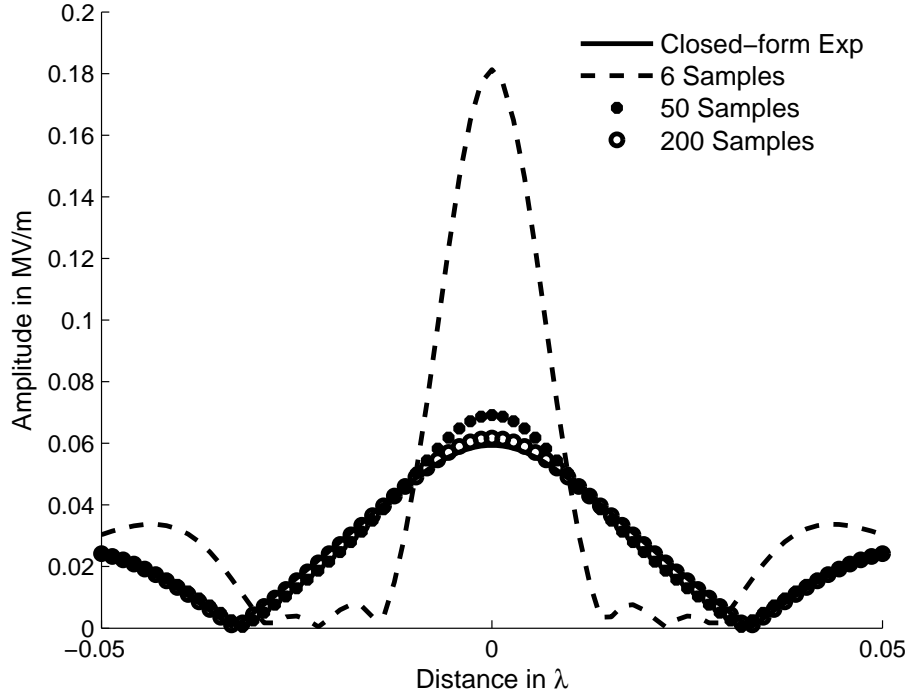


Figure 3.10: Amplitude variation of E_z at a $z = \lambda/50$ radiated by the current distribution shown in Fig. 3.9.

TOP-HALF ($0 \rightarrow H_1$)

$$E_{u_1} = -j30I_m \left[\frac{e^{-j\beta R_1}}{R_1} - \cos(\beta H_1) \frac{e^{-j\beta r}}{r} - ju_1 \sin(\beta H_1) e^{-j\beta r} \left(\frac{1}{r^2} + \frac{1}{j\beta r^3} \right) \right] \quad (3.2a)$$

$$E_{v_1} = \frac{j30I_m}{v_1} \left[(u_1 - H_1) \frac{e^{-j\beta R_1}}{R_1} - u_1 \cos(\beta H_1) \frac{e^{-j\beta r}}{r} - \frac{j \sin(\beta H_1)}{\beta r^3} e^{-j\beta r} (r\beta u_1^2 + jv_1^2) \right] \quad (3.2b)$$

BOTTOM-HALF ($-H_2 \rightarrow 0$)

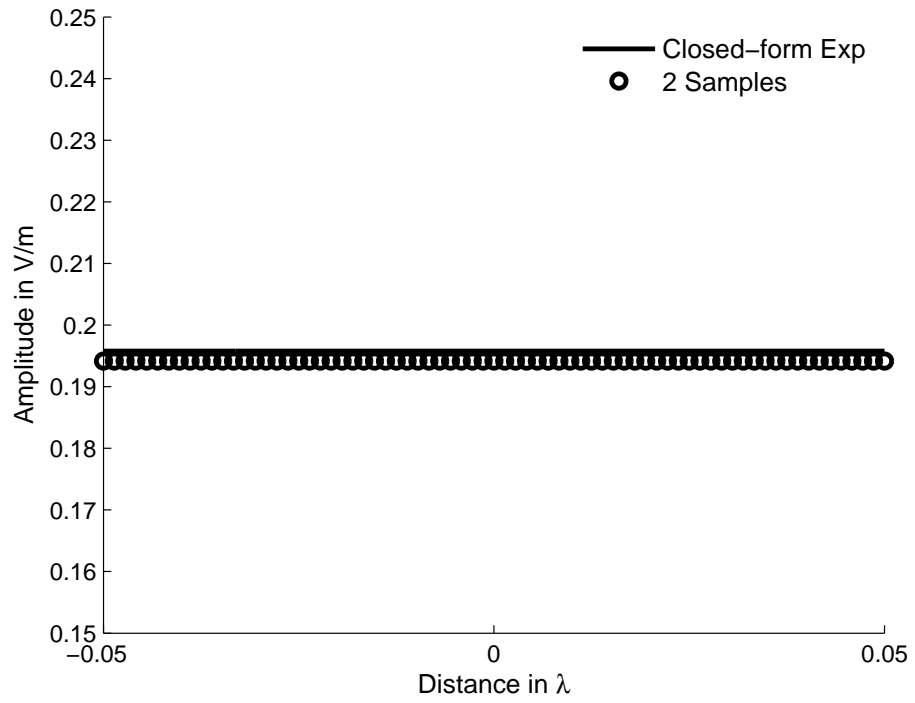


Figure 3.11: Amplitude variation of E_z at a $z = 500\lambda$ radiated by the current distribution shown in Fig. 3.9.

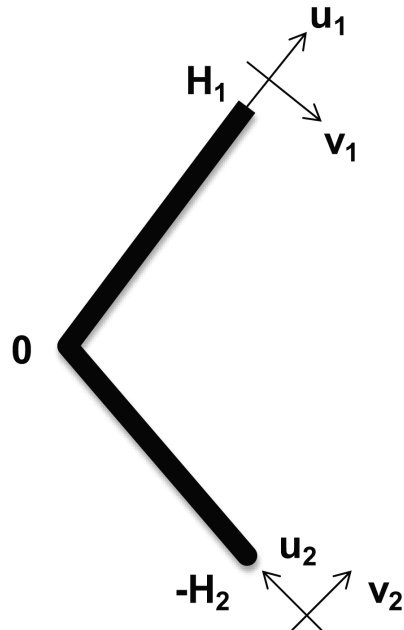


Figure 3.12: A bent wire.

$$E_{u_2} = -j30I_m \left[\frac{e^{-j\beta R_2}}{R_2} - \cos(\beta H_2) \frac{e^{-j\beta r}}{r} + ju_2 \sin(\beta H_2) e^{-j\beta r} \left(\frac{1}{r^2} + \frac{1}{j\beta r^3} \right) \right] \quad (3.3a)$$

$$E_{v_2} = \frac{j30I_m}{v_2} \left[(u_2 + H_2) \frac{e^{-j\beta R_2}}{R_2} - u_2 \cos(\beta H_2) \frac{e^{-j\beta r}}{r} + \frac{j \sin(\beta H_2)}{\beta r^3} e^{-j\beta r} (r\beta u_2^2 + jv_2^2) \right] \quad (3.3b)$$

where the directions \hat{u}_1 and \hat{u}_2 are unit vectors along the axis of the wire, while \hat{v}_1 and \hat{v}_2 are perpendicular to its axis, as shown in Fig. 3.12. From the above equations we can see that when v_1 or v_2 is 0, i.e., when the observation point is either along \hat{u}_1 (or \hat{u}_2) the electric field E_{v_1} (or E_{v_2}) becomes singular. In order to calculate the correct field values for these cases, we model the wire geometry with a sinusoidal current distribution as shown in Fig. 3.13, and use the DM approach with 200 samples. The E_y fields are calculated along a observation line parallel to \hat{y} , by using the expressions given in equations 3.2 and 3.3, as well as by using the DM approach. Fig. 3.14 plots the fields calculated by using these two approaches and they are seen to agree well with each other. We can also see from this figure that the value of the field monotonically increases from zero as we move away from the wire axis. Hence we set the field value to be zero along the wire axis whenever we are interested in the field value at a point located on the axis.

3.5.1 Numerical Results using Triangular Basis Functions

It is important to note the fact that the sinusoidal basis function closely resembles a triangular basis function (TBF), provided the support of the basis is less than or equal to $\lambda/10$. Hence we can use the closed form expressions given in equations 3.2 and 3.3 to calculate the field values for the most commonly used TBFs, whose supports are less than or equal to $\lambda/10$.

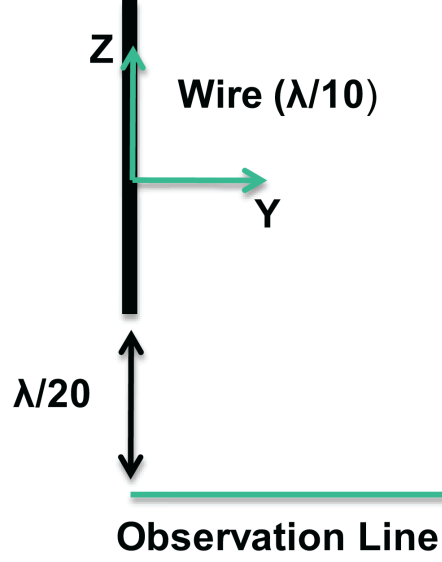


Figure 3.13: A wire geometry.

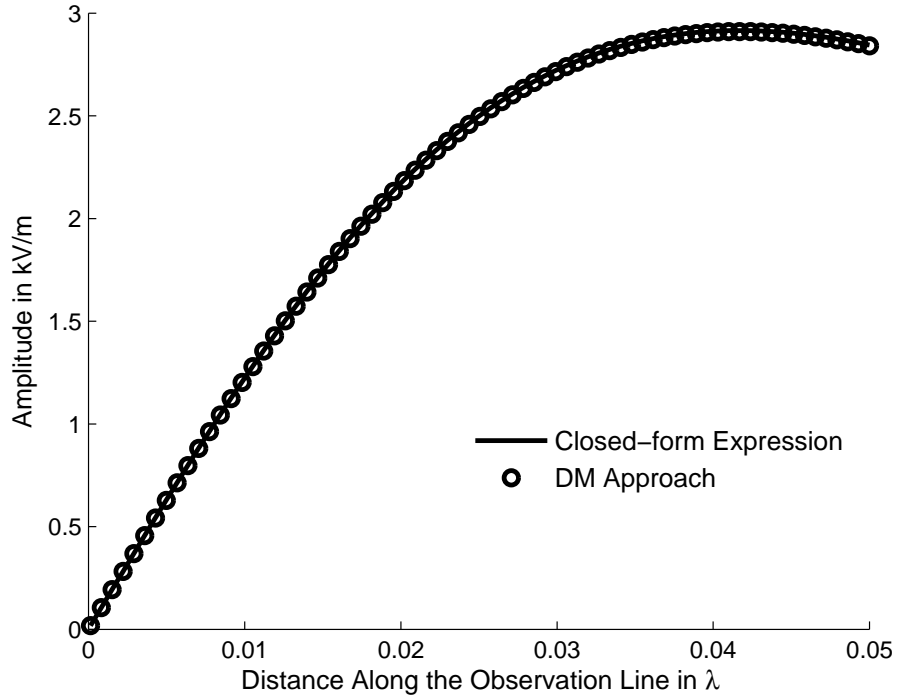


Figure 3.14: Amplitude variation of E_y along the observation line in λ for the wire geometry in Fig. 3.13.

For the first example we consider a PEC rod, whose length and diameter are λ and $\lambda/500$, respectively. It is illuminated by a plane wave, incident from broadside, as shown

in the Fig. 3.15. Fig. 3.16 compares the peak amplitude of the induced current in the PEC rod calculated by using the DM approach and closed form expressions, with those obtained from a commercial MoM package for different frequencies of the incident plane wave, ranging from 1 MHz to 10 GHz.

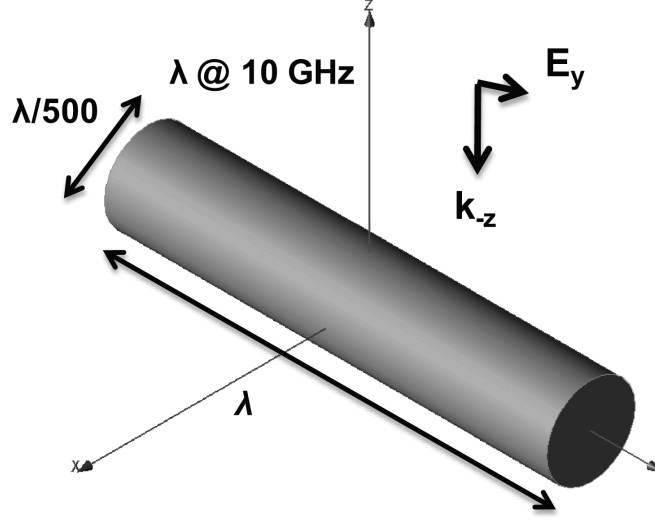


Figure 3.15: A PEC rod.

From Fig. 3.16 we can see that the results from the DM approach using closed-form expressions compare well with those from the commercial MoM solver. However, we have found that the commercial MoM solver failed when we go down below 10 Hz, while the DM approach is able to handle the problem without any special treatments or modifications. The number of TBFs used to model the wire varies with frequency, starting with 9 TBFs at 10 GHz and progressively decreasing to 1 at 1 MHz (or below), as listed in Table 3.5. We expect this to be the case since the variation in the current distribution on the wire varies less rapidly as we decrease the frequency. Incidentally, although it makes little difference in the accuracy level of the solution whether we use the same number of TBFs over the entire frequency range or decrease their number progressively, we find that the condition number of the interaction matrix improves when we use a variable number of TBFs with frequency, as may be seen from Fig. 3.17.

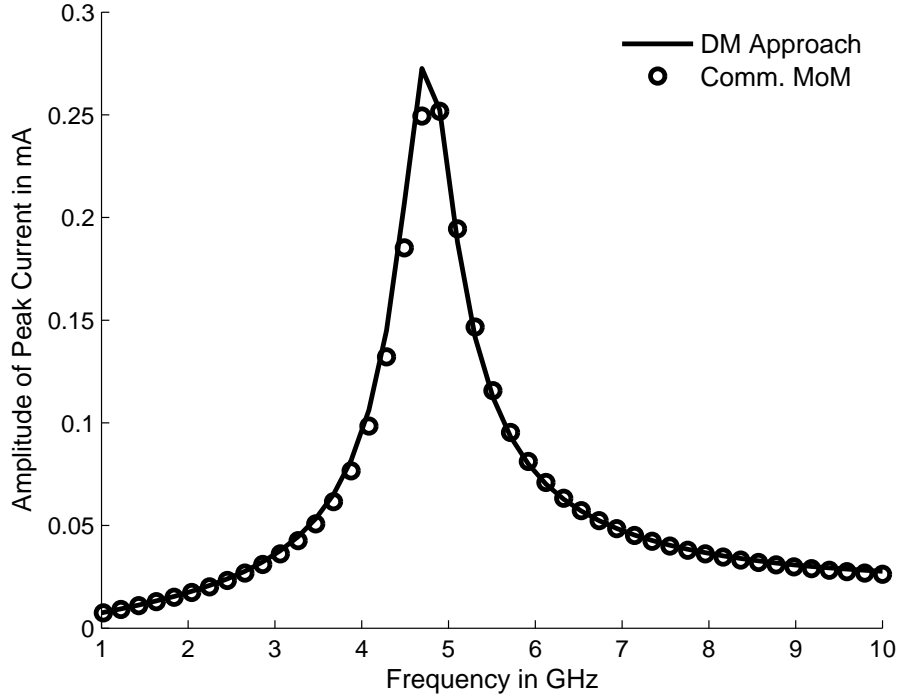


Figure 3.16: Frequency variation of peak current for the PEC rod in Fig. 3.15.

Table 3.5: Number of TBFs used in different frequency ranges for the PEC rod shown in Fig. 3.15.

Frequency Range	No. of TBFs Used
1 MHz - 1 GHz	1
1 GHz - 3 GHz	3
3 GHz - 5 GHz	5
5 GHz - 7 GHz	7
7 GHz - 10 GHz	9

In order to study the improvement in performance with the use of closed-form expressions, we consider a circular PEC loop with a diameter of $\lambda/23.3$ and a thickness of $\lambda/100$ at 1 GHz. It is illuminated by a plane wave, incident from the \hat{z} direction, and polarized along \hat{x} , as shown in Fig. 3.18. Fig. 3.19 compares the variation of the induced current calculated by using the DM approach with that derived by using the DM approach and closed-form expressions. Table 3.6 compares the times required for these

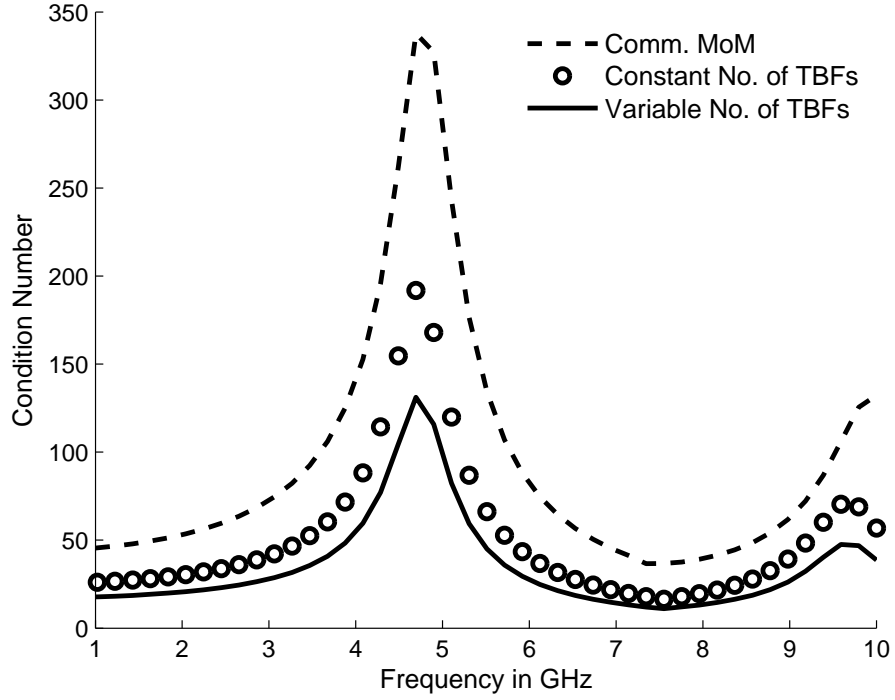


Figure 3.17: Frequency variation of condition number for the PEC rod in Fig. 3.15.

two approaches and we clearly see that the use of closed-form expression speeds up the process by a factor of 3.3 for this problem without compromising the accuracy, as may be seen by referring to Fig. 3.19.

Table 3.6: Comparison of simulation times using DM approach with and without closed-form expressions for the PEC loop shown in Fig.3.18.

Method	Simulation Time
DM Approach without Closed-form	0.53 seconds
DM Approach with Closed-form	0.16 seconds

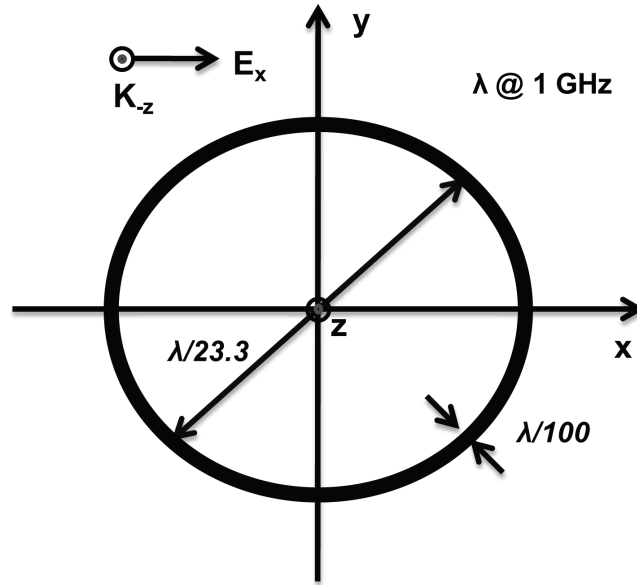


Figure 3.18: A PEC circular loop.

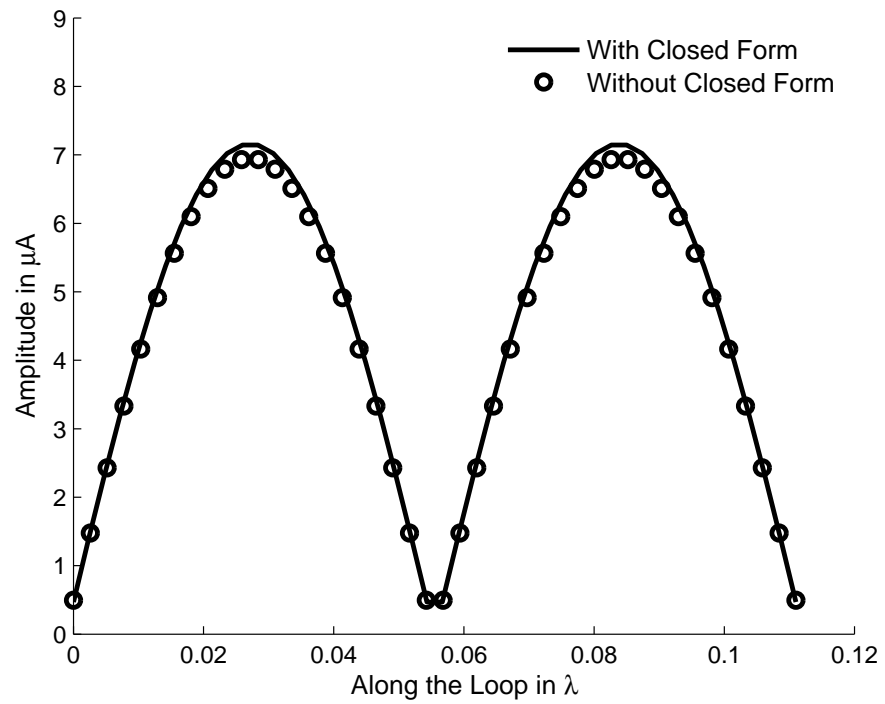


Figure 3.19: Amplitude variation of the induced current for the PEC loop in Fig. 3.18.

3.5.2 Numerical Results Obtained by using Rooftop Basis Functions

One of the most commonly used basis functions for representing current distributions on surfaces is the Rooftop. It is a two-dimensional basis function comprising of pulse basis function along one direction, and a triangular basis function along the other, as shown in Fig. 3.20. The current density distribution associated with a rooftop is given by:

$$J(x, y) = I_m \sin[k(H - |u|)] \text{rect}\left(\frac{x}{2H}\right) \text{rect}\left(\frac{y}{w}\right) \quad (3.4)$$

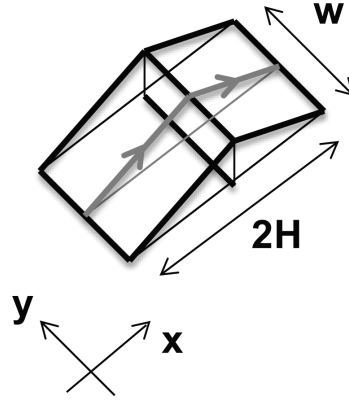


Figure 3.20: A Rooftop basis function.

In order to model this rooftop using the field expressions previously derived in this section, we represent the rooftop basis function with a number of TBFs that have the same maximum amplitude. We carried out a wide range of numerical experiments with the number of TBFs, and have found that we need to represent a rooftop with 7 TBFs to get accurate results. As an example, let us consider a square-shaped PEC plate, which is $\lambda/2$ on the side, and whose thickness is $\lambda/25$. The plate is illuminated by a plane wave traveling along the negative- z direction, as shown in the Fig. 3.21. The backscattered field, calculated by using the DM approach and closed-form expressions, is presented in Fig. 3.22, which also compares these results with the corresponding ones from a commercial

MoM package. To calculate the field directly at the center of the plate by using the DM approach, we average of the field over the footprint of the rooftop basis function at the center of the plate. We do this in the DM approach in order to improve its accuracy, instead of using point matching for this case, as we do for other locations on the plate.

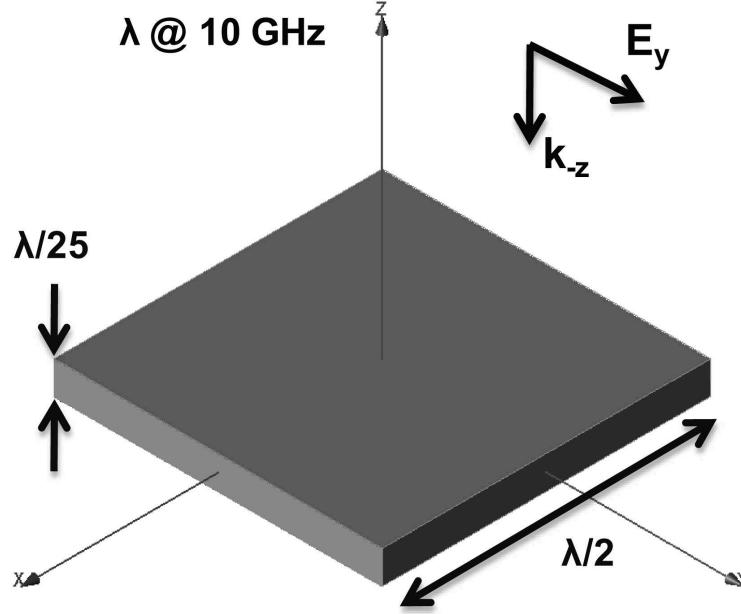


Figure 3.21: A PEC plate.

Table 3.7: Comparison of simulation times using the DM approach, with and without closed-form expressions, for the PEC plate shown in Fig.3.21.

Method	Simulation Time
DM Approach without Closed-form	69 seconds
DM Approach with Closed-form	57 seconds

Table 3.7 compares the time required by the DM approach with and without the use of closed form expressions. It is evident, from Fig. 3.22, that the use of closed form expression speeds up the process without compromising the accuracy, even when the observation point is close to the surface of the plate. To further improve the performance in terms of the CPU time without compromising the accuracy, we can use 7 rooftops to compute the self term, 5 rooftops to calculate the interaction between the rooftops

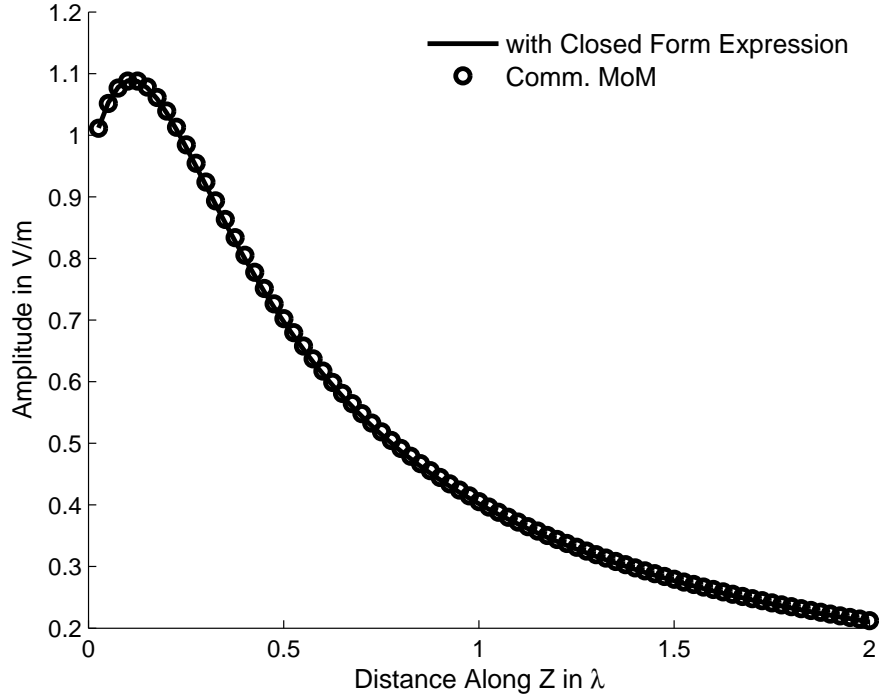


Figure 3.22: Amplitude comparison of backscattered electric field E_y from the PEC plate in Fig. 3.21.

located within a distance of $\lambda/10$; 3 rooftops for the calculation of interaction between the rooftops when this separation distance is greater than $\lambda/10$ but less than $\lambda/5$; and, a single TBF for separation distances greater than $\lambda/5$.

3.6 Some Embellishments to the Basic DM Approach

3.6.1 Incorporating Lumped Loads

Lumped loads are often used either to match the impedance of an antenna or to shift its resonance. The resonance behavior achieved by using lumped loads is often sharp, and requires a fine frequency sampling to capture this resonance behavior. From our experience, many of the commercial solvers fail to capture these resonances and it would

be useful to incorporate lumped loads in the DM approach to see if it performs better than the existing codes. Incorporating lumped loads in the DM approach is relatively simple, and is achieved by the addition of the lumped load impedance to certain matrix elements depending upon the spatial locations of the load.

For the first example, we consider a circular PEC loop with a diameter of 600 mm, a thickness of 18.6 mm and a lumped capacitor of 0.3 nF inserted in the loop, as shown in Fig. 3.23. The loop is fed with a voltage gap source. The frequency range of interest is 6 MHz to 11 MHz, and we expect a series resonance to occur around 8 MHz, between the lumped capacitance and the inductance of the loop. Fig. 3.23 compares the frequency variation of the input current, calculated by using the DM approach, with those obtained from the NEC code.

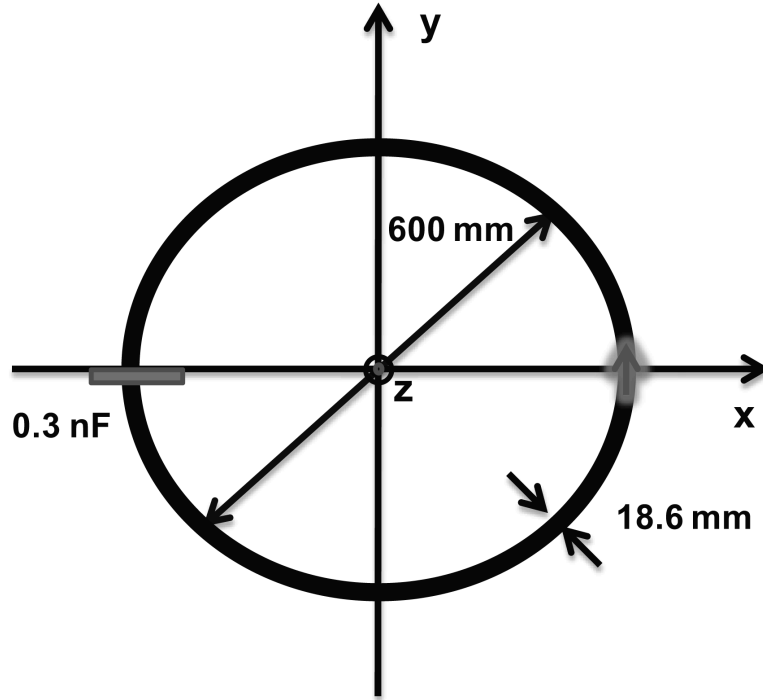


Figure 3.23: A PEC circular loop with a capacitor.

From Fig. 3.24 we can see that the comparison of the input current is good even though the loaded loop exhibits a sharp resonance.

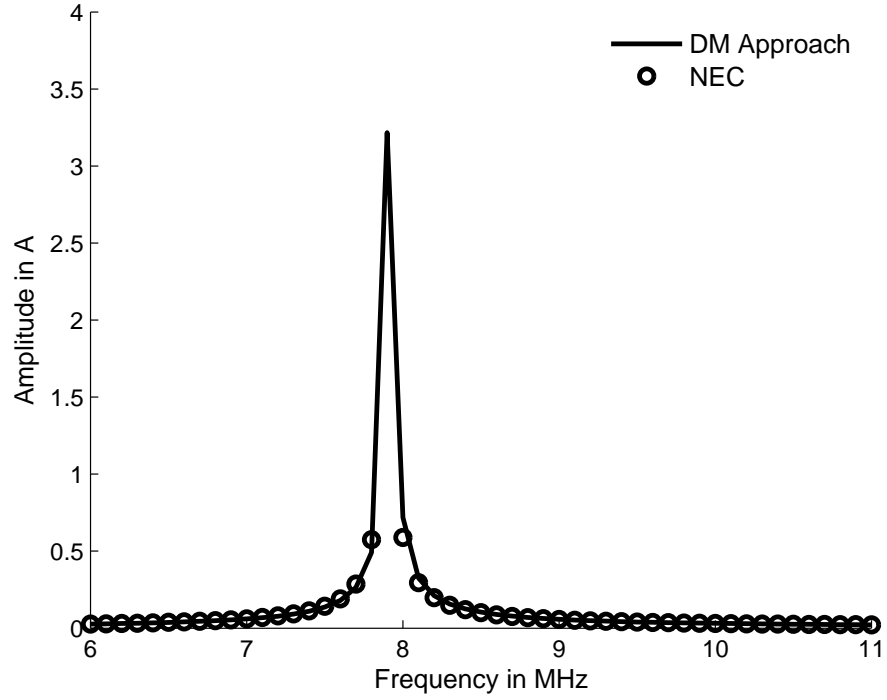


Figure 3.24: Frequency variation of the input current in a PEC loop shown in Fig. 3.23.

For the next example, we consider a power coil comprising of 4 loops, shown in Fig. 3.25, which is modeled by using 192 TBFs. Loop-1 is fed by using a voltage gap source. Fig. 3.26 compares the peak current in the output coil, i.e., the loop-4, obtained by using the DM approach, and compare it with the one generated by using the NEC code.

Fig. 3.26 shows a good comparison between the amplitude variations, however, there is a mismatch between the amplitude at the resonant frequency, which is attributable to the sharpness of the resonance, and the difference in the methodologies used in the DM approach and the NEC.

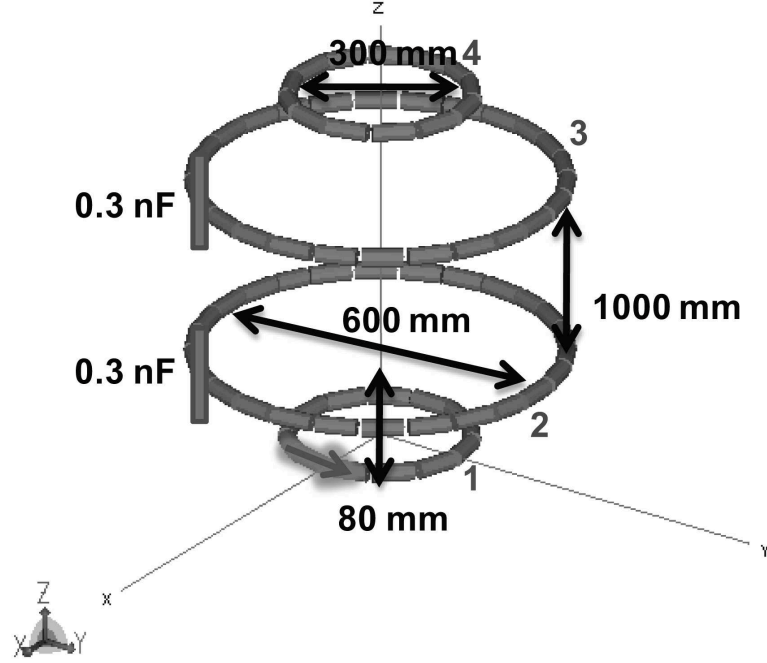


Figure 3.25: A geometry of a power coil.

3.6.2 Input Impedance of Nano Antennas

As we move towards the miniaturization of electronic devices, the sizes of the electronic components also follow suit. One of the important components of interest is the small antenna, the evaluation of whose input impedances becomes more challenging as the cross section of the small antenna becomes comparable to its length. A whole host of techniques have been proposed in the literature for computing the input impedance of antennas. Harrington has presented an expression given in (3.5), for evaluating the input impedance of an antenna by using the current induced on the same.

$$Z_{in} = -\frac{1}{|I_m|^2} \iint \mathbf{E} \cdot \mathbf{J}_s^* ds \quad (3.5)$$

Since the expression (3.5) is variational, it supposedly generates a result for the impedance that is second-order accurate even when the induced current \mathbf{J}_s inserted in (3.5)

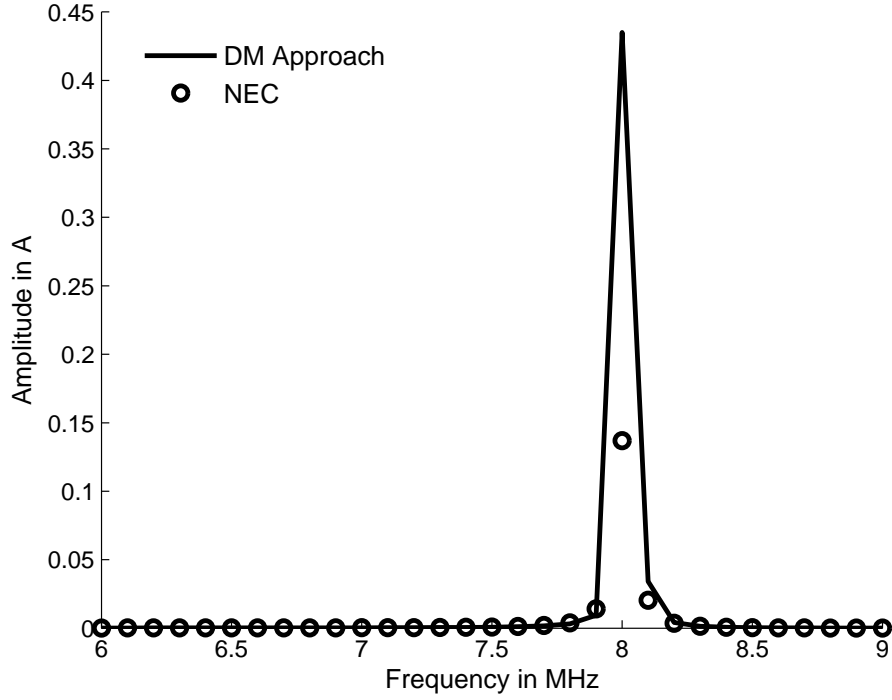


Figure 3.26: Frequency variation of the peak output current for a power coil shown in Fig. 3.25.

has only a first-order accuracy. However, we will show that by using the DM approach we can accurately calculate the input impedance of small antennas. Consider the vertical monopole antenna, shown in Fig. 3.27, which has a length of $\lambda/40$ and a thickness of $\lambda/500$ at 10 GHz. Fig. 3.28 shows the current variation along the antenna calculated by using the DM approach. Table 3.8 below summarizes the input impedance results computed by using the DM approach; with Harrington's formula in (3.5); and with a simplified transmission line model.

Table 3.8 shows that using the conventional truncated sinusoidal type of representation for the induced current in (3.5) yields results that deviate considerably from those computed accurately by employing the DM approach.

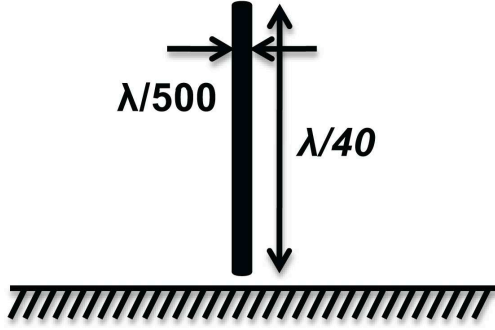


Figure 3.27: A vertical monopole antenna.

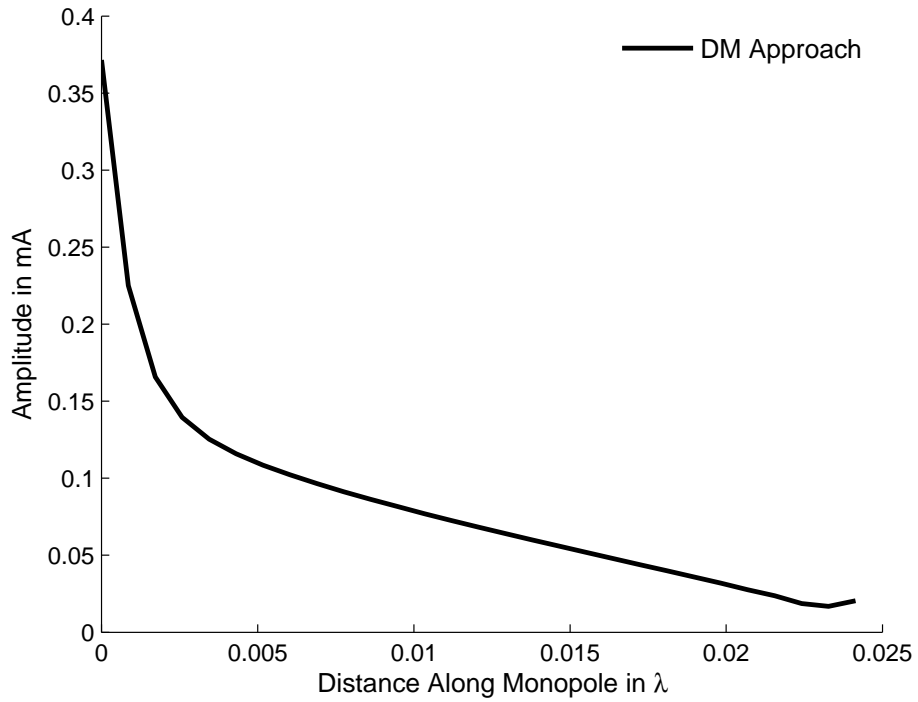


Figure 3.28: Amplitude variation of the current for a monopole shown in Fig. 3.27.

3.6.3 Irregular Geometries

Handling irregular geometries can be challenging, since we need to use different mesh sizes and basis functions to accurately model different parts of the geometry. In the conventional MoM as well as FEM, this variation in the mesh sizes can lead to a poorly conditioned matrix. To handle such geometries using the DM approach, we first calculate

Table 3.8: Comparison of input impedance calculated by using DM approach, Harrington's approach (3.5) and a simplified transmission model for the monopole shown in Fig.3.27.

Method	Input Reactance
DM Approach	-1.1916e+003j
Variational Formula (3.5)	-2.5216j
Simplified Transmission Model	-1.4080e+003j

the elements of the interaction matrix using the closest possible regular geometry, and then modify the corresponding elements with the ratio of areas of the footprints of the basis functions in the regular and the actual geometries.

Consider a PEC plate with a thickness of $\lambda/25$, shown in Fig. 3.29. The closet regular geometry is a $\lambda/2$ square plate with the same thickness, i.e., $\lambda/25$. The interaction matrix is generated by using the regular square PEC plate using the DM approach as described in the Section 3.5.2. This interaction matrix is then modified, to handle the actual geometry, by multiplying the difference in the foot prints of the roof top basis functions before calculating the currents. Fig. 3.30 compares the scattered electric field pattern, at a radial distance of 2λ , with $\phi = 45^\circ$, calculated by using the DM approach with those obtained from the commercial MoM solver at 5 GHz.

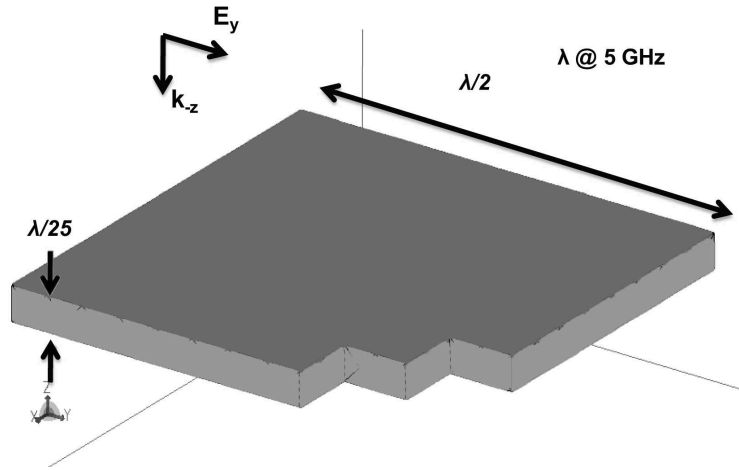


Figure 3.29: A PEC plate with a staircase corner.

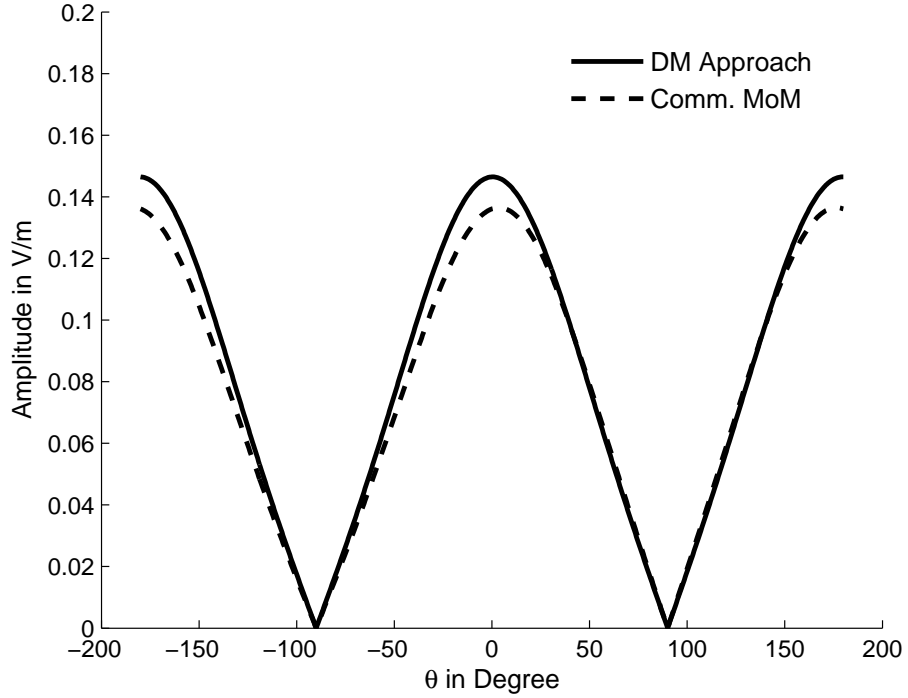


Figure 3.30: Amplitude comparison of scattered electric field E_θ at $\phi = 45^\circ$ from the PEC geometry in Fig. 3.29.

From Fig. 3.30 we find that the results from DM approach shows good comparison with those from the commercial MoM solver. However, it was found that when the geometry becomes thinner and the number of irregularities increase, the commercial MoM solver is not able to handle the problem, while the DM approach was able to do so with relative ease.

3.6.4 Curved Surfaces

Another object of interest is a faceted surface, which is difficult to handle with the conventional solvers when the geometry has sharp edges. Consider the corner reflector shown in Fig. 3.31, which has a height of $\lambda/2$ at 5 GHz and an included angle of 60° between the two faces. Fig. 3.32 compares the backscattered field along a line parallel to y-axis with

$z = \lambda/2$ calculated by using the DM approach (modeled with 180 rooftops), as described in the Section 3.5.2, with those computed by employing a commercial MoM solver.

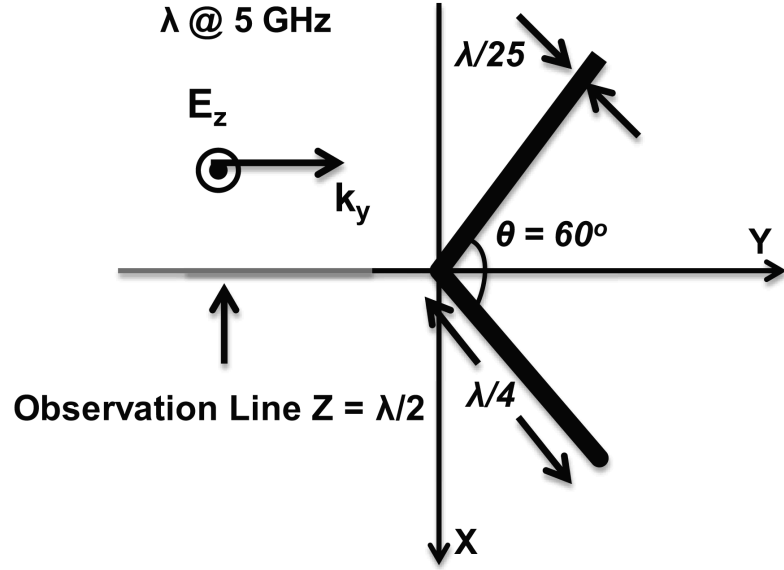


Figure 3.31: A corner reflector.

Fig. 3.32 shows a good comparison of the fields calculated by using the DM approach with those calculated from the commercial solver. However, we found that when we decrease the included angle between the faces to 5° or smaller, the commercial solver is unable to handle the problem, while the DM approach could without any difficulty.

For the second example we consider a faceted PEC surface shown in Fig. 3.33. It has a height of $\lambda/4$, a width of $\lambda/20$ and a thickness of $\lambda/25$ at 5 GHz. Fig. 3.34 compares the backscattered field calculated by using the DM approach (modeled with 40 rooftops), as described in the Section 3.5.2, with that calculated from a commercial MoM solver.

From Fig. 3.34 we see good comparison between the fields calculated by using the DM approach with those obtained from a commercial solver. Whenever we deal with either dielectric objects with curved surfaces, or those with thin curved geometries the commercial solver generates an ill-conditioned matrix, whose solution is questionable in terms of accuracy; however, the DM approach exhibits no such behavior.

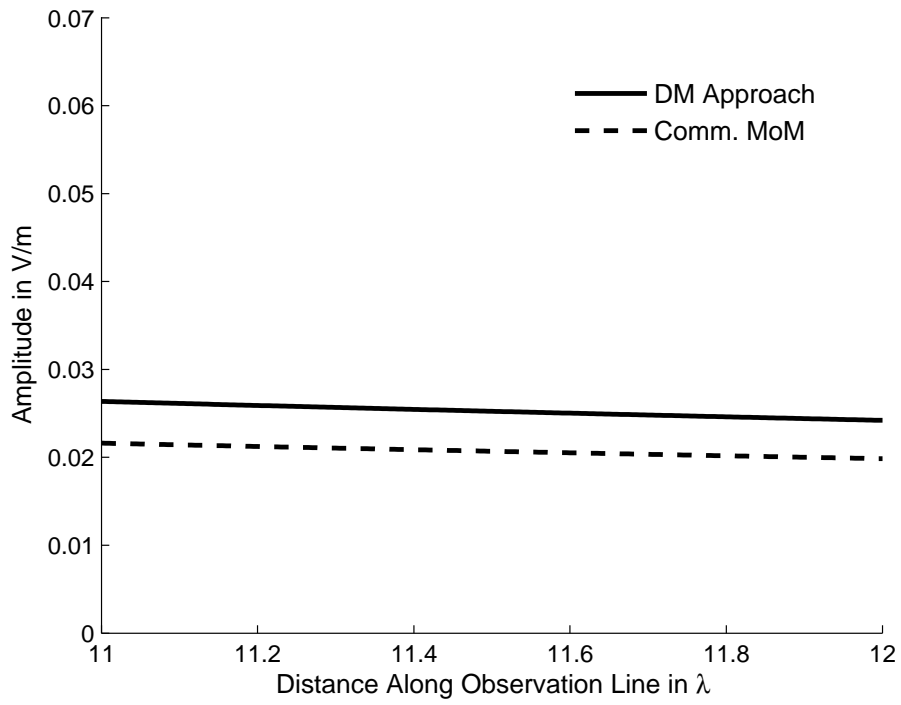


Figure 3.32: Amplitude comparison of backscattered electric field E_z from the corner reflector in Fig. 3.31.

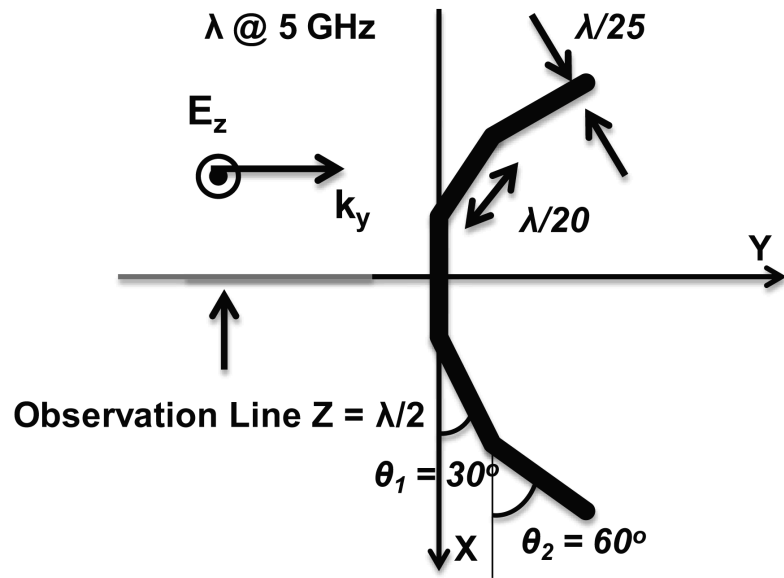


Figure 3.33: A faceted PEC surface.

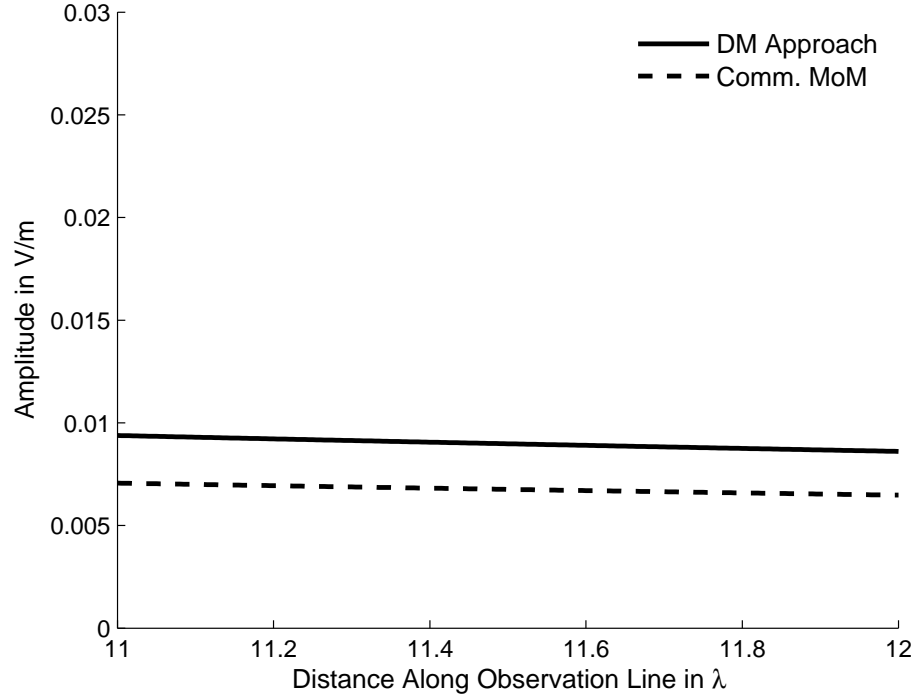


Figure 3.34: Amplitude comparison of backscattered electric field E_z from the faceted PEC surface in Fig. 3.33.

3.6.5 Geometries with Apertures

DM approach can handle geometries with apertures or slits with relative ease without requiring any modification to the approach. Consider a rectangular PEC plate, split at the center, with a gap of $\lambda/40$ and a thickness of $\lambda/25$ at 10 GHz, as shown in Fig. 3.35. Fig. 3.36 compares the backscattered field computed by using the DM approach as described in the Section 3.5.2, with that calculated by using a commercial MoM solver.

Fig. 3.36 shows good comparison between the two backscattered fields even as we approach the surface of the plate. If we decrease the split gap size to $\lambda/80$, the associated matrix in the commercial solver becomes ill-conditioned, while the associated matrix in the DM approach remains well conditioned regardless of the gap size.

For the next example, we consider a PEC square plate of side length of $\lambda/2$ with a

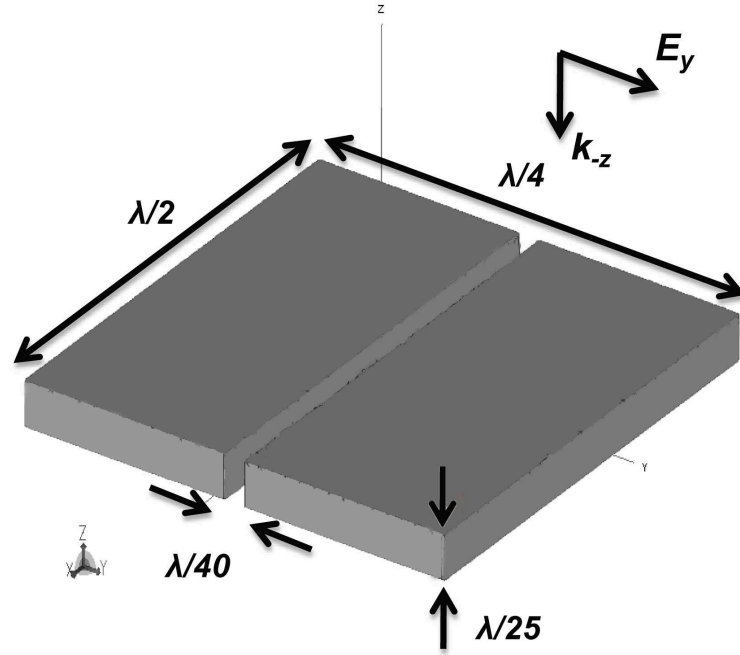


Figure 3.35: A PEC plate with a split.

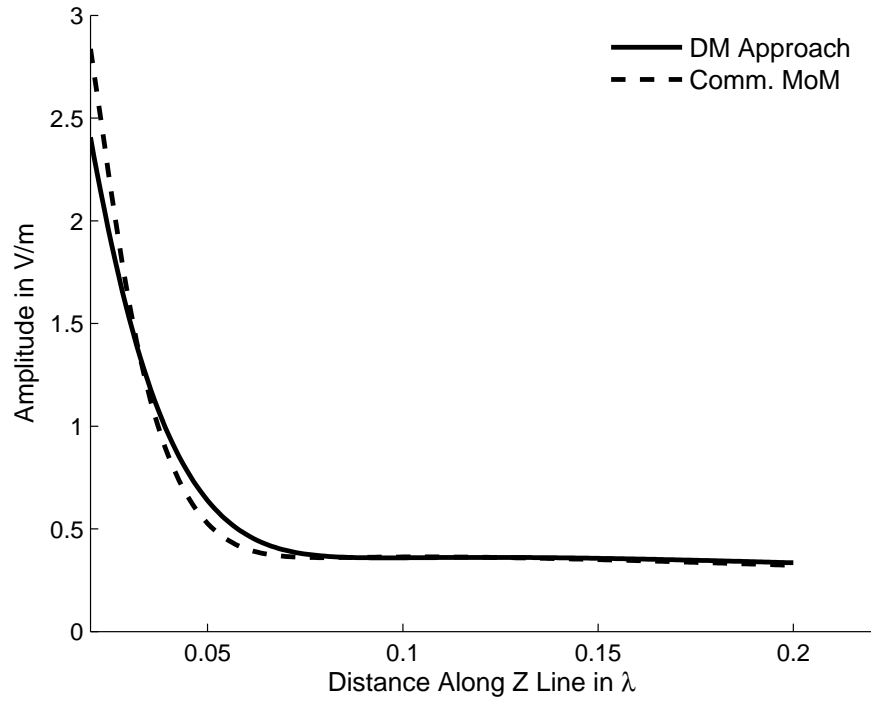


Figure 3.36: Amplitude comparison of backscattered electric field E_y from the PEC surface in Fig. 3.35.

square aperture of size $\lambda/20$, at a frequency of 10 GHz, as shown in Fig. 3.37. In order to model the aperture, the first step is to calculate the E-fields over the aperture. Hence we model a smaller plate of size $\lambda/4$ with the same aperture size using the DM approach without MBFs and calculate the dominant field component in the aperture, namely the E_y fields in this case. Using the E_y field so obtained, we compute the magnetic field current \vec{M}_x over the aperture. Once we know the equivalent magnetic current in the aperture, we can back it with a PEC surface by invoking the Huygens' principle. The total field will be a summation of two sets of fields: (i) scattered by the PEC square plate with the aperture closed, but in the presence of \vec{M}_x , solved by using rooftop basis function in the context of DM, as described in Section 3.5.2; (ii) fields radiated by \vec{M}_x , either when it is placed over a ground plane, or by $2\vec{M}_x$ in free space, if we make the assumption that the plane is infinitely large. However this approximation is justified since the fields radiated by $2\vec{M}_x$ over the surface $z = 0$ is concentrated only near the aperture and they rapidly decrease as we move away from the aperture, as shown in Figs. 3.38 and 3.39.

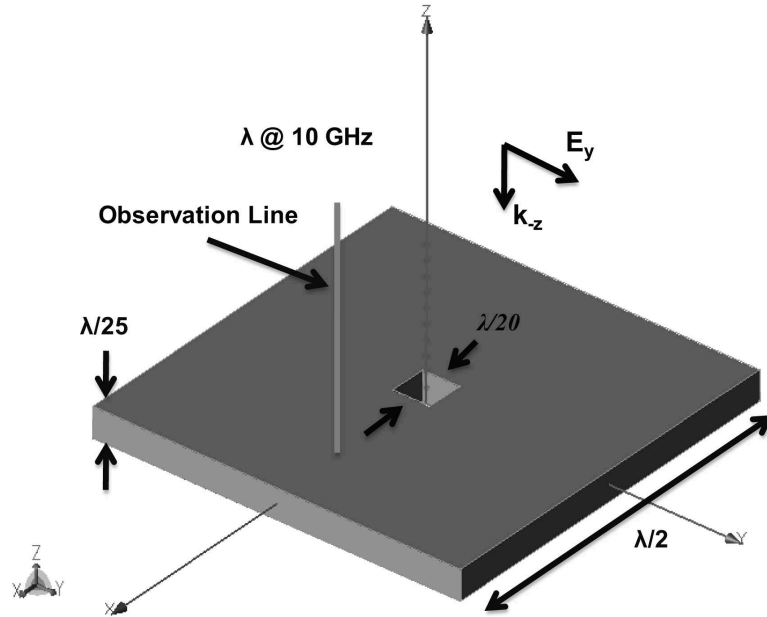


Figure 3.37: A PEC plate with a square slot.

Fig. 3.40 compares the amplitude of the backscattered field E_y calculated by using

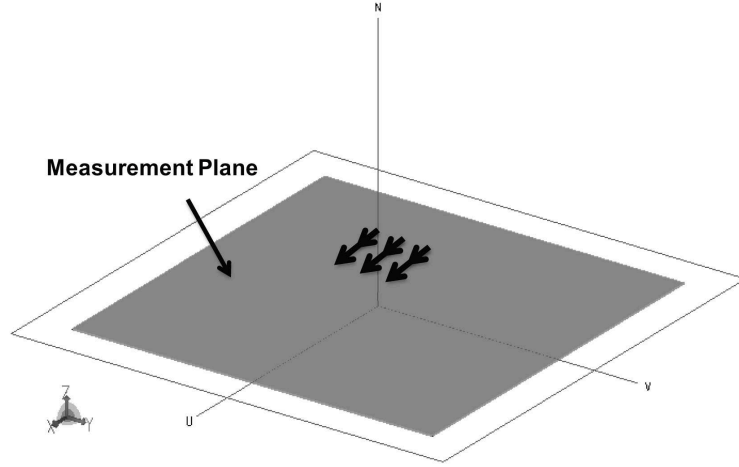


Figure 3.38: Equivalent magnetic current.

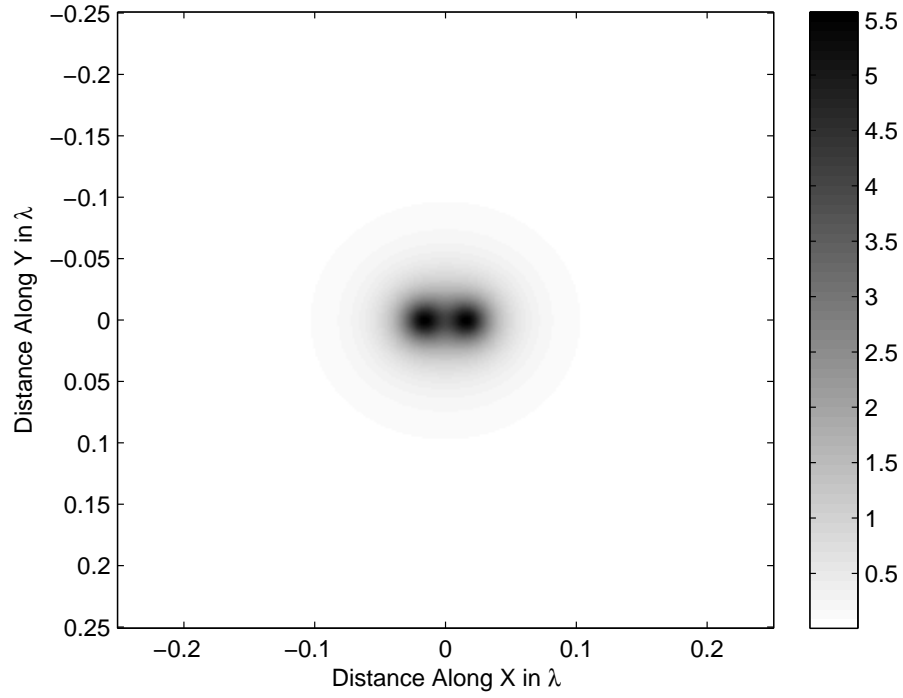


Figure 3.39: Amplitude variation of the radiated electric field E_y from the equivalent magnetic current in Fig. 3.38.

DM approach with those computed by using a commercial MoM solver. We have also used the same approach to solve the problem of a PEC plate with a rectangular slot as shown in Fig. 3.41 and the scattered fields from this geometry are plotted in Fig.

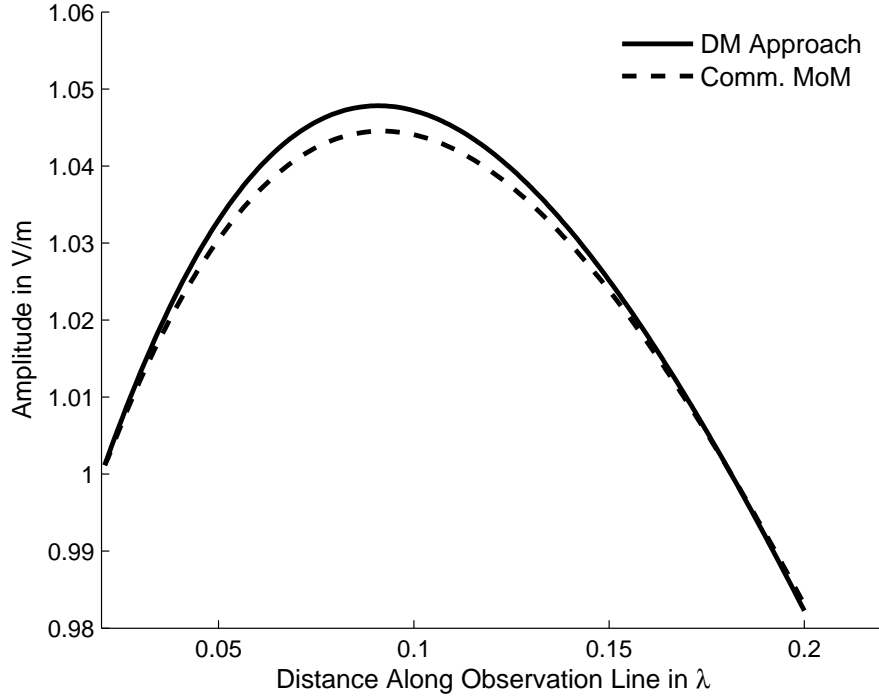


Figure 3.40: Amplitude comparison of backscattered electric field E_y from the PEC surface in Fig. 3.37.

3.42. Once again we find a good match between the results of the DM approach and those from a commercial MoM code for both of these plate geometries with apertures. However, as mentioned earlier for the case of the slit, the commercial solver breaks down for narrow-size apertures, while the DM approach handles it with relative ease.

3.6.6 Microstrip-based Structures

As the size of the semiconductor devices go down, the thickness of the microstrip substrate also becomes smaller. With increasing integration of electronic packages sharing the same substrate, the mutual coupling becomes critical, and often requires an accurate modeling. The thinness of the substrate, along with the finer widths of the signal traces challenge the existing CEM algorithms when used to calculate the electromagnetic response charac-

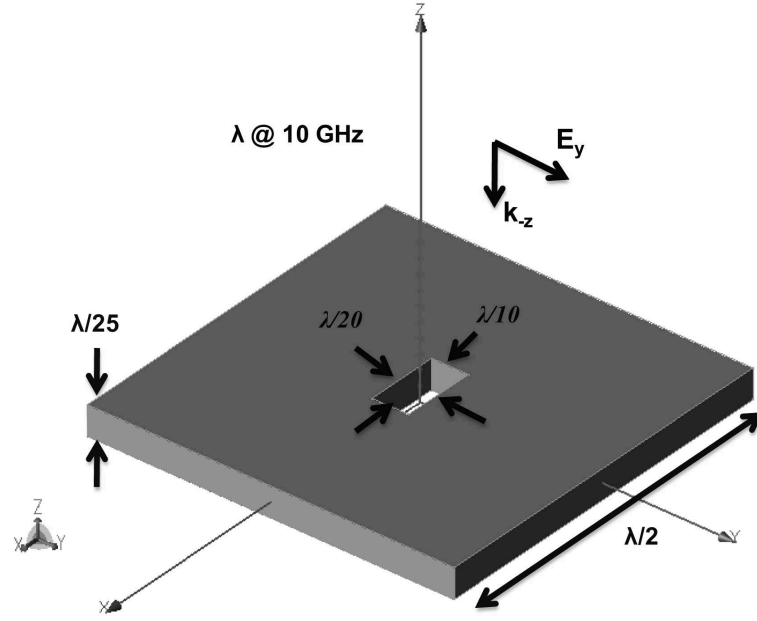


Figure 3.41: A PEC plate with a rectangular slot.

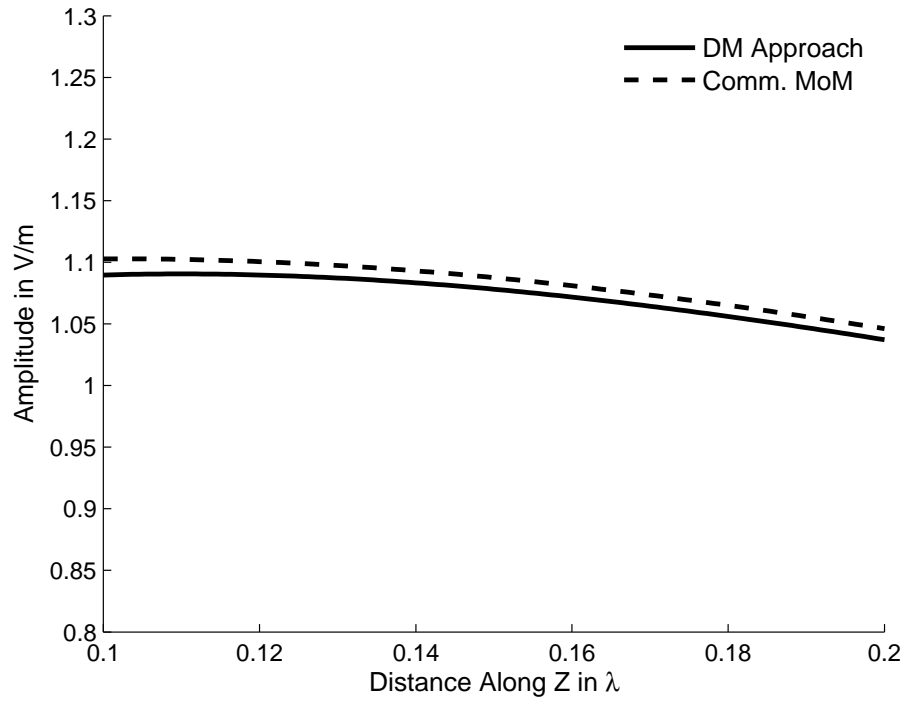


Figure 3.42: Amplitude comparison of backscattered electric field E_y from the PEC geometry in Fig. 3.41.

teristics of such packages. To demonstrate that the DM approach can handle geometries with fine structures, we consider the example of a microstrip transmission line shown in Fig. 3.43, whose length is 2λ and, which has free space as its substrate. The transmission line is modeled by using the DM approach with a voltage source exciting the line at one end ($x = -\lambda$), under the infinite ground plane approximation, which is typical. We use rooftops, as described in Section 3.5.2, to model the current densities J_x and J_y with $\lambda/10 \times \lambda/100$ and $\lambda/20 \times \lambda/20$, respectively, at a frequency of 10 GHz. Fig. 3.44 plots the variation of I_x along the trace calculated by using the DM approach and shows the standing wave pattern as expected.

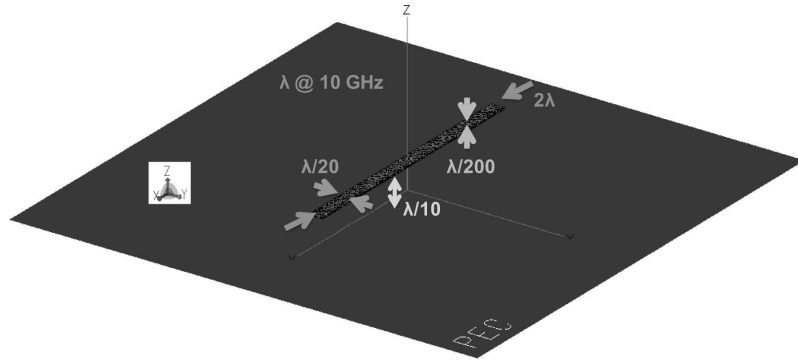


Figure 3.43: A microstrip geometry.

For the next example, we consider a similar microstrip geometry, as shown in Fig. 3.45. The line is illuminated by a plane wave traveling along the negative- z direction and polarized along \hat{x} . Fig. 3.46 compares the scattered field along \hat{z} , calculated using the DM approach, as described in the previous example, with those calculated by using a commercial MoM solver.

Fig. 3.46 shows a good comparison between the results generated by the DM approach and those derived from a commercial MoM solver. We point out that the advantage of using the DM approach lies in the fact that it continues to work well when we make the substrate thinner, add losses to it, and use even finer signal traces. The commercial solvers, on the other hand break down under these circumstances.

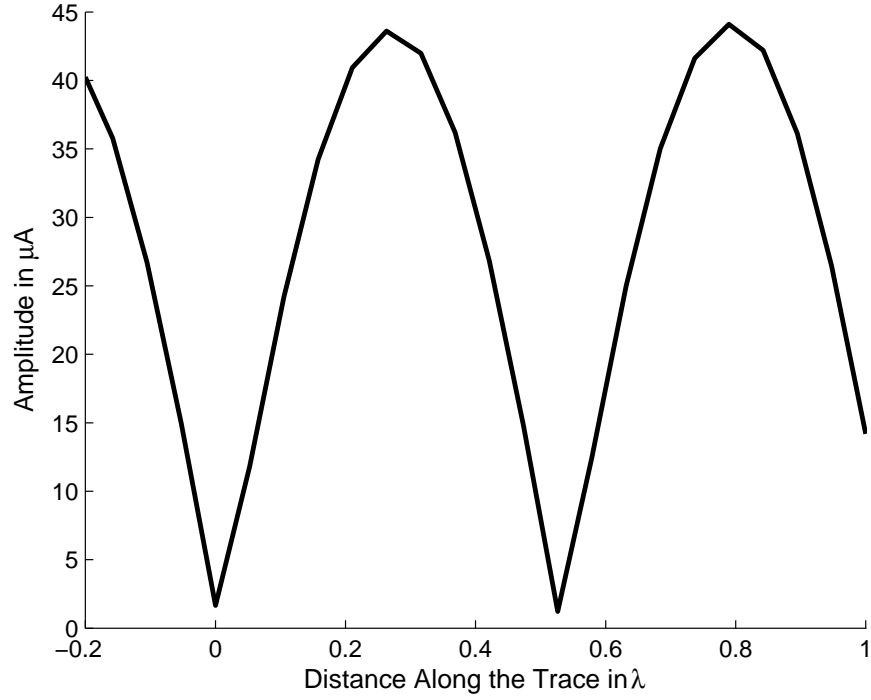


Figure 3.44: Variation of I_x along the trace of a microstrip line in Fig. 3.43.

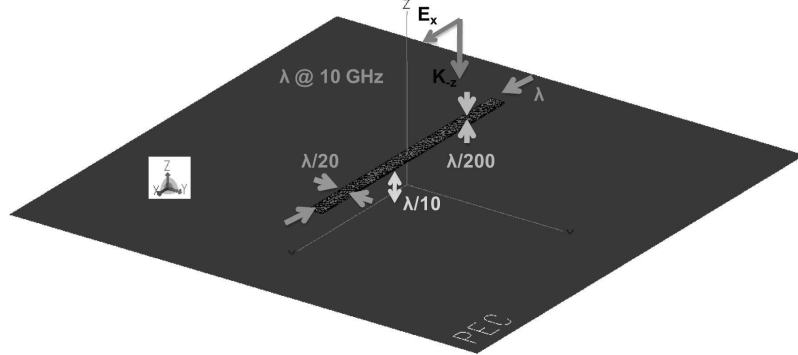


Figure 3.45: A microstrip geometry.

3.7 Observations and Conclusions

In this chapter, we have introduced certain refinements to the DM method to improve its computational efficiency. We have shown that the use of higher-order basis functions significantly reduces the number of unknowns, without compromising the accuracy and combines the DM with the CBFM technique helps reduce this number even further. The

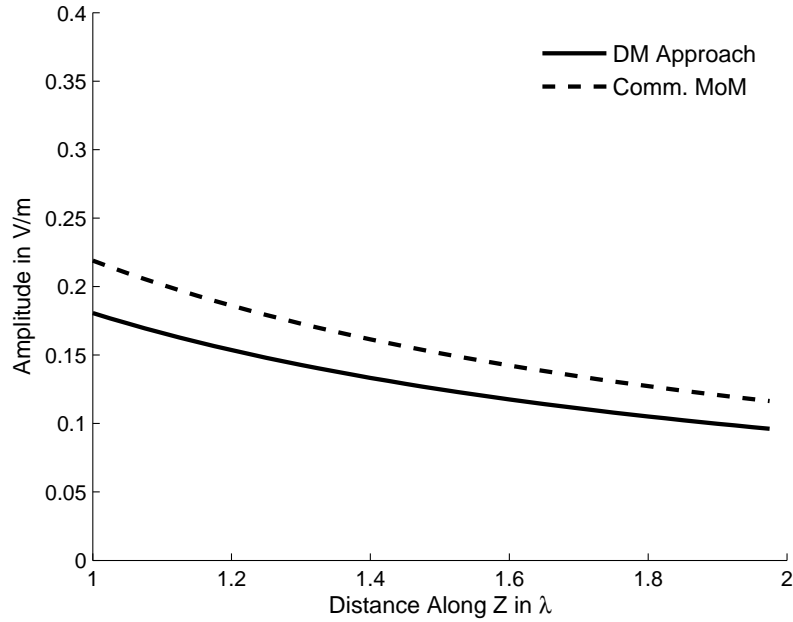


Figure 3.46: Amplitude comparison of backscattered field E_x from a microstrip line in Fig. 3.45.

use of closed-form expressions for the interaction matrix elements speeds up the process of matrix generation, regardless of the problem size. For electrically large problems, employing FMG helps to speed up the interaction matrix generation considerably.

We have shown how we can incorporate lumped loads in the DM approach and that it is able to capture sharp resonances even at low frequencies, where the commercial solvers become inaccurate or break down. The DM approach is able to accurately calculate the input impedance of small antennas; fields from irregular geometries; from faceted surfaces; from geometries with slot and slit; and, is able to model microstrip line type of geometries with fine features. In all of the above examples we have solved for, the matrices associated with the DM approach remained well-conditioned throughout the entire frequency range of interest, without the use of special treatments. However, this was not the case with Commercial MoM and FEM solvers, even after special treatments were incorporated in these solvers.

4. Recursive Update in Frequency Domain (RUFD)

4.1 Introduction

The time domain technique FDTD, is a versatile algorithm and handles Cartesian geometries with great ease. The FDTD algorithm is highly parallelizable, however as mentioned in Chapter 1, the FDTD algorithm requires long run times when an accurate solution is desired at low frequencies. Also, since it is a time domain algorithm, the method is neither well suited for dealing with dispersive media, as well as for deriving solutions for problems that involve high-Q structures. Given this background, it can be argued that a general-purpose frequency domain technique, which still preserves the salutary features of the time domain methods, would be very desirable addition to the CEM repertoire. Hence in this Chapter, we describe a novel method, called RUFD (Recursive Update in Frequency Domain), which is a general-purpose frequency domain technique, but which still preserves the salutary features of the time domain methods. RUFD is a frequency domain Maxwell-solver, which neither relies upon iterative nor on inversion techniques. The algorithm also preserves the advantages of the parallelizability—which is a highly desirable attribute of CEM solvers—by using the difference form of Maxwell’s equations.

4.2 RUFD Algorithm

In common with FDTD, the RUFD algorithm begins by using the difference form of Maxwell's equations to discretize them. Next, it utilizes a leap-frog algorithm, also similar to the FDTD, as proposed by Yee [15]. Consequently, RUFD may be viewed as the frequency domain counterpart of the FDTD, because it solves the CEM problem using a recursive updating procedure, rather than via matrix solution (based on inversion or iteration) commonly employed by other frequency domain methods. As a frequency domain solver, RUFD handles dispersive media with relative ease; it also avoids prolonged time-marching when solving low frequency problems, which is typical of time domain solvers. The formulation is based on modifying the original Maxwell's equation in a form that is convenient for recursive updating. These modified equations, originally proposed by Pflaum et al.[16], are given by:

$$\frac{e^{j\omega\tau}\hat{E}_h^{n+1} - \hat{E}_h^n}{\tau} = \frac{1}{\epsilon}\nabla_h \times \hat{H}_h^{n+\frac{1}{2}} e^{\frac{j\omega\tau}{2}} - \frac{\sigma}{\epsilon}e^{j\omega\tau}\hat{E}_h^{n+1} + S_E \quad (4.1a)$$

$$\frac{e^{\frac{j\omega\tau}{2}}\hat{H}_h^{n+\frac{1}{2}} - e^{-\frac{j\omega\tau}{2}}\hat{H}_h^{n-\frac{1}{2}}}{\tau} = -\frac{1}{\mu}\nabla_h \times \hat{E}_h^n - \frac{\sigma^*}{\mu}e^{\frac{j\omega\tau}{2}}\hat{H}_h^{n+\frac{1}{2}} + S_H \quad (4.1b)$$

where τ denotes the discrete iteration step; h is the mesh size; \hat{E}_h^n is the approximated electric field vector at points $n\tau$; $\hat{H}_h^{n+\frac{1}{2}}$ the approximated magnetic field vector at points $(n + \frac{1}{2})\tau$ and S_H and S_E are discrete source terms associated with the excitation.

If we let τ tend to zero in the above system of equations 4.2, we get:

$$\lim_{\tau \rightarrow 0} \frac{e^{j\omega\tau} - 1}{\tau} = j\omega \quad (4.2a)$$

We can also show that $\hat{E}_{h,\tau=0} = \lim_{\tau \rightarrow 0} \hat{E}_h(\tau)$ and $\hat{H}_{h,\tau=0} = \lim_{\tau \rightarrow 0} \hat{H}_h(\tau)$ are the solutions of 4.3:

$$j\omega\hat{E}_{h,\tau=0} = \frac{1}{\epsilon}\nabla_h \times \hat{H}_{h,\tau=0} - \frac{\sigma}{\epsilon}\hat{E}_{h,\tau=0} + S_E. \quad (4.3a)$$

$$j\omega\hat{H}_{h,\tau=0} = -\frac{1}{\mu}\nabla_h \times \hat{E}_{h,\tau=0} - \frac{\sigma^*}{\mu}\hat{H}_{h,\tau=0} + S_H. \quad (4.3b)$$

4.3 Stability Condition

The stability condition to be satisfied for the recursive scheme in (4.1) has been shown [16] to be:

$$\frac{\tau}{h} \leq \sqrt{\frac{\epsilon\mu}{8}} \quad (4.4)$$

However, we have found that using the Courant condition, given in (4.5), which is prescribed for the FDTD algorithm works equally well for the RUFD. Using (4.5) as opposed to (4.4) saves the simulation time by a factor of 2.

$$\frac{\tau}{h} \leq \sqrt{\frac{\epsilon\mu}{3}} \quad (4.5)$$

To ensure unconditional stability, even in the presence of usual numerical errors, we find that it is safe to use:

$$\frac{\tau}{h} \leq 0.995\sqrt{\frac{\epsilon\mu}{3}} \quad (4.6)$$

4.4 Source Settings

In the FDTD algorithm one can use either a hard or a soft source for excitation. For the implementation of the hard source one or more computational grid points are chosen and a particular field component at that point is assigned a specified value. Also, when using a hard source, one can remove the source from the computational grid once it is extinguished. In contrast to this, the source value is added to the field component at

the selected grid points if we use a soft source. Since RUFD is a recursive frequency domain technique, and the RUFD calculates the values directly in the frequency domain, we cannot remove them from the computational grid at any point of time; hence in RUFD we must always use a hard source.

4.5 Incorporating Lumped Resistance

Lumped resistance are often used to achieve a matched termination. In RUFD the lumped resistances can be implemented by using σ values in certain specific cells where the lumped source is to be located. The σ value for a given resistance R can be calculated by using:

$$\sigma = \frac{l}{RA} \quad (4.7)$$

where l is the transverse length, and A is the cross-sectional area of the cell. This total resistance can either be distributed over a few cells, by using series or parallel combinations, or lumped in to a single cell based on the problem at hand.

4.6 Absorbing Boundary Conditions

The boundary condition used for the mesh truncation in the computational domain is critical since it affects the accuracy of the simulations. It is commonly referred to as Absorbing Boundary Conditions (ABC) in the context of the FDTD algorithm. A variety of ABCs have been developed over the years for use in the FDTD algorithm. The simplest and computationally inexpensive one is the Mur ABC [17]. However the accuracy of this ABC is good only for the normal incidence and often cause reflections for other angles of incidence. Recently, a class of boundary conditions called Perfectly Matched Layers,

abbreviated as PML, has been introduced by Berenger [18], that are widely used in the FDTD algorithm. The Convolutional PML [19], also referred to as CPML, is the best in the class in terms of performance, even though it is computationally expensive. We have adapted and programmed both the Mur ABC and CPML type of ABCs in the RUFD algorithm. As we can see from Figs. 4.1 and 4.2, the performance of RUFD/CPML is superior to RUFD/Mur ABC, since the former is better able to suppress the reflections from the boundary. One can use either the Mur ABC or the CPML ABC, depending on the accuracy desired.

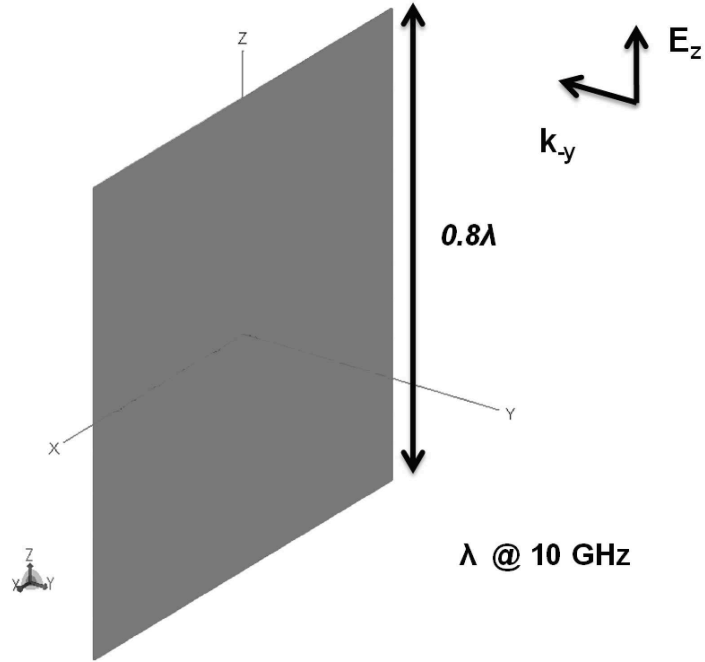


Figure 4.1: A square PEC sheet.

4.7 Types of Formulation

The RUFD algorithm has three types of formulation depending on the problem on hand. In this section we will describe each of them with some illustrative examples.

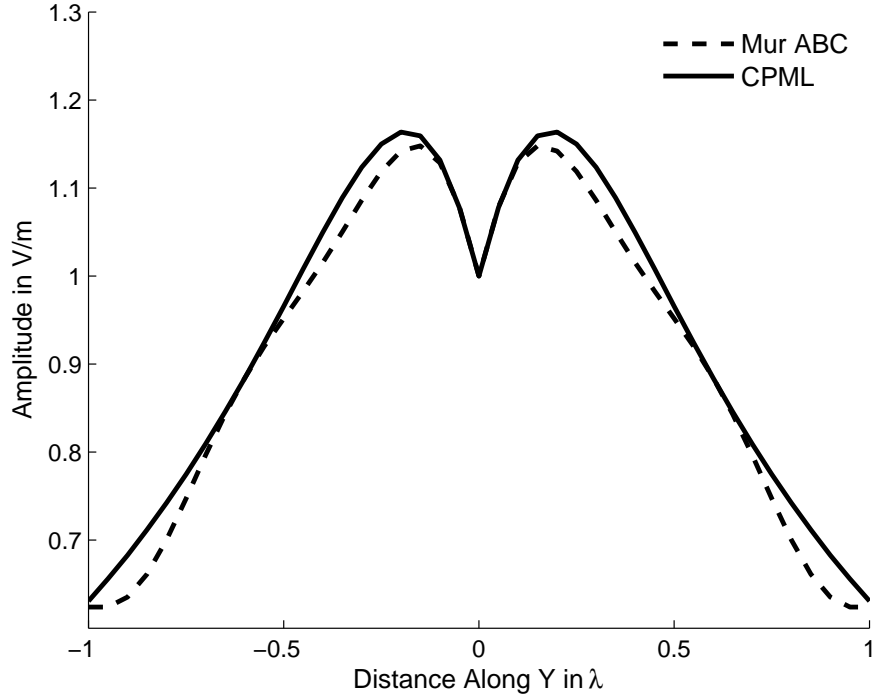


Figure 4.2: Amplitude variation of the scattered E_z from a square PEC sheet shown in Fig. 4.1.

4.7.1 Total Field Formulation

Total field formulation is used for antenna problems or problems which involve sources of finite support, as opposed to the plane wave type of source, which is unbounded. This type of formulation uses the total field throughout the computational domain; hence, it does not need any special modification to the RUFD update equations. As an example, let us consider a dipole antenna operating at 10 GHz, shown in Fig. 4.3, whose length and radius are $\lambda/2$ and $\lambda/100$, respectively. The dipole is fed by using a voltage source in a gap whose length is $\lambda/20$. Fig. 4.4 compares the feed current of the dipole antenna, calculated by using the RUFD total field formulation with those derived from a commercial MoM solver.

Fig. 4.4 shows good comparison between the feed current calculated by using the

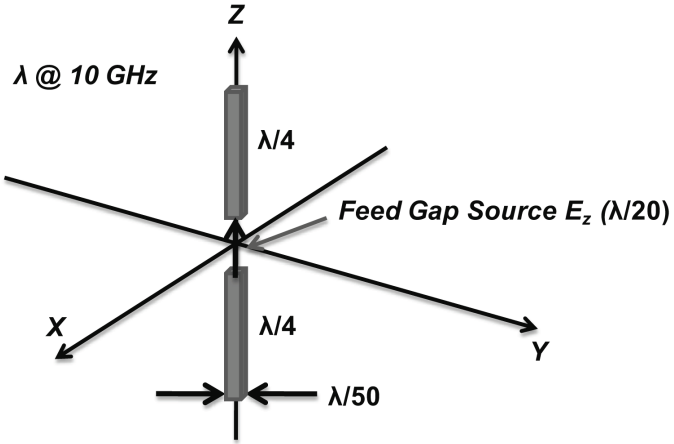


Figure 4.3: Geometry of a PEC dipole antenna (Not to Scale).

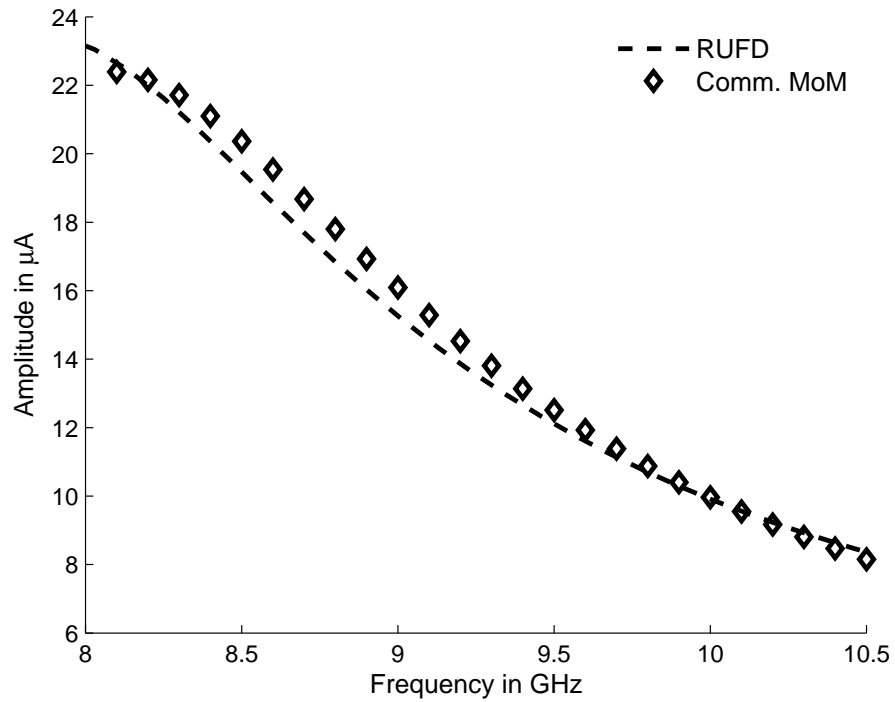


Figure 4.4: Amplitude variation of the feed current for a PEC dipole antenna shown in Fig. 4.3.

RUFD and a commercial MoM code. The antenna was modeled as a thin wire in the commercial MoM code, while in RUFD it was modeled by using a square PEC rod. The calculated currents followed the shape and amplitude but show a shift in the frequency because of the difference in the models used for the antenna in the two different solvers.

To compensate for this, the RUFD results the frequency axis was scaled by a factor of 1.1 to align the solution for the current distribution, derived by using the RUFD, with that obtained from the commercial MoM.

4.7.2 Total Field/Scattered Field Formulation

The ABCs are only designed to absorb the plane waves incident upon the boundary, and they can become unstable when a wave travels away from it. To handle this situation, which always occurs when we use a plane wave excitation, we employ what is known as as the total field/scattered field formulation [1]. In this formulation, we define an interior domain where we work with total fields, while in the region outside of this domain we use the scattered field (see Fig. 4.5), to ensure that the fields are always outgoing at the outer boundary, as the radiation condition dictates them to be. The scattered field region is usually chosen to be 5 cells thick. The fields at the boundary between the total and scattered field regions are suitably adjusted to ensure the satisfaction of the continuity condition.

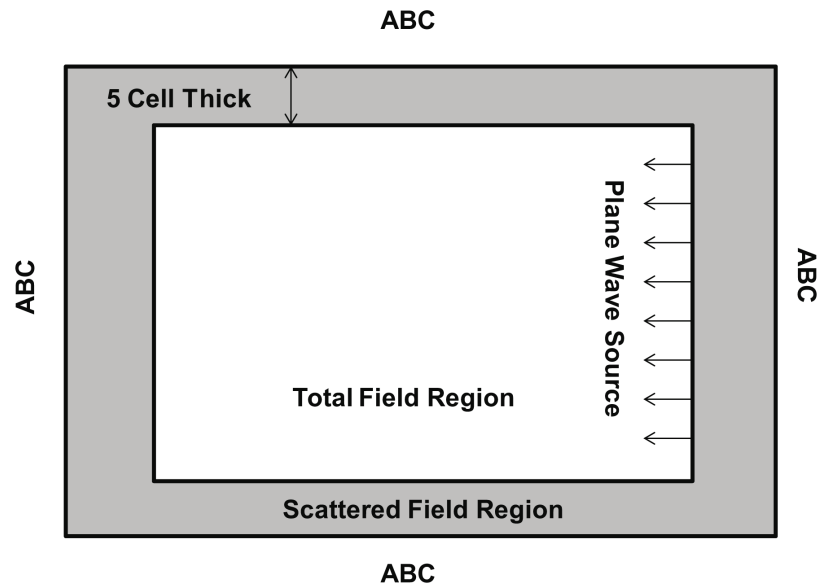


Figure 4.5: A 2D computational domain.

As an example consider a dielectric cube at 10 GHz, which is $\lambda/25$ on the side, shown in Fig. 4.6, which has a relative permittivity of 6. Fig. 4.7 compares the E_z -field scattered in the forward direction, calculated by using the total field/scattered field type of formulation in the RUFD, with those obtained from a commercial MoM solver. While formulating this problem in RUFD, a small value of $\sigma = 0.01$ was used within the dielectric cube to achieve stability.

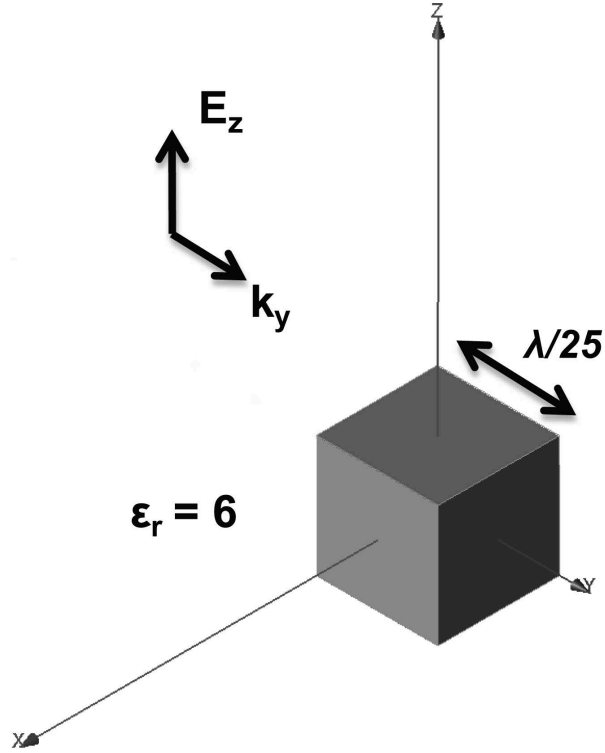


Figure 4.6: A dielectric cube.

Fig. 4.7 shows good comparison of the scattered field E_z calculated from the RUFD and the commercial MoM solver. Even though the commercial MoM was able to solve this particular geometry, it could not handle when a smaller PEC cube of size $\lambda/100$ was embedded within the dielectric cube (see Fig. 4.8), while the RUFD was able to solve the problem with ease.

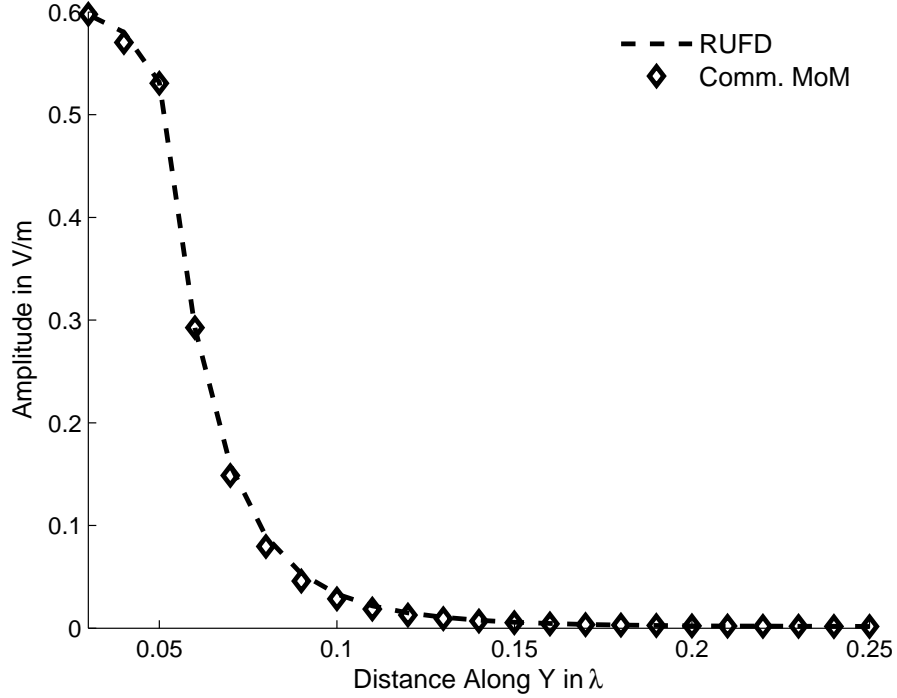


Figure 4.7: Amplitude variation of the forward scattered field E_z from a dielectric cube shown in Fig. 4.6.

4.7.3 Scattered Field Formulation

In the Scattered Field formulation, we work only with the scattered fields throughout the entire computational domain. We replace the objects with hard sources, whose values are derived from the scattered fields calculated by applying the boundary condition on the surface of the object. Because of this, we can use the scattered field formulation only for problems involving PEC objects alone. In other words, for scattering problems involving dielectric geometries alone, we must always use the total field/scattered field formulation. As an example consider the problem of calculating the scattering from a square PEC plate at 10 GHz, whose side length and thickness are 1.5λ and $\lambda/10$ as shown in Fig. 4.9. Fig. 4.10 compares the total E_z field calculated by using the RUFD with total field/scattered field formulation; RUFD with scattered field formulation; and, the commercial MoM. Table 4.1 compares the simulation times required by the RUFD and

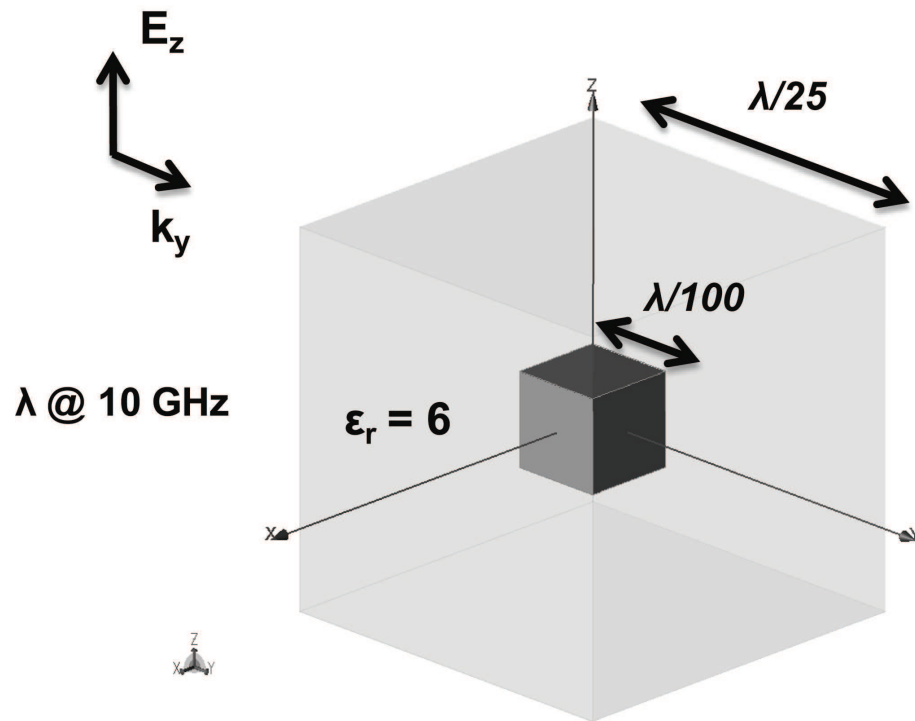


Figure 4.8: A PEC cube embedded in a dielectric cube.

the Commercial MoM for this problem.

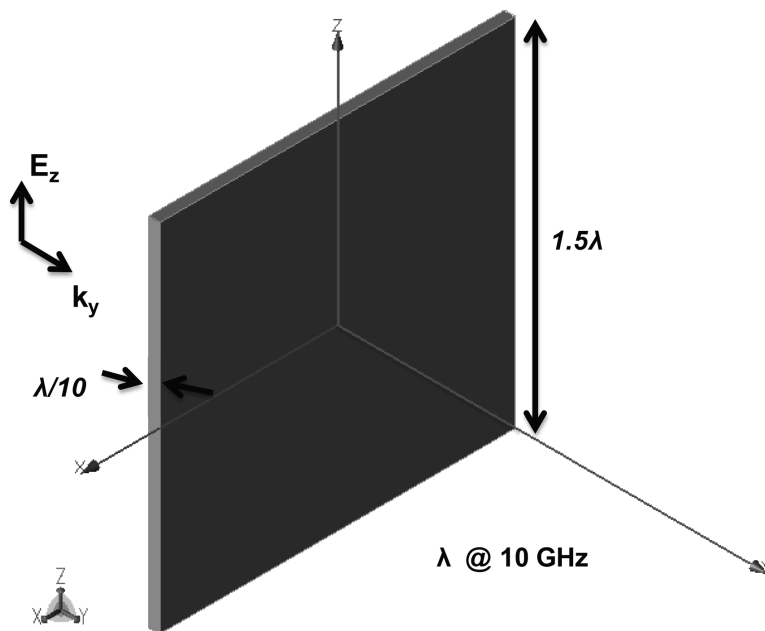


Figure 4.9: A square PEC plate.

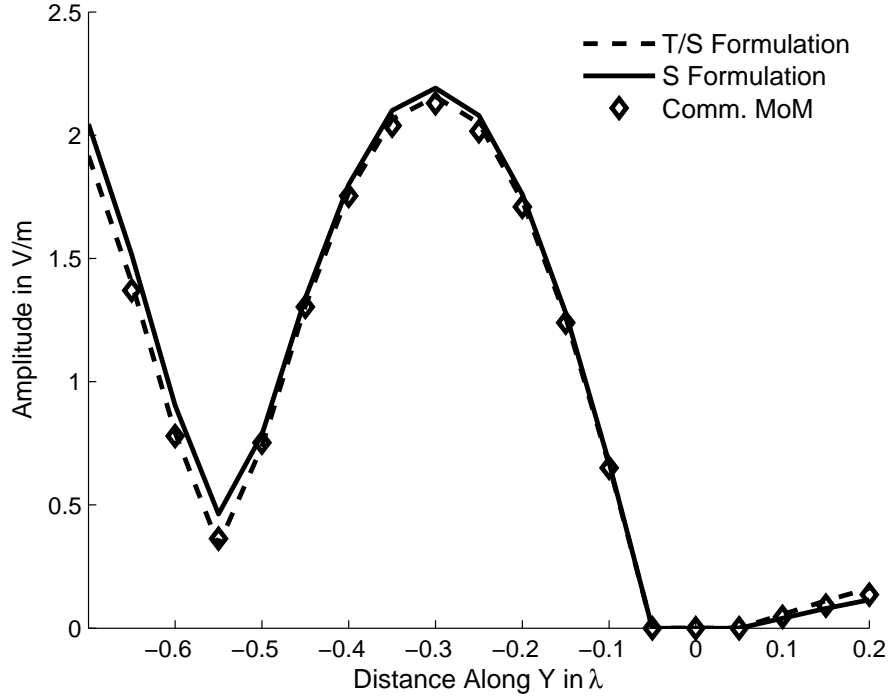


Figure 4.10: Amplitude variation of the total field E_z from a PEC plate shown in Fig. 4.9.

Table 4.1: Comparison of simulation times required by RUFD and the commercial MoM for the PEC plate shown in Fig. 4.9.

Method	Simulation Time
RUFD	19.36 s
Commercial MoM	20.5 s

As is well known, usually, the Finite methods are considerably more CPU-intensive, than the MoM, but the Table shows that for this example, which is typical, RUFD is quite competitive with the MoM. Furthermore, the proposed RUFD algorithm, which is a Finite method, can handle finite conductivities and inhomogeneous objects much more numerically efficiently and accurately than can the MoM code, which can become numerically unstable. Also the RUFD algorithm used here was a serial version and using a parallel version would speed up the computation considerably, whereas the MoM is not so easily parallelizable. Fig. 4.10 shows good comparison of the total field E_z calculated

using the RUFD and those obtained from the commercial MoM solver. We find that the results calculated using scattering or total field/scattered field formulations are consistent with each other and also with the commercial solver.

4.8 Performance Enhancement of RUFD

The RUFD algorithm, even though it is robust and accurate for handling a wide variety of problems, is not the most efficient. Since it is a frequency domain technique, even though it is similar to the FDTD algorithm because it is recursive, it solves problems only for a single frequency, as opposed to the FDTD algorithm, which generates the solution for a range of frequencies from a single simulation. In this section we will introduce a way to enhance the computational efficiency of the RUFD algorithm without compromising its accuracy.

4.8.1 Post-Processing

Fig. 4.11 shows the typical signature generated by an RUFD simulations, which shows that for this problem we need to iterate at least 2000 times to obtain the converged field value at the chosen point of interest. The information preceding the recursive step when convergence is achieved (2000 in this example) in RUFD is of no significance, since we only need to retain the final converged value unlike the FDTD algorithm. Thus, we can use methods to process the recursive signature during the initial stages of iteration to predict the final converged value that we are seeking, either by using the zero-frequency DFT, by employing the moving window average for smoothing, or by fitting the data using Vector Fitting Algorithm.

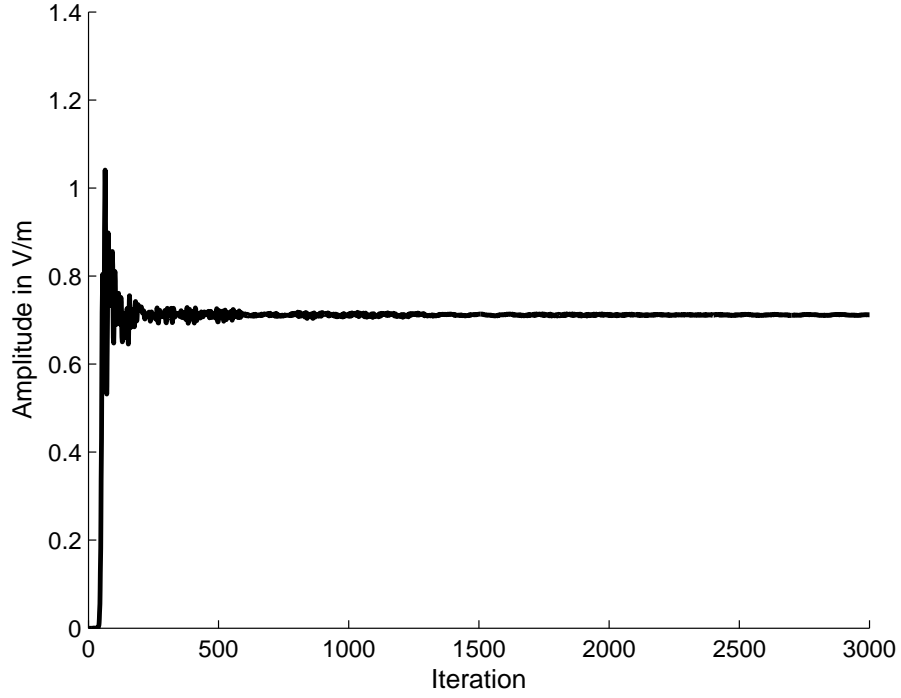


Figure 4.11: A typical signature generated in the RUFD algorithm.

As an example, let us consider the patch antenna operating at 8 GHz which is printed on a Duroid substrate ($\epsilon_r = 2.2$) that has a thickness of 0.794 mm, (see Fig. 4.12). The problem was solved by using the RUFD and further processing of the recursive signature was done by using vector fitting, polynomial fitting, and smoothing. Table 4.2 compares the number of iteration steps required by each of these techniques with the number of time steps required by a commercial FDTD solver.

Table 4.2: Comparison of iterations required by RUFD using different processing technique and the commercial FDTD for the patch antenna shown in Fig.4.12.

Method	Comm. FDTD	RUFD Alone	Vector Fit	Poly Fit	Smoothing
No. of Steps	8200	2000	1601	1218	1218

It is evident from the Table 4.2 that using post processing technique makes the RUFD algorithm computationally efficient, if not competing with the FDTD, dropping the fact that it is a frequency domain solver.

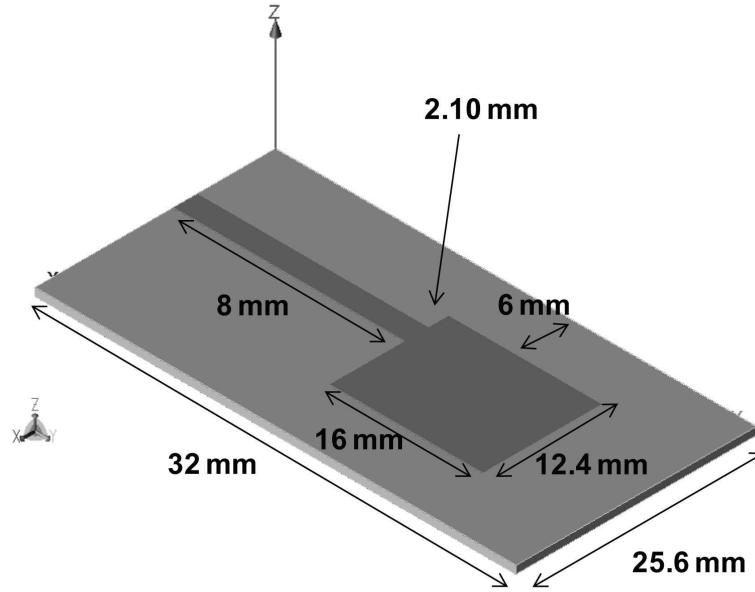


Figure 4.12: A patch antenna.

For the next example, we consider a waveguide filter as shown in Fig. 4.13 at 11.8 GHz.

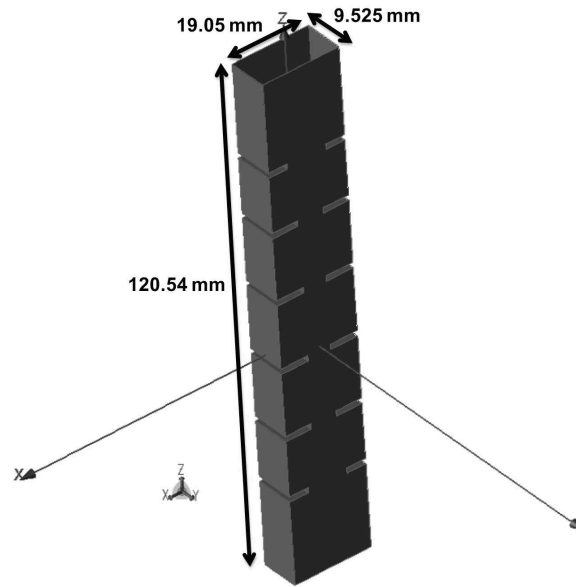


Figure 4.13: A waveguide filter.

Table 4.3 again shows that the post processing helps reduce the number of iterations, and the polynomial fit performs especially well. For the final example, we consider the

Table 4.3: Comparison of iterations required by RUFD using different processing technique for the waveguide filter shown in Fig.4.13.

Method	Comm. FDTD	RUFD Alone	Vector Fit	Polynomial Fit
No. of Steps	45540	27000	23585	20544

RF filter operating in the frequency range of 10 GHz. The filter is printed on a substrate with an $\epsilon_r = 2$, and a thickness of 1 mm, as shown in Fig. 4.14. Table 4.4 compares the number of iterations required by the RUFD alone, with smoothing, and the number of time steps required by commercial FDTD solver.

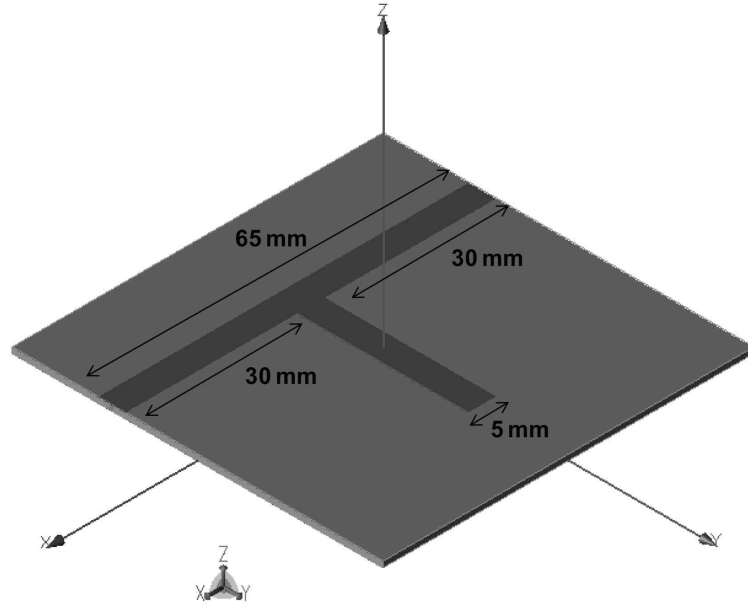


Figure 4.14: A RF filter.

Table 4.4: Comparison of iterations required by the RUFD, when using the smoothing technique for the RF filter shown in Fig.4.14.

Method	Comm. FDTD	RUFD Alone	Smoothing
No. of Steps	11300	12000	2100

From Table 4.4 we see that the smoothing algorithm reduce the number of iterations required by the RUFD quite significantly.

Until now we have only discussed about post processing techniques which do not modify the flow of the RUFD algorithm. An alternative is to do a online processing, by periodically updating the field values at all the nodes of the computational grid after smoothing. Consider the PEC plate problem shown in Fig. 4.9, which we have solved by using the RUFD, combined with a online processing where we update the E-field values at all the nodes of the computational domain, with the zero-frequency DFT values every 500^{th} step starting at the 400^{th} step. Fig. 4.15 compares the signature of the RUFD and compares it for the cases of with and without online processing. We find that online processing slows down the convergence, and hence the post-processing methods offer a better choice than does the online-processing method.

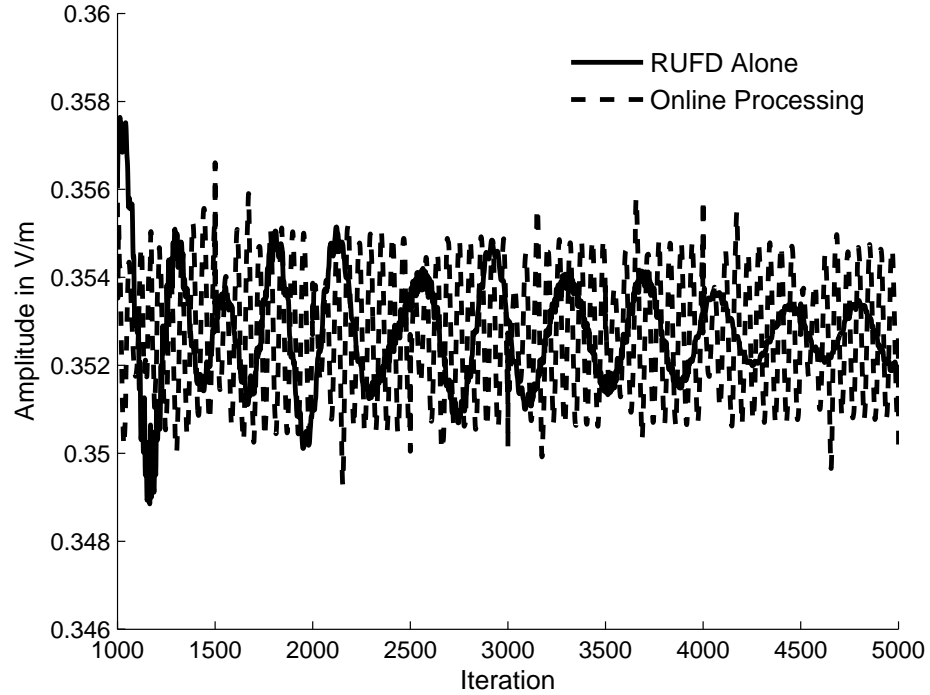


Figure 4.15: Signature generated in RUFD algorithm for a PEC plate shown in Fig. 4.9.

4.8.2 Effect of Time Step on Convergence

To study the effect of varying τ in the RUFD simulations, we consider a small square PEC patch, shown in Fig. 4.16, which operates at 10 GHz. We model the above problem by using the RUFD and the value of τ is varied as 0.995Δ , 0.595Δ and 0.0995Δ in three different RUFD simulations, where Δ is dictated by the Courant condition given in (4.6). Fig. 4.17 compares the scattered field E_y calculated by using the RUFD simulations with different values of τ , with those calculated by using the DM approach. Fig. 4.18 compares the variation of the field at a point from the three RUFD simulations.

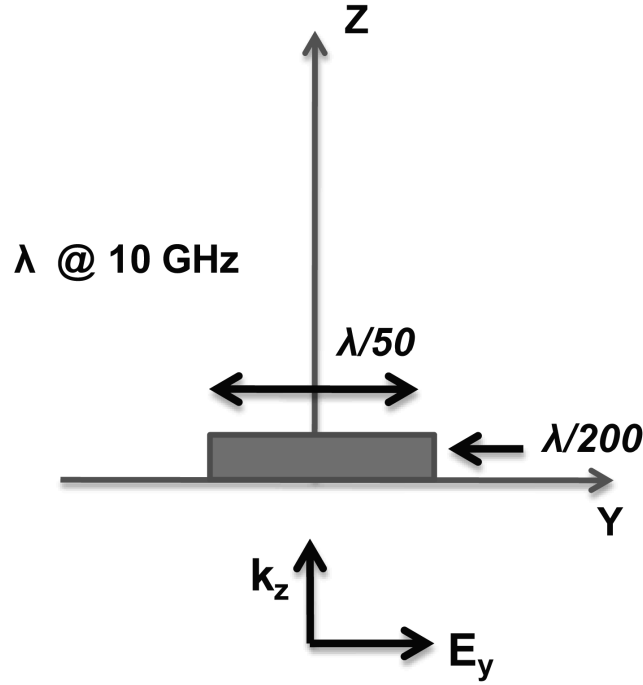


Figure 4.16: A square PEC patch.

From Fig. 4.17 we see that the RUFD results compare well with those obtained from the DM approach, irrespective of the chosen value for τ . However, from Fig. 4.18 we note that decreasing the value of τ , increases the sampling rate, and requires a larger number of iterations to achieve convergence. Also, increasing the value of τ beyond Δ leads to instabilities and, hence, an optimum choice for τ is as given in (4.6).

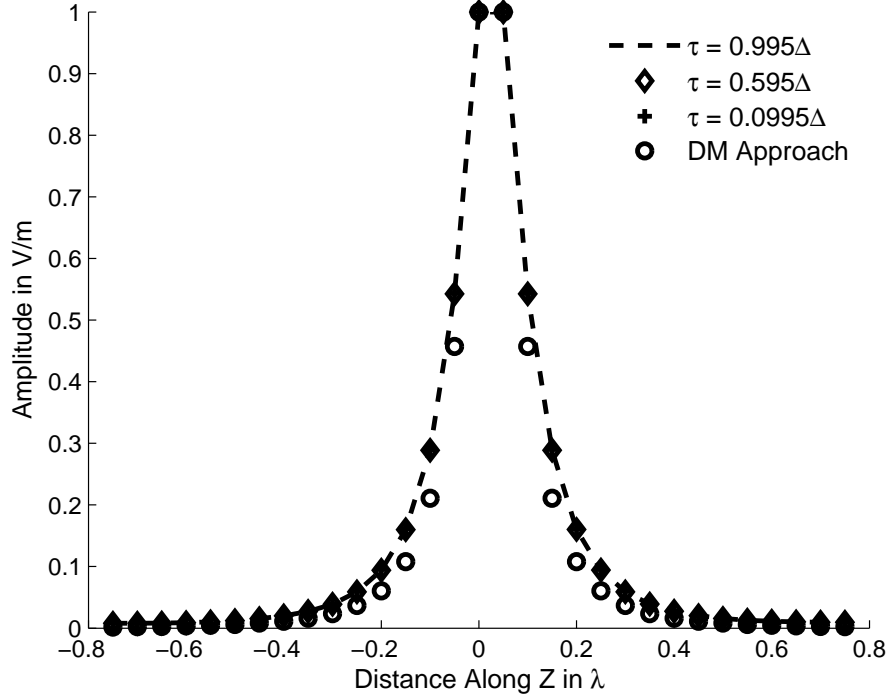


Figure 4.17: Amplitude variation of the scattered field E_y from a PEC patch shown in Fig. 4.16.

4.8.3 Effect of Losses on Convergence

To achieve a faster convergence, we use a small value of loss in the entire computational domain to damp out the oscillations in the RUFD. To study the effect of the loss on the convergence, we consider the patch antenna problem shown in Fig. 4.16, and vary the value of σ from 0 to 10 in the RUFD algorithm. Fig. 4.19 compares the scattered field E_y calculated by using the RUFD simulation using different values of σ , with those calculated by using the DM approach. Fig. 4.20 compares the variation of the field at a point, computed by using these RUFD simulations.

Fig. 4.19 shows good comparison with the results from the DM approach, irrespective of the chosen value for σ . Fig. 4.20 shows that convergence is achieved more quicker as we increase the value of σ . However, with a very high value of σ serves to

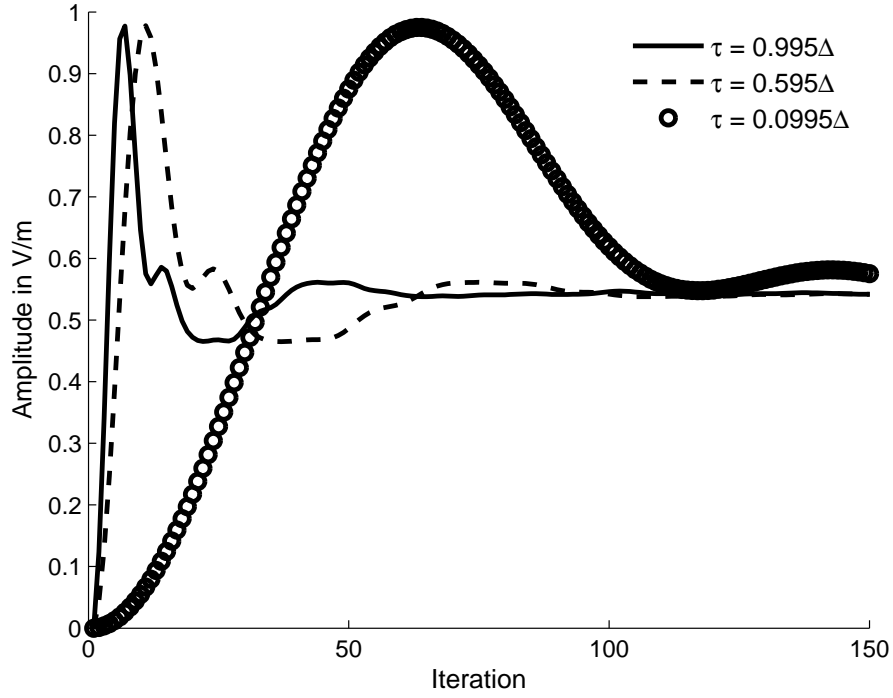


Figure 4.18: Signature generated in RUFD algorithm for a PEC patch shown in Fig. 4.16.

dampen the final, converged, field values. Hence, in order to maintain a good accuracy, and achieve a faster convergence at the same time, we use a moderate value of σ , namely 0.01. for instance. From the plots of the signature shown in Fig. 4.20, we find that the field values peak up initially and then settle out, as we continue the iteration until we reach convergence. Hence an intuitive approach would be to start with a higher value for σ and decrease it in steps as we continue with the simulation. Even though this approach results in a faster convergence, the accuracy is compromised somewhat, say about a factor of 10%.

4.8.4 Initializing Using DM Approach

In order to speed up the convergence in the RUFD algorithm, the field nodes in the computational grid of RUFD are initialized by using DM approach. As an example, we

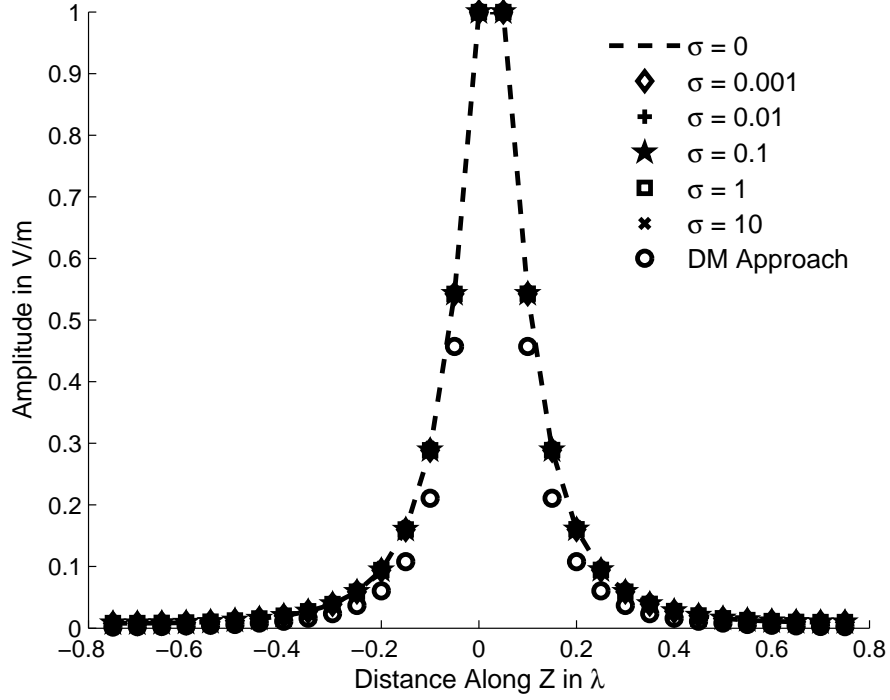


Figure 4.19: Amplitude variation of the scattered field E_y from a PEC patch shown in Fig. 4.16.

have revisited the PEC patch problem, shown in Fig. 4.16, and have it solved by using the RUFD, using initial values obtained from the DM approach. Fig. 4.21 compares the scattered field value E_y calculated by using RUFD simulations, with and without initialization, and with those calculated by using the DM approach. Fig. 4.22 compares the variation of the field at an observation point obtained from these RUFD simulations.

From Fig. 4.21 we see that the results compare well with those obtained from the DM approach, irrespective of the initialization. Furthermore, Fig. 4.22 shows that while using initialization from the fields derived from the DM approach helps to decrease the overshoot of the signature, it does not result in a faster convergence.

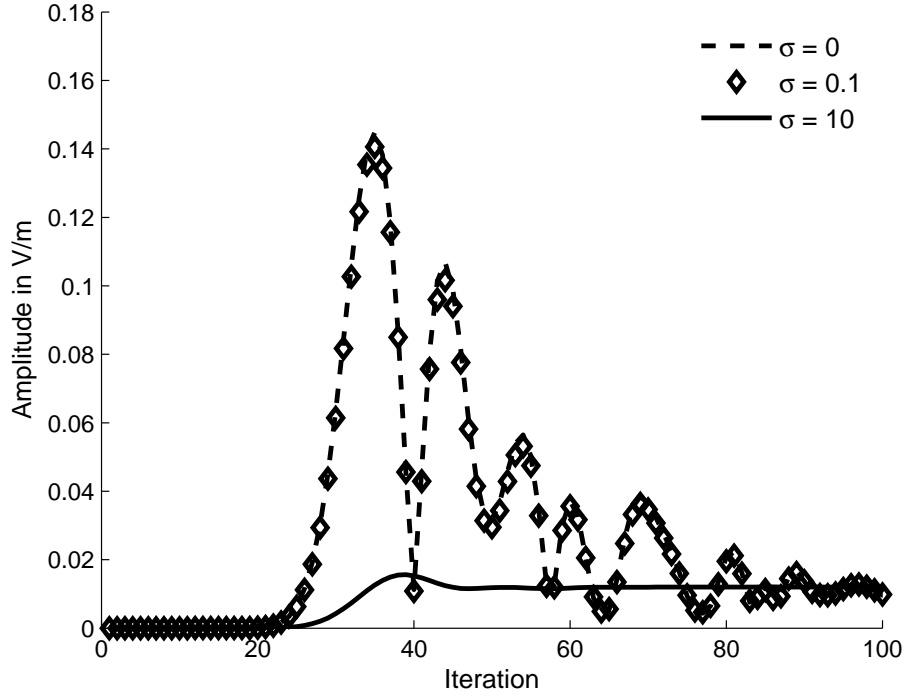


Figure 4.20: Signature generated in RUFD algorithm for a PEC patch shown in Fig. 4.16.

4.8.5 S-Parameter Calculations

Scattering parameters are used to define the frequency behavior of circuits and can be calculated by using the RUFD, either by using open terminations or matched terminations for the circuit ports. In general, the frequency dependent scattering parameter $S_{ij}(f)$ using matched termination can be defined as follows [20]:

$$S_{ij}(f) = \frac{V_i(f)}{V_j(f)} \sqrt{\frac{Z_{oj}(f)}{Z_{oi}(f)}} \quad (4.8)$$

where $V_i(f)$ and $V_j(f)$ are the voltages at ports i and j, $Z_{oi}(f)$ and $Z_{oj}(f)$ are the characteristic impedances of the lines connected to these ports. The matched termination in the RUFD can be achieved either by using the method mentioned in Section 4.5 or by making the CPML touch the port of the circuit. Both of these approaches are found

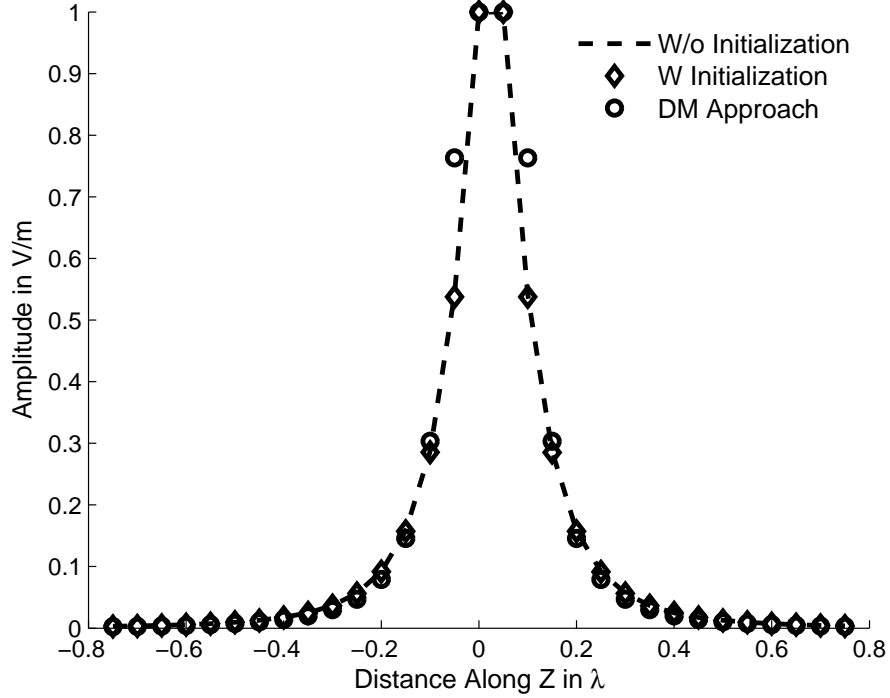


Figure 4.21: Amplitude variation of the scattered field E_y from a PEC patch shown in Fig. 4.16.

to produce the same results. In order to calculate the S-parameters for the feed line we need to decompose the current into forward and backward traveling waves, which can be calculated by using the Prony's method [21, 22]. When using open termination for S-parameter calculation, we use the formula proposed in [23], which requires the decomposition of the waves in all the ports into forward and backward traveling waves, and we can again use the Prony's method for this purpose.

As an example, let us consider the RF filter shown in Fig. 4.14. Figs. 4.23 and 4.24 compares the S-parameters, calculated by using the RUFD, with those obtained from the transmission line model (TL model).

Fig. 4.23 shows that the S_{11} values, obtained from the RUFD and transmission line models compare well with each other. However, Fig. 4.24 shows a slight difference between the S_{21} values because of the infinite substrate assumption that there is in the

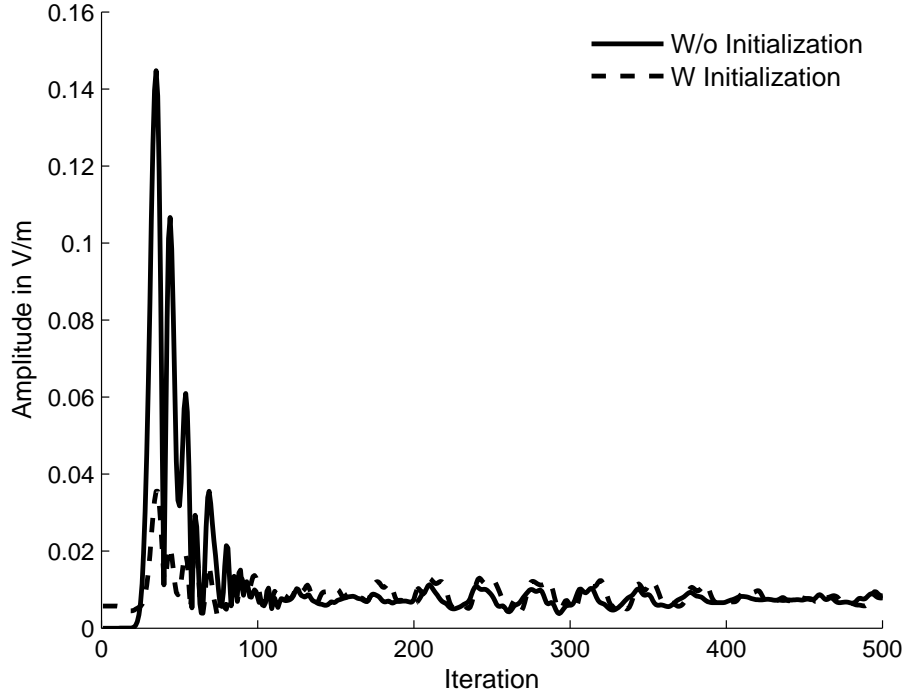


Figure 4.22: Signature generated in RUFD algorithm for a PEC patch shown in Fig. 4.16.

TL model. The RUFD has the potential to calculate the S-parameters of circuits with finite substrates which the MoM solvers cannot readily handle because they assume that the substrate dimensions are infinite by using the layered medium Green's function.

4.8.6 Sub-Gridding Approach

Sub-Gridding approach in the FDTD enables one to use different mesh sizes in selected regions of the computational domain, and the same principle has been adopted in the RUFD to handle multiscale problem. The problem geometry considered is shown in Fig. 4.25. A fine mesh was used in a part of the domain, which is indicated as the sub-gridding region in the Fig. 4.25, and a buffer region was used to enable smooth transition between the coarse and sub-gridded regions. Two test problems were solved by using the RUFD with sub-gridding, one with the source located in the coarse region, while the other with

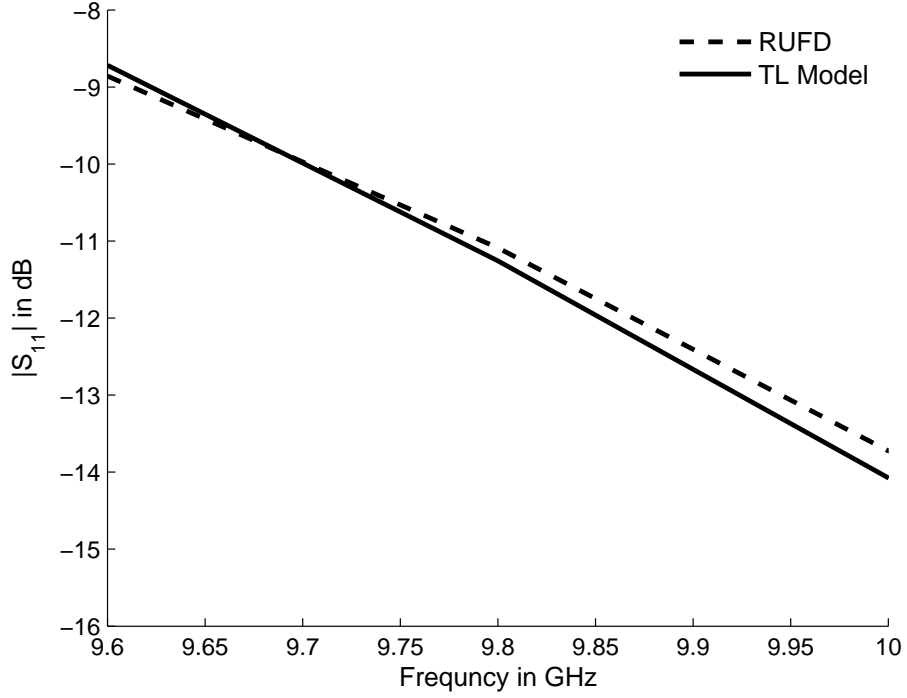


Figure 4.23: Variation of S_{11} for the RF filter shown in Fig. 4.14.

the source placed inside the sub-gridding region. The sub-gridding approach became unstable in both of these cases, irrespective of the value chosen for τ , as it very often the case with sub-gridding algorithms implementation in the FDTD. However, because of the nature of the RUFD algorithm the same sub-gridding can be achieved using a method called Multi-Grid, proposed in the Chapter 5.

4.8.7 Improving the Computational Efficiency

While the proposed RUFD algorithm has a number of salutary features, as pointed out above, it has two disadvantages listed below:

- Takes a longer time for moderate and high-Q problems, such as the case examples shown in Figs. 4.12 and 4.13.

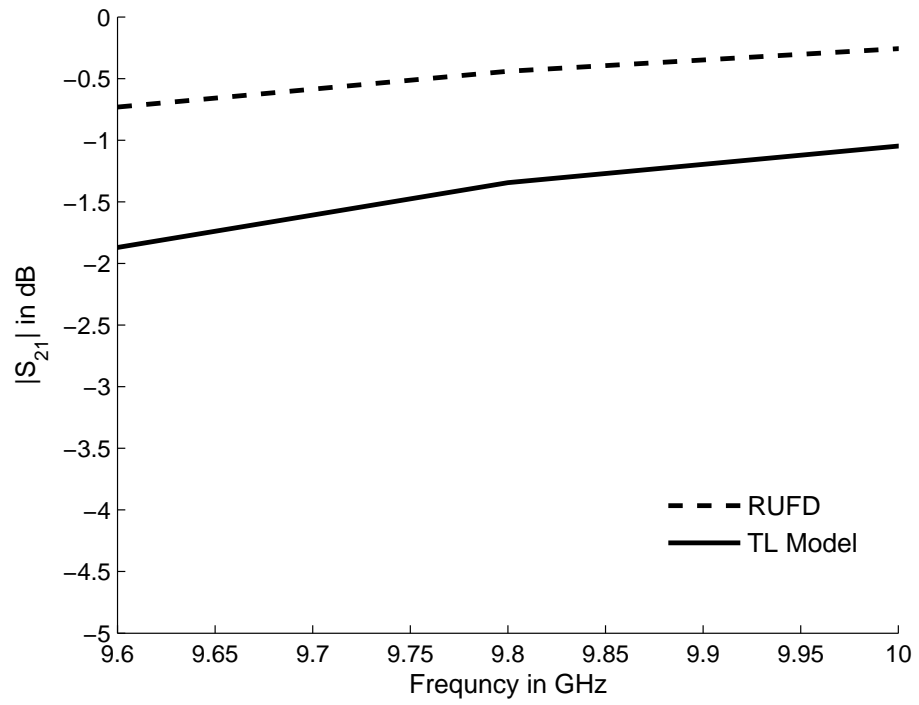


Figure 4.24: Variation of S_{21} for the RF filter shown in Fig. 4.14.

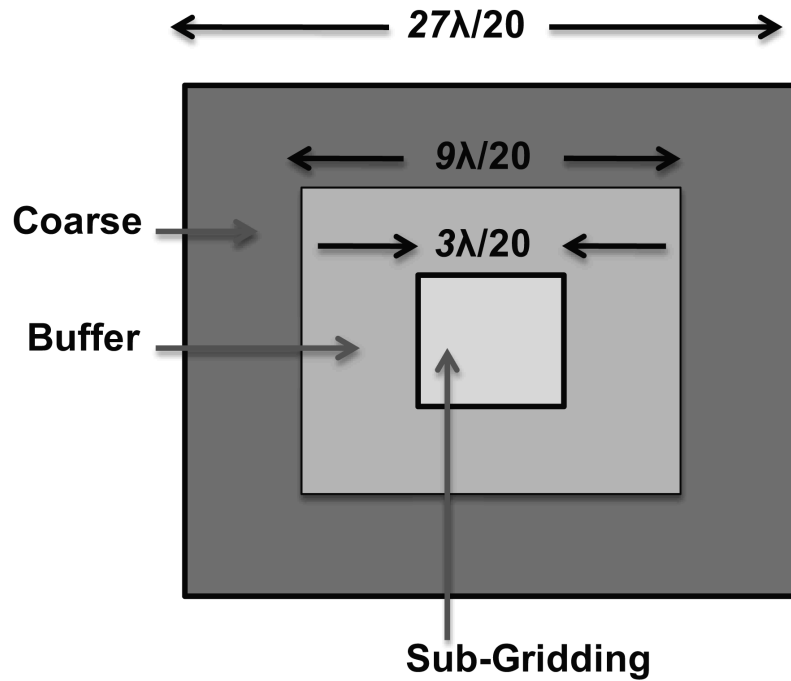


Figure 4.25: A computational domain with sub-gridding.

- In contrast to the FDTD, the update equations are complex, and they require twice the memory as compared to that needed in the conventional FDTD.

To overcome these drawbacks, we have modified the original RUFD algorithm to address the issues mentioned above, and have also incorporated new strategies to accommodate non-conformal objects, to deal with low frequencies and to develop a new ABC which is computationally efficient than the PML. The result is the ν FDTD algorithm described in the Chapter 6, whose update equations are entirely in the real domain.

The patch antenna problem shown in Fig. 4.12 was solved by using the ν FDTD and the number of steps required is compared in the Table 4.5, with those for the conventional FDTD and RUFD with smoothing.

Table 4.5: Comparison of iterations required by ν FDTD, RUFD using Smoothing and the commercial FDTD for the patch antenna shown in Fig.4.12.

Method	Commercial FDTD	RUFD with Smoothing	ν FDTD
No. of Steps	8200	1218	972

Table 4.5 clearly shows that the ν FDTD algorithm perform better not only compared to the RUFD, but also with the commercial FDTD solver. The waveguide filter shown in Fig. 4.13 was also solved using ν FDTD and the required number of time steps are shown in the Table 4.6.

Table 4.6: Comparison of iterations required by ν FDTD, RUFD using polynomial fit for the waveguide filter shown in Fig.4.13.

Method	Commercial FDTD	RUFD with Poly Fit	ν FDTD
No. of Steps	45540	20544	10000

Tables 4.5 and 4.6 shows that the computational efficiency of the ν FDTD is atleast 50% better than that of the RUFD algorithm even after using the best available post-processing techniques in the RUFD.

4.8.8 Calculation of Frequency Response

Often designers are interested in electromagnetic response over a band of frequencies instead of just few. Since RUFD is a frequency domain technique, it calculates the response only at one frequency from a single simulation run; hence it is computationally expensive to calculate for multiple frequencies. One way to address this issue would be to run a number of frequencies using the RUFD, and then interpolate the results for in between frequencies by using either vector fitting, or polynomial fitting. However, when the frequencies are separated by more than 20% of the simulation frequency and for the frequencies in-between, we initialize the RUFD computational grid with field values calculated through interpolation based on the results obtained previously at other frequencies, before we begin the simulation. We improve the convergence of the RUFD algorithm by following this procedure, which is different from what we found when we used the initialization values from the DM approach we mentioned in the Section 4.8.4.

To demonstrate the proposed approach of frequency interpolation just described above, we consider the problem of scattering by a PEC sheet, shown in Fig. 4.1 with the objective of generating the results at a frequency of 10 GHz. Initially, we solve the problem for frequencies of 9 GHz and 11 GHz, using the RUFD scattering formulation, and then interpolate the field values for 10.5 GHz at all the nodes in the computational domain. This interpolation fails to predict the field values at 10 GHz with the desired accuracy; hence we use these interpolated data to initialize the RUFD computational grid before starting with the RUFD iteration at 10 GHz to achieve faster convergence. Fig. 4.26 compares the results calculated by using the RUFD with and without the initialization step, and we see that the two results compare well. Thus, we have demonstrated that we can speed up the convergence of the RUFD by using initialization in the way we have described above.

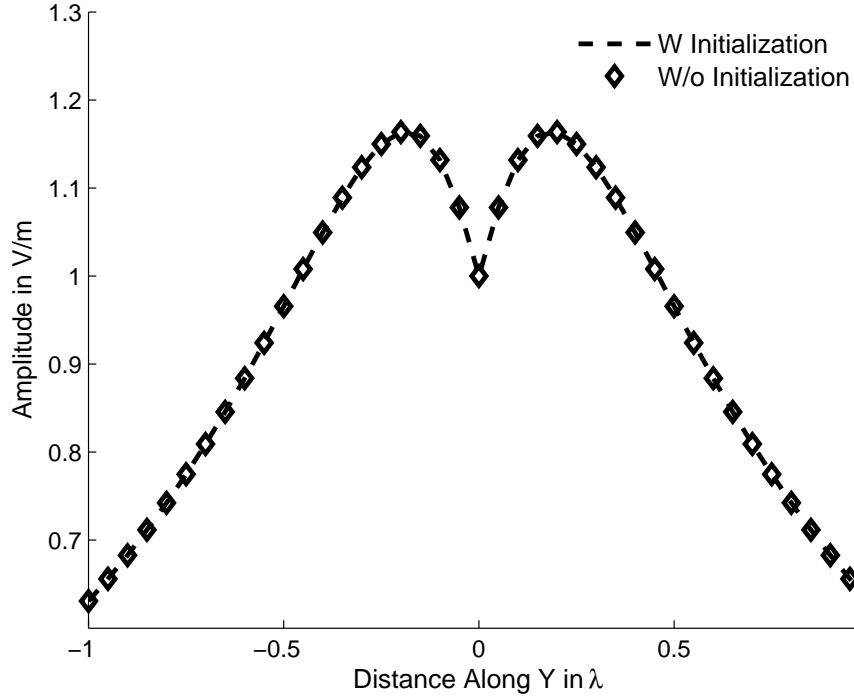


Figure 4.26: Amplitude variation of the backscattered field E_z from a PEC sheet shown in Fig. 4.1.

Another way to calculate the frequency response is to use ν FDTD described in Chapter 6, which is able to handle multiple sources, operating at different frequencies and using them we can generate the results for a number of frequencies from a single simulation run. Even when we use a single frequency source in the ν FDTD we can process the results for frequencies within the 5% bandwidth around the source frequency used during simulation.

4.9 Observations and Conclusions

As alluded to in Section 4.1, the RUFD algorithm is highly parallelizable. This is because, unlike the FEM, it utilizes the difference form of Maxwell's equations. Also, since RUFD uses the Yee cells, its meshing requirements are relatively simple. Moreover, since RUFD

solves the Maxwell's equations in a recursive manner, without using either iteration or inversion, the problems of dealing with ill-conditioned matrices, or constructing robust pre-conditioners are totally avoided. Also, as a frequency domain solver, it can handle dispersive media, including plasmonics, relatively easily without any need for Drude or Debye model as required in FDTD algorithm.

A number of technique has been discussed in this Chapter to further enhance the performance of the RUFD. These include frequency interpolation schemes to generate the initial values of the fields in the entire computational domain; introducing losses in the computational domain; and, post-processing methods, which speed up the convergence significantly.

It has also been mentioned that the RUFD has been used as a stepping stone to a new improved version of the FDTD, called the ν FDTD, described in detail in the Chapter 6.

5. On the Hybridization of RUFD

Algorithm

5.1 Introduction

The direct solution of multiscale problems by means of conventional CEM methods—be it FEM, FDTD or MoM—is highly challenging, even with the availability of modern supercomputers, because we need to use a large number of DoFs (degree of freedom) to accurately describe objects with fine features, which might share the computational domain with other large objects. For instance, if a thin-wire is located in an inhomogeneous medium along with other large-scale objects, and the thickness of the wire is only a small fraction of the wavelength in the medium, then we must use a very fine mesh to accurately capture the nuances of its geometry. This, in turn, leads to a large number of DoFs when there are other large objects also present in the computational domain along with the thin wire whose shape may be arbitrary.

Dealing with multiscale objects often forces us to compromise the accuracy (relaxing the numerical discretization process when attempting to capture the small-scale features) in order to cope with the limited available resources in terms of CPU memory and time. In this chapter we introduce a scheme that combines the RUFD and the DM approach

to solve multiscale problems in a numerically efficient manner. Our objective is to handle objects with fine features with the DM approach, and not directly with the RUFD which would require us to use a fine mesh (see Fig. 5.2 for the problem shown in Fig. 5.1), at the cost of increased computational burden when compared to that for a problem without fine features.

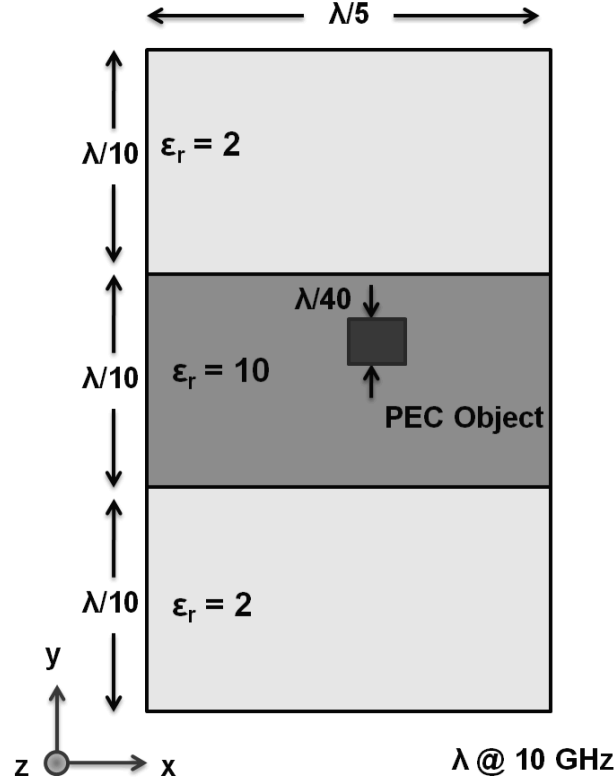


Figure 5.1: A multiscale problem.

The main advantage of this hybrid method is that it does not require local mesh refinement for objects with fine features (Fig. 5.3). In fact, the region surrounding the small/thin structure is extracted from the original domain and two different numerical techniques are used for dealing with the two problems. The coupling of the object with the remaining part of the computational domain is achieved by using the fields radiated by the previously extracted region. As a result, the presented method does not place a heavy burden on the CPU time and memory as do the conventional approaches when dealing

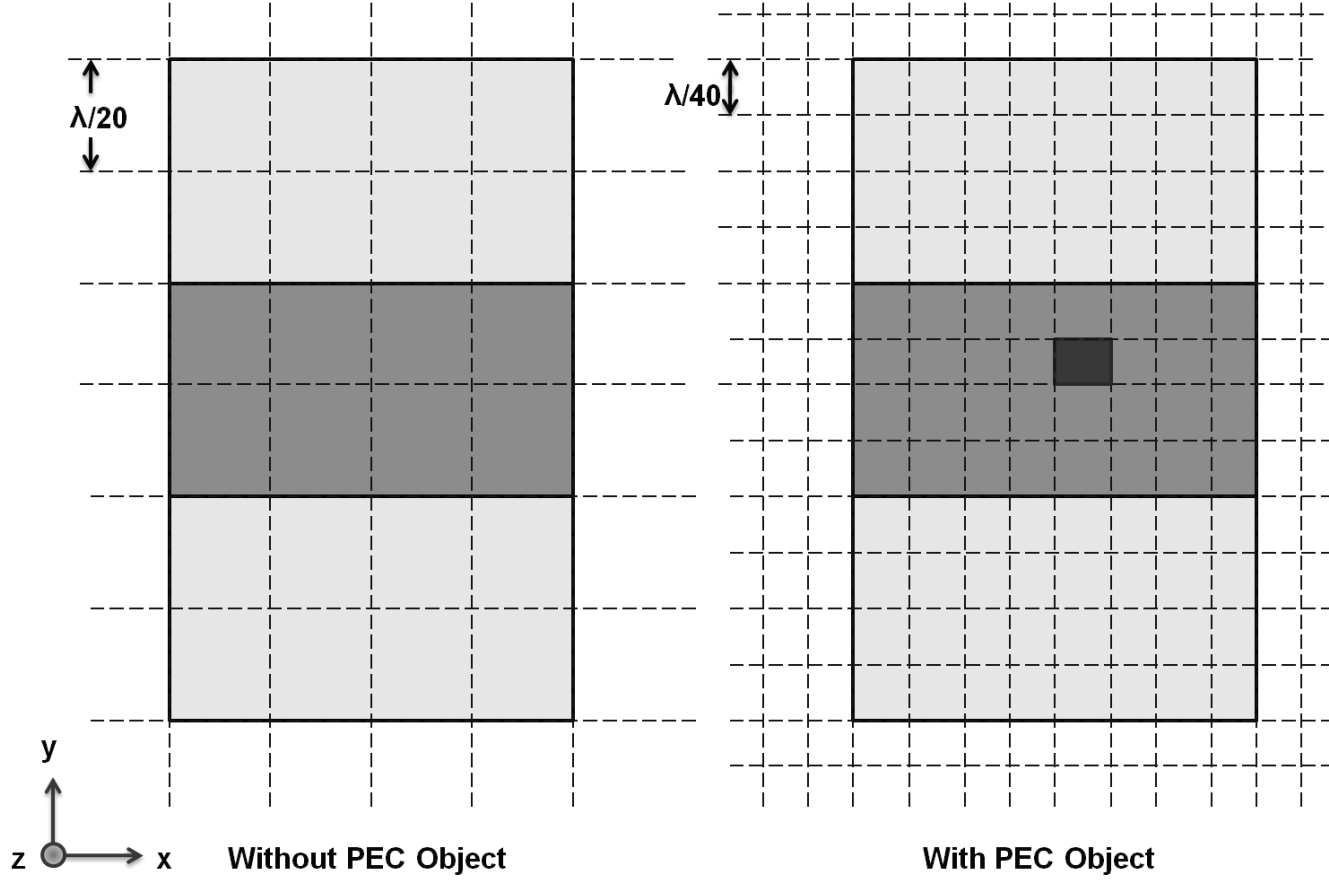


Figure 5.2: A multiscale problem meshed for RUFD simulation.

with multiscale problems. The DM/RUFD method introduced herein can be implemented either in an iterative or in a self-consistent manner.

The proposed method is especially useful for modeling wire antennas located in the vicinity of inhomogeneous structures, as well as for simulating interconnect structures in integrated circuits, which typically have fine features.

5.2 Iterative Approach

Both the iterative and self-consistent hybrid implementations - the latter to be described in the following section - begin by extracting a region surrounding the small object from

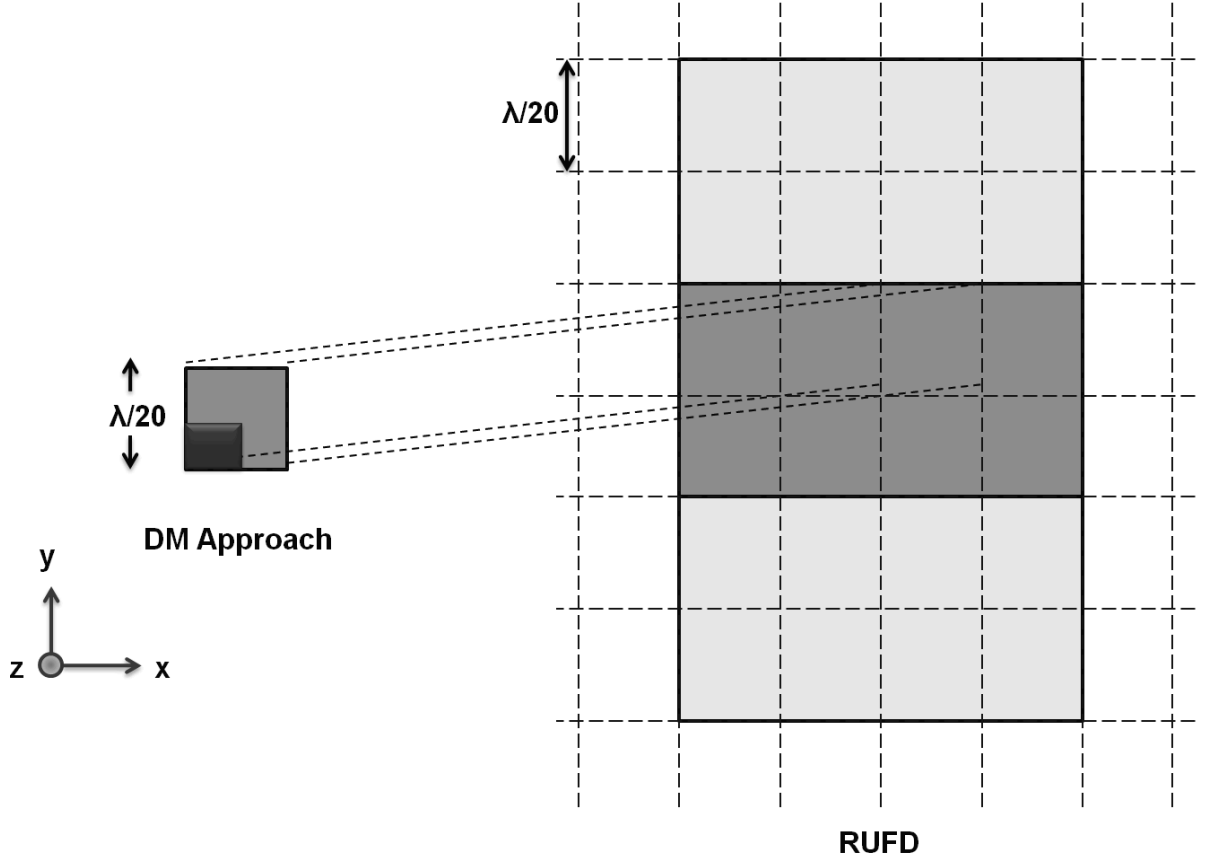


Figure 5.3: A multiscale problem meshed for hybrid RUFD simulation.

the RUFD domain. A 2-D representation of the hybrid problem is shown Fig. 5.3.

Let us assume that two objects, a large PEC plate and a PEC wire, which is small compared to the operating wavelength, are located in the RUFD computational domain, which is excited by a gap source, at 10 GHz as shown in Fig. 5.4. The hybrid-iteration algorithm begins by solving the small object (dipole antenna in this case), which may be PEC, or dielectric (or a combination thereof) is treated by using the DM approach described in Chapters 2 and 3, in the absence of large structure.

Next, the fields scattered by the large structure are derived by using RUFD and a source excitation comprising of the fields radiated by the small object.

These scattered fields are evaluated at the boundary of the extracted region and then

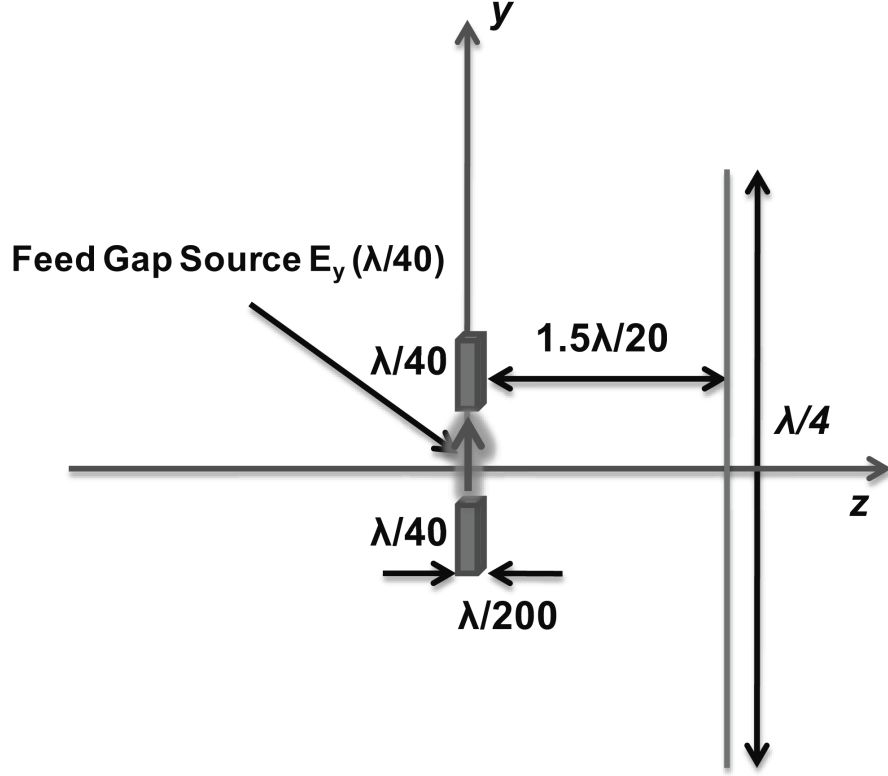


Figure 5.4: A $\lambda/20$ dipole antenna over a finite ground plane (not to scale).

interpolated to obtain the incident fields at the locations of each of the basis function used to model the dipole in DM approach. Following this, the right hand side of the matrix equation, generated using the DM approach for the dipole is modified, by superposing the feed and the fields scattered by the larger structure. Next, the matrix equation is solved for the weight coefficients of the dipole moments, as a first step in the iteration process. Then we again solve for the fields scattered by the large object when illuminated by the fields radiated by the small object, derived by using the recently calculated weight coefficients of the current in the small object.

The iteration process is continued, by repeating the steps described above. The process is terminated when numerical convergence has been achieved and the difference between the results obtained at the k -th and $(k-1)$ -th iteration steps is below a chosen threshold say 10^{-3} . Fig. 5.5 compares the amplitude of the scattered field E_y calculated

by using the RUFD iterative hybrid approach with those obtained from a commercial MoM solver.

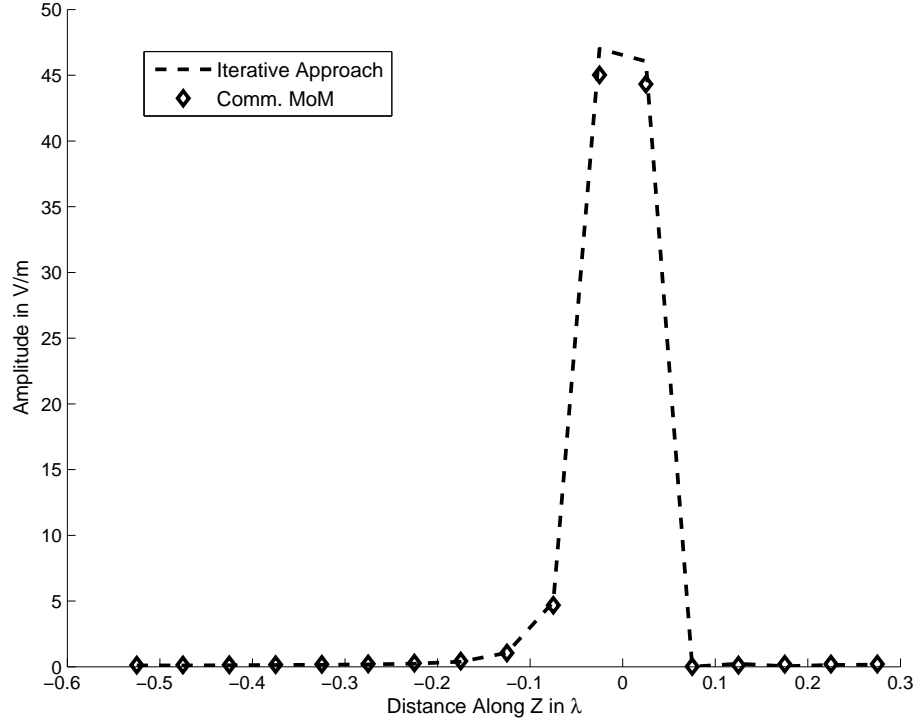


Figure 5.5: Amplitude comparison of E_y field for the multiscale problem shown in Fig. 5.4.

Fig. 5.5 shows the scattered fields calculated by using the RUFD hybrid iterative method compares well with those obtained from a commercial MoM code. The commercial MoM code was able to handle this problem with ease since the large object was modeled as a PEC sheet, however when the PEC sheet is replaced by a thin PEC plate, the CPU time and the memory required by the commercial MoM increases, as will be demonstrated in the next section.

5.3 Self-Consistent Approach

The self-consistent type of hybrid implementation also begins by extracting from the RUFD domain a region surrounding the small object (see Fig. 5.3). However, this time the entire problem is solved in a single step by directly inverting a composite matrix equation, which is constructed as follows. First, the impedance matrix for the small problem is set up independently of the rest, by using the DM approach; the right hand side vector for source is computed and stored. Next, we compute the field radiated by the current distribution on the small object at the location of the large object and solve for the scattered field on its surface by imposing the boundary condition with the fields produced by the small object as the incident field on the large object. The fields scattered by the large object are computed in the entire computational domain by using a RUFD simulation carried out by using a coarse mesh, and then interpolated in the region containing the small object to obtain a new excitation vector for the DM system. Now the matrix equation is solved for the weight coefficients associated with the currents on the small object, and the final scattered fields are calculate as a weighted superposition of the contributions from the small and large objects.

To illustrate the procedure, let us consider a dipole antenna of length $\lambda/2$ over a finite ground plane, operating at 10 GHz as shown in Fig. 5.6. Fig. 5.7 compares the scattered field calculated by using the self-consistent approach as described above, with those calculated by using the iterative approach and the commercial MoM code. Table 5.1 compares the computational resources required by the self-consistent and iterative approaches.

Fig. 5.7 shows good comparison of the scattered field calculated by using the self consistent approach, with those calculated by using the iterative procedure and the commercial MoM code, with the exception of observation points located near the source

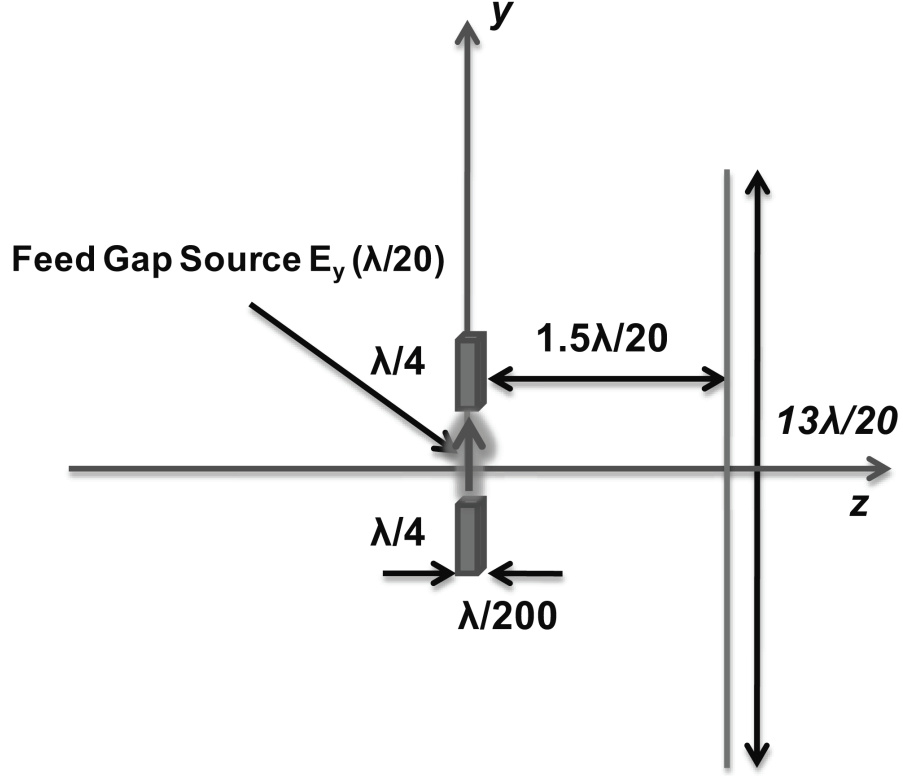


Figure 5.6: A $\lambda/2$ dipole antenna over a finite ground plane (not to scale).

Table 5.1: Comparison of computational resources required by the different RUFD hybrid approaches for the multiscale problem shown in Fig. 5.6.

	Self-Consistent Approach	Iterative Approach
Peak Memory	483 MB	481 MB
Simulation Time	172.3 s	601 s

region. Table 5.1 shows that the results calculated by using the iterative approach are more accurate, though they have a longer run time in comparison to the self consistent approach. In order to demonstrate the key advantage of using the hybrid RUFD, the PEC sheet in Fig. 5.6 was replaced by a PEC plate of thickness $\lambda/20$. The problem was solved by using the self-consistent approach and the variation of scattered field E_y is plotted in Fig. 5.8. Table 5.2 compares the computational resources required by the self-consistent approach with those needed by the commercial MoM. From Fig. 5.8 and the Table 5.2,

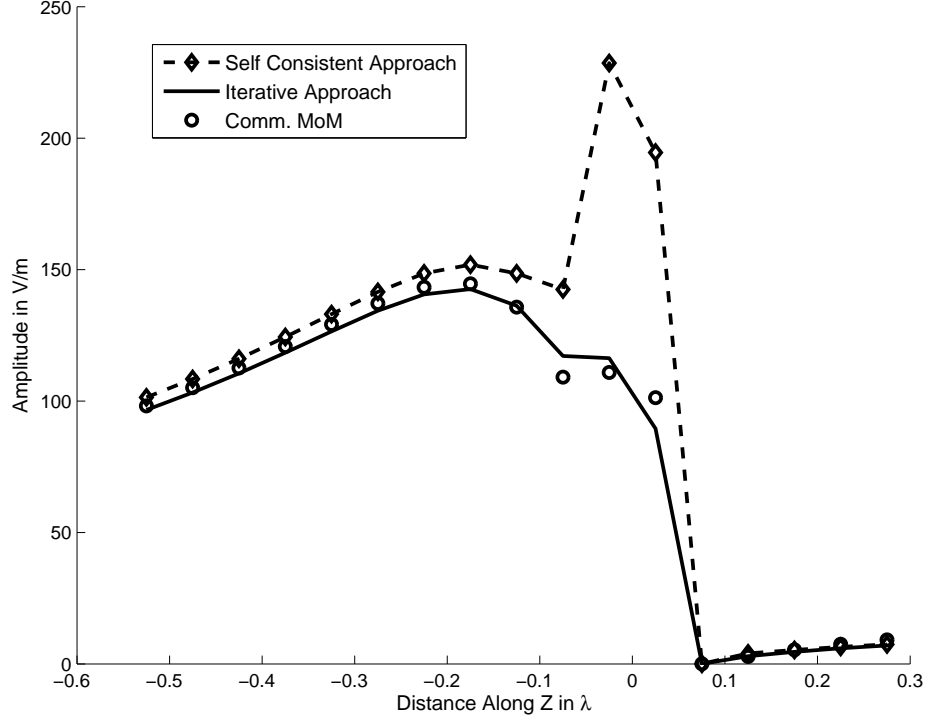


Figure 5.7: Amplitude comparison of E_y field for the multiscale problem shown in Fig. 5.6.

we find that the self-consistent approach outperforms the commercial MoM code, both in terms of memory and simulation time.

Table 5.2: Comparison of computational resources required by the self-consistent approach with those required by the commercial MoM.

	self-Consistent/RUFD brid	Hy- Comm. MoM
Peak Memory	248 MB	543 MB
Simulation Time	71 s	224.75 s

For the next example we consider a $\lambda/20$ diameter sphere, comprising of human muscle ($\epsilon_r = 22 - j18$), and located above a PEC sheet as shown in Fig. 5.9. The sphere is illuminated by a plane wave at a frequency of 10 GHz. The problem is solved by using the self-consistent approach described previously in this section, with a slight modification needed to handle the plane wave source being used in this example, as opposed to a feed-

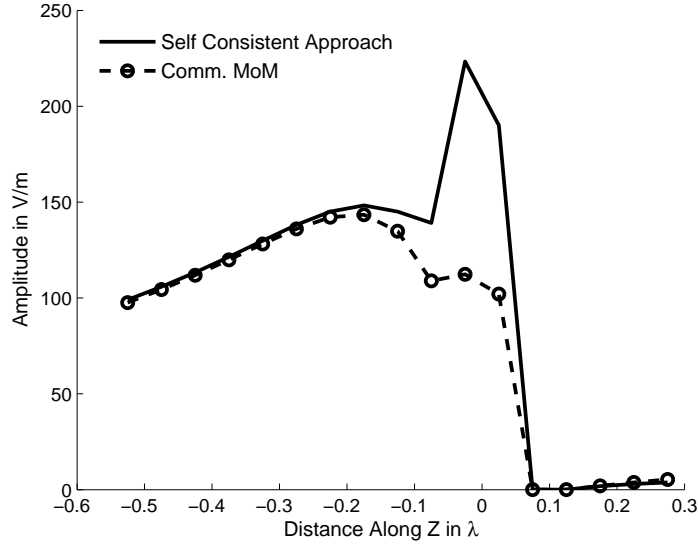


Figure 5.8: Amplitude comparison of E_y field for the multiscale problem with a $\lambda/20$ thick finite ground plane.

gap source that we had dealt with in the previous example. Fig. 5.10 compares the scattered E_y -field, calculated by using the RUFD hybrid approach with those obtained from a commercial MoM code.

As seen from Fig. 5.10, the scattered fields calculated by using the RUFD hybrid approach compares well with those calculated by using a commercial MoM code.

For the next example, we consider a PEC loop, with a thickness of $\lambda/200$ and a diameter of $\lambda/20$, as shown in Fig. 5.11. The loop is placed above a finite ground plane, with a side length of λ , and its scattering and radiation characteristics were investigated at a frequency of 10 GHz. The problem was first solved by using a feed gap source and then with a plane wave illumination, polarized along \hat{y} and traveling along the negative- z direction, both by using the self-consistent approach. Fig. 5.12 compares the E_y -field for the radiation problem calculated by using the self-consistent approach with those obtained from the NEC code. Fig. 5.13 compares the results for the total field E_y for the scattering problem—calculated by using the self-consistent approach—with those obtained from the

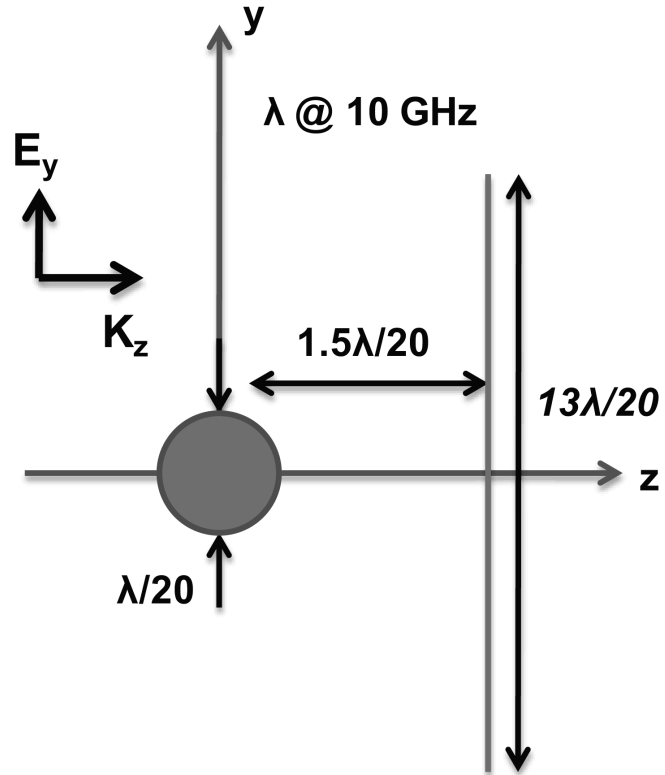


Figure 5.9: A lossy sphere over a finite ground plane (not to scale).

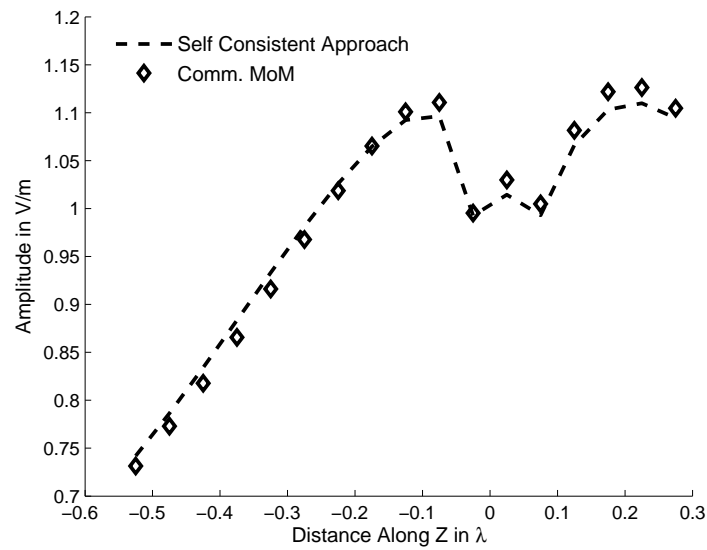


Figure 5.10: Amplitude comparison of scattered E_y field for the problem shown in Fig. 5.9.

commercial MoM.

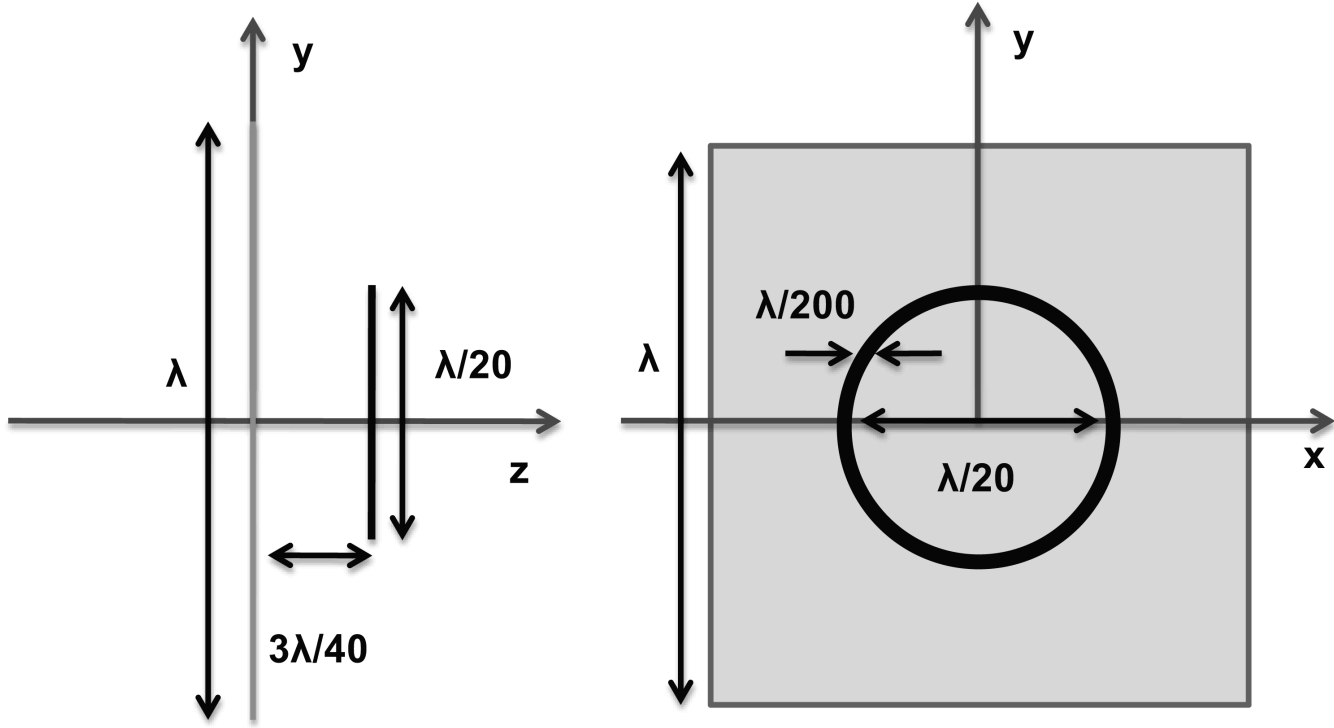


Figure 5.11: A circular loop over a finite ground plane (not to scale).

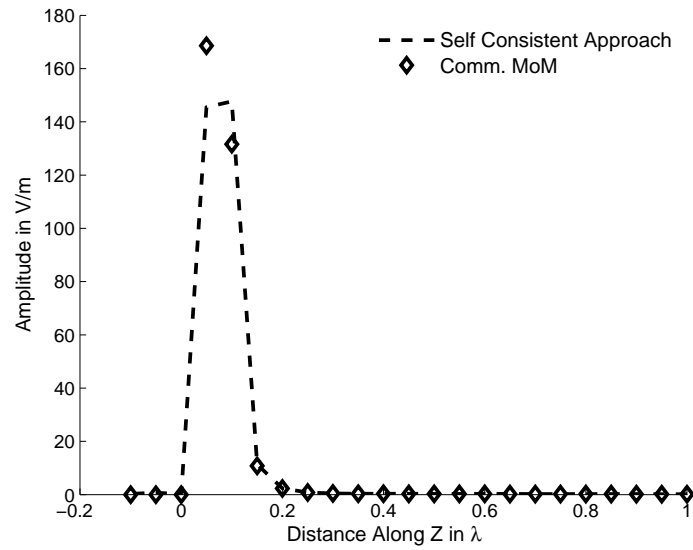


Figure 5.12: Amplitude comparison of E_y field for the loop shown in Fig. 5.11 with a feed gap source.

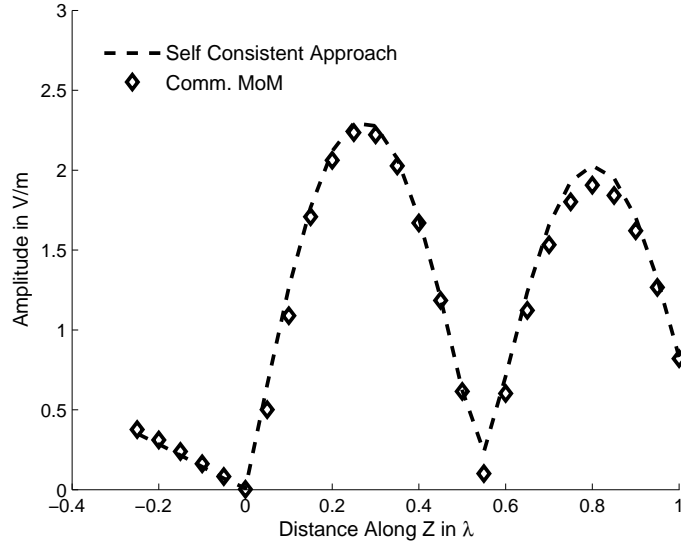


Figure 5.13: Amplitude comparison of total E_y field for the loop shown in Fig. 5.11 with a plane wave illumination.

From Figs. 5.12 and 5.13 we see that good comparison between the E_y -field calculated by using the self-consistent approach, and those obtained from the commercial MoM solver. Although the commercial solver was able to handle this problem with ease, the efficacy of the self-consistent approach becomes evident when the size of the small object is reduced further to $\lambda/200$.

5.4 Vicinity of PML

The effectiveness of the PML determines the accuracy of the RUFD simulations, and the separation distance of the PML boundary from the objects located inside the simulation domain determines the computational requirements. Hence, in order to determine the optimum location of the PML boundary from the objects in the RUFD simulation domain, we consider a square PEC sheet of size $8\lambda/100$, illuminated by a plane wave, polarized along \hat{z} and traveling along negative-y direction at a operating frequency of 10 GHz. The

variation of the scattered E_z -field is compared for different distances, between the PML and the PEC sheet, namely $\lambda/40$, $\lambda/20$ and $3\lambda/40$. Fig. 5.15 shows that the scattered field, calculated by using the RUFD, is relatively insensitive to the separation distance between the PEC sheet and the PML boundary, by using a commercial MoM solver. It also shows that the scattered field calculated by using the RUFD compare well with those computed by using a commercial MoM solver.

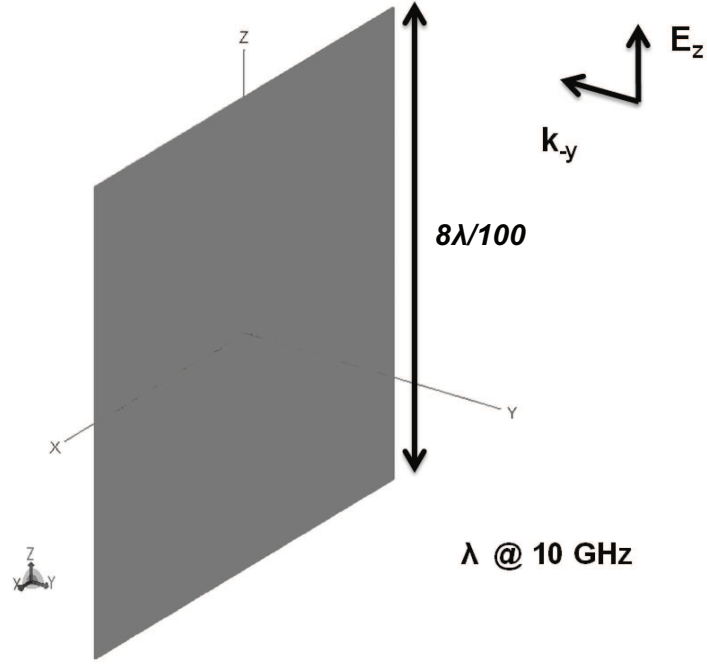


Figure 5.14: A square PEC sheet.

5.5 Multi-Grid Approach

As pointed out in Section 5.1, modeling the fine features of a multiscale problem (see Fig. 5.2) by using the RUFD is computationally very expensive. To handle this problem in a more efficient way, a sub-gridding approach was investigated. However, it was found that a stable implementation of sub-gridding could not be achieved. Hence, we introduce a multi-grid approach where the fine features in the problem are handled separately by using

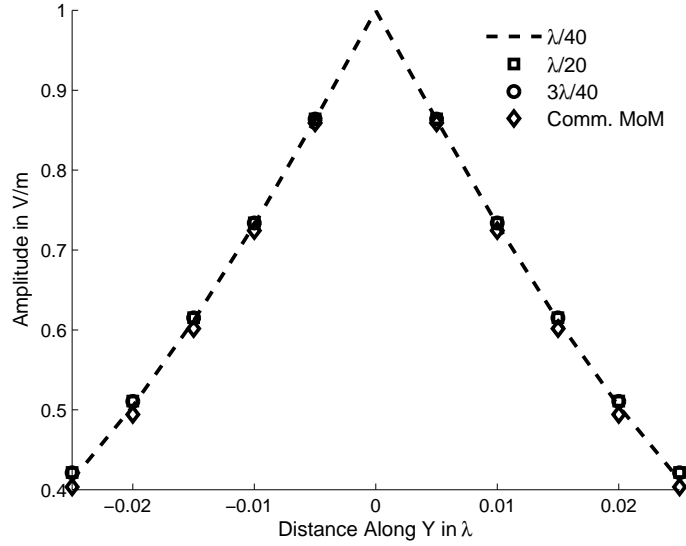


Figure 5.15: Amplitude comparison of scattered E_z field for different distances between the PML boundary and the PEC sheet shown in Fig. 5.14.

a fine mesh for the RUFD computational grid, as shown in Fig. 5.16. As we can see from this figure, the only difference between the hybrid RUFD and multi-grid approaches is that the extracted region in the multi-grid method is solved by using a RUFD simulation carried out with a fine mesh, as opposed to the DM method employed in the context of the hybrid RUFD approach. The key difference between the sub-gridding and multi-grid approaches is to that, the fine mesh and the coarse mesh are interfaced at every iterative step in the sub-gridding approach, while the fine meshed computational domain is simulated first, and then interfaced with the coarse-mesh simulation, in the multi-grid method.

To demonstrate the above procedure, we consider a thin square PEC plate, as shown in Fig. 5.17. The plate is illuminated by a plane wave at a frequency of 10 GHz and we are interested in calculating the scattered E_y -field along the \hat{z} -direction, at observation points ranging from -0.5λ to 0.3λ . If we use the conventional RUFD simulation for this problem, we would need to mesh the entire computational domain with a mesh size of at least $\lambda/400$ (using the thumb rule of using at least two cells to model the thickness of the plate) along

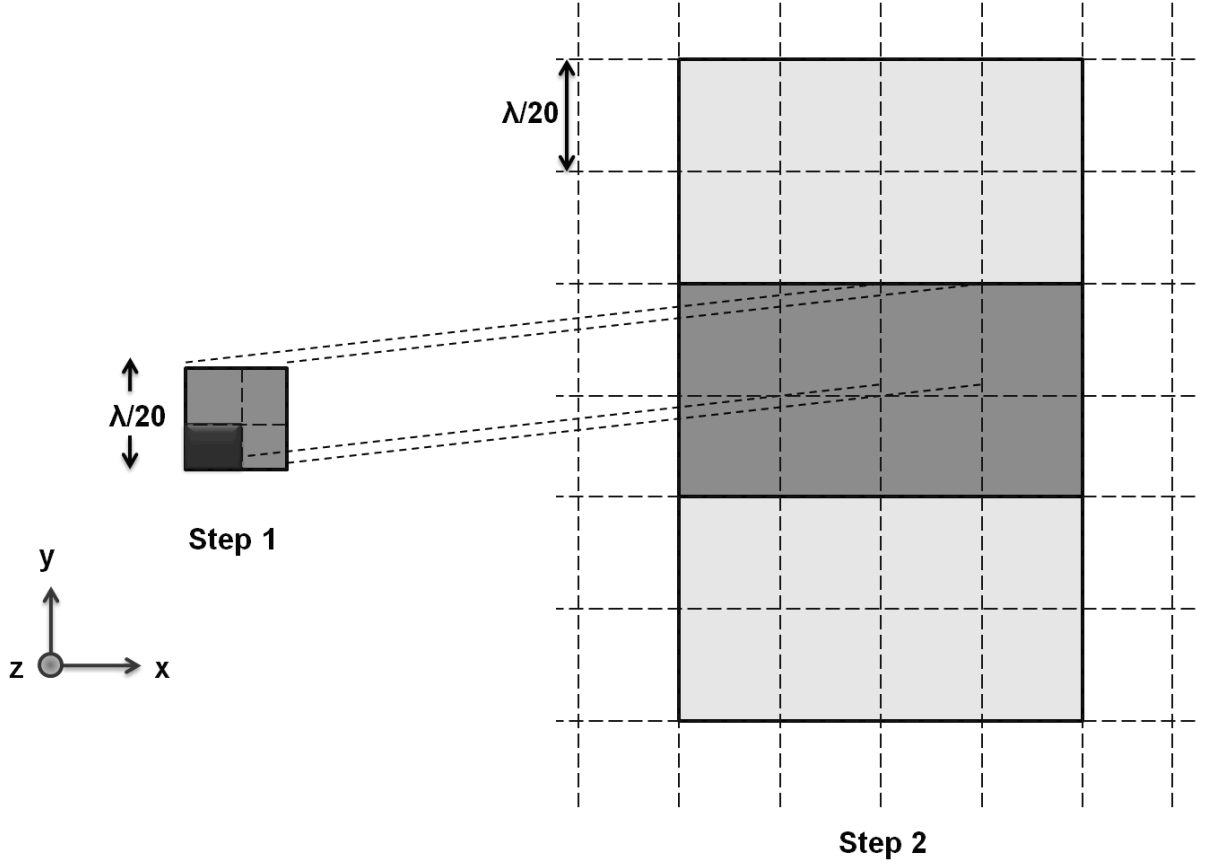


Figure 5.16: A multiscale problem meshed for multi-grid RUFD simulation.

the \hat{z} -direction. However, in the multi-grid method we first define a $17\lambda/20 \times 17\lambda/20 \times \lambda/20$ region, which contains the plate and mesh it with a $\lambda/20 \times \lambda/20 \times \lambda/200$ grid, in the x-, y- and z-directions, respectively. This fine meshed region is first simulated by using the RUFD/scattered field formulation, and then the converged fields so derived are interfaced with the coarse-grid RUFD region, to compute the desired scattered fields. Fig. 5.18 compares the scattered E_y -field calculated by using the multi-grid approach with those obtained by using a commercial MoM solver.

Fig. 5.18 shows a good comparison between the fields calculated by using the multi-grid approach with those obtained from the commercial MoM solver. We find that the multi-grid approach reduces the computational requirements by a large factor in comparison to the time and memory requirements of the conventional RUFD algorithm, without

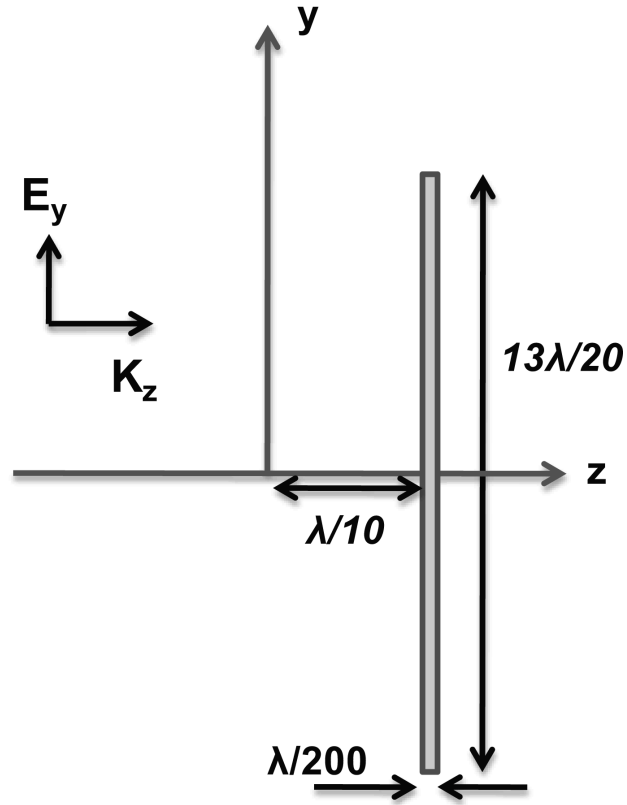


Figure 5.17: A square PEC plate.

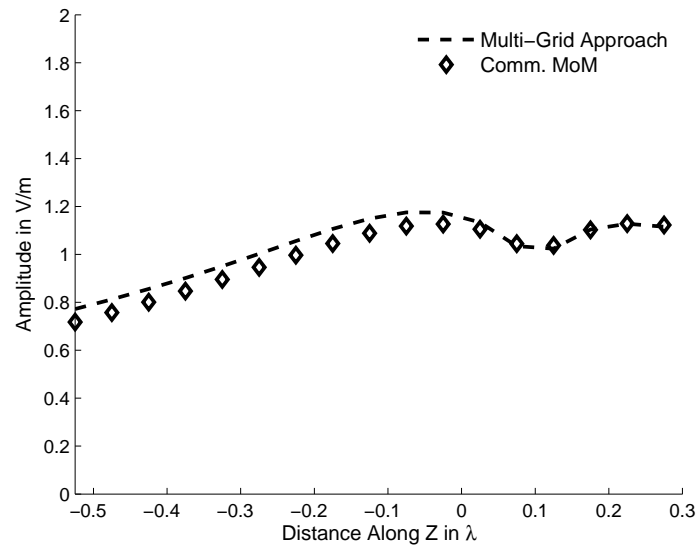


Figure 5.18: Amplitude comparison of scattered E_y field for the PEC plate shown in Fig. 5.17.

compromising the accuracy.

For the next example we consider the problem of scattering by a loop placed over a square PEC plate, at a frequency of 10 GHz, is λ in the side and it has a thickness of $\lambda/200$, as shown in Fig. 5.19. In this problem we use the self-consistent hybrid approach, where the small loop is modeled by using the DM approach, while the plate is handled via the multi-grid approach. The converged fields from these simulations of the loop geometry and the plate, are then used in a coarse grid RUFD simulation, which is meshed by using a cell size of $\lambda/20$. The Fig. 5.20 compares the calculated scattered E_y -field derived by using the multi-grid approach, with those obtained from a commercial MoM code. The comparison is seen to be good.

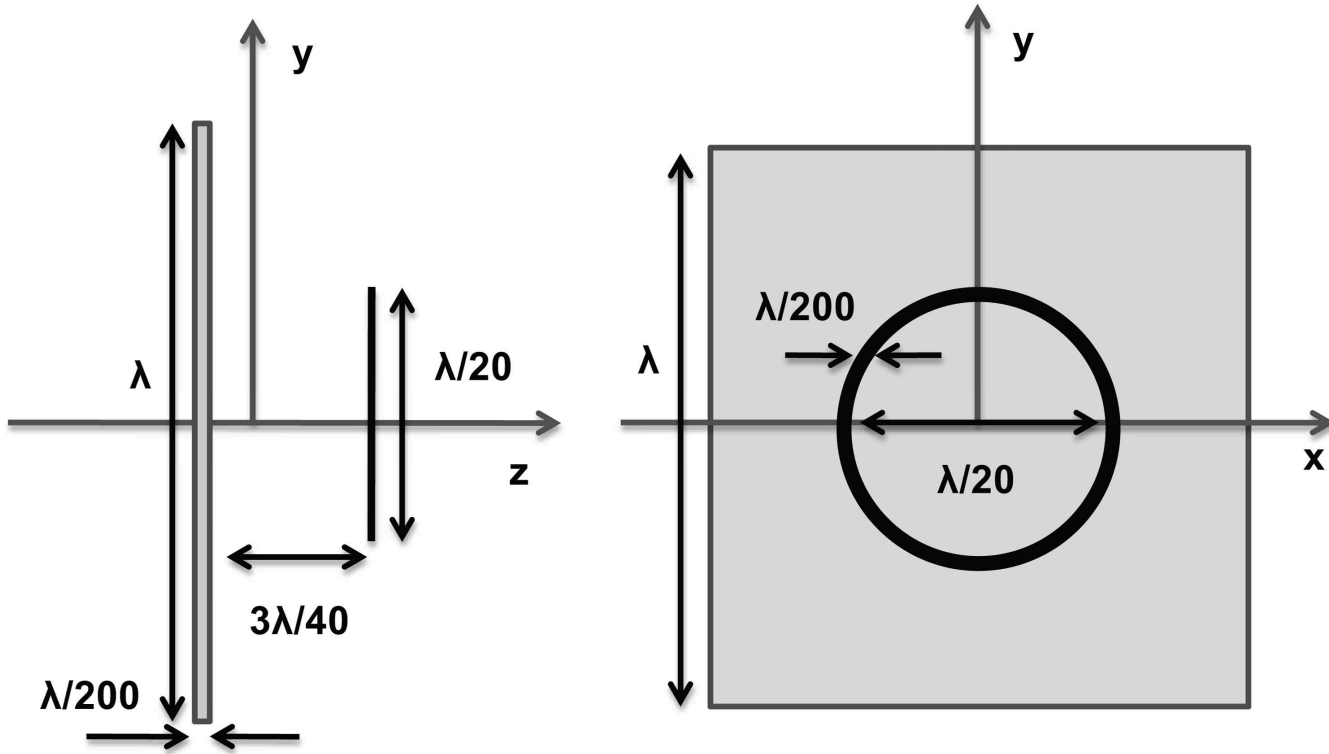


Figure 5.19: A PEC loop over a finite ground plane (not to scale).

Next, we consider an antenna problem, as shown in Fig. 5.21, where a PEC helix operating at 10 GHz, is placed over a finite PEC sheet whose thickness is $\lambda/200$. The

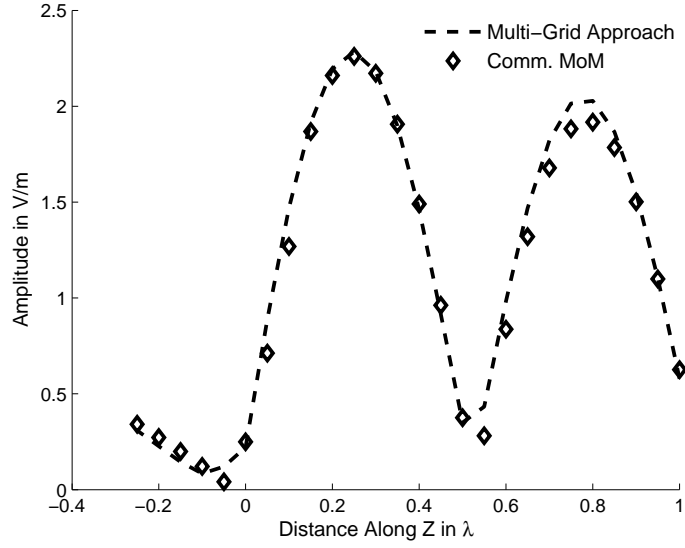


Figure 5.20: Amplitude comparison of scattered E_y field for the PEC loop shown in Fig. 5.19.

Helix is fed by using a voltage gap source. We use the same procedure, as described above for the previous example to solve this problem. The E_z -field radiated by the helix is calculated along the observation line $x = 0$ and $y = 1.5\lambda/20$. Fig. 5.22 is compares the computed E_z -field with that obtained by using a commercial MoM code, while Table 5.3 compares the simulation resources required by the multi-grid approach with that for the commercial MoM code. Fig. 5.22 shows that there are some differences between the two results, although they show similar trends. This difference can be attributed to the different source models used in these two approaches.

Table 5.3: Comparison of computational resources required by the multi-grid approach and the commercial MoM solver for the helix problem shown in Fig. 5.21.

	Mult-Grid Approach	Comm. MoM
Peak Memory	218 MB	373 MB
Simulation Time	118.8 s	198.4 s

From Table 5.3, we see that the multi-grid approach is computationally more efficient than the commercial MoM. Also, the commercial MoM was able to handle this problem

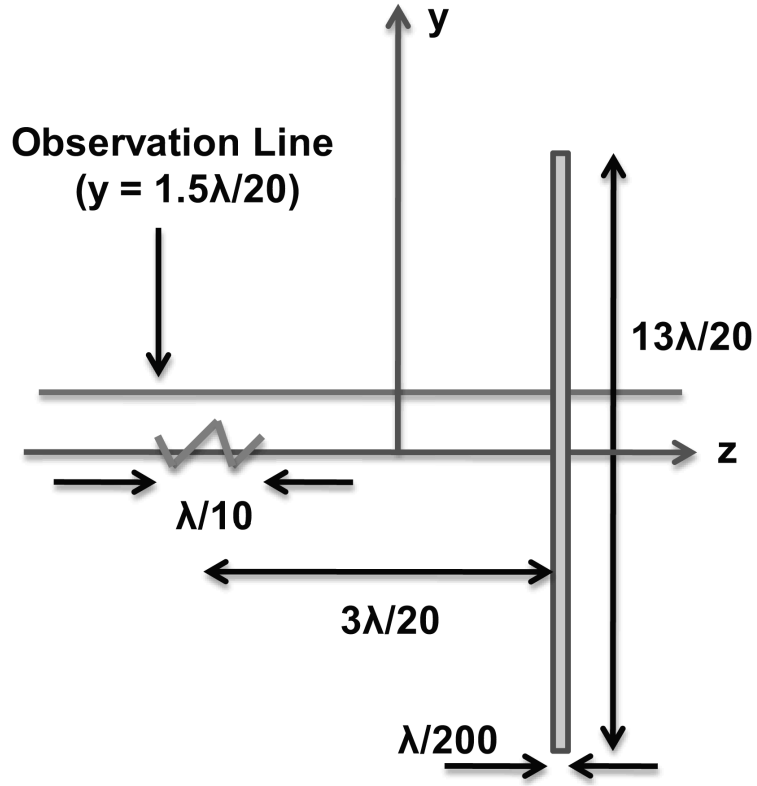


Figure 5.21: A PEC helix over a finite ground plane (not to scale).

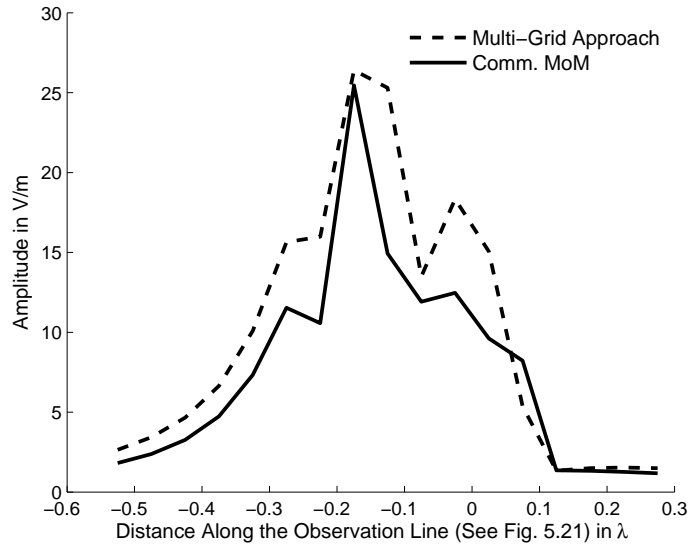


Figure 5.22: Amplitude comparison of radiated E_z field for the PEC helix shown in Fig. 5.21.

with relative ease, since we used a thin-wire model for the helix even though we included the finite thickness while modeling in DM approach during the RUFD hybrid simulation. However, when we include the finite thickness in the commercial MoM code, as we do in the RUFD in a routine manner, the performance of the commercial MoM becomes poor, as can be seen from the next example.

For the last example, let us consider a dipole antenna of length $\lambda/2$ operating at 10 GHz, placed over a finite ground plane of length $13\lambda/20$ and thickness $\lambda/200$, as shown in Fig. 5.23. Fig. 5.24 compares the radiated field E_y is calculated along the \hat{z} -direction by using the multi-grid approach and is compared with those generated by using the commercial MoM. The dipole was modeled in the commercial MoM in two different ways, namely: (i) as a thin wire; and (ii) cylinder with a finite radius of $\lambda/400$. Table 5.4 compares the the computational resources required by the multi-grid approach, the commercial MoM/wire model and the commercial MoM/cylinder model. We find, once again that the multi-grid approach is computationally more efficient than the commercial code; however, its accuracy is comparable to that of the MoM code.

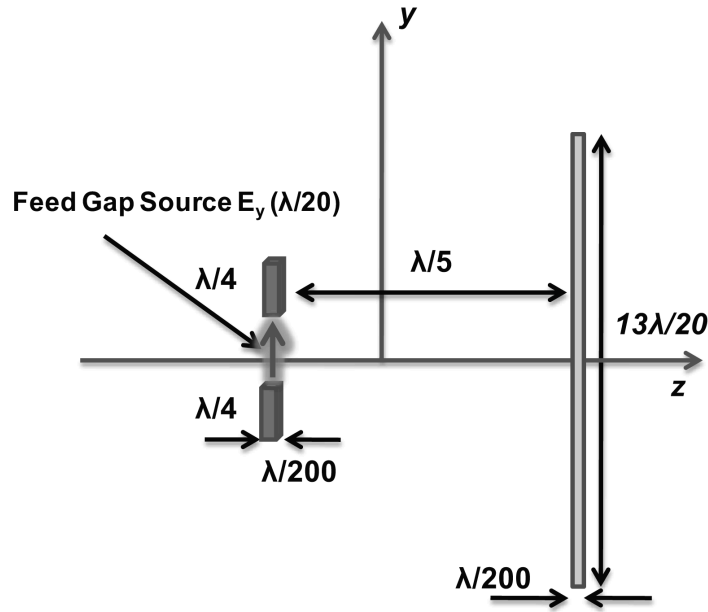


Figure 5.23: A PEC dipole placed over a finite ground plane (not to scale).

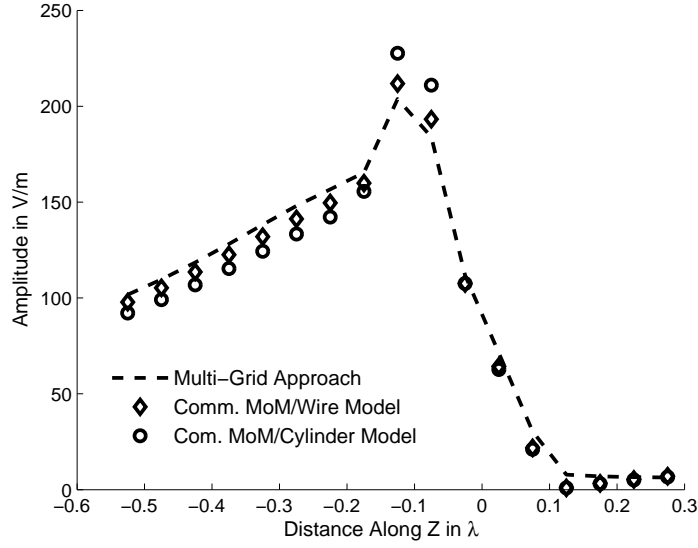


Figure 5.24: Amplitude comparison of radiated E_y field for the PEC dipole shown in Fig. 5.23.

Table 5.4: Comparison of computational resources required by the multi-grid approach and the commercial MoM solver for the dipole problem shown in Fig. 5.23.

	Multi-Grid Approach	Comm. MoM/Wire Model	Comm. MoM/Cylinder Model
Peak Memory	345 MB	459.2 MB	387 MB
Simulation Time	115.6 s	187.4 s	194.3 s

5.6 Handling Inhomogeneous Objects with Fine Features

The complexity of the multiscale problem increases when an object has either a lossless or lossy dielectric coating. The efficacy of the hybrid RUFD in handling such multiscale problems will be demonstrated in this section with illustrative examples.

5.6.1 Large Objects with Coating

Whenever a large object has a thin dielectric coating, we use a multi-grid approach, described in the previous section, to model this type of multiscale problems. Let us consider the dipole antenna problem, which is shown in Fig. 5.25, and which operates at 10 GHz. The PEC plate is coated with $\epsilon_r = 6$ and the coating is $\lambda/200$ thick. We use a multi-grid approach to model the plate; DM approach to model the dipole antenna; and, a coarse grid RUFD to calculate the interaction between them. Fig. 5.26 compares the radiated E_y -fields calculated by using the hybrid RUFD approach with those generated by using the commercial MoM code. Table 5.5 compares the computational resources required by the hybrid RUFD approach with that needed by the commercial MoM.

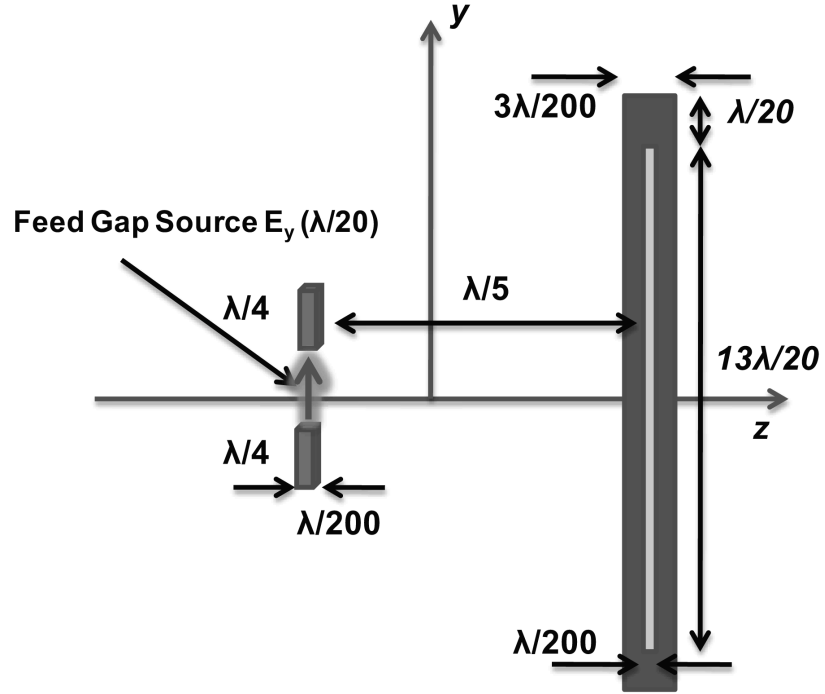


Figure 5.25: A PEC dipole placed over a coated finite ground plane (not to scale).

From Fig. 5.26 and Table 5.5 we find that the hybrid RUFD outperforms the commercial MoM code. It is important to recognize the fact that we can directly incorporate lossy coating in the proposed hybrid approach, while in the MoM or FEM based solvers,

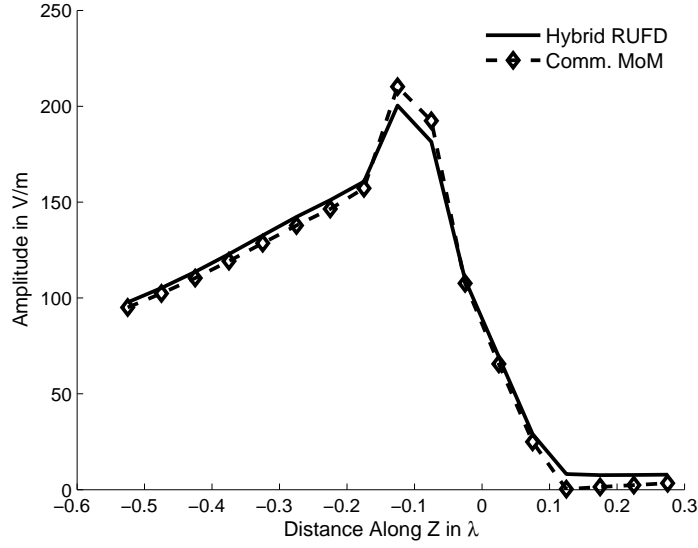


Figure 5.26: Amplitude comparison of radiated E_y field for the PEC dipole shown in Fig. 5.25.

Table 5.5: Comparison of computational resources required by the multi-grid approach and the commercial MoM solver for the dipole problem shown in Fig. 5.25.

	Multi-Grid Approach	Commercial MoM
Peak Memory	270.8 MB	646.2 MB
Simulation Time	97.4 s	276.2 s

special treatments are required to incorporate losses, and doing so also increases the computational cost.

5.6.2 Coated Small Objects

For multiscale problems involving coated small objects, we use the DM approach to model them, in a manner described in Section 2.5.1. As an example, let us consider a dipole antenna operating at 10 GHz, which is coated with $\lambda/100$ thick dielectric layer with $\epsilon_r = 6$, as shown in Fig. 5.27. The dipole antenna is modeled by using the DM approach, and it is found that the effective thickness of the coated wire is $1.8\lambda/200$. Fig. 5.28 compares

the radiated E_y -field calculated by using the hybrid RUFD approach, with that obtained from the commercial MoM, and Table 5.6 compares the required computational resources.

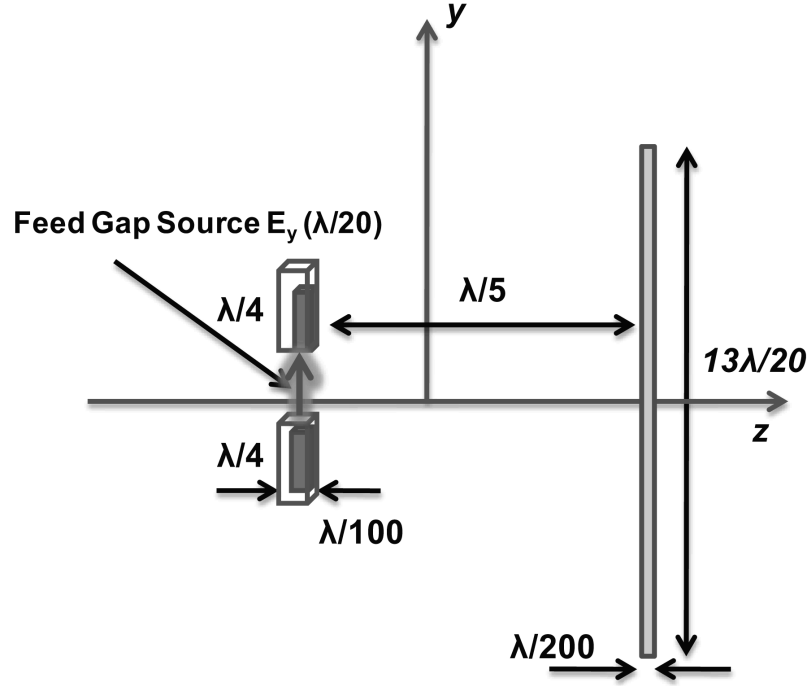


Figure 5.27: A coated PEC dipole placed over a finite ground plane (not to scale).

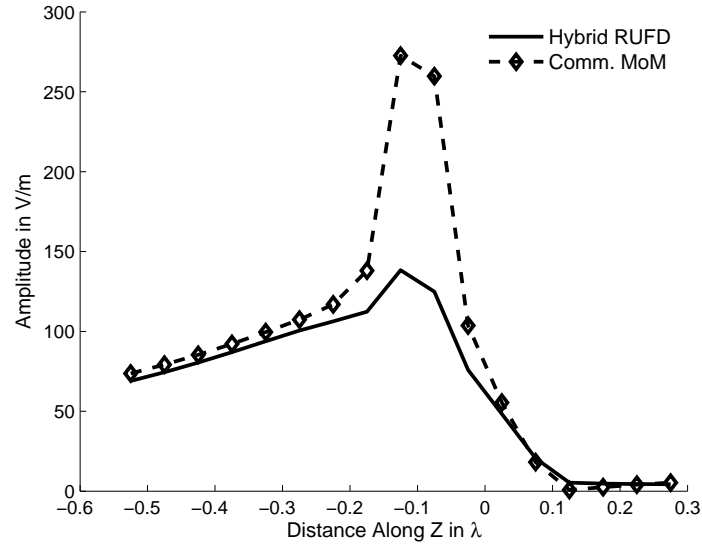


Figure 5.28: Amplitude comparison of radiated E_y field for the PEC dipole shown in Fig. 5.27.

Table 5.6: Comparison of computational resources required by the multi-grid approach and the commercial MoM solver for the coated dipole problem shown in Fig. 5.27.

	Multi-Grid Approach	Commercial MoM
Peak Memory	201.1 MB	1219.7 MB
Simulation Time	106.6 s	1028.9 s

We should point out that the difference in the field behaviors near the feed gap, as seen from Fig. 5.27, is attributable to different source models used in these two approaches. Table 5.6 shows that the hybrid RUFD is computationally efficient, by a large factor, when compared to the commercial MoM code.

5.7 Observations and Conclusions

In this chapter, a novel approach for handling multiscale problems, which combines the DM method with the newly developed recursive technique in the frequency domain, was introduced. It was shown that this hybrid scheme preserves the salutary features of the FDTD algorithm, including convenient mesh generation and parallelization on multiple processors; and yet, it is convenient for handling dispersive and high-Q structures.

We have shown how the DM approach and the RUFD algorithm may be combined to solve multiscale problems accurately and efficiently, and the performance of the resulting hybrid scheme has been found to be superior to those of some well known and widely used CEM codes, both in terms of accuracy and computational efficiency. We have also introduced a multi-grid approach, which takes advantage of the fact that the PML boundary can be brought closer to an object than in conventional schemes. In this approach a part of the computational domain is meshed with a fine grid, while the rest of the domain employs the conventional $\lambda/20$ discretization. The use of such a hybrid scheme enables us

to model objects with fine features in a computationally efficient manner. We have shown, by using a number of illustrative examples, how to hybridize, both the DM approach and the multi-grid approach with the RUF algorithm, in order to solve multiscale problems numerically efficiently.

6. New Finite Difference Time Domain (ν FDTD) Algorithm

6.1 Introduction

The conventional time domain technique FDTD demands extensive computational resources when solving low frequency problems, or when dealing with dispersive media. To tackle some of these challenges, the conventional techniques are often modified in a manner that is tailored to solve a particular problem of interest. However, more often than not, these tailored methods turn out to be computationally expensive, and they often lead to instabilities. Hence, it is useful to develop techniques that can overcome the above limitations, while preserving the advantages of the existing methods. The ν FDTD (New FDTD) technique, which is described in this chapter, is a new general-purpose field solver, which is designed to tackle the above issues using some novel approaches, that deviate significantly from the legacy methods that only rely on minor modifications of the FDTD update algorithm.

6.2 ν FDTD Solver

The ν FDTD solver is a hybridized version of conformal FDTD (CFDTD) [24], and a novel frequency domain technique called the Dipole Moment Approach (DM Approach) described in Chapter 2. This blend of time domain and frequency domain techniques empowers the solver with potential to solve problems that require:

- Calculating low frequency response accurately and numerically efficiently
- Handling non-Cartesian geometries such as curved surfaces (see Fig. 6.1) accurately without staircasing
- Handling thin structures, with or without finite losses (see Fig. 6.2)
- Dealing with multi-scale geometries (see Fig. 6.3)

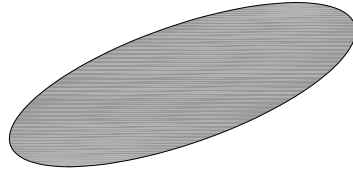


Figure 6.1: An elliptical geometry.

Advantages Some of the notable features of ν FDTD are:

- Unlike the conventional FDTD, the mesh-size utilized by the ν FDTD is not dictated by the finest feature of the geometry, and this size is usually maintained at the

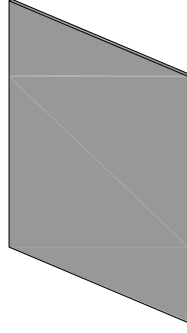


Figure 6.2: A very thin sheet.

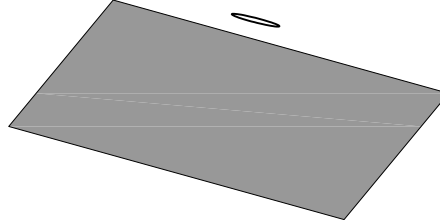


Figure 6.3: PEC loop over a finite ground plane.

conventional $\lambda/20$ level. This helps to reduce the computational burden by a large factor.

- The ν FDTD algorithm incorporates a novel post-processing technique which requires relatively few time steps, in comparison to the number of steps required by the conventional FDTD.

6.3 Low Frequency Response

Despite many advances in Finite methods, such as the FEM and the FDTD, as well as in integral-equation-based techniques such as the MoM, it still remains a challenge to ac-

curately calculate the low frequency response for radiation and scattering problems. The frequency domain techniques, such as the FEM and MoM, both experience difficulties at low frequencies, because they have to deal with ill-conditioned matrices at these frequencies. On the other hand, while the time-domain-based techniques, such as the FDTD, can accurately generate results at high frequencies, usually above 1 GHz, the same cannot be said about their performance at low frequencies. This is not only because the FDTD results are often corrupted by the presence of non-physical artifacts at low frequencies, but also because the FDTD requires exorbitantly large number of time steps for accurate calculation of the response. The required number of time steps can exceed a few million in some cases before convergence is achieved.

As an example, let us consider a 32 port connector circuit example shown in Fig.6.4. This connector geometry has been analyzed by using a commercial FDTD solver and the variation of the transmission co-efficient S_{21} is plotted in Fig.6.5 as a function of the frequency, and we observe that the results shows ripples that are numerical artifacts. Table 6.1 compares the number of time steps required for the solution to converge at different frequencies for the connector geometry. It can be inferred from this Table that the number of time steps required for the convergence increases as we go down in frequency, and eventually it becomes totally impractical to solve the problem at very low frequencies. Accurate calculation of the low frequency response becomes especially critical in the area of RF and digital circuits, since inaccurate results can affect the causality behavior of the overall system. The ν FDTD utilizes a new technique, which is based on analytic continuation of the results derived at higher frequencies, and which is implemented by using the DM Approach and related techniques. This new technique is universal in nature, and it covers the entire range of frequencies, including the limiting case of $f \rightarrow 0$. Also, the ν FDTD can handle both the RF/Digital circuit problems as well as the radiation/scattering problems with same ease, by employing unique methodologies tailored

for each of these categories. We present these methodologies in detail in the sections that follow.

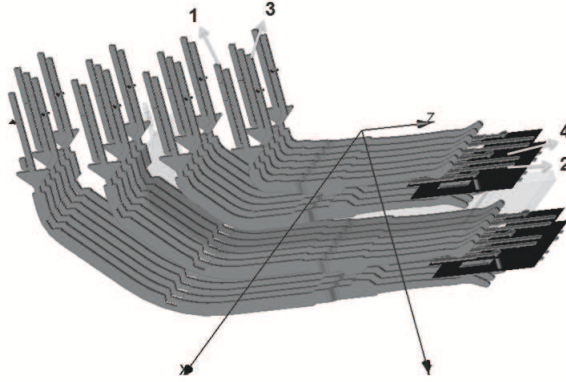


Figure 6.4: A 32 port connector with a overall dimension of 5.6 x 11.88 x 27.35 mm (Housing not shown here).

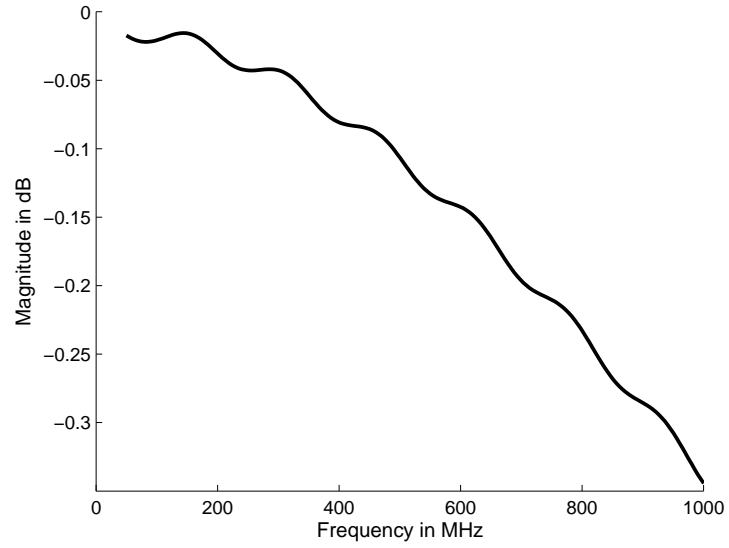


Figure 6.5: Variation of the transmission co-efficient S_{21} for the 32 port connector shown in Fig.6.4.

Table 6.1: Comparison of time steps required for convergence for the circuit shown in Fig.6.4.

Frequency	10 MHz	1 MHz	1 Hz
Time Steps in Millions	0.7	7	70

6.3.1 RF and Digital Circuits

Consider the variation of the isolation co-efficient S_{31} shown in Fig.6.6 for the connector geometry(Fig.6.4). This plot is divided into three regions, namely:

- Region-1: Low-frequency regime
- Region-2: Validation region
- Region-3: High-frequency regime

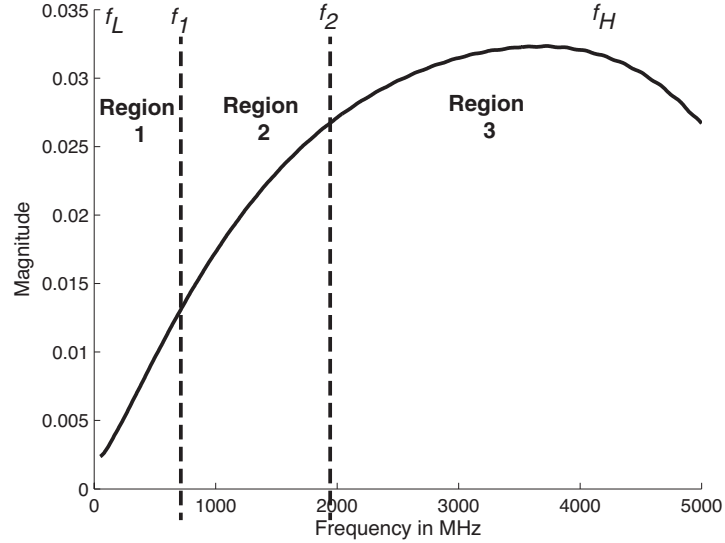


Figure 6.6: Variation of the isolation co-efficient S_{31} for the 32 port connector shown in Fig.6.4.

There are four frequency values which delimit the above three regions. The frequency f_L describes the lowest frequency of interest defined by the user. The frequency f_1 , which divides the regions 1 and 2, is typically chosen to be between 500 MHz to 1000 MHz, while the frequency f_2 dividing the regions 2 and 3 is chosen to be on the order of $2f_1$ or $3f_1$.

The frequency f_H is the user input indicating the highest frequency of interest. In each of these three regions the results are calculated by using a different method. The results in the high frequency regime are generated by using the conventional FDTD, using a DC Gaussian pulse as the excitation source, whose 3dB cut-off frequency is set to be f_H . In the low frequency regime, the results are generated by using the proposed new technique, which involves the following steps:

1. Smooth the “DC Gaussian” Results.
2. Fit the curve from f_L to f_1 with the DC values, using a quadratic, for instance. The choice of f_1 can be fine-tuned based on the quality of the resulting fit.
3. Validate the smoothed “DC Gaussian” results in region-2 by comparing them with those generated by “single frequency” simulations at a few points (typically 2 or 3).

We have recalculated the results for the 32-port connector geometry, shown in Fig. 6.4, by using the above method. The new results for the variation of the transmission co-efficient S_{21} and the isolation co-efficient S_{31} are shown in Figs. 6.7 and 6.8. From these figures we can clearly see that the conventional FDTD simulation utilizing the DC Gaussian pulse does not generate an accurate low frequency response and has numerical artifacts, while the ν FDTD does not suffer from the same.

For the next example, we consider an 8-port connector as shown in Fig. 6.9, which operates in the frequency range 50-800 MHz. Fig. 6.10 compares the variation of S_{31} calculated by using the ν FDTD with those obtained by using the DC Gaussian in the conventional FDTD algorithm. Again we find that the DC Gaussian results show spurious spikes, while the ν FDTD was able to calculate it accurately.

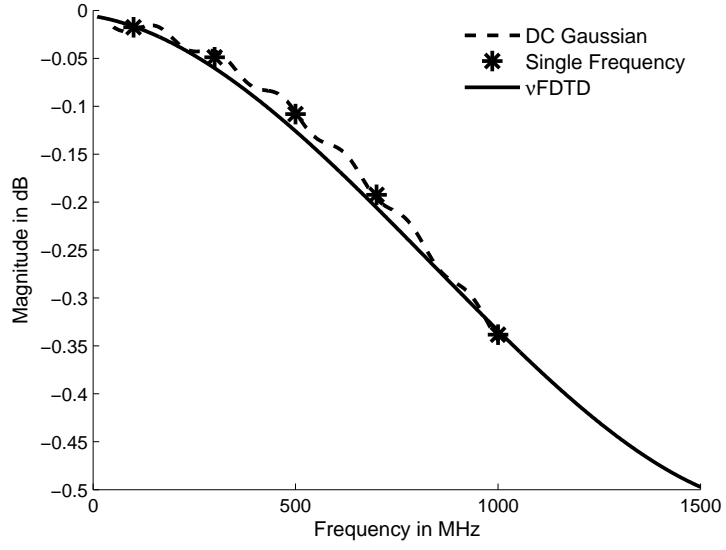


Figure 6.7: Variation of the transmission co-efficient S_{21} for the 32 port connector shown in Fig.6.4 calculated using ν FDTD.

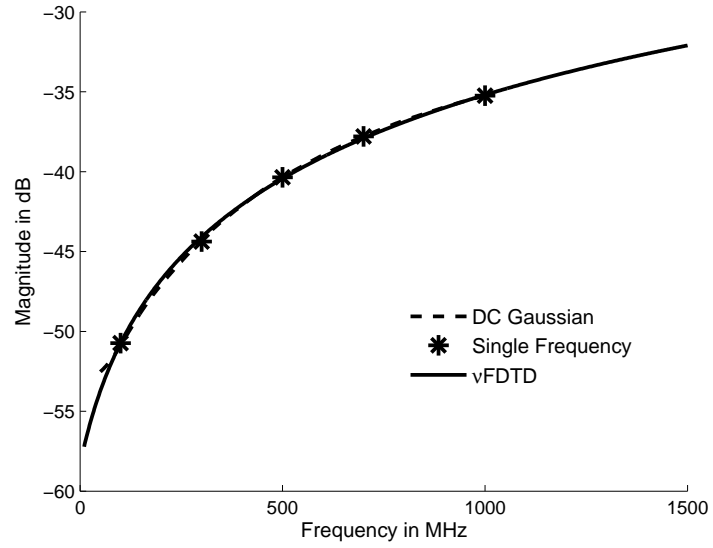


Figure 6.8: Variation of the isolation co-efficient S_{31} for the 32 port connector shown in Fig.6.4 calculated using ν FDTD.

6.3.2 Scattering Problems

In this section we turn to the solution of scattering problems by using the ν FDTD. The methodology for handling the radiation and scattering problems are different from those

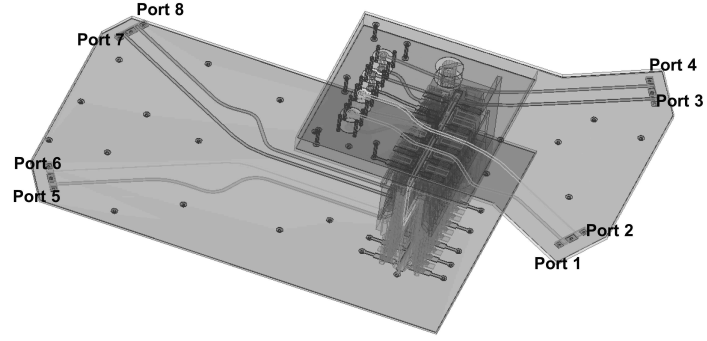


Figure 6.9: A 8 port connector (Housing not shown here).

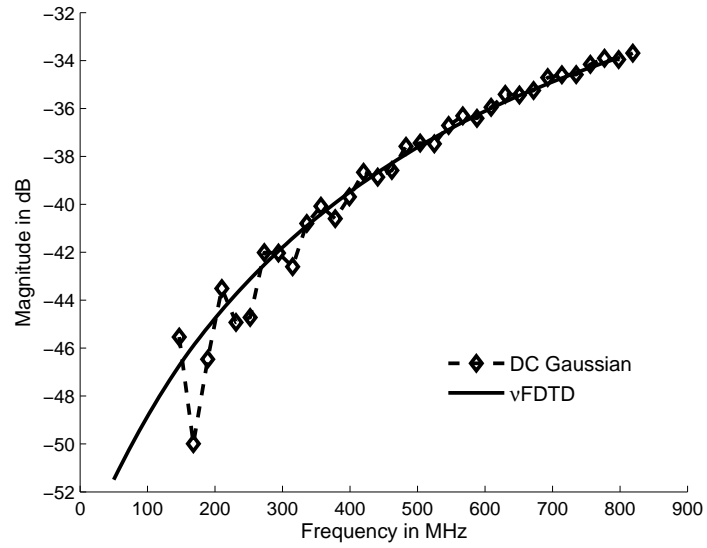


Figure 6.10: Variation of the S_{31} for the 8 port connector shown in Fig.6.9.

used for the RF/Digital circuits, as we will explain below. For the high frequency regime, we use the conventional FDTD, and use a Gaussian excitation source to generate the results. However, we employ a different procedure, as outlined below, in the low frequency regime:

1. Run a “Single Frequency” simulation at a frequency f_1 , where the largest dimension of the geometry is $\lambda/100$, to calculate the fields at a point located $\lambda/20$ from the surface of the object.
2. Extract the dipole moment by using the analytical expressions for the field radiated

by an infinitesimal dipole [8] from the field values calculated above.

3. Use the extracted dipole moment to calculate the results from f_L to f_2 , where f_L is the lowest frequency of interest, and f_2 is typically chosen to be $2f_1$ or $3f_1$. It has been found that the results generated by using this dipole moment is not only valid for frequencies as low as 0, but also up to frequencies where the largest dimension of the geometry becomes $\lambda/10$; hence it enables us to dovetail the low frequency results, seamlessly, with the lower end of the high frequency response.
4. Validate the “DC Gaussian” results in the range between f_1 and f_2 by comparing them with those calculated by using the analytical expression at a few points (typically 2 or 3).

In order to extract the dipole moment from the single frequency simulation, one can either use the method proposed by Furse [25], or use the DFT to process the time signature. In the Furse method, we choose two samples of the time signature and we fit the time signature to a sinusoidal curve using those two samples. Even though this method looks computationally inexpensive when compared to the DFT approach, the choice of the two samples determines the accuracy of the method, and these samples should not lie within the transient region; hence we always use the DFT to extract the DM because of its robustness.

As an example application of the procedure just outlined, we consider a sphere with a diameter of $\lambda/20$, with λ defined at 10 GHz. The sphere is illuminated by a plane wave traveling in the negative-z direction, with its E-field polarized along y. Fig.6.12 compares the fields calculated by the proposed technique, in the frequency range of 1 Hz to 30 GHz, with those derived analytically. We find that the fields calculated by using the proposed technique based on DM extraction exhibits good agreement with those calculated by using the analytical expression. The small deviation between the two

curves is attributable to the staircase modeling of the sphere in the conventional FDTD, and it can be corrected by using an effective radius in the analytical expression. It is important to recognize the fact that we have used the same technique to calculate the response over the entire frequency range, including frequencies as low as 1 Hz, without using either the quasi-static approximation or other special treatments that are employed in the conventional computational electromagnetic (CEM) techniques. Even after the use of special treatments in the existing techniques, such as the FEM and MoM, the accuracy of the low-frequency solution is often questionable because of the large condition numbers of the associated matrix. Thus, despite all the special treatments implemented in these methods to address the low frequency breakdown problem, it is totally impractical to go down to frequencies on the order of 1 Hz in the existing techniques.

The amplitude variation of the scattered field with the distance along z , calculated by using the proposed technique, is shown in Fig. 6.13 for a frequency of 1.8 GHz. This plot also compares the results with those calculated by using analytical expressions. Again we find good agreement between the ν FDTD results and those generated from the analytical expression for a $\lambda/67$ sphere, for the chosen frequency of 1.8 GHz. The field variation derived by using the ν FDTD matches well with that generated from the analytical expression, both in the near and far field regions.

For the next example we consider a PEC cube of side length $\lambda/20$, as shown in Fig. 6.14 at a frequency of 10 GHz. Fig. 6.15 plots the scattered E_y -field as a function of frequency, calculated at $z = 2.5\text{mm}$ ($\lambda/12$ at 10 GHz), by using the ν FDTD, and compares them with those obtained by using the DM approach. The comparison is seen to be good even at a frequency of 1 Hz.

Based on the illustrative examples presented above, we list below some of the advantages of the proposed method:

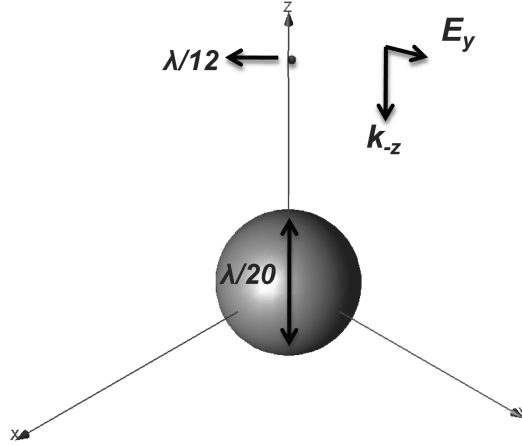


Figure 6.11: A PEC sphere of diameter $\frac{\lambda}{20}$ at 10 GHz.

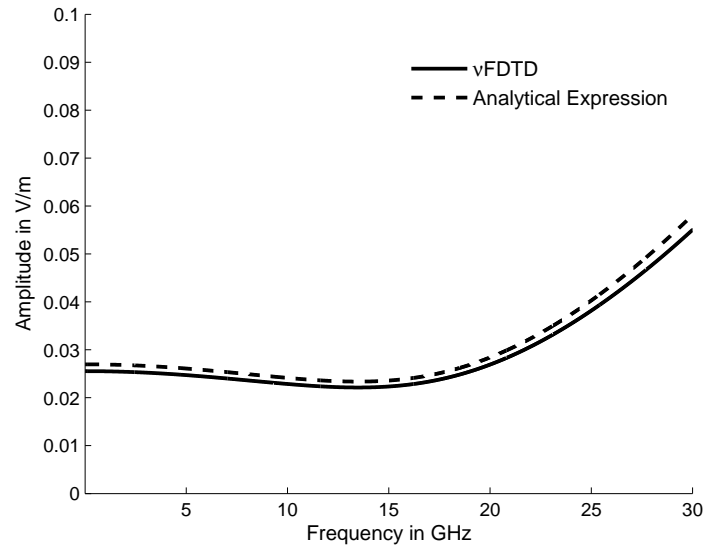


Figure 6.12: Amplitude variation of the scattered E_y at a point $z = 0.25\text{cm}$ with frequencies from 1Hz to 30 GHz.

- RF and Digital Circuit Problems:

Efficient for constructing low frequency solution, compared to the long runs in FDTD.

- Scattering Problems:

(a) Can be used for *an arbitrary geometry*.

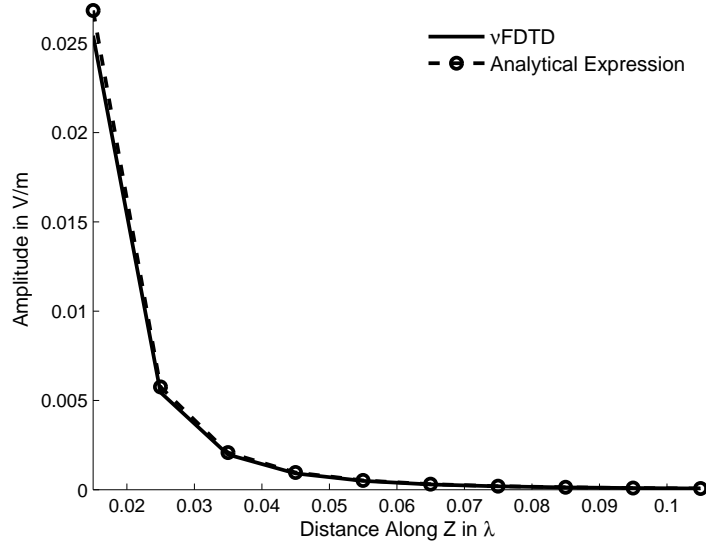


Figure 6.13: Amplitude variation of the scattered E_y with distance along z from $\frac{\lambda}{67}$ to $\frac{\lambda}{10}$, at 1.8 GHz.

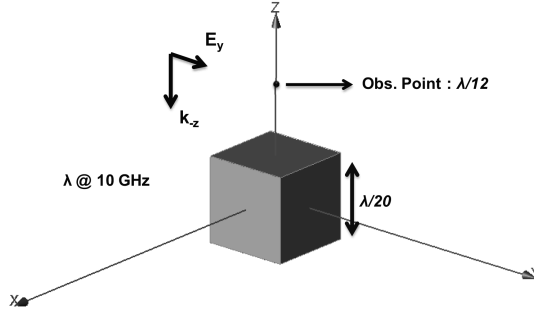


Figure 6.14: A PEC cube of side length $\frac{\lambda}{20}$ at 10 GHz.

- (b) Can be used to efficiently calculate not only the frequency response, but the *near and far fields* as well.

6.4 Non-Cartesian Geometries

The conventional FDTD uses a staircase-approximation to model non-Cartesian geometries, as shown in Fig. 6.16, and requires the use of a very fine mesh to mitigate the effects of this staircase approximation when dealing with curved objects. This, in turn, makes

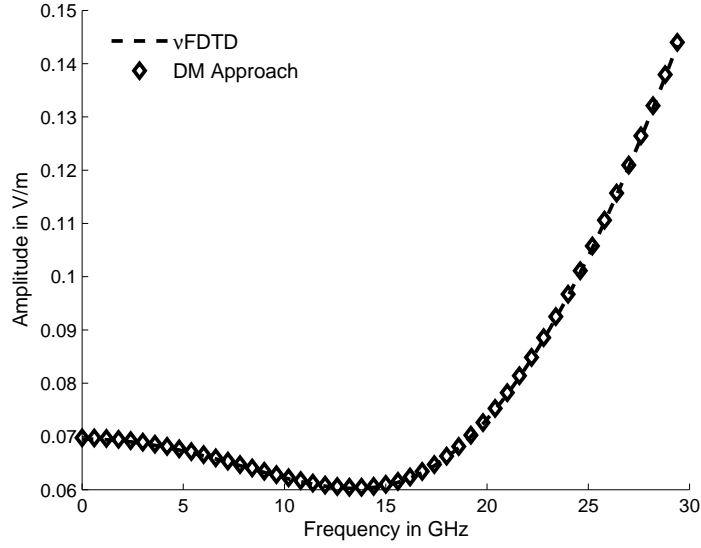


Figure 6.15: Amplitude variation of the scattered E_y at a point with frequencies from 1Hz to 30 GHz.

the simulation computationally expensive, both in terms of memory and CPU time. Even though methods such as FEM and MoM can handle curved geometries with much ease because they do not restrict themselves to a Cartesian type of meshing, often they are not necessarily the most computationally efficient when dealing with inhomogeneous media. Hence, it would be advantageous to modify the existing FDTD algorithm so that it can handle curved geometries, enabling us to conveniently model arbitrary objects, regardless of their material parameters. In the past, a generalization of the conventional FDTD, namely the CFDTD algorithm [24], has been developed for this purpose. In CFDTD, the magnetic field update equations are modified by using the areas of the partially-filled cells, as opposed to those of the entire cells.

To explain the concept, we consider a partially filled cell, shown in Fig. 6.17. The equation for this partially-filled cell is derived by using Farady's law, to get:

$$\oint_{C_1} \vec{E} \cdot d\vec{l} = -\mu \frac{\partial}{\partial t} \int_{S_1} \vec{H} \cdot d\vec{s} \quad (6.1)$$

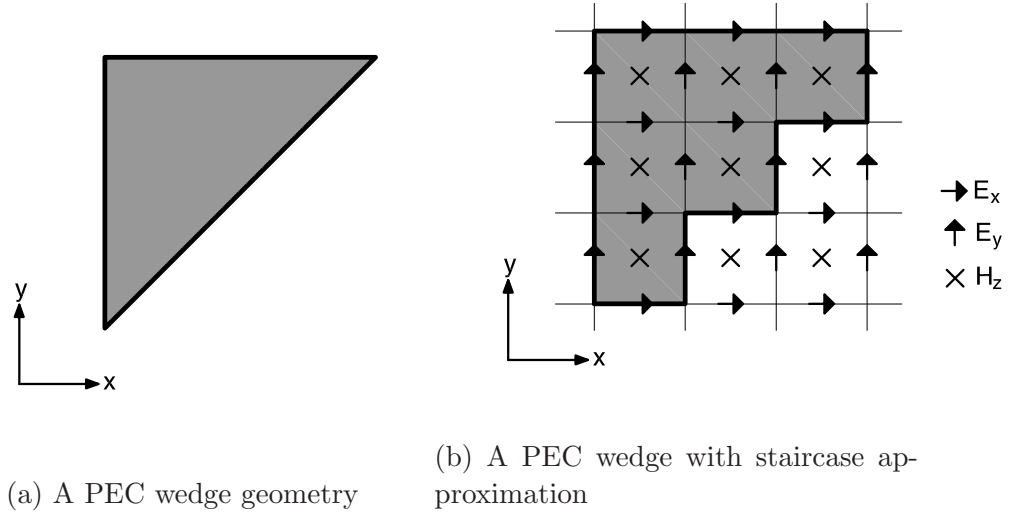


Figure 6.16: Meshing of a non-Cartesian geometry by the conventional FDTD

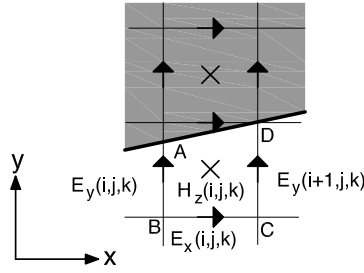


Figure 6.17: A partially-filled cell.

where C_1 is the loop ABCDA and S_1 is the area enclosed by loop C_1 . Upon discretizing this equation, we obtain:

$$H_z^{n+\frac{1}{2}}(i, j, k) = H_z^{n-\frac{1}{2}}(i, j, k) - \frac{dt}{\mu S_1} [-E_y^n(i, j, k) \cdot l_{AB} + E_x^n(i, j, k) \cdot dh + E_y^n(i+1, j, k) \cdot l_{CD}] \quad (6.2)$$

The update magnetic equation for the partially-filled cell is shown above in (6.2). But, as $S_1 \rightarrow 0$, this modified update equation becomes unstable since, as we see from

(6.2), the expression for the updated H contains S_1 in the denominator. The update equation can be modified to circumvent this instability problem that arises when the partial area is small, albeit at the cost of compromising the accuracy. Hence, in order to improve the accuracy, we propose two new approaches to handling the non-Cartesian geometries.

6.4.1 Asymptotic Method

In this asymptotic type of implementation, the field values as opposed to the update equations, are modified by using the local field solution. The proposed new technique is described below:

- For the partially filled cells with a fill factor $\leq 50\%$, the E -fields are updated by using the H -fields calculated by using the modified CFDTD equation given in (6.2).
- For the partially filled cells with a fill factor $> 50\%$, the E fields are updated by using local solutions generated based on the concepts of reflection or diffraction, rather than by using the H -fields employed in the CFDTD approach.

Because we use the asymptotic method to compute the reflection or diffraction coefficients, the proposed technique requires a “single frequency” simulation. However, this technique can be extended to “DC Gaussian” simulations with a slight modification as described in the next Section 6.4.2. Also, the proposed technique can be extended to dielectrics and inhomogeneous geometries without any modification, while the CFDTD cannot handle either of them without compromising the accuracy.

Let us consider the case of a square PEC sheet whose sides are approximately 4λ (λ referenced at 10 GHz), and are inclined at an angle of 0.72° with respect to the x-axis,

as shown in Fig.6.18. The tilt angle has been chosen to be 0.72° so that the edges of the sheet are offset only by $\pm\lambda/40$ above or below the x-axis, i.e., half the FDTD cell size of $\lambda/20$. We calculate the amplitude variation of the scattered E_x field at a frequency of 10 GHz, when the plate is illuminated by a plane wave, which travels along the negative-y direction and is polarized along x. Fig.6.19 compares the results obtained by using the proposed technique, with those returned by the CFDTD, and by a commercial MoM code, for the same problem. The results generated by using the proposed technique show good agreement with the results from the commercial MoM, while the CFDTD results exhibits spurious ripples in the lit region because of the instability problem encountered in the CFDTD algorithm when the area $S_1 \rightarrow 0$. What is more, this is even true when a fine mesh size of $\frac{\lambda}{160}$ is used in the CFDTD, in contrast to the $\frac{\lambda}{20}$ mesh size used in ν FDTD. Table 6.2, presents a comparison of the mesh size and the memory requirements, and shows that the proposed technique easily out-performs the CFDTD, which still suffers from inaccuracies, even when a very fine mesh is used.

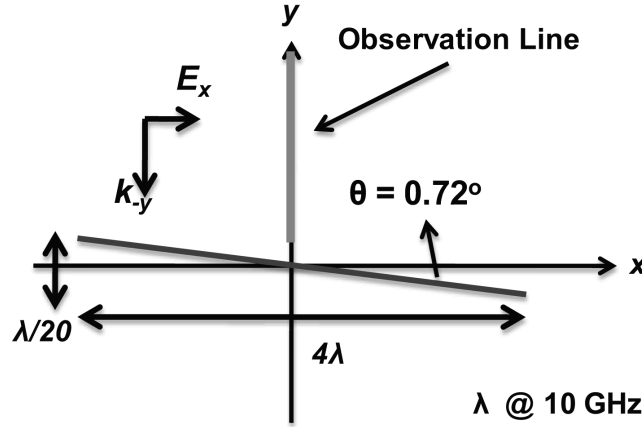


Figure 6.18: A inclined PEC sheet(not to scale).

For the next example, let us change the inclination of the PEC plate in the previous problem from 0.72° to 1.43° . Fig. 6.20 compares the scattered E_x -field calculated by using the ν FDTD/Asymptotic method, with those obtained by using the CFDTD algorithm with a mesh size of $\lambda/160$, and with the commercial MoM code results. We again find

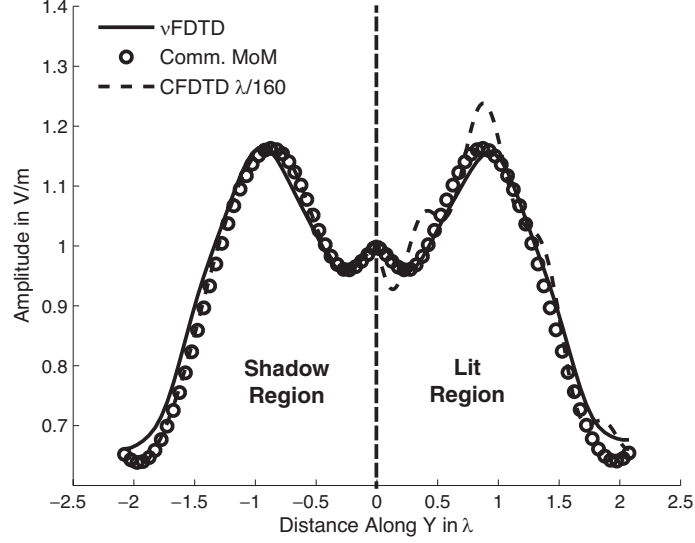


Figure 6.19: Amplitude variation of the scattered E_x with distance along y at 10 GHz.

Table 6.2: Comparison of mesh size and memory required for convergence for PEC geometry shown in Fig. 6.18.

Parameter	ν FDTD	CFDTD ^a
Mesh Size Used	$\frac{\lambda}{20}$	$\frac{\lambda}{160}$
Memory Required	413 MB	31 GB

^a Results still have numerical artifacts

that the results from the ν FDTD match well with those obtained by using the commercial MoM, while the results from the CFDTD show spurious ripples due to the instability problem alluded to above.

For the next example, we consider a faceted PEC surface (see Fig. 6.21) projected length is λ at a frequency of 10 GHz. Fig. 6.22 compares the backscattered E_z -field calculated by using the ν FDTD is compared with those obtained from: (i) the CFDTD with a mesh size of $\lambda/20$; (ii) a commercial MoM code; and (iii) a commercial FEM. Again we find that the results calculated by using the ν FDTD compares well with those

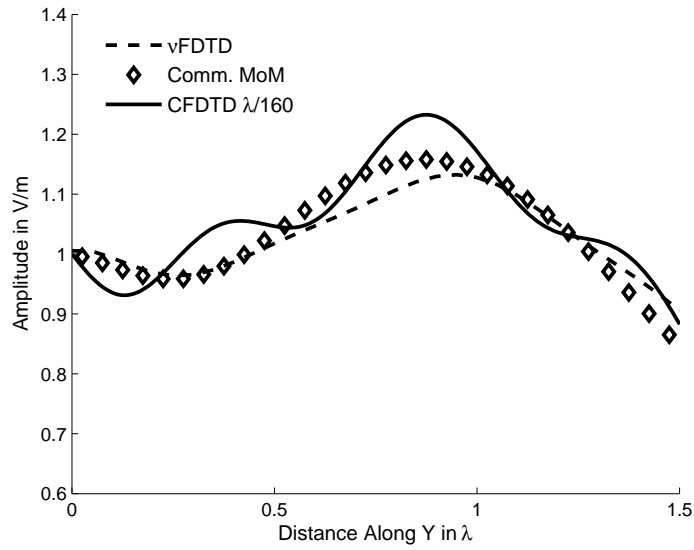


Figure 6.20: Amplitude variation of the scattered E_x with distance along y at 10 GHz.

obtained from the commercial MoM code, while the results from the commercial FEM code shows numerical artifacts.

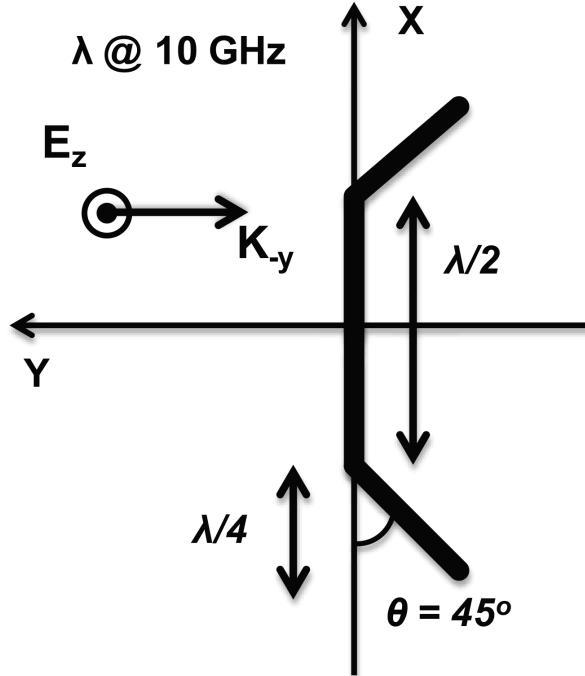


Figure 6.21: A faceted PEC surface (not to scale).

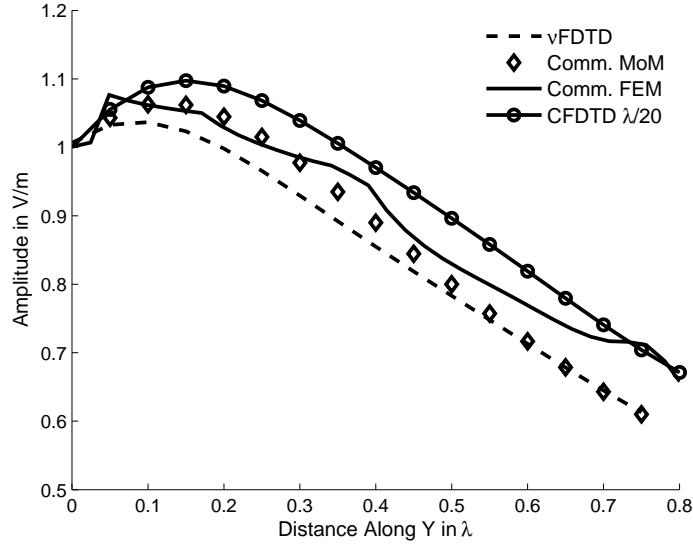


Figure 6.22: Amplitude variation of the backscattered E_z with distance along y at 10 GHz.

For the next example, let us consider a PEC wedge of side length 4λ , as shown in Fig. 6.23. Fig. 6.24 plots the scattered field at a frequency of 10 GHz along the specular direction, obtained by using ν FDTD, and compares them with those obtained by using the CFDTD with a mesh size of $\lambda/50$; with a commercial MoM code; and, with a commercial FEM code. We find a good comparison between the scattered fields calculated by using the ν FDTD with those obtained from the commercial MoM code, while the results from the CFDTD and the commercial FEM codes show spurious ripples.

For our next example, we consider a finite PEC cylinder, as shown in the Fig. 6.25, with a height of $21\lambda/20$ at a frequency of 10 GHz, for the next example. In order to calculate the field in the asymptotic limit in the ν FDTD method, we use the fields scattered by an infinite PEC sheet multiplied by the factor f , defined in (6.3)

$$f = \sqrt{\frac{a'}{r}} \quad (6.3)$$

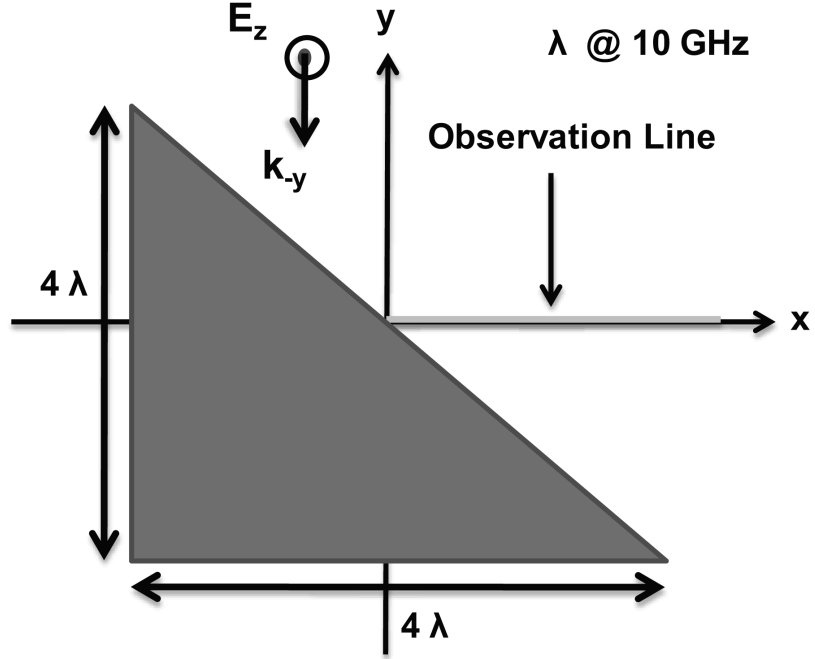


Figure 6.23: A PEC wedge.

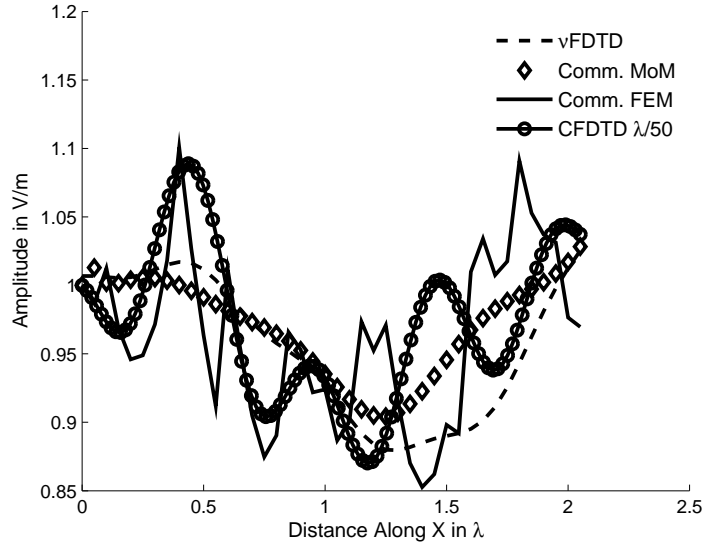


Figure 6.24: Amplitude variation of the scattered E_z with distance along x at 10 GHz.

where a' is the effective phase center and r is the distance of the observation point from the effective phase center. Wide range of numerical experiments have shown that this effective phase center for a PEC cylinder is always $0.5a$, where a is the radius of the cylinder.

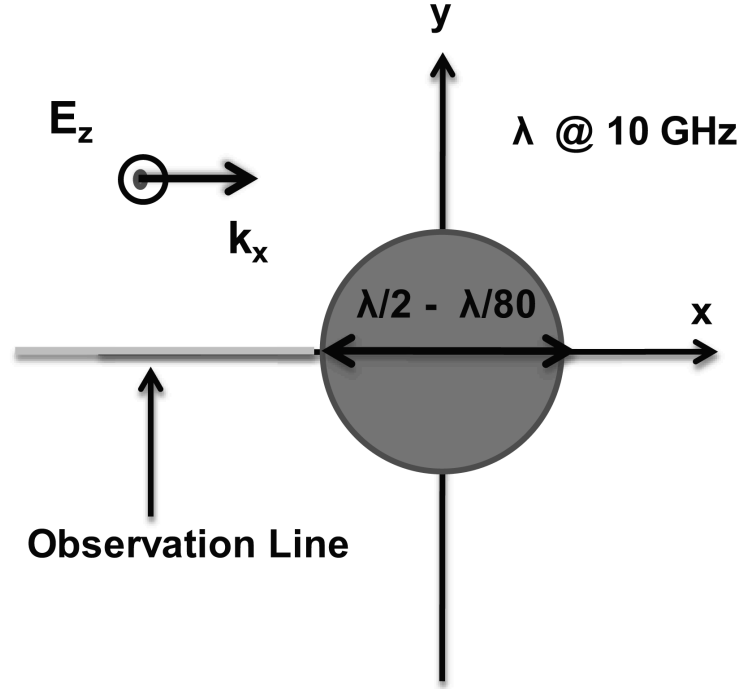


Figure 6.25: A PEC cylinder.

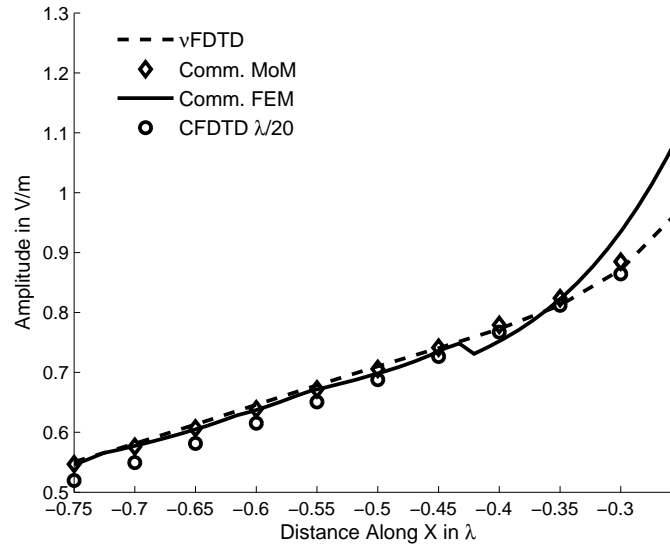


Figure 6.26: Amplitude variation of the backscattered E_z with distance along x at 10 GHz.

Fig. 6.26 compares the backscattered E_z -fields calculated by using the ν FDTD with those obtained from the CFDTD with a mesh size of $\lambda/20$; with a commercial MoM code; and, with a commercial FEM code. We find that the fields calculated by using the ν FDTD

shows good comparison with those obtained by using the commercial MoM solver. The results calculated using the commercial FEM shows numerical artifacts and the CFDTD does not generate the correct scattered field on the surface of the cylinder; however the ν FDTD is able to solve this problem with good accuracy.

While modeling dielectric objects using the CFDTD approach, the partially-filled cells are smeared an average dielectric constant over the entire volume of the cell. The asymptotic method proposed here can be used as an alternative, to model dielectric objects without any modifications, and with better accuracy than that of the CFDTD method. As an example, let us consider the dielectric slab of thickness $\lambda/8$ at a frequency of 10 GHz, with $\epsilon_r = 4.2$ as shown in Fig. 6.27. Fig. 6.28 compares the backscattered E_z -field calculated by using the ν FDTD with those generated by using the CFDTD, and with the commercial FEM code. We find that the results generated by using the commercial FEM and CFDTD codes show spurious ripples, while the those from the ν FDTD have a smooth behavior, which is realistic.

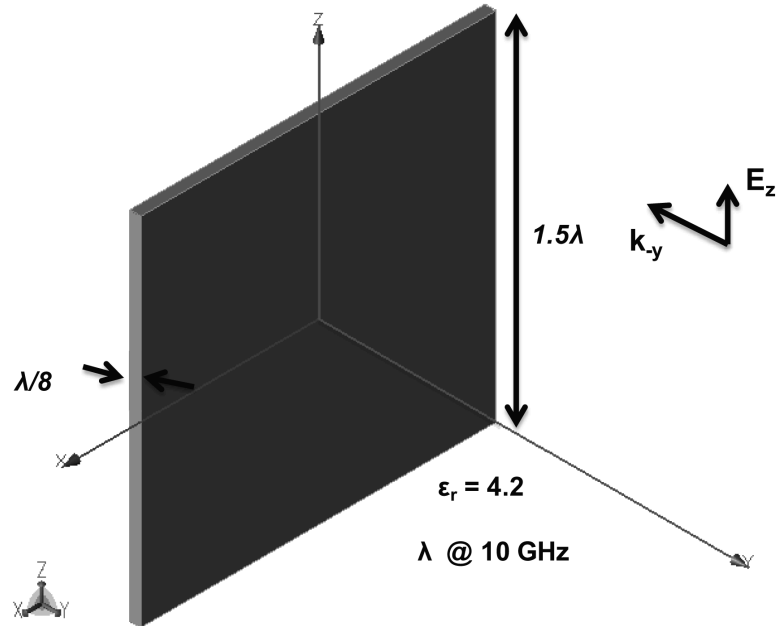


Figure 6.27: A dielectric slab (not to scale).

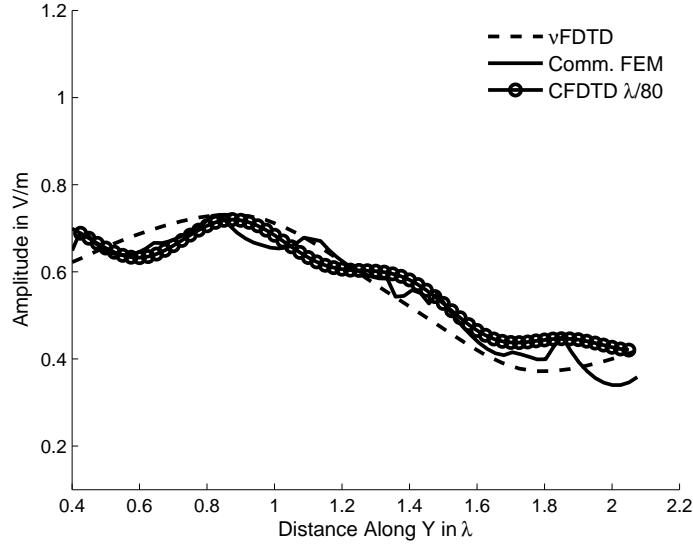


Figure 6.28: Amplitude variation of the backscattered E_z with distance along y at 10 GHz.

In order to demonstrate the efficacy of the ν FDTD method, we vary the thickness of the slab, and choose it to be $9\lambda/80$, $10\lambda/80$ and $11\lambda/80$ at a frequency of 10 GHz. We calculate the phase variation at $y = \lambda/40$ and plot it in Fig. 6.29, which shows the comparison of the phase variation against the thickness, generated by using the infinite slab analytical expression; the CFDTD; and a commercial FEM code. We find that the results calculated by using the ν FDTD compares well with those obtained from the analytical expressions for the infinite slab, while the results generated by using the other methods deviate from the analytical results.

6.4.2 Averaging Technique

As mentioned earlier in Section 6.4.1, the proposed ν FDTD technique requires a “single frequency” simulation because we use the asymptotic limit to compute the reflection or diffraction coefficients. In this section we describe a modified approach in which we use the “DC Gaussian” simulation that enables us to generate results for a wide range of

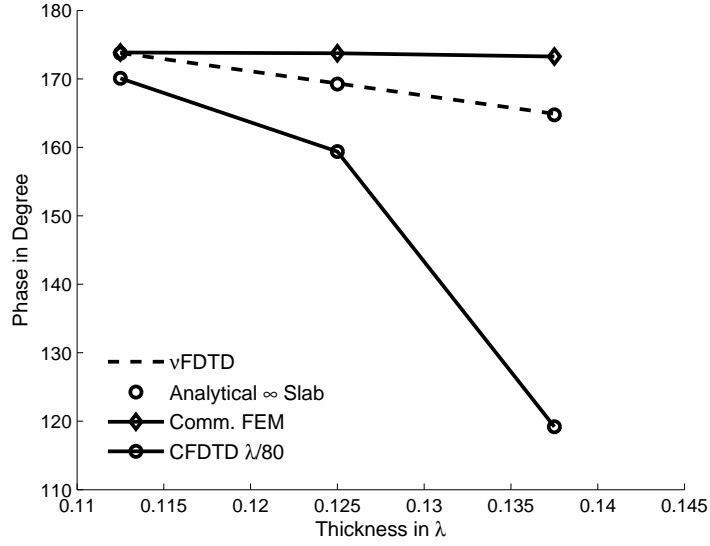


Figure 6.29: Phase variation of the backscattered E_z at $y = \lambda/40$.

frequencies. In order to demonstrate the usefulness of this approach, we consider the example of a rectangular cylinder of height 4λ at a frequency of 10 GHz, which has mitered corners as shown in Fig. 6.30. The problem is handled in three steps as shown in Fig. 6.31 and we use scattered field type of formulation in all of these steps. Even though it shows three steps, it is important to note the fact that we need only two simulations as the calculation of the scattered field in step 2, is trivial using the boundary condition. The simulation for the first step does not call for any modifications to the FDTD algorithm. However, for the third step we need to modify the field value at the nodes of the partially filled cells by using the weighted average of the fields at these nodes, obtained from steps 1 and 2, based on the partially filled space in the actual geometry.

Fig. 6.32 compares the backscattered E_y -fields calculated by using the ν FDTD, and with those generated by using the commercial MoM code and the comparison is seen to be good. For the next example, we consider the faceted PEC geometry shown in Fig. 6.33, whose projected footprint is 4λ at a frequency of 10 GHz. Fig. 6.34 compares the backscattered E_y -field, calculated by using the ν FDTD/Averaging technique, and with

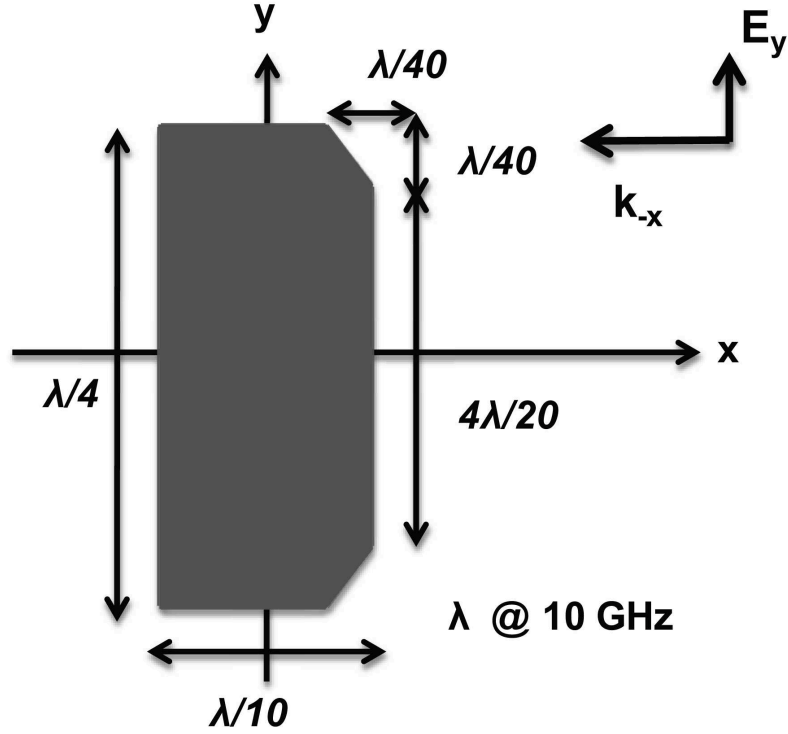


Figure 6.30: A PEC rectangular cylinder with mitered corner.

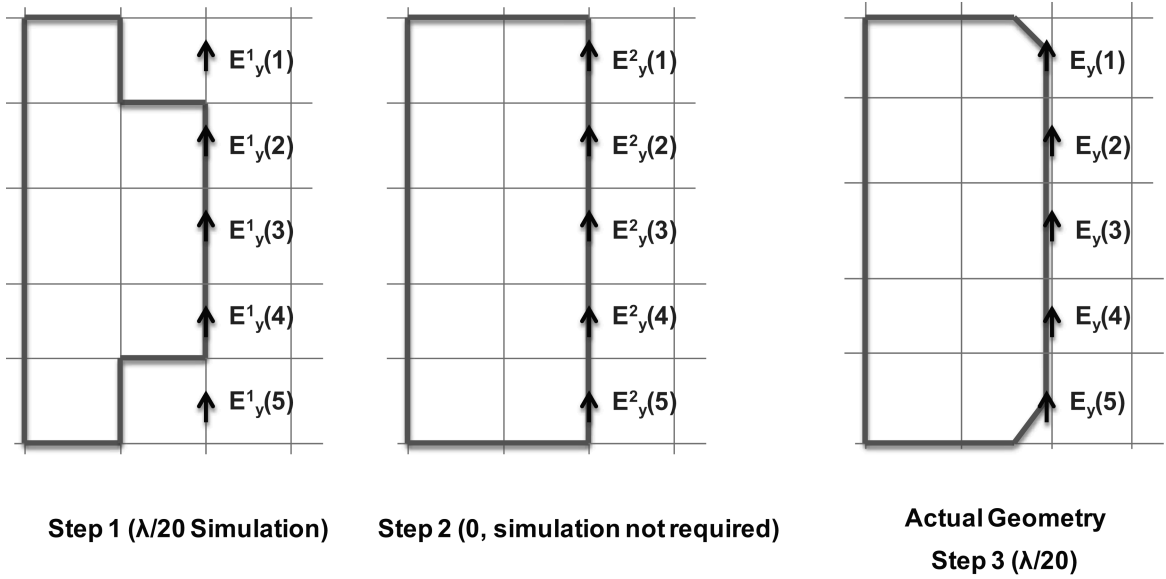


Figure 6.31: Principle behind the averaging technique.

those obtained from a commercial MoM solver. From Fig. 6.34, we find that the solution generated by using the commercial MoM code shows a spurious spike near the surface of

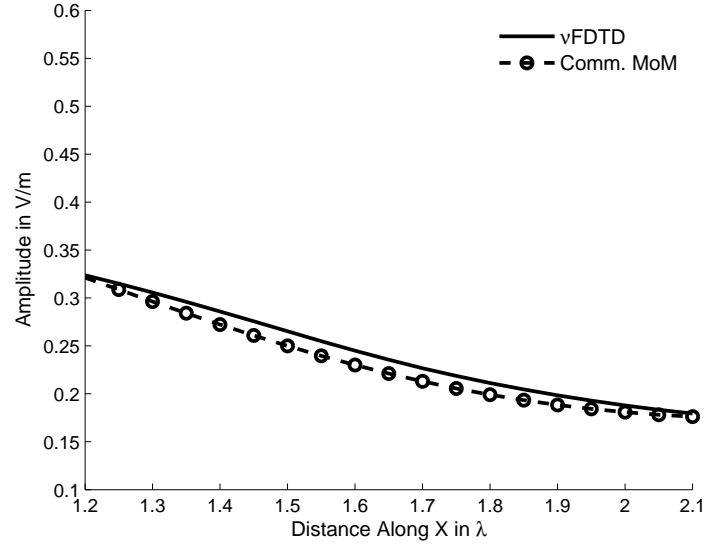


Figure 6.32: Amplitude variation of the backscattered E_y with distance along x at 10 GHz.

the geometry, while the ν FDTD results are smooth.

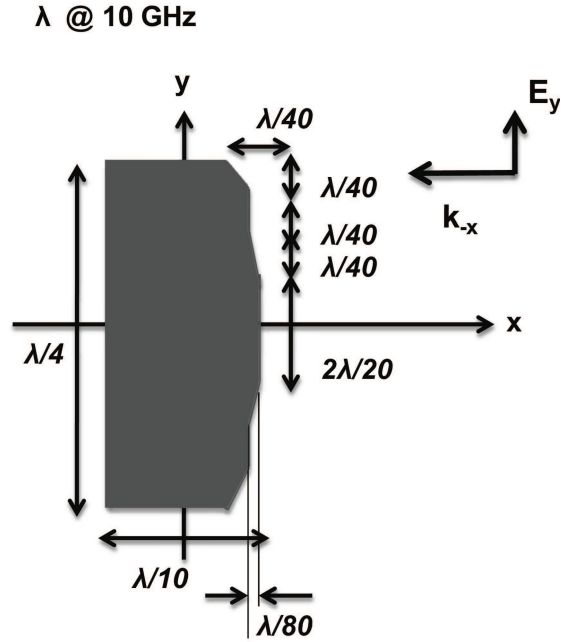


Figure 6.33: A faceted PEC geometry (not to scale).

For the last example, we consider a curved PEC surface of height 4λ at a frequency of 10 GHz, as shown in Fig. 6.35. Fig. 6.36 compares the scattered E_y -fields calculated

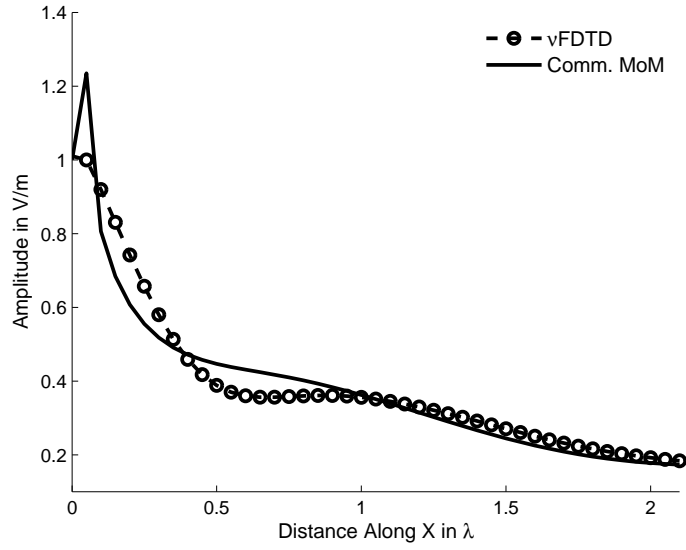


Figure 6.34: Amplitude variation of the backscattered E_y with distance along x at 10 GHz.

by using the ν FDTD method, and with those from a commercial MoM code, and once again we find that the comparison is good.

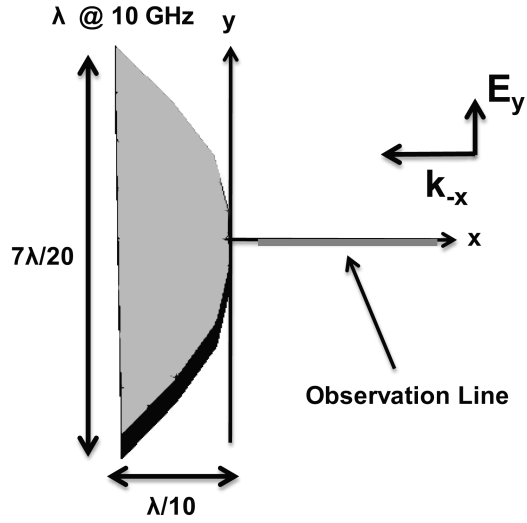


Figure 6.35: A curved PEC surface (with a height of 4λ).

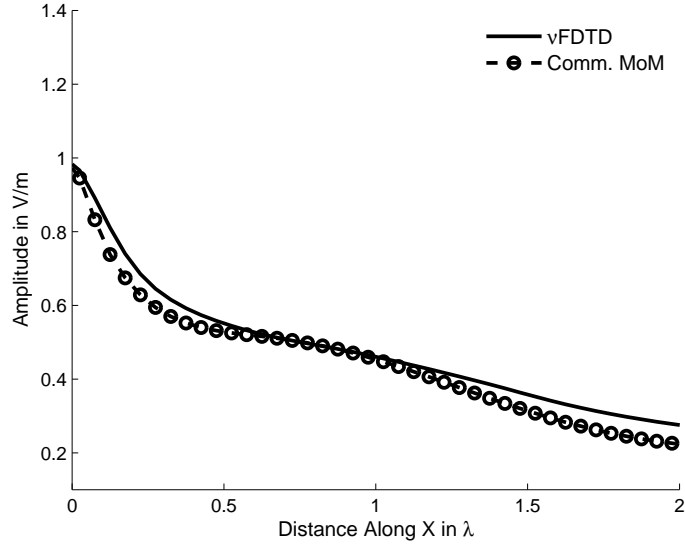


Figure 6.36: Amplitude variation of the scattered E_y at 10 GHz.

6.4.3 Advantages

Below, we summarize some of the advantages of the proposed method. They are:

- (a) Usable for *arbitrary geometries*, even if the surfaces do not coincide with the Cartesian mesh, e.g., thin sheets, with or without a slant.
- (b) More accurate than the conventional Conformal FDTD.
- (c) Retains $\lambda/20$ cell size even for thin, slanted and curved bodies, offering memory advantage and computational efficiency over conventional conformal FDTD.
- (d) Free of instability problems even when the fractional area of the partially filled cell is very small, even when it tends to zero.
- (e) Can be extended to dielectric objects, with just a few modifications.

6.5 Multiscale Problems

In order to handle multiscale problems, we appeal to the ideas of the hybrid RUFD approach described in the Chapter 5. Since the ν FDTD method is a time domain technique, it has the possibility to generate results over a wide band of frequencies from a single simulation run, which is not the case with the RUFD approach. In ν FDTD we can handle multiscale problems in three different ways, based of the dimension and the complexity of the small objects involved in the problem. All the three approaches begin by identifying a smaller region around the small object, as shown in Fig. 6.38, for the test problem in Fig. 6.37. The test problem consist of a small dipole of length $\lambda/100$ polarized along the \hat{x} direction, and operating at 10 GHz. In order to model this problem by using the conventional FDTD, we need a cell size of at least $\lambda/200$ and it becomes computationally expensive when we choose such a small cell size. Here we propose hybrid techniques to alleviate this problem.

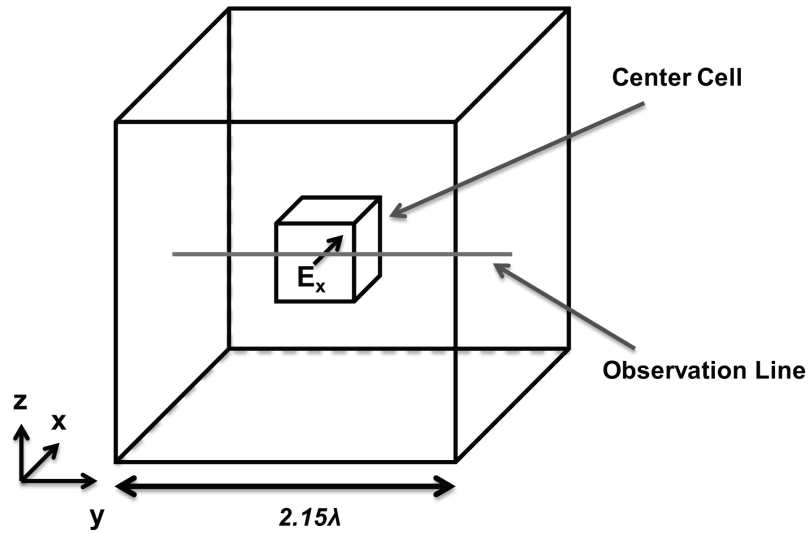


Figure 6.37: A computational domain with small dipole.

Since in this test case the dipole is very small compared to the operating wavelength, we can use the quasi-static dipole moment approach described in Section 2.6. The fields generated by the quasi-static formulation is always real and can be directly interfaced with

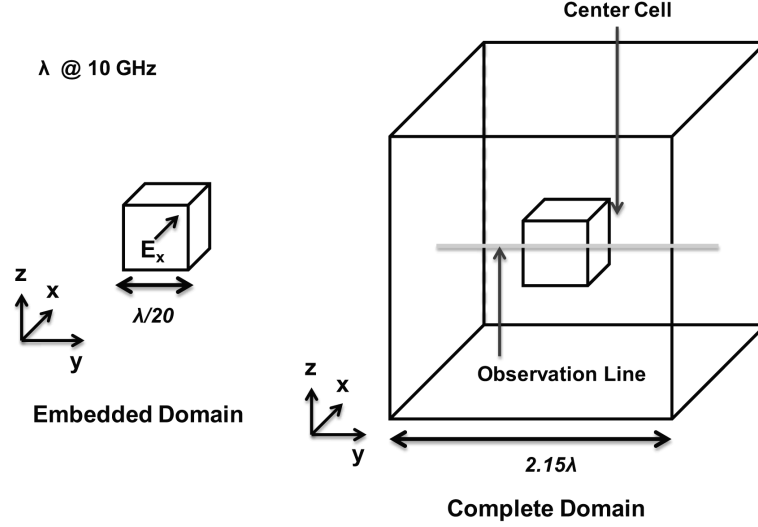


Figure 6.38: Approach handling for multiscale problems in FDTD.

the coarse-grid FDTD algorithm. When the size of the object becomes electrically large, the fields generated by the dipole moment approach will no longer be real. Hence for this case, we can turn to the “single frequency” version of the coarse-grid FDTD simulation.

Another alternate approach to handling this situation is to adapt the RUFD/multi-grid approach, described in earlier Section 5.5. The main advantage of using the multi-grid approach with the FDTD algorithm is that we can generate results for a wide range of frequencies from a single simulation run, even when modeling electrically large objects. The cell size for the embedded fine-mesh domain is chosen such that it is a fraction of the cell size used in the coarse-grid simulation, to ensure a smooth interface between the simulations by making the time step used in these simulations as an multiple of each other. The test problem was solved by using the three different approaches described above and the calculated radiated E_x -field is compared in Fig. 6.39 with those obtained from the analytical expression. We used a cell size of $\lambda/20$ for coarse grid simulations in all the three hybrid approaches, and all the three approaches were found to be unconditionally stable. The embedded fine-mesh domain was modeled by using a cell size of $\lambda/400$ in the multi-grid approach. Fig. 6.39 shows that the results calculated by using the different

hybrid approaches match well with each other, and with those obtained from the analytical expression.

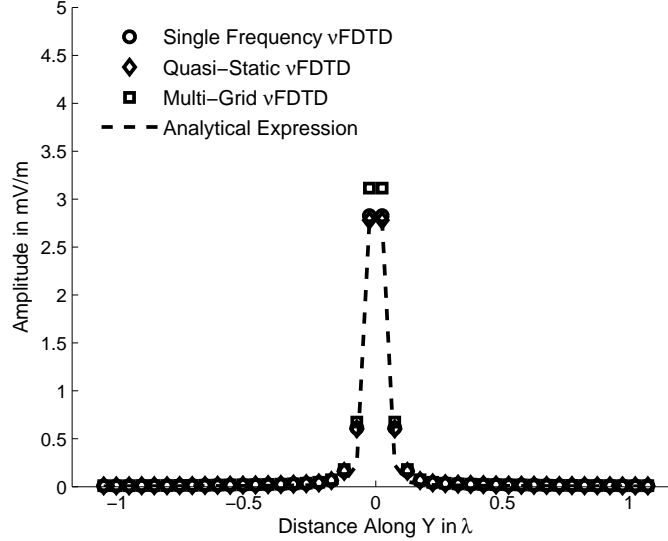


Figure 6.39: Amplitude variation of the radiated E_x at 10 GHz.

6.6 Performance Enhancement

In this section we introduce ways to further enhance the computational efficiency of the ν FDTD algorithm without compromising its accuracy.

6.6.1 Signal Processing Techniques

In this section we show how time advantage can be gained by using signal processing to determine where to terminate the FDTD simulations by checking its convergence in the frequency domain instead of in the time domain. Consider a multi-layer problem shown in Fig. 6.40, which is infinite extent along the \hat{y} and \hat{z} direction. It consists of a foam layer, with $\epsilon_r = 1.08$, loss tangent = 0.007, and a thickness of $\lambda/50$ at a frequency of 400 MHz,

sandwiched between the E-Glass layers ($\epsilon_r = 3.95$, loss tangent = 0.012 and a thickness of $\lambda/1250$ at a frequency of 400 MHz). The problem was modeled by using the conventional FDTD with periodic boundary conditions to render it finite. Fig. 6.41 shows the time signature at the origin generated by using the conventional FDTD and shows that the signature is ringing even after 200,000 time steps. Fig. 6.42 shows the variation of the transmitted E_y -fields at the origin in the frequency range of 3 to 450 MHz, calculated by using the conventional FDTD and compared with those obtained from the ν FDTD. Table 6.3 compares the number of time steps required in these two approaches.

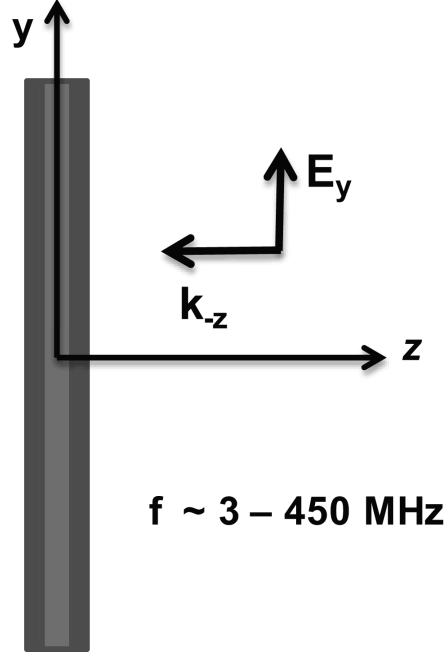


Figure 6.40: A multilayer problem (not to scale).

Table 6.3: Comparison of time steps required by conventional FDTD and ν FDTD for the multilayer problem shown in Fig.6.40.

Frequency	Conventional FDTD	ν FDTD
3 MHz	200000 steps ^a	4000 steps

^a Time signature yet to converge

We find, from Fig. 6.42 and Table 6.3, that the ν FDTD is more accurate, especially

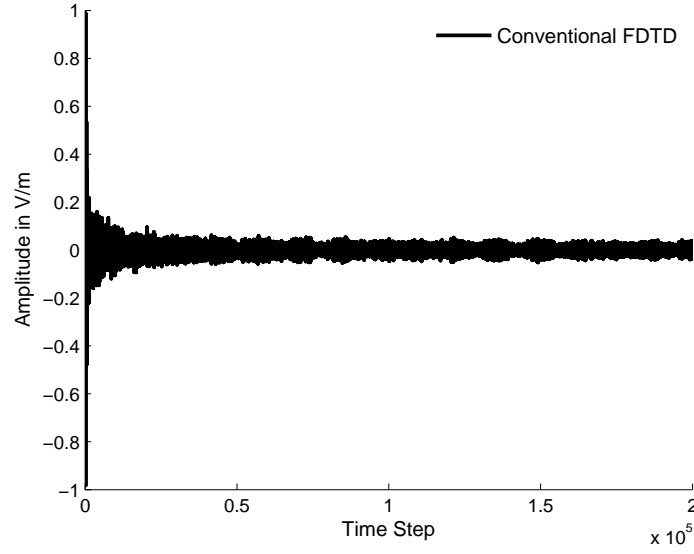


Figure 6.41: Time signature at the origin from the conventional FDTD for the multilayer problem shown in Fig. 6.40.

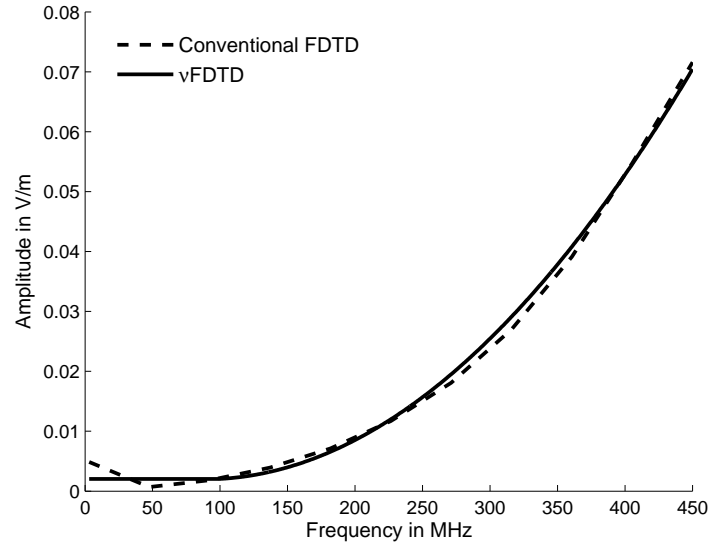


Figure 6.42: Frequency variation of the transmitted field E_y amplitude at the origin for the multilayer problem shown in Fig. 6.40.

at the lower end of the frequency range and is also computationally more efficient when compared to the conventional FDTD. It is important to note the fact we are able to generate the solution for the entire frequency range of interest using the ν FDTD, with a single simulation run of 4000 time steps.

6.6.2 Absorbing Boundary Condition

Another important factor that affects the accuracy and efficiency of the FDTD simulations is the boundary conditions used to truncate the computational domain. Even though there are many boundary conditions that can be used, for mesh truncation, the most widely used and effective one is the Convolutional Perfectly Matched Layer, or more commonly known as CPML [19]. Even though the CPML is effective, it is computationally expensive. It is possible to reduce the computational expense, with little loss of accuracy, by using a new algorithm, which is based on the impedance boundary condition (IBC). Here the tangential E-Fields at the end of the computational domain are calculated from the H-fields based on the impedance relationship:

$$E_{tan} = \eta \cos \theta \hat{n} \times \vec{H} \quad (6.4)$$

where η is the intrinsic impedance of the medium and θ is the incident angle. However, from many experiments we have found that the use of either η or $\eta \cos \theta$ has little effect on the accuracy of the simulation. In the proposed approach, the H-fields at the boundaries of the computational domain are still updated by using the conventional FDTD update equations, while the E-fields are derived by using the IBC. In order to ensure that the algorithm is unconditionally stable we use 90% of the Courant condition to determine the time step.

To study the frequency characteristics of the IBC, we consider a 2D computational domain, as shown in Fig. 6.43. We use a point source for excitation, with a frequency of 1 GHz, and locate it at the center of the domain. Fig. 6.44 shows the variation of field at the observation point *A* in the frequency range of 300 MHz to 1 GHz, calculated by using the ν FDTD/IBC, and compares it with those obtained by using the ν FDTD/CPML, and the comparison is seen to be good. However, the IBC approach is computationally

inexpensive, when compared to the CPML, and the time advantage of the ν FDTD/IBC over the CPML is a factor of 2 for this example. We should mention that this advantage would be considerably higher for 3D problems.

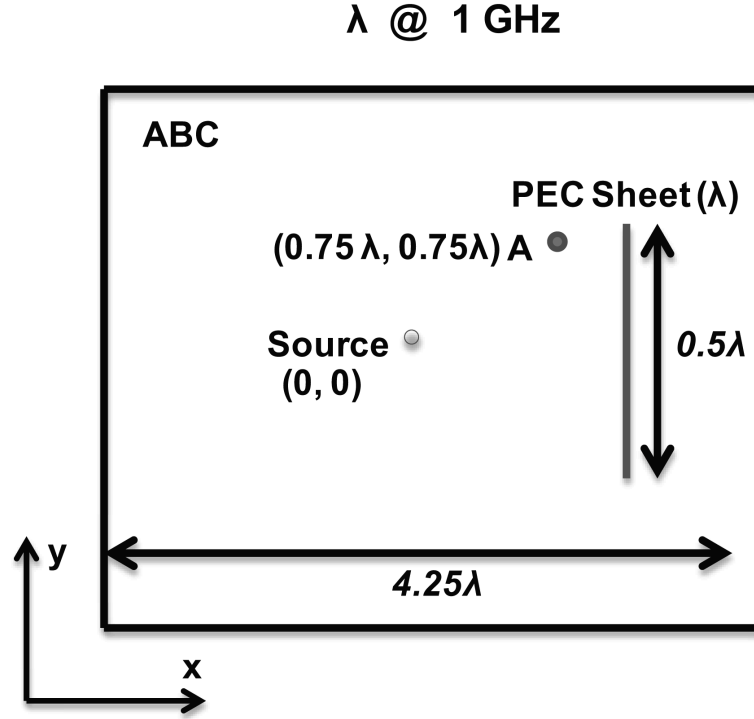


Figure 6.43: A 2D computational domain.

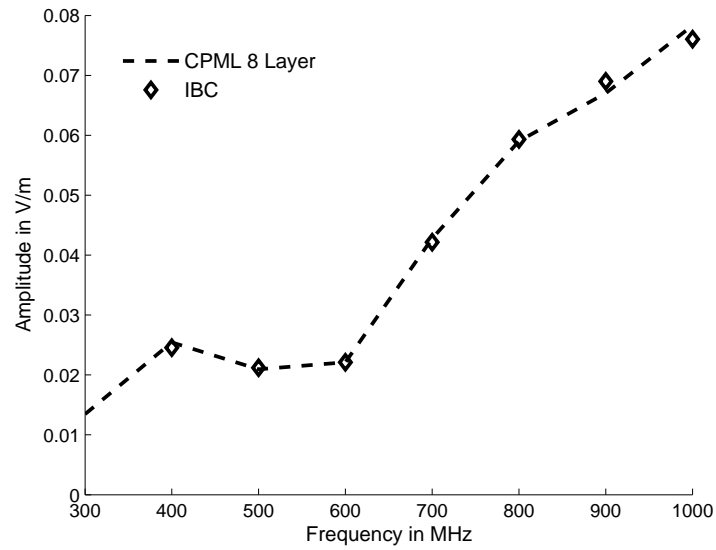


Figure 6.44: Frequency variation of the E_y -field amplitude at point A shown in Fig. 6.43.

Next we study the effect of the proximity of the ABC for a 2D computational domain, shown in Fig. 6.45, at a frequency of 1 GHz. Fig. 6.46 compares the E_y -field at point A for different dimensions of the computational domain, calculated by using: (i) the ν FDTD with IBC with angle dependence as in (6.4); (ii) without angle dependence, assuming the incidence to be normal at all points on the boundary; and, (iii) using ν FDTD/CPML with 8 layers. Fig. 6.46 shows good comparison between the results calculated from these three approaches and we also find that ignoring the angle dependence has little effect on the accuracy much.

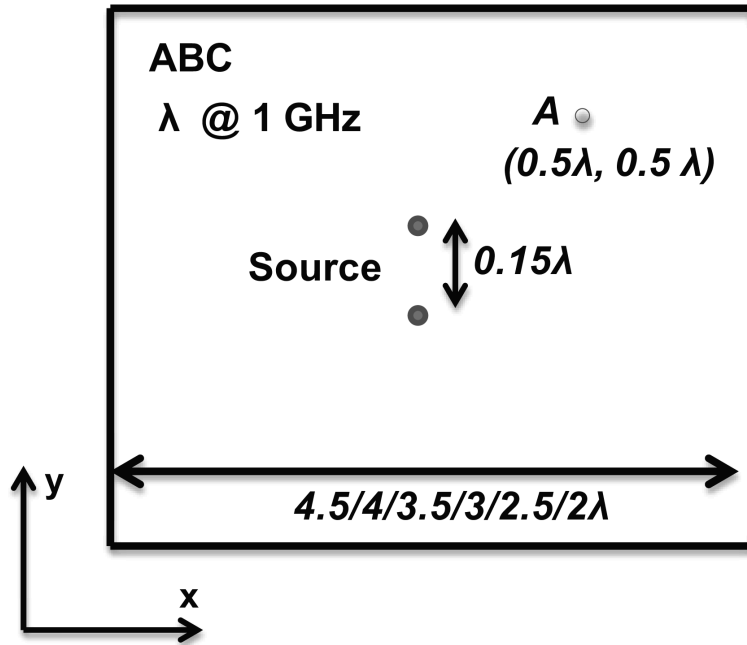


Figure 6.45: A 2D computational domain.

The results presented in Figs. 6.48 and 6.49 for the dipole geometry (see Fig. 6.47) illustrate the accuracy of the proposed algorithm, which requires much less CPU time and memory than those required by the CPML. However, work is still in progress to further improve the accuracy of the proposed boundary condition and to test its applicability to a wider class of problems.

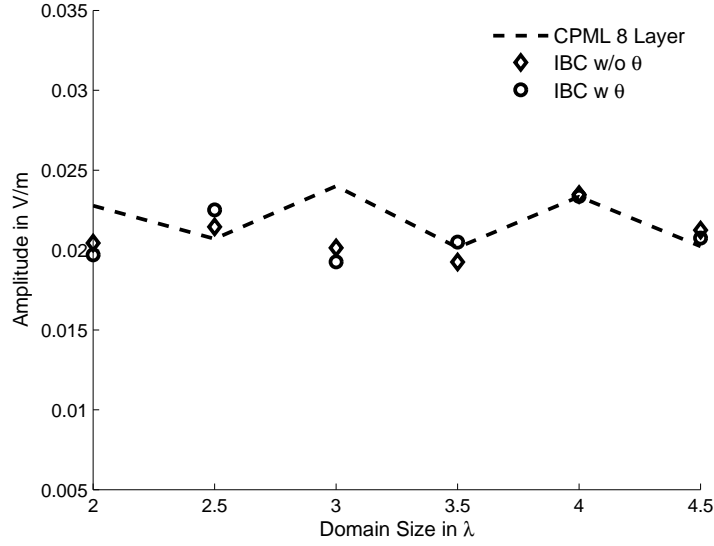


Figure 6.46: Amplitude variation of the E_y -field at observation point A, for different domain sizes for the problem shown in Fig. 6.45.

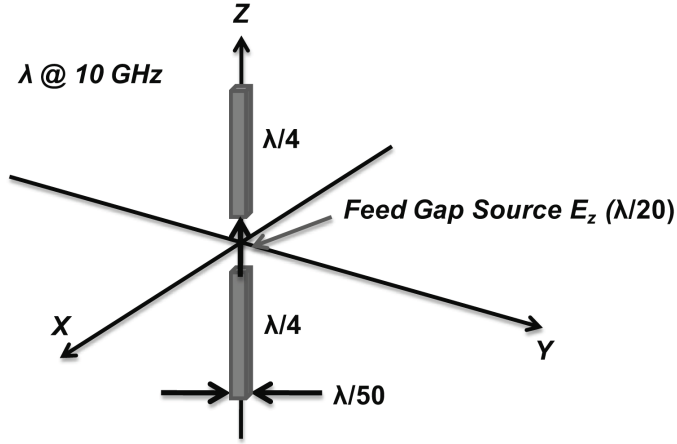


Figure 6.47: Geometry of a PEC dipole (not to scale).

6.6.3 Well-Logging Applications

Another area of interest in which ν FDTD is found to outperform the conventional CEM algorithms is well-logging application. Consider the stratified medium, shown in Fig. 6.50, whose geometry is typical for the case of well logging problems. The frequency range of interest is typically 1 KHz to 1 MHz. Fig. 6.51 shows the incident pulse received at the observation point, while Fig. 6.52 shows the reflected pulse from the interface received at

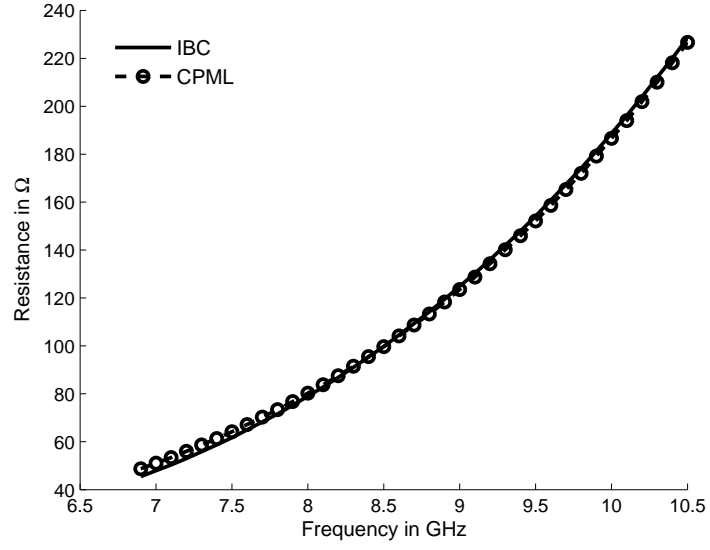


Figure 6.48: Variation of input resistance with frequency for the PEC dipole.

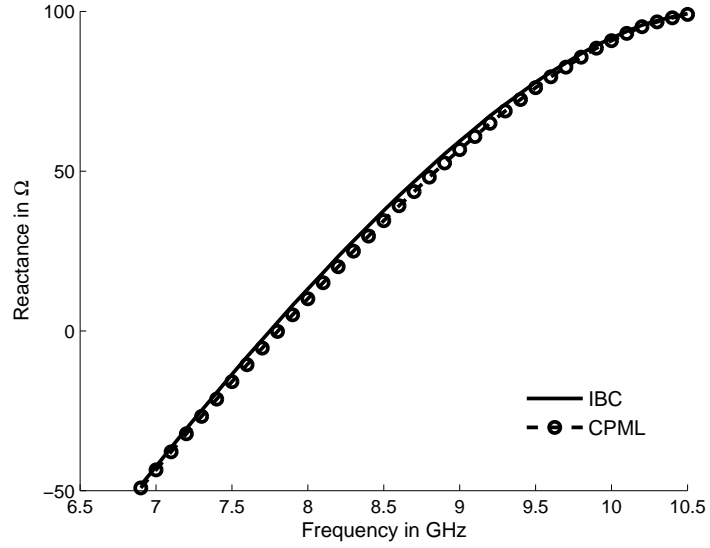


Figure 6.49: Variation of input reactance with frequency for the PEC dipole.

the observation point calculated by using the ν FDTD. At the low frequencies of interest in this problem, commercial solvers are typically unable to handle the problem, while the ν FDTD is able to analyze it with ease without requiring any modifications.

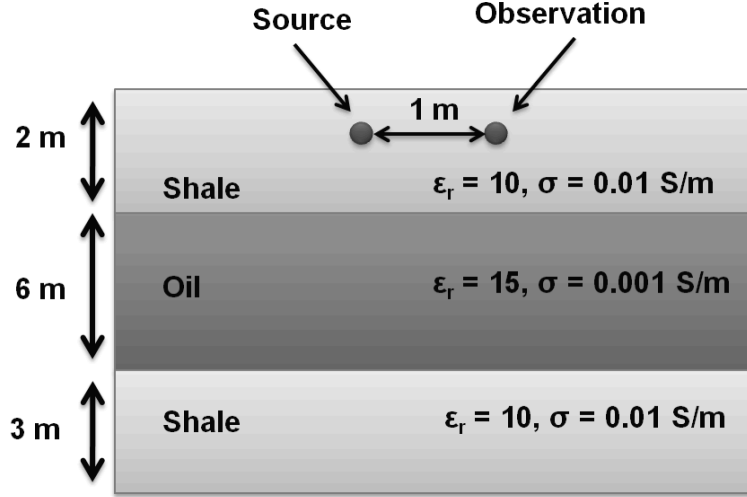


Figure 6.50: Geometry of a stratified medium with oil (not to scale).

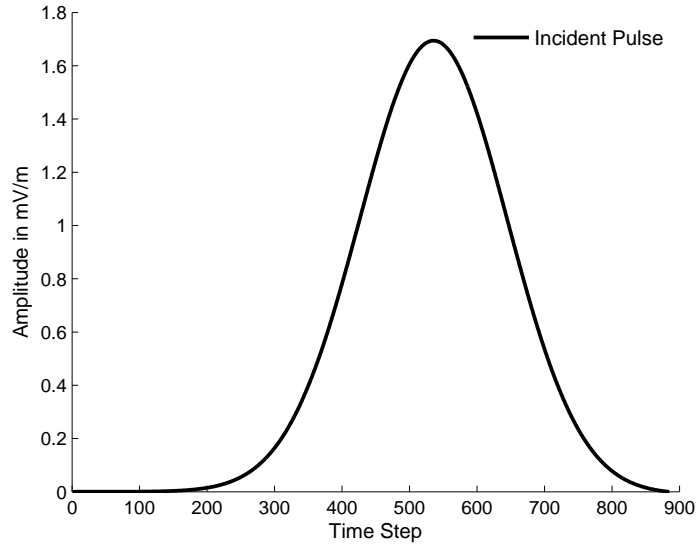


Figure 6.51: Variation of E_x component of the incident pulse.

6.7 Observations and Conclusions

In this chapter, we have introduced the ν FDTD solver, which is a blend of time and frequency domain techniques that can generate accurate electromagnetic responses at low frequencies; handle non-Cartesian geometries accurately without any instability issues that are often encountered in the conventional CFDTD; model multi-scale geometries

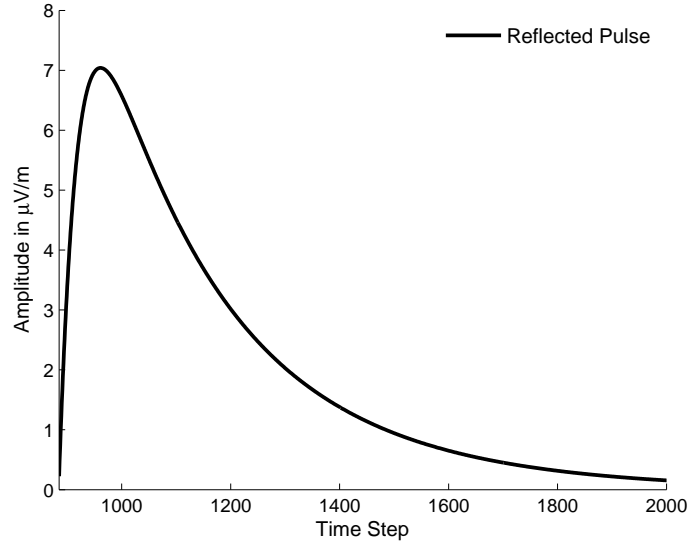


Figure 6.52: Variation of E_x component of the reflected pulse.

accurately; and, handle lossy/lossless thin structures with ease. In all the cases for which we have carried out comparison studies with the existing algorithms and commercial codes, the ν FDTD was not only accurate but also computationally the most efficient. We have also introduced a new boundary condition for the mesh truncation, which is numerically efficient both, from the points of view of CPU time and memory as compared to the widely used CPML algorithm, without a noticeable compromise in the relative accuracy of the computed results. We have also pointed out that the ν FDTD is able to handle low-frequency problems, such as well-logging, that are typically computationally expensive not only because of the large problem size, but also because of low frequency range of interest, often beyond the capability of existing commercial solvers. Finally, since ν FDTD builds on the conventional FDTD to solve different types of problems, its performance can be further enhanced by parallelizing the algorithm [19], which can be carried out as easily as in the case of the conventional FDTD.

7. Conclusions and Future Work

The objective of the thesis has been to address some of issues encountered in computational electromagnetics. In Chapter 2, we have presented a new physics-based approach for formulating MoM problems that is based on the use of dipole moments (DMs), as opposed to the conventional Green's functions. We have shown that there are no singularities that we need to be concerned with in the DM formulation. Yet another salutary feature of the DM approach is its ability to handle thin and lossy structures, whether they are metallic, dielectric-type, or even combinations thereof. The technique is valid over the entire frequency range, from low to high, and it does not require the use of loop-star or other special types of basis functions in order to mitigate the low frequency problem.

In Chapter 3, we have introduced certain refinements to the DM method to improve its computational efficiency. We have shown that the use of higher-order basis functions significantly reduces the number of unknowns, without compromising the accuracy and combines the DM with the CBFM technique helps reduce this number even further. The use of closed-form expressions for the interaction matrix elements speeds up the process of matrix generation, regardless of the problem size. Towards this end, future work is required to extend the closed-form expressions for modeling dielectric and inhomogeneous objects. For electrically large problems, employing FMG helps to speed up the interaction matrix generation considerably. We have shown how we can incorporate lumped loads in the DM approach and that it is able to capture sharp resonances even at low frequencies,

where the commercial solvers become inaccurate, or break down. The DM approach is able to accurately calculate the input impedance of small antennas; fields from irregular geometries; from faceted surfaces; from geometries with slot and slit; and, is able to model microstrip line type of geometries with fine features.

Chapter 4 introduced the RUFD algorithm which is highly parallelizable and its meshing requirements are relatively simple. Moreover, since RUFD solves the Maxwell's equations in a recursive manner, without using either iteration or inversion, the problems of dealing with ill-conditioned matrices, or constructing robust pre-conditioners are totally avoided. Also, as a frequency domain solver, it can handle dispersive media, including plasmonics, relatively easily without any need for Drude or Debye model as required in the FDTD algorithm. A number of techniques have been introduced to further enhance the performance of the RUFD, such as: (i) frequency interpolation schemes to generate the initial values of the fields in the entire computational domain; (ii) introducing losses in the computational domain; and, (iii) post-processing methods, which speed up the convergence significantly.

In Chapter 5, we have shown how the DM approach and the RUFD algorithm may be combined to solve multiscale problems accurately and efficiently, and the performance of the resulting hybrid scheme has been shown to be superior to those of some of the well known and widely used CEM codes, both in terms of accuracy and computational efficiency. We have also introduced multi-grid approach where a part of the computational domain is finely meshed when compared to the rest of the domain. We have shown with many illustrative examples, how to hybridize both the DM approach and the multi-grid approach with RUFD algorithm to solve fine featured multiscale problems efficiently.

In Chapter 6, we have introduced the ν FDTD, which uses the RUFD as a stepping stone to obtain a new improved version of the FDTD. Using many illustrative examples,

ν FDTD has been shown to generate accurate electromagnetic responses at low frequencies; handle non-Cartesian geometries accurately without any instability issues that are often encountered in the conventional CFDTD; model multi-scale geometries accurately; and, handle lossy/lossless thin structures with ease. We have also introduced a new boundary condition for the mesh truncation, which is numerically efficient, both from the points of view of CPU time and memory, as compared to the widely used CPML algorithm, without a noticeable compromise in the relative accuracy of the computed results. However, work is still in progress to improve its accuracy and to test its applicability to a wider class of problems. We have also demonstrated the efficacy of the ν FDTD when used to solve well-logging problems that are typically computationally expensive, not only because of the large problem size, but also because of low frequency range of interest. Also, we have pointed out that since ν FDTD relies upon the conventional FDTD to solve different types of problems, its performance can be further enhanced by parallelizing the algorithm, which would be desirable.

Publications from this Dissertation

Book Chapters

- “An Efficient Dipole-Moment-based Method of Moments (MoM) formulation”, *Computational Electromagnetics: Recent Advances and Engineering Applications*, Springer-Verlag, New York, to be published July 2013.
- “New Finite Difference Time Domain(ν FDTD) Electromagnetic Field Solver”, *Computational Electromagnetics: Recent Advances and Engineering Applications*, Springer-Verlag, New York, to be published July 2013.

Journals

- “Numerically Efficient Method of Moments Formulation valid Over A Wide Frequency Band including Very Low Frequencies”, *IET Microwaves Antennas & Propagation*, Vol. 6, Issue 1, Page(s): 46-51, 2012.
- “The Dipole Moment (DM) and Recursive Update in Frequency Domain (RUFD) Methods: Two Novel Techniques in Computational Electromagnetics”, *URSI Radio Science Bulletin 338*, September 2011.

Conference Proceedings

- “ ν FDTD: A Novel Algorithm for Improving Conformal FDTD Method”, accepted for *IEEE International APS and UNSC/URSI National Radio Science Meeting*, 2013.
- “A New Impedance Boundary Condition for FDTD Mesh Truncation”, accepted for *IEEE International APS and UNSC/URSI National Radio Science Meeting*, 2013.

- “ ν FDTD: A Novel Algorithm for Dealing with Curved Objects in the Context of FDTD”, in Proc. of *IEEE International APS and UNSC/URSI National Radio Science Meeting*, 2012.
- “Estimating effective Depth of Gas Wellbore Using Electromagnetic Techniques”, in Proc. of *IEEE International APS and UNSC/URSI National Radio Science Meeting*, 2012.
- “A New Efficient Numerical Technique for the Analysis of Microstrip Circuits Characterized by Rough Profiles”, in Proc. of *IEEE International APS and UNSC/URSI National Radio Science Meeting*, 2012.
- “Formulating Matrix Equations in the Context of MoM by using the Dipole Moment (DM) Method instead of Green’s Functions”, in Proc. of *The International Conference on Electromagnetics in Advanced Applications (ICEAA)*, Cape Town - South Africa, September 2012.
- “On the Hybridization of Dipole Moment (DM) and Finite Methods for Efficient Solution of Multiscale Problems”, in Proc. of *The 5th European Conference on Antennas and Propagation*, 2011.
- “A numerically efficient approach to metamaterial (MTM) modeling”, in Proc. of *International Workshop on Antenna Technology (iWAT)*, 2011.
- “Accurate Computation of Input Impedance of Nano Antennas”, in Proc. of *IEEE International APS and UNSC/URSI National Radio Science Meeting*, 2011.
- “A Universal and Numerically Efficient Method of Moments Formulation Covering a Wide Frequency Band”, in Proc. of *IEEE Antennas and Propagation Society International Symposium*, Spokane - WA, July 2011.

- “A Universal Approach for Generating Electromagnetic Response over a Wide Band Including Very Low Frequencies”, in Proc. of *IEEE International APS and USNC/URSI National Radio Science Meeting*, 2011.
- “Singularity-Free Approach for the Evaluation of the Matrix Elements in the Context of the Method of Moments Based on the Use of Closed-Form Expressions for the Fields Radiated by the Subdomain Basis Functions”, in Proc. of *IEEE International APS and USNC/URSI National Radio Science Meeting*, 2010.
- “A Universal Dipole-Moment-Based Approach for Formulating MoM-Type Problems without the Use of Green’s Functions”, in Proc. of *The 4th European Conference on Antennas and Propagation*, 2010.
- “Numerical Solution of Scattering from Metallo-Dielectric composites via the CBFM applied in Conjunction with the Dipole Moment Approach (DMA)”, in Proc. of *IEEE International APS and USNC/URSI National Radio Science Meeting*, 2010.
- “RUFD: A General-purpose, Non-Iterative and Matrix-Free CEM Algorithm for Solving Electromagnetic Scattering and Radiation Problems in the Frequency Domain”, in Proc. of *20th International Symposium on Electromagnetic Theory*, Germany, August 16-19, 2010.
- “On the Hybridization of RUFD Algorithm with the DM Approach for Solving Multiscale Problems”, in Proc. of *20th International Symposium on Electromagnetic Theory*, Germany, August 16-19, 2010.
- “A New-Dipole-Momentbased MoM Approach for Solving Electromagnetic Radiation and Scattering Problems”, in Proc. of *IEEE International APS and USNC/URSI National Radio Science Meeting*, 2009.
- “A Novel Technique for Electromagnetic Modeling of Extremely Small Objects”,

in Proc. of *IEEE International APS and USNC/URSI National Radio Science Meeting*, 2009.

Bibliography

- [1] R. Garg, *Analytical and computational methods in electromagnetics*. London: Artech House, 2008.
- [2] A. F. Peterson, S. L. Ray, and R. Mittra, *Computational methods for electromagnetics*. New Jersey: IEEE Press, 1997.
- [3] D. K. Cheng, *Field and wave electromagnetics*. Addison-Wesley, 1989.
- [4] R. F. Harrington, *Field computation by moment methods*. New York: The Macmillan Company, 1968.
- [5] R. Mittra, *Computer techniques for electromagnetics*. New York: Hemisphere Publishing Corporation, 1987.
- [6] R. F. Harrington, *Time-harmonic electromagnetic fields*. New Jersey: IEEE Press, 2001.
- [7] J. Bringuier, “Multi-scale techniques in computational electromagnetics,” Ph.D. dissertation, The Pennsylvania State University, 2010.
- [8] C. A. Balanis, *Antenna theory: analysis and design*. New Jersey: John Wiley & Sons, 2005.

- [9] S. Rao, D. Wilton, and A. Glisson, "Electromagnetic scattering by surfaces of arbitrary shape," *IEEE Trans. Antennas and Propagation*, vol. 30, no. 3, pp. 409–418, 1982.
- [10] E. Lucente, A. Monorchio, and R. Mittra, "An iteration-free MoM approach based on excitation independent characteristic basis functions for solving large multiscale electromagnetic scattering problems," *IEEE Trans. Antennas and Propag.*, vol. 56, pp. 999–1007, April 2008.
- [11] R. Mittra and K. Du, "Characteristic basis function method for iteration-free solution of large method of moments problems," *Progress In Electromagnetics Research*, vol. 6, pp. 307–336, 2008.
- [12] N. Mehta, "Numerical analysis of frequency selective surfaces," Master's thesis, The Pennsylvania State University, 2010.
- [13] S. J. Kwon and R. Mittra, "Impedance matrix generation by using fast matrix generation (FMG) technique," *Microwave and Optical Technology Letters*, vol. 51, pp. 204–213, January 2009.
- [14] E. C. Jordan and K. G. Balmain, *Electromagnetic waves and radiating systems*, ser. Prentice-Hall electrical engineering series. Prentice-Hall, 1968.
- [15] K. S. Yee, "Numerical solution of initial boundary value problems involving maxwell's equations in isotropic media," *IEEE Trans. Antennas and Propag.*, vol. 14, no. 3, pp. 302–307, May 1966.
- [16] C. Pflaum and Z. Rahimi, "An iterative solver for the finite-difference frequency-domain (FDFD) method for simulation of materials with negative permittivity," *Numer. Linear Algebra Appl.*, vol. 14, no. 0, pp. 1–6, 2009.

- [17] G. Mur, "Absorbing boundary conditions for the finite-difference approximation of the time-domain electromagnetic field equations," *IEEE Trans. on Electromagnetic Compatibility*, vol. 23, pp. 377–382, 1981.
- [18] J. P. Berenger, "Three-dimensional perfectly matched layer for the absorption of electromagnetic waves," *J. Comp. Phys.*, vol. 127, p. 363–379, 1996.
- [19] W. Yu, R. Mittra, T. Su, Y. Liu, and X. Yang, *Parallel finite-difference time-domain Method*. London: Artech House, 2006.
- [20] A. Taflov and S. C. Hagness, *Computational electrodynamics – the FDTD method*. MA: Artech House, 2005.
- [21] K. Naishadham and X. P. Lin, "Application of spectral domain prony's method to the FDTD analysis of planar microstrip circuits," *IEEE Trans. on Microwave Theory and Techniques*, vol. 42, pp. 2391–2398, 1996.
- [22] M. A. Schamberger, S. Kosanovich, and R. Mittra, "Parameter extraction and correction for transmission lines and discontinuities using the finite difference time domain method," *IEEE Trans. on Microwave Theory and Techniques*, vol. 44, pp. 919–925, 1996.
- [23] T. K. Sarkar, Z. A. Maricevic, and M. Kahrizi, "An accurate de-embedding procedure for characterizing discontinuities," *International Journal of Microwave and Millimeter-Wave Computer-Aided Engineering*, vol. 2, no. 3, pp. 135–143, 1992.
- [24] W. Yu and R. Mittra, "A conformal FDTD software package modeling antennas and microstrip circuit components," *IEEE Trans. Antennas and Propagation*, pp. 28–39, 2000.

- [25] C. M. Furse, “Application of the Finite Difference Time Domain method to bioelectromagnetic simulations,” *Applied Computational Electromagnetics Society Newsletter*, 1997.

VITA

Kadappan Panayappan was born on 26th December 1984 in Chennai, Tamilnadu, India. He completed his high school from Saint Mary's Anglo Indian Higher Secondary School, Chennai, India in 2002. He obtained his Bachelors in Engineering in Electronics and Communication Engineering from Anna University, Chennai, India in 2006. In 2008, he obtained his Master of Technology in RF and Microwave Engineering from Indian Institute of Technology, Kharagpur. In August of 2008, he joined the Department of Electrical Engineering at The Pennsylvania State University, USA where he continued as a graduate research assistant obtaining his PhD in May 2013. His research interests include Finite Difference Time Domain (FDTD) method, hybrid techniques to enhance the performance of FDTD, low frequency electromagnetic response, handling multiscale problems, improving the performance of conformal FDTD, parallel programming and processor specific optimization.